Filtered Rayleigh Scattering with an Application to Force Component Decomposition

Sean William Powers

Dissertation submitted to the Faculty of the
Virginia Polytechnic Institute and State University
in partial fulfillment of the requirements for the degree of

Doctor of Philosophy
in
Aerospace Engineering

K. Todd Lowe, Chair
Joseph A. Schetz, Co-chair
Rakesh K. Kapania
Gregory Young

April 6, 2023
Blacksburg, Virginia

Keywords: Filtered Rayleigh Scattering, Auto-Processing, Rake Replacement, Control Volume Analysis, Force Decomposition

Copyright 2023, Sean Powers

Filtered Rayleigh Scattering with an Application to Force Component Decomposition

Sean William Powers

(ABSTRACT)

Filtered Rayleigh scattering (FRS) is a powerful optical-based technique that allows for simultaneous, non-intrusive measurement of three-component velocity, static temperature, and static density. It is uniquely suited to measure turbomachinery forces, which can be divided into core and bypass forces, as well as thrust and drag, using control volume analysis, specifically the extended parallel expanded streamtube method developed in this work. However, post-processing raw FRS data into usable data and defining the control volume can be challenging. The post-processing scheme uses non-linear fitting methods, such as non-linear least-squares or particle swarm optimization, to minimize the fit error between a simulated spectrum and an experimentally measured spectrum. Once the minimum error solution is obtained, the fitted variables, including static temperature, static density, and velocity, can be extracted while accounting for unwanted scattering sources, such as Mie and background scattering. To validate this model, several experiments were conducted, culminating in a planar FRS measurement in the exhaust of the Honeywell TFE731-2 turbofan engine. The core and bypass flow streams were separated using classic turbulence model schemes, such as the maximum transverse gradient of the mean velocity. The results of this test showed a minimal difference of only 0.2% between the FRS-measured total force and the force balance-measured total force, with an uncertainty of approximately 2% in the FRS total force. The core and bypass separation allowed the bypass ratio to be calculated with an error of approximately 2%. However, the uncertainty of the core and bypass forces was approximately 10% due to the uncertainty in the dividing location between the two flow streams. Overall, this combined methodology provides a way to accurately measure forces and decompose those forces into individual components in aerodynamic flows, specifically turbomachinery. These results pave the way for future in-flight force measurement capabilities.

This work received support from Pratt & Whitney through the Center of Excellence at Virginia Tech.

Filtered Rayleigh Scattering with an Application to Force Component Decomposition

Sean William Powers

(GENERAL AUDIENCE ABSTRACT)

Filtered Rayleigh scattering (FRS) is a laser-based measurement technique that makes use of the scattering of light off particles that are much smaller than the wavelength of light that hits them (i.e., Rayleigh scattering of air molecules). The scattered laser light is altered after encountering particles in predictable ways that can be related to changes in velocity, temperature, and density. However, other sources of scattered light interfere with the pure Rayleigh scattering signal such as Mie and background scattering. Mie scattering is the scattering of light off particles that are much bigger than the wavelength of light that hits them (i.e., dust particles suspended in air). Background scattering is the laser light scattered off physical objects that reflect back into the region of interest. The different types of scattering are accounted for with intensive modeling and iterative fitting schemes where the error between simulated data and experimental data is minimized. This fit allows for velocity, temperature, and density information to be extracted from the measured scattered light. This iterative scheme is then applied to experimental measurements on the ground with mini turbojet engines as well as full-scale turbofan engines. A data grouping technique is derived such that the total measured force using FRS can be divided into individual contributions from different parts of the engine. These developed techniques have laid the foundation for future in-flight measurements of engine forces.

This work received support from Pratt & Whitney through the Center of Excellence at Virginia Tech.

Acknowledgments

Many individuals deserve my acknowledgment and thanks for their contribution and support throughout my time here at Virginia Tech. I would like to start with my co-advisor Dr. Joseph Schetz. It was because of his trust and unwavering support in me as a sophomore in my undergraduate studies that I have been afforded such amazing opportunities as attending graduate school, earning my Master's degree, and so many more that I have yet to realize. Secondly, I would like to extend my greatest gratitude to Dr. Todd Lowe for allowing me to join a world-class research team as a sophomore as well as for his mentorship and leadership during my Ph.D. studies. This appointment allowed me the opportunity to learn from the best and brightest minds that Virginia Tech has to offer. I would like to thank both of these gentlemen for supporting and shaping me into the best engineer, student, and researcher that I could be. None of this would have been possible without their trust in me. I would also like to thank Dr. Rakesh Kapania and Dr. Gregory Young for teaching and guiding me in the use of fundamental techniques in the classroom as well as many seen in this dissertation. Without their continual guidance and willingness to answer my questions, this would not have been possible.

I would like to thank Pratt & Whitney for funding this research and for providing excellent opportunities through the continued partnership at Virginia Tech's Center of Excellence. I would also like to acknowledge and thank Dr. Charles Haldeman, Andy Consiglio, Al Krejmas, and many others at Pratt & Whitney for their insightful technical discussions and project feedback. It is your feedback and support that helped progress this project and me as an engineer.

Next, I would like to acknowledge the necessary support of my friends, many of whom I have met during my years at Virginia Tech as an undergraduate and now a graduate student. I have enjoyed our time together in and outside of the lab and will always cherish our life-long friendship. I would also like to thank my team members Evan Warner, Garrett Pitt, Keaton Hanley, Matt Boyda, Mady Bundy, and Dr. Gwibo Byun for helping me grow and providing valuable assistance at every step of the way.

Finally, I would like to dedicate this dissertation to my family who has always supported me in my many endeavors. To my mom and stepdad, Angie and Jason Smith, my dad, Todd Powers, and my sisters, Ashley and Bekah Smith, I love you.

Sean W. Powers

Attributions

Several professors and colleagues contributed to the research and writing contained in this dissertation. A brief description of their contributions is included below:

Dr. K. Todd Lowe and Dr. Joseph A. Schetz are co-advisors and committee chairs for this research. Both provided extensive guidance on the research plan, secured research funding, and provided editorial revisions and advice on the analysis presented in this dissertation.

Dr. Rakesh K. Kapania and Dr. Gregory Young are advisors for this research. They provided editorial revisions and advice on all the analyses presented in this dissertation.

Dr. Gwibo Byun is an aerospace and ocean engineering research scientist. He provided invaluable mentorship and assistance in every aspect of this work. He is the second author of most of the papers contained in this dissertation.

Dr. Charles Haldeman, Andy Consiglio, and Al Krejmas are technical fellows at Pratt & Whitney. They provided extensive guidance on the research plan and facilitated weekly technical discussions.

Contents

List of Figures **x**

List of Tables **xix**

1 - Introduction **1**

1.1 Dissertation Structure and Contents 2

1.2 Achievements 4

1.2.1 Publications 5

2 - Literature Review **6**

2.1 In-Flight Control Volume Development 6

2.1.1 Description of Current Industry Practices and Methods 6

2.1.2 Theoretical Methods 14

2.1.3 Comparison of Industry Methods and Theoretical Methods 21

2.1.4 Simulation and Experimental In-Flight Force Examples 22

2.2 Filtered Rayleigh Scattering 26

2.2.1 Fundamental Description 27

2.2.2 Data Processing Techniques 30

2.2.3 Applications and Challenges 37

2.3 Knowledge Gaps 41

2.3.1 In-Flight Control Volume 42

2.3.2 Filtered Rayleigh Scattering 43

2.3.3 In-Flight Control Volume and Filtered Rayleigh Scattering Technique Combination 44

3 - Processing Techniques and Algorithms for Filtered Rayleigh Scattering Images Including Mie and Background Scattering Contributions 46

3.1 Modeling and Simulation 48

3.1.1 Theoretical Modeling 48

3.1.2 Uncertainty Analysis 71

3.1.3 Simulated Experiment 76

3.2 Experimental Investigation Techniques 78

3.2.1 Camera Calibration 78

3.2.2 Camera Registration 80

3.2.3 Wavenumber Finding 83

3.2.4 Laser Vector Finding 85

3.3 Final Experimental Data Processing 86

3.3.1 Benchtop Freejet 86

3.3.2 JetCat P100-RX TurboJet 92

3.4 Final Remarks and Discussion 107

3.5 Nomenclature 108

4 - Filtered Rayleigh Scattering Measurement Technique Validation in Engine Applications and Boundary Layers 111

Abstract 112

Nomenclature 112

4.1 Introduction 112

4.2 Filtered Rayleigh Scattering 113

4.2.1 Rayleigh Scattering Theory 113

4.2.2 Filtered Rayleigh Scattering Theory 114

4.3 Test Setup 114

4.3.1 Simulation Setup 115
4.3.2 Experimental Setup 115
4.4 FRS Result Comparison to Probe and CFD Results 117
4.4.1 Non-Binned Results 117
4.4.2 Binning Statistics and Results 119
4.5 Conclusions 122
Acknowledgements 122
References 122

5 - Control Volume Analysis for Experimental Force Accounting 124

Abstract 125
Nomenclature 125
5.1 Introduction 127
5.2 Control Volume Techniques and Current Extension 128
5.2.1 Technique Selection 128
5.2.2 Extended PES Method 131
5.3 Uncertainty Derivation 133
5.3.1 Random Uncertainty 134
5.3.2 Bias Uncertainty 135
5.3.3 Control Volume Uncertainty 136
5.3.4 Total Uncertainty 137
5.4 Simulated Experiment as a Test Case of the EPES Method 138
5.4.1 Simple Simulation Setup 138
5.4.2 Simple Simulation Results 139
5.5 Conclusions 142
Acknowledgements 143

References 143

6 - Experimental Turbofan Ground Force Measurement and Accounting using Filtered Rayleigh Scattering and Control Volume Analysis 146

Abstract 147

Nomenclature 148

6.1 Introduction 149

6.2 Filtered Rayleigh Scattering Measurement Technique 150

6.2.1 Theory and Modeling 150

6.2.2 Fitting Scheme 152

6.3 Experimental Setup at the Virginia Tech TurboLab 153

6.4 Filtered Rayleigh Scattering Results 155

6.5 Uncertainty Analysis 159

6.5.1 Random Uncertainty 159

6.5.2 Bias Uncertainty 161

6.5.3 Control Volume Uncertainty 162

6.5.4 Total Combined Uncertainty 162

6.6 Conclusions 164

Acknowledgements 165

References 166

7 - Conclusions and Outlook 167

7.1 Conclusions 168

7.2 Outlook 170

References 172

List of Figures

2.1 Industry standard station numbering system. 7

2.2 Overall performance method for a single-spool fixed-nozzle turbojet. 9

2.3 Gas-Path/Nozzle method for a single-spool fixed-nozzle turbojet. 10

2.4 Gas-Path/Nozzle method for a turbofan. 11

2.5 Control volume used to solve the compound flow analysis method. 11

2.6 CFA process flow map. 12

2.7 Left: Example traversing rake arrangement. Right: Traversing rake used on a North American Vigilante with J-79 engines. 13

2.8 Control volume development timeline. 15

2.9 Cutaway view of three-dimensional energy method control volume. 17

2.10 Mechanical energy outflow rate expansion. 19

2.11 Viscous dissipation rate expansion. 19

2.12 Parallel-streamtube force estimation method, with thrust definition streamtubes (red), and profile drag definition streamtubes (blue). 20

2.13 Drawn control volume, drag equations, and SUBOFF configuration. 22

2.14 Left: Comparison of the surface integral and the wake integral results. Right: Contribution of pressure and momentum fluctuation terms. 23

2.15 Left: Example engine boundary conditions w/o modeling engine internals. Right: Engine/wing combination meshing. 24

2.16 Left: Jet-propelled aircraft; control volumes/boundaries. Middle: Integration volumes V_V and V_W for viscous drag and wave drag. Right: Drag bar chart. 24

2.17 Left: Half-model KH3Y. Right: Methodology comparisons. 25

2.18 Upper left: No flow reference signal. Upper right: Higher temperature. Bottom left: Higher density. Bottom right: Higher velocity. 28

2.19 Rayleigh scattering after a molecular filter is used to attenuate the laser light. 28

2.20 FRS signal created from molecular Rayleigh scattering and background scattering (from walls and/or windows). Left: Background and molecular Rayleigh scattering spectra. Middle: Transmission profile of the atomic/molecular filter. Right: Convolution of the scattered light spectrum and transmission profile resulting in the FRS signal. 29

2.21 Left: FRS geometry and measured velocity components for a single camera/laser pair. Right: Transformation matrix of the velocity into a global, orthogonal system denoted U, V, and W in modified form for three cameras. 30

2.22 Examples of Rayleigh scattering lineshapes. The black lines are modeled by the S6 model. The red lines are the SVSA approximation. 33

2.23 Left: Example images using a calibration plate with six different cameras. Right: Calibration results show all six cameras in 3D space compared to the calibration plate. 34

2.24 From left to right: noisy image, Gauss filtering, Total variation, Neighborhood filter, translation invariant wavelet thresholding, and NL-means algorithm. . 35

2.25 Mesh optimization on a 2-D CT image slice (a) of the kidney. Initial (b) and optimized (c) discretizations with 61 nodes; and initial (d) and optimized (e) discretizations. 36

2.26 Flow characterization for axisymmetric flow (left three figures) and distorted flow (right figure). Measured = pitot-probe. Rayleigh = FRS. 38

2.27 Composite Rayleigh spectral lineshape. 39

3.1 Tenti S6 model results using various numbers of nodes. RMSE and generation time are also included. The right side shows the normalized percent difference between the "true spectra" and the different nodal levels. 50

3.2 Support vector spectrum approximation (SVSA) comparison to the Tenti S6 model with a different number of nodes. RMSE and generation time are also included. The pink charts on the right represent the normalized percent difference between the Tenti S6 model and SVSA model at different nodal levels. 52

3.3 Normalized Rayleigh-Brillouin scattering lineshape model comparison. Similar to that shown by Doll et al. Left: Rayleigh-Brillouin scattering lineshape comparison. Right: Max normalized difference to $RBS - S6$. Plotted for $\theta = 90°$, $T_s = 300\ K$, and $\rho_s = 1.225\ kg/m^3$ 53

3.4 Normalized $RBS - S6$ Rayleigh-Brillouin scattering lineshape dependencies. Left: Static temperature. Middle: Static density. Right: Scattering angle. . . 54

3.5 Rayleigh model dependencies on static temperature, static density, and scattering angle. 55

3.6 Simplified scattering angle visual. 56

3.7 Effect of Mie and background scattering on final scattering signal. Generation parameters: T_s of 300K, θ of 90°, ρ_s of 1.1 kg/m^3, Mie_{IR} and $Bknd_{IR}$ of 0.1 and 0.01, and V of 100 m/s. Note: Background scattering shown shifted relative to other scattering due to non-zero velocity. 57

3.8 Iodine transmission spectrum (Forkey spectrum) for an iodine vapor cell. Representative RBS signal is also included. 59

3.9 Experimentally found iodine transmission spectrum. Note that the flat line of the transmission is sensor-dependent. Left: Log scale. Right: Linear scale. 59

3.10 PD fit (blue circles) to theoretical transmission spectrum (red line) to back out scanned wavenumbers. 60

3.11 Spectra comparison between the theoretical transmission spectrum as well as the experimentally found iodine transmission spectrum. 60

3.12 Comparison of hybrid iodine transmission model and theoretical transmission model. 61

3.13 1-3: Example convolutions with the I_2 transmission spectrum in black, the total scattering spectrum in blue, and the FRS signal in red. Bottom Right: Final convolved spectrum in blue plotted with the individual contributions from the three example frequencies. The center wavenumber is approximately 18788.4 cm^{-1}. Printed with permission from Warner et al. 62

3.14 Calculating the convolved signal. Top left: Pure Mie scattering convolution. Top right: Pure background scattering convolution. Bottom left: Pure Rayleigh-Brillouin scattering convolution. Bottom right: Total convolution and pure Rayleigh-Brillouin scattering convolution. 63

3.15 Convolution spectra dependencies on flow properties. X-axis is $\Delta Wavenumber$ ($\Delta\nu$) and Y-Axis is intensity in arbitrary units. Shown using the $RBS - S6$ Rayleigh-Brillouin scattering model. Constants when variable is not being varied: $V = 0\ m/s$, $T = 300\ K$, $\rho = 1.18\ kg/m^3$, $\theta = 90°$, $Mie_{IR} = 0.25$, and $Bknd_{IR} = 0.5$. 66

3.16 Convolution spectra using other Rayleigh models. Showing dependence on velocity, static temperature, static density, scattering angle, Mie scattering and background scattering. 67

3.17 Top two charts: Mie and background scattering effects with and without a velocity of 100 m/s. Bottom two charts: Mie and background combined scattering effects with and without a velocity of 100 m/s. 68

3.18 Non-linear least-squares model fitting. Picture one is the start and picture six is the best-fit case. Y-axis is intensity in arbitrary units while the X-axis is the number of points along the spectra. 70

3.19 Convergence of solved variables over 900 iterations. 71

3.20 Monte Carlo results at various SNR levels with each Rayleigh scattering model using a 95% confidence interval. 72

3.21 Examples of various SNR levels (in dB) using the FRS curve. 73

3.22 Averaging lower SNR spectra to create an effectively higher SNR averaged spectrum. 73

3.23 Examination of the effect of averaging schemes and non-linearity effect. The right side charts represent the normalized percent difference between the average output and average input curves. 74

3.24 Simulated planar data of a non-heated freejet. 76

3.25 Processed simulated data of a non-heated freejet. Top: SNR = 20 dB. Bottom: SNR = 30 dB. 77

3.26 Example of one camera simulated calibration using SolidWorks. Pictured are the camera location, the camera field-of-view, and the calibration plate itself. 78

3.27 Left: One-camera calibration. Top right: Two-camera calibration. Bottom right: Three-plus camera calibration. Green areas represent less than a 1% error in X, Y, and Z world coordinates, yellow represents a potentially significant error, and red represents not calibratable. Charts to the side show planar constant results with the red coordinate axes having a significant error. 80

3.28 Left: Original calibration plate images. Right: Cropped and warped images. Viewed as if both images were taken from a head-on perspective. 81

3.29 Left: Camera one bad registration. Right: Camera two bad registration. . . 81

3.30 Addition of a shape on the calibration images to help with image registration. 82

3.31 Correct correlation and registration of the calibration images. 83

3.32 Graphical representation of the particle swarm algorithm. Modified from Chen et al. 84

3.33 Experimentally found wavenumber. Left: Flow-on wavenumber fitting. Right: Flow-off wavenumber fitting (purple circles) overlaid onto the flow-on (blue circles) fitting result. 84

3.34 Example of the laser calibration process. 85

3.35 Benchtop non-heated freejet. 87

3.36 Approximate view from the camera of the laser plane above the jet exhaust. 87

3.37 Post-processing flow chart to achieve the six output variables. 88

3.38 One-component axial velocity rotation. 89

3.39 Multi-level processing on the benchtop freejet. Top left: Scattering angle. Top middle: Static temperature. Top right: Axial velocity. Bottom left: Mie intensity ratio. Bottom middle: Background intensity ratio. Bottom right: Static density. 90

3.40 Blue and black: FRS results transformed into total results to compare with the total measurements made by the probe. Red: Normalized percent difference between probe data and FRS data. 91

3.41 Post-processing development and comparisons. 92

3.42 Simple JetCat mounting and wiring at Virginia Tech's turbo-machinery lab (TurboLab). 93

3.43 Left: JetCat P100-Rx mass flow of air. Right: JetCat P100-RX mass flow of fuel from Davis et al. 94

3.44 Top left: Filtered Rayleigh scattering signal from each product individually. Top right: Comparison of combustion product mixture to air. Bottom: Percent difference in the filtered Rayleigh scattering signal over the wavenumbers investigated. 95

3.45 Left: Zoomed-out view of the JetCat in flow-on conditions with the beam dump near the bottom of the image. Right: Zoomed-in view of the JetCat in flow-on conditions with a long exposure time to see the jet plume. Jet plume in laser sheet visible in both images. 96

3.46 Total temperature and total pressure traverse setup in the exhaust of the JetCat. 97

3.47 Left: Example image of incomplete combustion leading to large amounts of soot in the exhaust. Right: Complete combustion with a clean laser sheet. . 98

3.48 Iodine transmission spectrum (Forkey spectrum) with a zoomed-in view of the tripe-trough region. 99

3.49 Monte Carlo results at various SNR levels with the $RBS - D$ Rayleigh scattering model using a 95% confidence interval. 100

3.50 Geometry and measured velocity components for a single camera/laser pair from Cadel et al. 100

3.51 Auto-processed results for scattering angle, static density, static temperature, And Mie and background intensity ratio. 102

3.52 Left: Sensed velocity charts from each camera. Right: Sensed velocity converted to orthogonal velocity components. 103

3.53 Swirl angle. Positive is clockwise. Left: 5-hole probe measurement data from Coulon et al. Right: FRS results. 104

3.54 Blue: Vertical (left) and horizontal (right) probe line and FRS data taken at approximately 100 mm. Error bars are shown with 95% confidence bounds. Right: Normalized percent difference between the probe data and FRS data in red. 106

4.1 A: Laser Rayleigh scattering signal (LRS). B: T_s influence. C: ρ_s influence. D: $\overrightarrow{V}$ influence. 114

4.2 FRS technique. The iodine transmission (τ_{I_2}) spectrum in A1 and B1 is convolved with the total Rayleigh scattering spectrum (S_{TOT}) to produce the final FRS spectrum (S_{FRS}) in A2 and B2. 114

4.3 ANSYS Fluent simulation results at 75% corrected fan speed (CFS). 115

4.4 TFE731-2 experimental setup CAD. 115

4.5 A: High-speed inlet with associated static pressure and strain gauge measurement locations as well as the two boundary layer probes. B: View inside the OTS. C: View outside the OTS. D: Entire setup looking from the engine upstream. E: Entire setup looking from the bellmouth downstream. 116

4.6 A: Camera module (Cam Mod or CM) locations and fields-of-view. B: Filtered image of optical rake. C: Unfiltered image of optical rake. 116

4.7 Axial velocity comparison between all three techniques. A: Linear y-scale. B: Log y-scale. 117

4.8 Temperature comparison between FRS and CFD. A: Static temperature. B: Total temperature. 118

4.9 Density comparison between FRS and CFD. A: Static density. B: Total density. 118

4.10 Pressure comparison between all three techniques. A: Static pressure. B: Total pressure w/ linear Y-scale. C: Total pressure w/ log Y-scale. 119

5.1 Overview of aerodynamic force decomposition methods throughout history. An example six-sided control volume is included in the bottom right. 127

5.2 Force decomposition methods. A: Near-field. B: Alternative near-field. C: Far-field. D: Hybrid near-field/far-field. Core cowling was removed for clarity. Reworked from Drela. 129

5.3 Modified parallel expanded streamtube method applied to a turbofan engine where the bounds are defined by the exhaust plume edge instead of a mass-conserving streamtube. Exhaust expansion is exaggerated and is due to the growth of entrained freestream flow. 130

5.4 Extended parallel expanded streamtube method control volumes where the exhaust stream has been decomposed into core and bypass streams. Exhaust expansion is exaggerated and is due to the growth of entrained freestream flow. 131

5.5 Dividing streamsurface separating the core and bypass flow as well as the exhaust plume boundary dividing the bypass and freestream flow. Exhaust expansion is exaggerated and is due to the growth of entrained freestream flow. 132

5.6 Visuals for uncertainty sources. A: Planar random uncertainty. A Gaussian distribution between -1 and 1. B: Planar bias uncertainty. C: Control volume uncertainty. 133

5.7 Monte Carlo histogram of mean subtracted $\bar{V}$. Skewness and kurtosis values show the non-normal distribution of this equation. The black line plotted is a normal distribution for reference. The numbers used are from the simple simulation which is discussed later. 134

5.8 A: Unblended profiles of measured variables. B: Measured variable values approximating a Honeywell TFE731-2 in-flight at Mach 0.5. C: Blended profiles of measured variables using hyperbolic tangent smoothing. 138

5.9 Required planar values to compute the total and component forces. A: Axial velocity. B: Square of the axial velocity gradient. C: Static density. D: Expanded velocity. 139

5.10 A: Core and bypass bound using the max of the square of the velocity gradient. B: Separation of flow streams. C: 95% confidence interval in the CV bounds using the CV uncertainty quantification framework. 140

6.1 A: Baseline Rayleigh scattering spectrum. B: Higher temperature Rayleigh scattering spectrum. C: Higher density Rayleigh scattering spectrum. D: Higher velocity Rayleigh scattering spectrum. E: Filtered Rayleigh scattering technique. F: Final convolution after frequency scanning. 151

6.2 Comparison of minimum search algorithms. A: Styblinski-Tang function. B: Derivative-free minimum search algorithm. C: Particle swarm optimization minimum search algorithm. 153

6.3 A: View of engine cell with all three camera modules visible. B: Simple CAD model showing the location of the force balance. C: Calibration plate (FRS measurement plane) location in the exhaust of the Honeywell TFE731-2. D: Nominally 532 nm wavelength laser sheet made by a scanning mirror mounted on the wall. 154

6.4 Raw FRS images from the experiment. Images were taken at the same time in a low iodine transmission region. A: Image from the filtered camera showing large Mie scattering effects in the core. B: Image from the unfiltered camera in which the laser sheet is visible along with the core and bypass regions. . . 156

6.5 Planar FRS results for the exhaust flow of a Honeywell TFE731-2. Green indicates directly measured quantities. Orange indicates derived quantities. Note: All figures have a 2x2 median filter applied. 157

6.6 Axial velocity contour with in-plane velocity vectors. Four representative spectra with plotted measured spectra in red and fitted modeled spectra in blue. 158

6.7 Grouping of data into flow streams using the square of the axial velocity gradient. A: Clear indicators of the mixing layer between the three different regions. B: Maximum of the squared velocity gradient shown in magenta representing the dividing line between the flow streams. C: Final data grouping. 158

6.8 Monte Carlo simulation results to get one-sigma (68%) primary uncertainties. A: Background scattering intensity ratio. B: Mie scattering intensity ratio. C: Static density. D: Static temperature. E: Sensed velocity. 160

6.9 Finding the control volume error by using confidence bounds and calculating the force through that area. A: Highlighted maximum locations. B: Grouped data points to be included in error calculation. Two decimal points are used to show relative magnitudes. 162

6.10 Error influence coefficients (EICs) for all uncertain variables. X is a placeholder variable. A: Log scale. B: Linear scale. 164

List of Tables

3.1 Overview of Rayleigh-Brillouin scattering models, spectrum generation time, type of model, and the operation limits for each model. ML = Machine Learned. 53

3.2 Threshold value for each solved variable. 70

4.1 FRS 3-component velocity results within the camera module field-of-view overlap region with approximate 95% confidence uncertainty bounds. 118

5.1 Primary uncertainties for random 140

6.1 Force results using FRS and control volume analysis. 159

6.2 Two-sigma (95%) confidence intervals for all random uncertainty values. Values to the left of the triple vertical line are directly measured by FRS. Two decimal points are used to show relative magnitudes. 160

6.3 Two-sigma (95%) confidence intervals for all random uncertainty values that are not dependent on FRS measurements or flow type. 161

6.4 Bias uncertainty values (one-sigma—68%) to be used with the SUMU method. Values to the left of the triple vertical line are directly measured by FRS (values to the right are derived). Values to the right of the double vertical line are not dependent on FRS measurements. Two decimal points are used to show relative magnitudes. 161

6.5 Final force results with uncertainty values. Two-sigma (95%) confidence intervals as defined by the SUMU method. Magnitude and percent error is given. 163

[This page intentionally left blank]

Chapter 1 - Introduction

Direct measurement of in-flight forces remains an elusive, high-value, piece of information for not only engine manufacturers but airframers as well. The challenge of installing the instrumentation needed to take this data on a moving vehicle, in real flight conditions, has so far proven to be insurmountable due to the time, money, and physical hardware needed to do so. To overcome this challenge, a plethora of studies have been conducted to establish reliable techniques that use data gathered in a ground test to correlate to in-flight conditions. While these wide-ranging techniques have advantages and disadvantages they all result in low-uncertainty force calculations on the ground. However, the correlation to in-flight force is complex and long-winded. This introduces a significant increase in uncertainty compared to the ground force result. On top of the correlated force problem, engineers have very little to work with when considering flow visualization. Currently, engineers must largely rely on computational fluid dynamics (CFD) for in-flight flow visualization using correlated boundary conditions from ground tests.

The ultimate dream of any experimental aerodynamicist is an experimental technique that can provide flow visualization and temporal/spatial resolutions comparable to CFD solutions. Such a technique would require several key characteristics; 1) non-intrusive, 2) three-dimensional capability, and 3) hardware to support spatial/temporal needs and design space constraints. Three-dimensional measurement capabilities and the hardware needed for such a technique have been demonstrated in seeded techniques like particle image velocimetry (PIV) and Doppler global velocimetry (DGV). However, due to the seeding particles, these are intrusive measurements. The seeding particles can be expensive, time-consuming to manufacture or introduce, and may be highly difficult to inject into the flow.

An emerging technique called filtered Rayleigh scattering (FRS) promises non-intrusive planar measurements of three-component velocity, static temperature, and static density. The only key characteristic it cannot currently meet is a fully three-dimensional volume measurement and time-resolved values. Imagine using fiber optics to route a laser line/sheet anywhere onto a flight vehicle along with fiber imaging bundles for the cameras. This kind of application would allow for actual in-flight measurements of time-averaged forces. It should be noted that recent pushes for time-resolved filtered Rayleigh scattering have begun chipping away at this constraint.

This research aims to combine theoretical control volume methods with the FRS tech-

nique to provide a state-of-the-art measurement and flow visualization technique. This dissertation will focus on expanding the fidelity of FRS data processing and gathering with an experimental application of theoretical measurements to prove novel in-flight force measurement techniques. This includes exhaust measurements in a mini turbojet engine (JetCat), high-accuracy boundary layer measurements in the inlet of a Honeywell TFE731-2 turbofan, and full planar exhaust measurements in the same Honeywell TFE731-2 turbofan engine. These experiments are used to validate the combination of the FRS technique and extended parallel expanded streamtube method (control volume method) through static ground force measurement comparisons. This work paves the way for future in-flight force measurements using the combined control volume and FRS technique.

1.1 Dissertation Structure and Contents

This dissertation is divided into the following chapters:

Chapter 1: Provides a general introduction to the topic, the motivation of the research, and an overview of the dissertation.

Chapter 2: Provides the background for the research and an extensive literature review of the topics discussed within this dissertation.

Chapter 3: Presents the processing algorithm needed for the work in this dissertation. Several models are compared and a detailed description is given to the modeling process. This is the long-form version of a manuscript titled "Numerical Benchmarking and Experimental Validation of a Model-Based Processor for Filtered Rayleigh Scattering Flow Measurements" that is planned to be submitted to *Measurement Science and Technology*. This work provides the benchmarking and validation needed for this model-based method for interpreting FRS measurement data.

Chapter 4: Presents a research manuscript under review for journal submission and accepted into the *Conference Proceedings of ASME Turbo Expo 2023* titled "Filtered Rayleigh Scattering Measurement Technique Validation in Engine Applications and Boundary Layers." This work addresses the opportunity to replace physical rakes with optical rakes through fil-

tered Rayleigh scattering. A combination of specially designed boundary layer total pressure probe rake measurements, FRS measurements, and computational fluid dynamics (CFD) results in the inlet of a Honeywell TFE731-2 turbofan are presented. These results are compared and contrasted with a focus on results from the centerline of the inlet down to near the wall where a significant portion of the boundary layer has been measured. The inlet efficiency is calculated and compared from all three methods. This work was also nominated for best paper.

Chapter 5: Presents a research manuscript in preparation for submission to *AIAA Journal* titled "Control Volume Analysis for Experimental Force Accounting." This work shows a control volume methodology framework (extended parallel expanded streamtube method) including uncertainty analysis that has been extended from previous work. This work allows for a rigorous definition and decomposition of forces in aerodynamic flows. Backing to the analysis is given through a simple analytic example. This framework can be applied to many different measurement techniques that extend past FRS.

Chapter 6: Presents a research manuscript in preparation for submission to *AIAA Journal* titled "Experimental Turbofan Ground Force Measurement and Accounting using Filtered Rayleigh Scattering and Control Volume Analysis." This work is the culmination of all other works in this dissertation. A planar FRS exhaust measurement in the Honeywell TFE731-2 is taken which is then used in conjunction with the extended parallel expanded streamtube method to calculate the total force and then decompose that force into core and bypass components. These results are compared to a force balance with high accuracy.

Chapter 7: Presents the conclusions regarding the overall research efforts and an outline for the remaining learning needed for in-flight applications is provided. Challenges associated with both control volume methodology and filtered Rayleigh scattering are discussed. Emphasis is put on cutting-edge FRS technology that is pushing the boundaries of what is possible and may open up future possibilities with this work.

Formatting of each chapter's contents and citation style may deviate due to the different publication guidelines of the journal in which they have or will be published

1.2 Achievements

Key outcomes of the present research include:

- Development of an auto-processing algorithm for raw FRS data that is capable of producing planar scattering angle, static temperature, three-component velocity, static density, Mie scattering intensity ratio, and background scattering intensity ratio values. The algorithm uses a non-linear multi-variable least-squares iterative approach to retain high speeds and accuracy with an option to use a particle swarm optimization algorithm to increase accuracy but at slower speeds.

- Investigation of existing Rayleigh (Rayleigh-Brillouin) scattering models (analytic, numerical,a nd machine-learned) with comparison at different flow properties including combustion gas mixtures for implementation towards engine measurements.

- FRS primary uncertainty quantification through Monte Carlo simulations with comparison to Cramér-Rao Lower Bound (CRLB) analysis. Derived uncertainty analysis including random, and bias error using propagation of uncertainty.

- FRS validation experiments to compare simulated data to experimental data including random and bias uncertainty.

- First quantitative FRS boundary layer measurement through inlet testing on the Honeywell TFE731-2 high-speed inlet.

- Physical rake replacement argument made with FRS results from measurement inlet testing on the Honeywell TFE731-2 high-speed inlet where statistical methods were used to characterize FRS as well as drive down FRS measurement uncertainty.

- Control volume methodology for force decomposition derived and an uncertainty framework built considering random, bias, and control volume error using propagation of uncertainty.

- Planar FRS measurement in the exhaust of the Honeywell TFE731-2 turbofan resulted in highly accurate force measurement with core and bypass force contribution decomposition. First-of-its-kind measurement.

1.2.1 Publications

The scientific publications of the author during his Ph.D. work are listed in this section.

Peer-Reviewed Publications:

- Powers, S., Byun, G., and Lowe, T., "Numerical Benchmarking and Experimental Validation of a Model-Based Processor for Filtered Rayleigh Scattering Flow Measurements.,'" *Measurement Science and Technology.* [To be submitted]

- Powers, S., Byun, G., and Lowe, T., "Filtered Rayleigh Scattering Measurement Technique Validation in Engine Applications and Boundary Layers.,'" *ASME Turbo Expo 2023.* [Recommended for Journal and Best Paper]

- Powers, S., Hanley, K., Lowe, T., and Schetz, J., "Control Volume Analysis for Experimental Force Accounting," *AIAA Journal.* [To be submitted]

- Powers, S., Byun, G., Lowe, T., and Schetz, J., "Experimental Turbofan Ground Force Measurement and Accounting using Filtered Rayleigh Scattering and Control Volume Analysis," AIAA Journal. [To be submitted]

Conference Proceedings

- Powers, S., Warner, E., Byun, G., Lowe, T., "Auto-Processing of Filtered Rayleigh Scattering Images Including Mie and Background Scattering Contributions." In *Proceedings of the 20th International Symposium on Application of Laser and Imaging Techniques to Fluid Mechanics, 2022.* Novel Measurement Techniques. pgs. 1095 - 1116.

Presentations

- Powers, S., Byun, G., and Lowe, T., "Filtered Rayleigh Scattering Measurement Technique Validation in Engine Applications." Presented at *Advanced Instrumentation, Diagnostics and Controls for Applications in Turbomachinery (AIDCAT), 2022.*

Chapter 2 - Literature Review

The following sections will present the literature review that was completed for in-flight force measurement techniques including control volumes and filtered Rayleigh scattering (FRS) techniques. The literature between the two will be bridged by briefly explaining the concept of combining the techniques and showing relevant literature on comparable work.

2.1 In-Flight Control Volume Development

The following subsections are meant to give a detailed look into current in-flight force measurement techniques, describe the experimental and simulation work applying these techniques, and then describe the gap in the current literature. A large emphasis has been given to current industry standards and the complexity behind those techniques. The current work aims to present a methodology that can circumvent the current complexity while retaining the same magnitude of uncertainty. To do this, new and old theoretical methods will be discussed which are then used and extended in this dissertation.

2.1.1 Description of Current Industry Practices and Methods

The current resource for guiding and standardizing approaches to in-flight force measurements is the SAE aerospace information report 1703A (SAEAIR 1703A [1]). This article reviews the major processes for in-flight forces and gives a detailed look into basic definitions, analytical methods, and ground-based methods. However, this document states "There are no industry or government standards for determining in-flight forces or the associated uncertainty at present". Therefore, this document as well as its accompanying document (SAEAIR 1678B - Uncertainty of In-Flight Thrust Determination [2]), are only meant to serve as guides for the selection of methodologies. These two documents serve as the main body of information for the current in-flight force "in-practice" or "industry standard" methodologies. However, many more SAE documents exist for specific applications such as SAEAIR 4605-Propeller/Propfan In-Flight Thrust Determination [3], SAEAIR 5450 - Advanced Ducted Propulsor In-Flight Thrust Determination [4], and SAEAIR 5771A - The Measurement of Engine Thrust in an Altitude Test Facility [5]. The following descriptions will aim to define current methods for turbojets and turbofans so only SAEAIR 1703A and SAEAIR 1678B will be examined thoroughly.

SAE AIR1703A - In-Flight Thrust Determination

Distinguishing between in-flight thrust and drag forces can be ambiguous because the forces acting on the propulsion system can be difficult to define and nearly impossible to measure. Therefore, a consistent station numbering system must be used. These station numbers increase from inlet to exhaust as well as from the core to the bypass duct as seen in Fig. 2.1 from Ref. [1]. This is consistent with SAE ARP755D - Aircraft Propulsion System Performance Station Designation and Nomenclature [6].

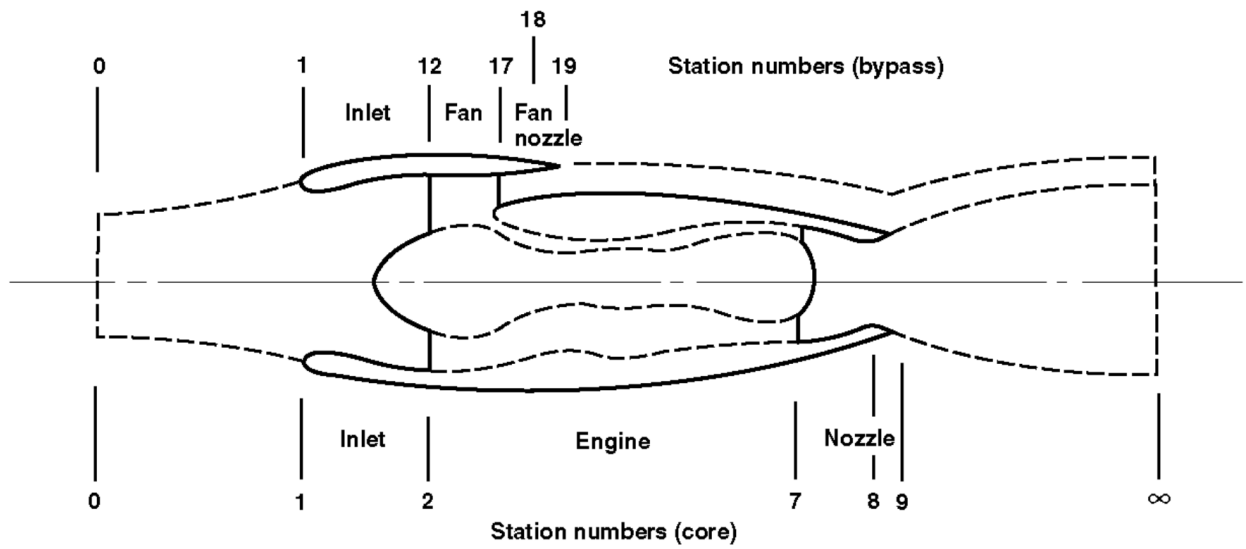

Figure 2.1: Industry standard station numbering system.

SAE AIR1703A points to three major methods that could be used for determining in-flight forces. The first is called the "Overall Performance" method. This method requires no special instrumentation within the engine gas flow path. Instead, the method relies on the use of an engine model or correlation curves that predict engine performance with minimal inputs. The model requires a large test matrix that encompasses all of the parameters that might be varied in-flight. Generally, these matrices can be completed with ground-level test facility (GLTF) data and altitude test facility (ATF) data that is accompanied by simulation data. The uncertainty of this method is generally higher than others because it cannot easily account for things such as environmental effects, inlet distortion, nozzle pressure ratio, engine deterioration, the thermal state of the engine, and control tolerances, to name a few. These uncertainties cause this method to be rarely utilized in practice. Instead, gas-path/nozzle methods that utilize gas-path instrumentation to determine engine performance with the accompanying overall performance method have become the industry standard. The overall

performance method is used as a sanity check for more complex methods.

An example of the overall performance method as applied to a turbojet can be seen in Fig. 2.2 from Ref. [1]. Little, but specific, information is needed to calculate the net thrust (Eq. 2.1). N is the engine rotational speed in RPM, T_t is the total temperature, P_t is the total pressure, P_s, is the static pressure, A is the area at that station, F_G is the gross thrust (Eq. 2.2), W is the mass flow rate, V is the velocity, θ_t is the ram-temperature ratio, and δ_t is the ram-pressure ratio. As stated previously and obvious from Fig. 2.2, this method relies heavily on correction factors and calibrations. This makes the final net thrust result reliant on uncertain parameters resulting in an even more uncertain final result.

$$F_N = F_G - F_R = W_9 V_9 + (P_{S9} - P_{S0})\, A_9 - W_0 V_0 \tag{2.1}$$

$$F_G = W_9 V_9 + (P_{S9} - P_{S0})\, A_9 \tag{2.2}$$

The "Gas-Path/Nozzle" methods make use of calibrated measurements of gas-generator-flow properties at various stations in the engine (Fig. 2.1). The basis of these methods is the determination of nozzle gross thrust and ram drag, which is often done separately. Such measurements require detailed knowledge and low uncertainty values for geometry, operating conditions, and secondary flows such as fuel addition, service bleed, and leakage. This type of information is available at the cost and time for the design, installation, calibration, and potential maintenance of special hardware needed to take these measurements. The pay-off is that this force determination method is insensitive to core performance as well as installation effects and lower uncertainty compared to the overall performance method is achievable.

The two most common examples of gas-path/nozzle methods are the area-pressure method (F/AP) and the mass flow-temperature method ($F/W\sqrt{T}$). For both of these techniques, the engine is considered to be a "gas generator" supplying flow at pressure and temperature to the exhaust nozzle. Thrust is then calculated from predicted nozzle performance. Therefore, the measurement of inlet total pressure and nozzle exit static pressure is important. On top of this, the mass flow-temperature method requires the nozzle inlet mass flow and total temperature to be known. The only difference between the F/AP and $F/W\sqrt{T}$ methods is how the ideal thrust is calculated. In practice, both methods are generally mixed in different ways depending on the engine application. The gas-path/nozzle method as applied to a turbojet can be seen in Fig. 2.3 from Ref. [1].

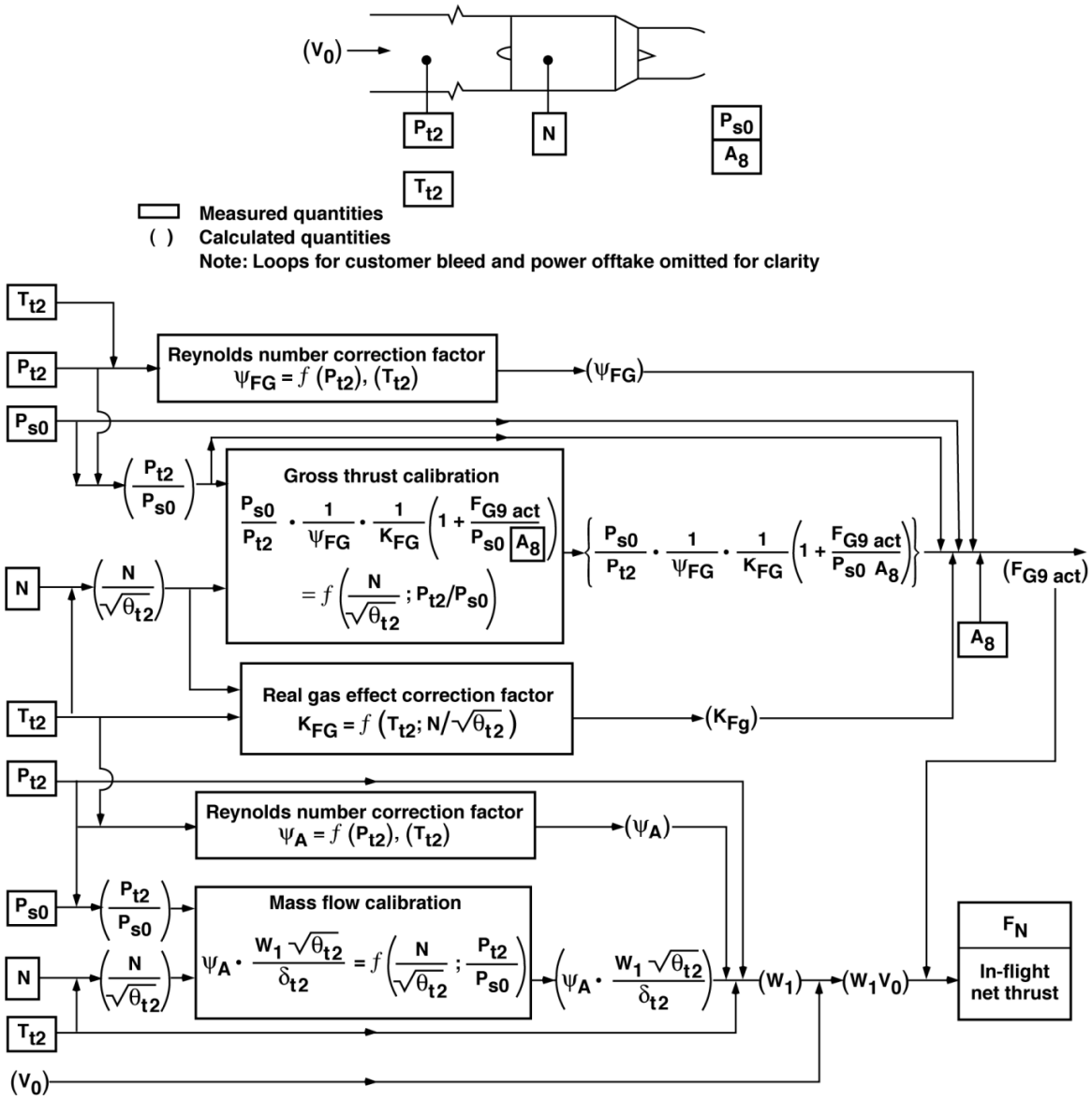

Figure 2.2: Overall performance method for a single-spool fixed-nozzle turbojet.

Figure 2.3 shows a methodology combining the F/AP and $F/W\sqrt{T}$ methods. Many of the same definitions are used in the overall performance method. However, note that the engine RPM is based on the low-pressure engine spool, and stations 8 and 16 must also be measured. This can be compared directly to Fig. 2.2. It is seen that the gas-path/nozzle method does away with all of the correlations/calibrations making it attractive to the industry as it is easier to bookkeep.

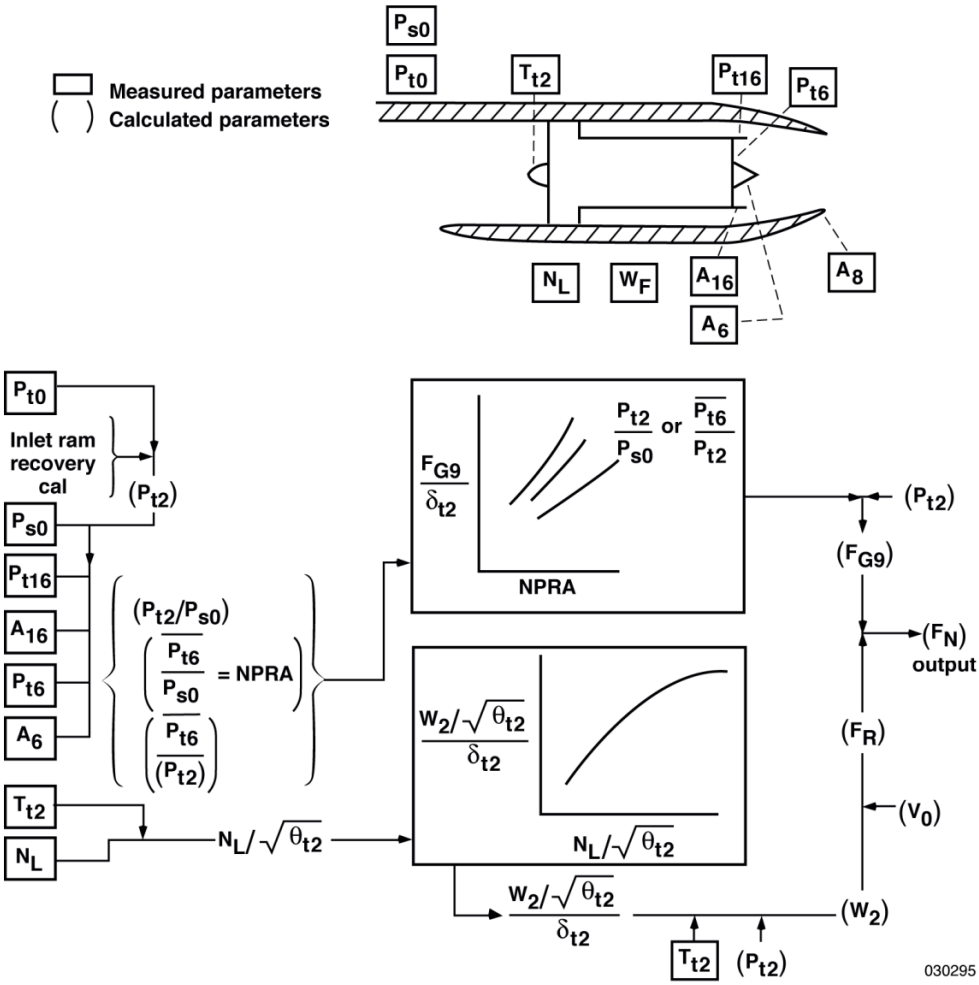

Figure 2.3: Gas-Path/Nozzle method for a single-spool fixed-nozzle turbojet.

Figure 2.4 from Ref. [1] serves to show that as the application increases in complexity (turbojet vs. turbofan), so too does the method for calculating forces. The complexity of this method has increased interest in a newly proposed method based on compound flow analysis (CFA). As before, this method requires detailed information about the geometry and operating conditions. These can be found in two ways. The first is through extensive rig test data. The second is through computational fluid dynamics (CFD). Once the data is processed, a control volume is drawn around the exhaust. The control volume is drawn assuming three distinct flow streams exist. These are the unmixed bypass flow, the mixed flow, and the unmixed core flow. These regions are placed with the assumption that no mixing occurs between the duct exit and the nozzle exit. Several constant static pressure assumptions at the exit plane are also needed. An example control volume can be seen in Fig. 2.5 from Ref. [1]. In practice, these control volume bounds will not be easy to define.

This definition leads to an approximate answer with errors varying depending on how these bounds are drawn. More to come on this later.

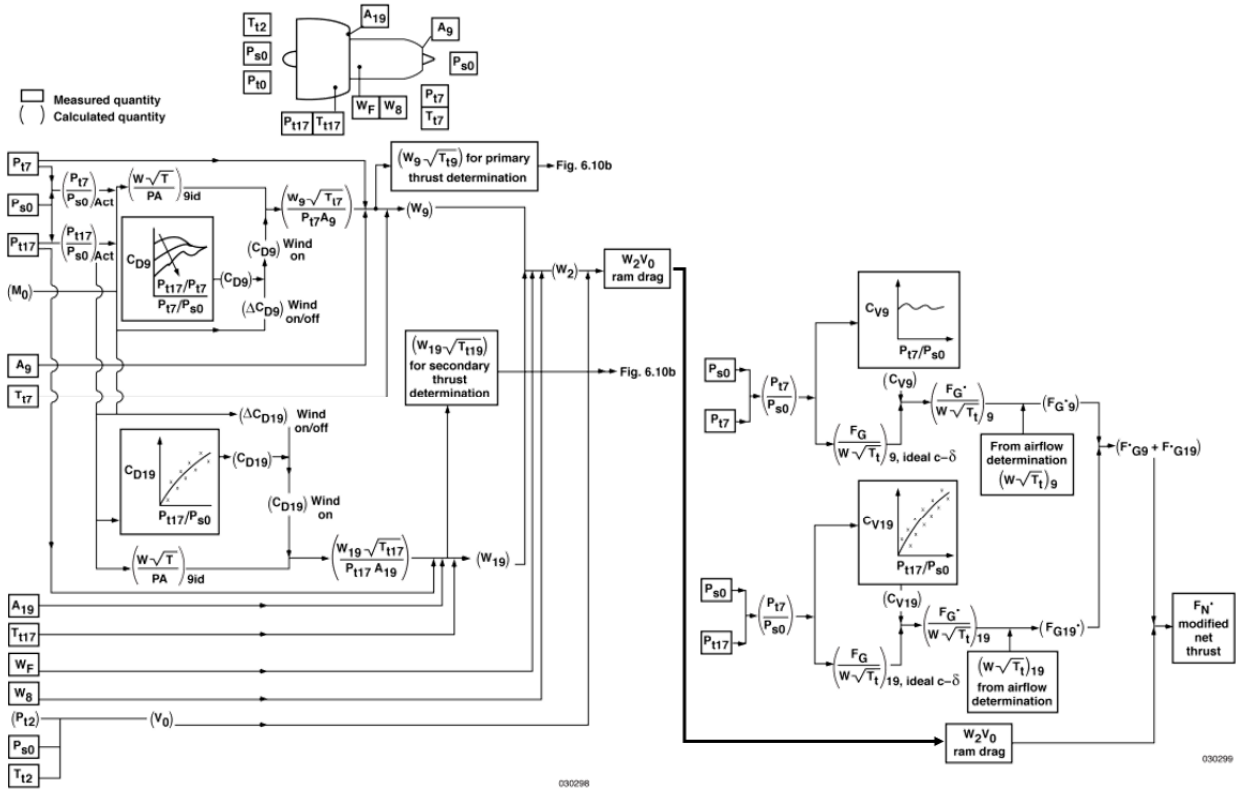

Figure 2.4: Gas-Path/Nozzle method for a turbofan.

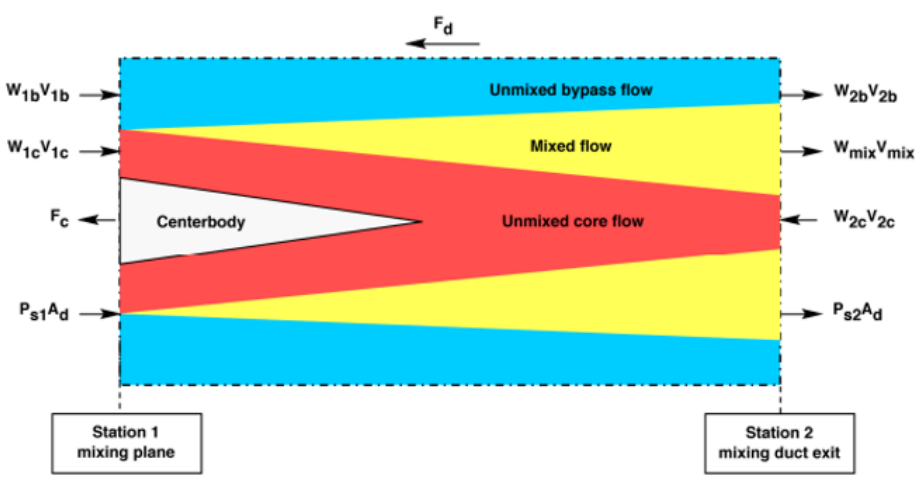

Figure 2.5: Control volume used to solve the compound flow analysis method.

Iterative numerical schemes are used to solve for flows that satisfy pressures and temperatures at the nozzle inlet and the static pressure at the mixing plane as well as retain

continuity. This scheme can be seen in Fig. 2.6 from Ref. [1]. Calculating the parameters needed in steps 1 through 4 are non-trivial and are laid out in great detail in SAEAIR 1703A. These details have been omitted here.

All three of these methods (overall performance, gas-path/nozzle, and CFA) have varied levels of fidelity and work required to get the data needed. As the operating conditions, geometry, and engine type increase in complexity, the force determination also increases in complexity. At a certain point, physical probe limitations are met. This could be the sheer number of probes needed, challenging operating conditions (Ex. combustor), or simply the time and money needed to manufacture and install such a measurement scheme. The next section will examine some examples of how the industry has done this in the past.

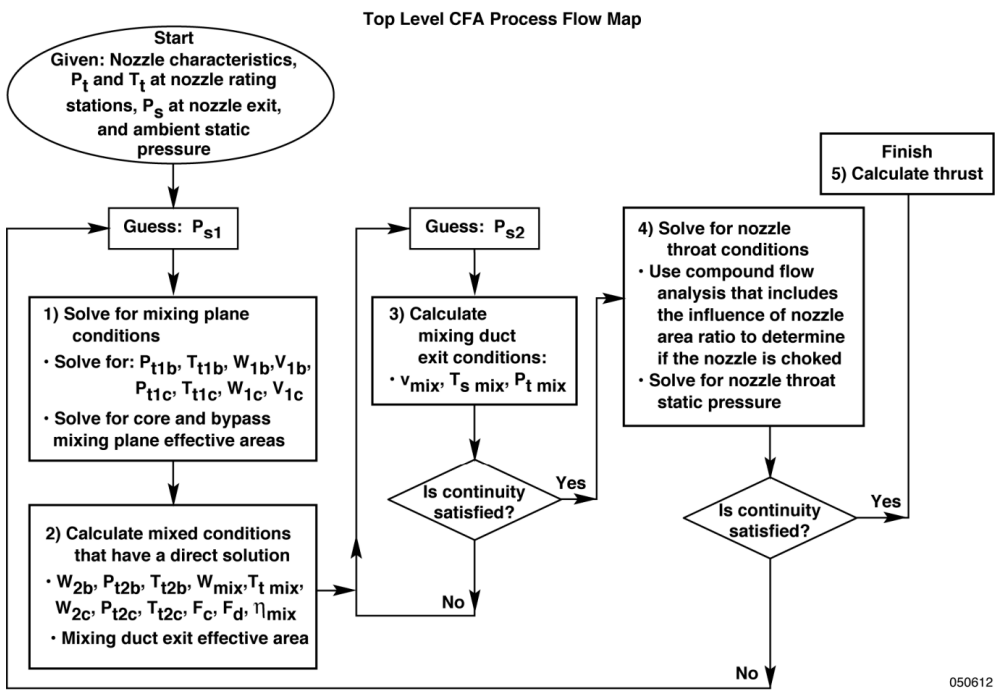

Figure 2.6: CFA process flow map.

In-Flight Force Probe Measurement

Getting the parameters in flight to solve any of the previously mentioned methods is a non-trivial task. Especially in the exhaust. While relatively mundane to do on the ground, even the simplest of measurements must be thoroughly thought out when transitioning to in-flight. Up until recently, a nozzle exit traverse method was the preferred method to calculate such parameters [1]. A probe rake attached to a traverse would measure the gas

properties at the nozzle exit and integrate over the area to obtain velocity, pressure force, and mass flow. To do this, the rake must measure the total and static pressure, as well as the total temperature. However, this method suffers from two major problems. The first is the ability of the probes to withstand such a harsh environment for prolonged periods of time. The trade-off between survivability and data acquisition time must be considered carefully. Secondly, the physical size of the probes will limit the spatial resolution of the measurement. The required spatial resolution will have to be carefully considered when making the trade-offs between physical size which affects both spatial resolution and temporal resolution.

The location and number of individual measurements required are highly reliant on the specific application. A simple turbojet with mostly uniform exhaust gas properties would need fewer measurements/measurement locations than a large turbofan, for example. To properly evaluate how many probes are needed, ground tests are required. The rake size and pivot locations have to be designed in a way that allows the rake to gather data over the entire exhaust plane. Examples of such hardware can be seen in Fig. 2.7 from Refs. [1] and [7]. Today, the use of this method has fallen out of favor in the industry for its limited application due to engine complexity and probe design complexity.

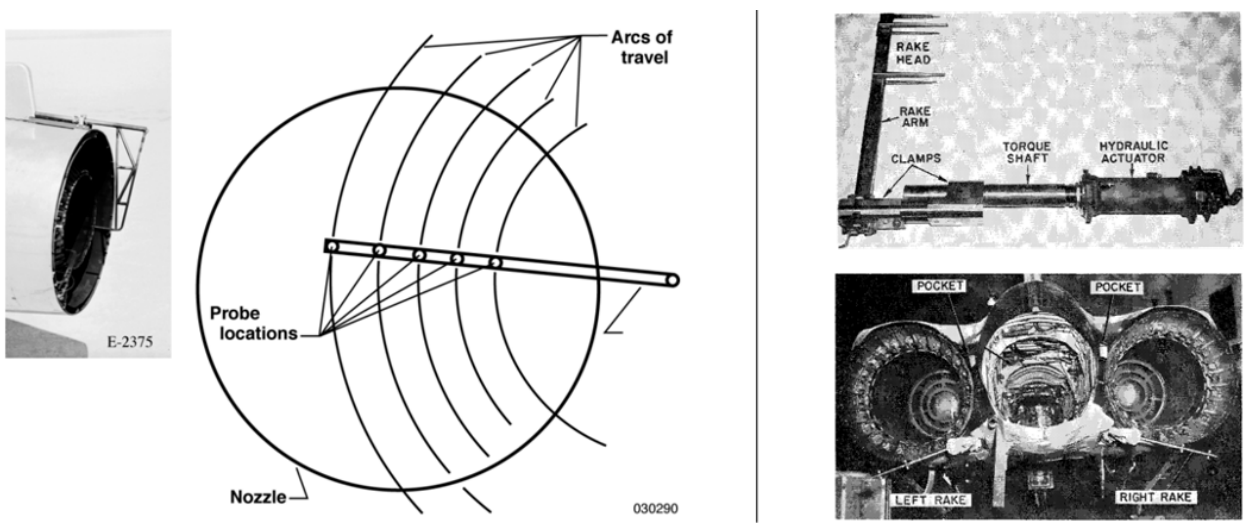

Figure 2.7: Left: Example traversing rake arrangement. Right: Traversing rake used on a North American Vigilante with J-79 engines.

Although not gone into detail here, a force balance can be installed inside the airframe mounts (trunnions) to directly measure the force of the engine and nozzle assembly. This method has traditionally had limited success. This is due to the high degree of difficulty of applying the instrumentation to mounts, recording the loads, and determining the in-flight tare forces between the airframe and engine. However, Ref. [8] by Conners et al. shows that

this can be done accurately, albeit with careful consideration.

Summary

Many methods exist to realistically measure in-flight forces. All of the methods presented so far have been proven and used extensively. However, none remain easy to execute and no consensus has been made on which one to use. Almost all require some sort of ground testing before flight testing. This ranges from creating models based on ground data to simple testing of hardware on the ground. The key takeaway here is that ground testing and flight testing are very different. In terms of flight testing, the methodology must be proven and agreed upon before ever seeing any of the data. These problems will be touched upon again at the end of this section.

Uncertainty of in-flight forces can be determined through the combination of statistical and engineering concepts which must be applied to each step in the calculation process. A detailed breakdown of how this directly applies to in-flight forces can be found in SAEAIR 1678B [2]. The steps described in this document follow standard error build-up practices for generalized probe measurements. The only difference is that the document provides uncertainty values/equations for specific models used in in-flight force methods. This procedure has been optimized to save time and money. The details of this optimization can be found in SAEAIR 5925 - Measurement Uncertainty Applied to Cost-Effective Testing [9].

2.1.2 Theoretical Methods

While the SAEAIR documents are extremely important, they lack detail for methods that are widely used in experimentation and research. This section will look at methods that are available at a wind tunnel scale and then build up to how some of these can be used on a full-scale, in-flight thrust measurement which is different than as described by the SAE AIR documents. All known methods will be touched upon with a specific emphasis on the most up-to-date methods near the end. A graphical interpretation of the control volume development timeline is shown in Fig. 2.8.

In general practice, wind-tunnel balance measurements are used to determine performance values such as lift and drag without the presence of a propulsion device [10]. In the presence of a propulsor, the balance measurement will only provide the net force in the axial

direction, therefore, no breakdown of thrust and drag can be made. Even without a propulsor, the resulting drag data cannot be broken down into components such as parasite drag and induced drag. To address this, many methods have been published that analyze the flow of an aerodynamic body using a control volume (CV), which is used to relate the body forces to the wake and flow far-field [11]. These methods focus primarily on determining the drag breakdown from wake measurements and offer little to no analysis for determining thrust. However, they are still worth reviewing as a few minor tweaks allow these to be thrust and drag measurement methods.

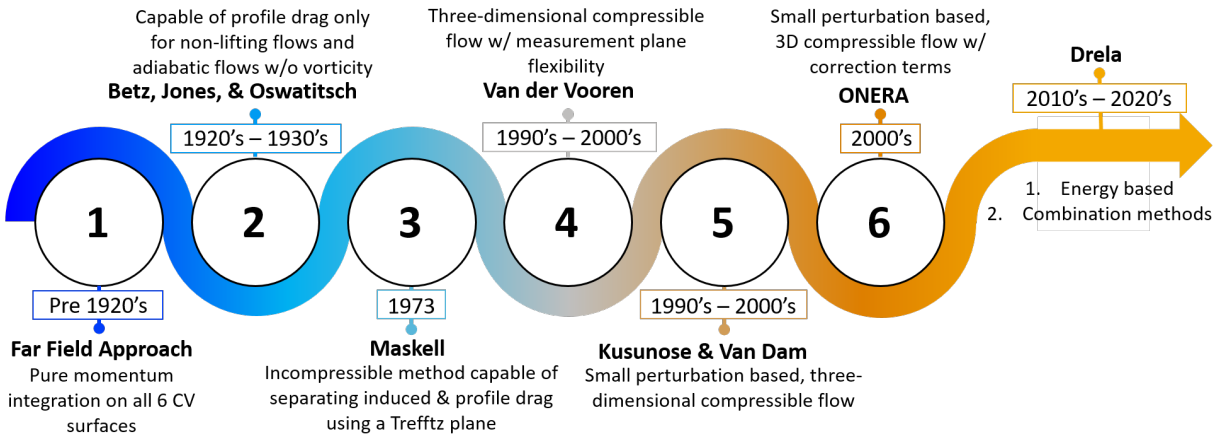

Figure 2.8: Control volume development timeline.

The far-field approach outlined in Méheut et al. [10] is the simplest control volume approach and is directly comparable to the balance measurements that can be determined inside a wind tunnel. This approach is based on the integration of the momentum equation inside of a closed volume, however, only the total drag (no breakdown of individual components) can be found. It is used as the basis for all methods to follow and laid the groundwork for more complex analysis. Simplifications to the far-field approach were undertaken by Betz et al. [12], Jones et al. [13], and Oswatitsch et al. [14], which allow for simple drag calculations in non-lifting flows and adiabatic flows without vorticity. Maskell et al. [15] took these ideas a step further and introduced the general incompressible method capable of separating parasite and induced drag into distinct components using a Trefftz plane. To deal with the three-dimensional compressible flow, the Van der Vooren formulation [16, 17] is needed, which builds on the work by Maskell. This formulation uses only a wake survey and the assumption that the flow is both isentropic and adiabatic from the wake survey plane location to the Trefftz plane. However, the Van der Vooren method can only be used when the entire flow field stagnation pressure remains higher than the upstream static

pressure. If this is not the case, the drag of this area cannot be computed. The Kusunose [18] and Van Dam [19] methods can be used to get around this. They are based on the small-perturbation assumption. But these methods are arguable since in some cases, the perturbations of velocity are not small, particularly in scenarios such as high-lift, or if the propulsor is included in the analysis.

Méheut et al. [10] compared all the previously mentioned control volume methods to their new methods called the ONERA formulations [20, 21]. These formulations are very similar to the Kusunose and Van Dam methods. Upon comparison with numerical simulations, the various force methods led to different results. As expected, the various assumptions allow them to work well in some cases but not in others. Overall, the Van der Vooren method worked best across several different flow cases. These methods have an inherent flaw, the more successfully they compare to numerical analysis, the more complex they get. The separation of drag components into parasite and induced drag, as well as the contributions from each physical body, get harder to interpret as complexity rises. Drela [11, 22] aims to simplify the analysis by introducing two new methods termed the "Power Balance Method" and the "Jones/Young Method". The power balance method is derived using a control volume approach based on mechanical power and kinetic energy flow with little to no assumptions needed. The Jones/Young method is derived from Jones' [13] incompressible method and Young's [23] compressible method. Both of these methods will be detailed in the following subsections as they are the most up-to-date and most applicable to applications that this Ph.D. dissertation will focus on.

Power Balance Method

In this method, Drela [11] aims to simplify the analysis by deriving a control volume approach based on mechanical power and kinetic energy flow. This kind of approach accounts for interference effects that are not captured by the previous methods. The energy control volume approach relies on little to no assumptions and is, therefore, more rigorous, and allows for a much more detailed energy breakdown. The control volume is subdivided into two different sub-volumes. The outer volume referred to as S_o, has flat surfaces upstream and downstream. The side outer volume is a cylindrical surface. This makes the forward and aft surfaces circular. This cylindrical surface is referred to as S_o^{SC}. The aft surface is a Trefftz plane and is referred to as S_o^{TP}. Note that the front circular surface is not given a special identifier as the future breakdown of this method will show that no information is

needed from this plane, only the freestream flow values. Finally, the inner volume is referred to as S_B and lies on the body's surface. The three-dimensional control volume can be seen in Fig. 2.9 as a 2D planar slice.

The defined control volume must follow several rules for the analysis to work and remain simplified. The outer boundary must be oriented such that 1) the Trefftz plane is perpendicular to the freestream velocity, and 2) the outer cylindrical boundary is parallel to the freestream velocity. Using Fig. 2.9 as a reference, this means the Trefftz plane must sit in the YZ-plane and the entire cylindrical boundary must remain parallel to the X-axis. Two more rules are used to keep the analysis simple 1) all the vortical fluids must leave out of the Trefftz plane and 2) the rear boundary is big enough to capture all energy except supersonic oblique waves, which will leave through the side cylindrical boundary. This means the Trefftz plane will need to be quite large and will vary from system to system. In summary, these limits are imposed so that a large Trefftz plane can be used to capture all flow effects besides potential shock waves.

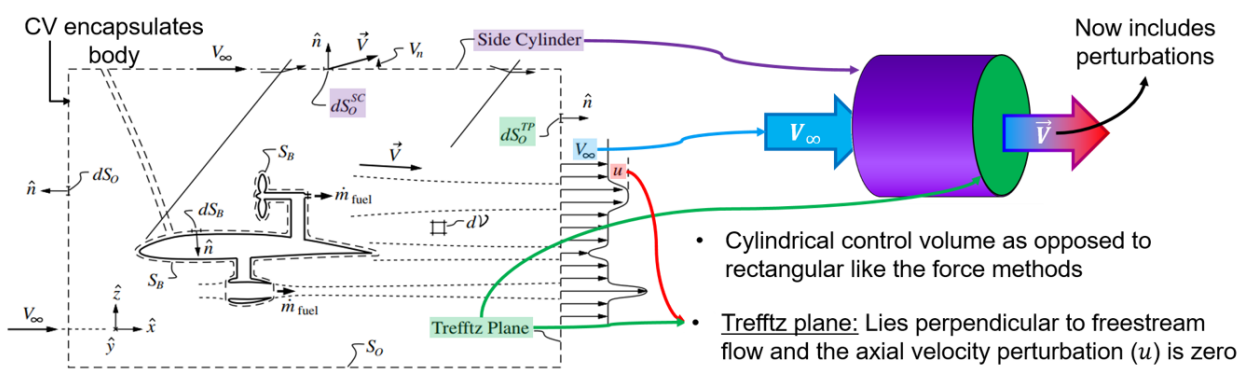

Figure 2.9: Cutaway view of three-dimensional energy method control volume.

Drela's method, like the previous control volume methods, starts with the time-averaged momentum equation in its divergence form (Eq. 2.3). The left side of this equation is the divergence of momentum, the right side of the equation has the negative gradient of static pressure plus the divergence of the viscous stress tensor. Dotting this equation with velocity leads to the mechanical (kinetic) energy in divergence form (Eq. 2.4).

$$\text{(momentum)}\ \nabla \cdot (\rho \mathbf{V}\mathbf{V}) = -\nabla p + \nabla \cdot \overline{\overline{\tau}} \tag{2.3}$$

$$\text{(mechanical energy)}\ \nabla \cdot \left(\rho \mathbf{V} \frac{1}{2} V^2\right) = -\nabla p \cdot \mathbf{V} + \left(\nabla \cdot \overline{\overline{\tau}}\right) \cdot \mathbf{V} \tag{2.4}$$

Equation 2.4 can be expanded using standard vector identities and integrated over the entire control volume after applying the divergence theorem (Gauss' theorem) which results in the integral mechanical power balance equation (Eq. 2.5).

$$P_S + P_V + P_K = \dot{\epsilon} + \Phi \tag{2.5}$$

Where P_S is the shaft power, P_V is the volumetric power, P_K is the kinetic energy inflow rate, $\dot{\epsilon}$ is the mechanical energy outflow rate, and Φ is the viscous dissipation rate. The power terms on the left side of Eq. 2.5 represent the total mechanical power supply/inflow. The two terms on the right represent the power consumption/outflow. The major goal of this energy method is to determine the total power required for flight, which is done through the prediction of the right-hand side terms. The integral equations for the left-hand side power terms will not be explored here but can be found in the article by Drela [11]. The expansion of the mechanical energy outflow rate can be seen in Fig. 2.10. The expansion of the viscous dissipation rate can be seen in Fig. 2.11.

Looking at Fig. 2.11, given the required streamwise gradient information, the dissipation term is not easily calculated outside of a computational domain. Drela provides some simplifications that can be used in specific cases to aid in the dissipation calculation (dissipation sources described by Denton et al. [24, 25]). However, in an actual physical application, this will lead the final answer to have some error. Especially if it cannot be measured at all. Besides this, Figs. 2.10 and 2.11 describe the energy method well.

A major difference between the energy method and all force methods discussed in this review is that the force methods are all drag-breakdown methods and do not attempt to account for thrust. In other words, all models in these methods have no thrust-producing propulsion elements. They do, however, take the pylon and engine nacelles supporting these propulsion elements into account. This is true both in numerical analysis and in any supporting experiments. On the other hand, Drela's energy method accounts for propulsion elements including thrust-producing elements. If the control volume was drawn just around a wing-mounted engine and not the entire airplane, the energy method would result in the net energy coming from both the thrust and drag of those components. This energy can be related to the net force via the freestream velocity. However, as stated previously, the individual thrust and drag components cannot be obtained. Whereas the force methods can provide a complete drag-breakdown, albeit without a propulsor. It is possible to draw the

control volume in such a way with the energy method to determine the individual drag and thrust components. However, the control volume bounds would be somewhat ambiguous leading to inaccuracies. This is a common theme and will be discussed in detail later.

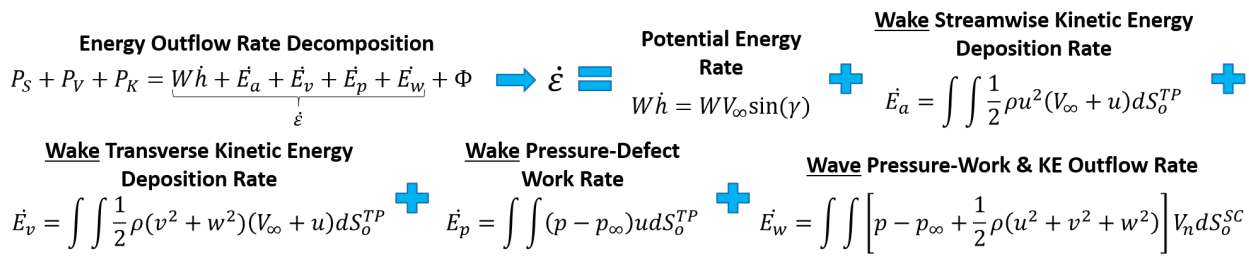

Figure 2.10: Mechanical energy outflow rate expansion.

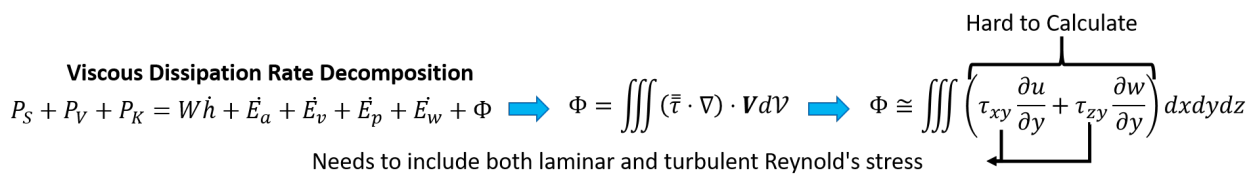

Figure 2.11: Viscous dissipation rate expansion.

Jones/Young Method or Parallel Expanded Streamtube Method

A simpler approach compared to the energy method described above is an approximate force method. Drela [22] refers to this method as either the "Jones/Young Method" or the "Parallel Expanded Streamtube Method". This approach is used to estimate the thrust of the propulsor and the profile drag of the airframe. It does this by estimating the streamwise momentum in the Trefftz plane. All transverse forces are not considered (no induced drag). Importantly, the measurement plane does not have to be the Trefftz plane. It can be any convenient transverse planar surface. These surfaces can be seen in Fig. 2.12 from Ref. [22].

The profile drag can be written as seen in Eq. 2.6. Again, this integration is performed at any transverse planar surface S_N downstream of the aircraft as shown in blue in Fig. 2.12.

$$D_{p_{JY}} = \iint (V_\infty - \bar{V})\rho \mathbf{V} \cdot \hat{\mathbf{n}} dS_N \tag{2.6}$$

$$(\rho \mathbf{V} \cdot \hat{\mathbf{n}})_{TP} dS_{TP} = (\rho \mathbf{V} \cdot \hat{\mathbf{n}})_N dS_N \tag{2.7}$$

The reason Eq. 2.6 can be taken anywhere and is equivalent to taking it over the Trefftz plane (TP subscript) is via the mass conservation relation for any trailing streamtube (seen in Eq. 2.7). The symbol $\bar{V}$ represents the "expanded" speed that a streamtube has after it flows from one state (local: V, p, p_t, h_t) to a far state (Trefftz plane: $\bar{V}, \bar{p}, \bar{p}_t, \bar{h}_t$). $\bar{V}$ can be represented by rewriting the stagnation pressure for either incompressible or compressible flow (Eqs. 2.8 and 2.9). The use of Eqs. 2.8 and 2.9 means that the streamtube from S_N to S_{TP} is assumed to be isentropic such that $\bar{p}_t = p_t$ and $\bar{h}_t = h_t$, and also that S_{TP} is at freestream pressure.

$$\text{(Incompressible) } \bar{V}(p_t) = \sqrt{2\frac{p_t - p_\infty}{\rho}} \tag{2.8}$$

$$\text{(Compressible) } \bar{V}(p_t, h_t) = \sqrt{2h_t\left[1 - \left(\frac{p_\infty}{p_t}\right)^{\frac{\gamma-1}{\gamma}}\right]} \tag{2.9}$$

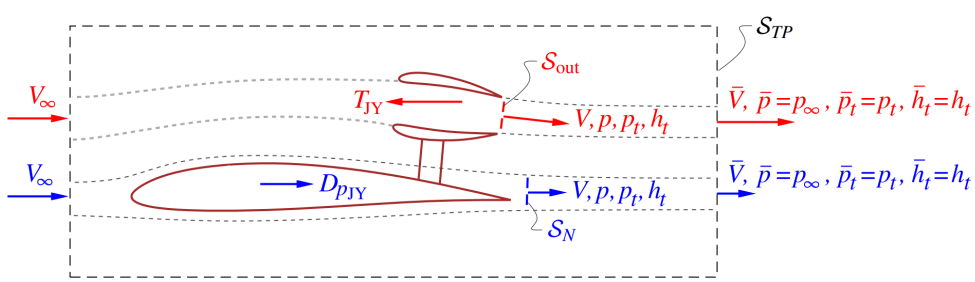

Figure 2.12: Parallel-streamtube force estimation method, with thrust definition streamtubes (red), and profile drag definition streamtubes (blue).

Equation 2.6 can be transformed from a drag equation to a thrust equation by noting that when applied to a propulsor, the thrust will produce a negative profile drag and the net mass outflow (fuel flow) must be included. The result is Eq. 2.10. The approximate application of this equation can be seen in red in Fig. 2.12. Equations 2.6 and 2.10 can be compared to the exact force equation which must be integrated at the Trefftz plane (Eq. 2.11). These equations are very similar.

$$T_{JY} = \iint (\bar{V} - V_\infty)\rho \mathbf{V} \cdot \hat{\mathbf{n}} dS_{Out} + \dot{m}_{fuel} V_\infty \tag{2.10}$$

$$F_x = \iint \left[\rho u(V_\infty - u) + p_\infty - p\right] dS_{TP} - \dot{m}_O V_\infty \tag{2.11}$$

As stated when discussing the energy method, drawing the control volume is somewhat ambiguous. For example, Fig. 2.12 does not show streamtubes over the nacelle surface. These streamtubes could be included in the thrust calculation resulting in a net thrust or they can be included in the drag build-up which would result in gross thrust. This example highlights the trouble in deciding which streamtubes get included in the numbers being reported (thrust versus drag).

Summary

A timeline of the development of the control volume methodology spanning 100 years was given and briefly explained. Two methods were focused on, the power balance method as well as the Jones/Young method for their versatility and modernity. The power balance method relies on equations in the form of energy and can be used anywhere downstream of the model, albeit with several assumptions and the inability to calculate the dissipation terms in an actual experiment. The Jones/Young method is a far-field method that uses near-field data and an "expanded" streamtube velocity correction term to correlate the near-field results to the far-field Trefftz plane.

Many more control methods exist for specific applications. A few of note are described by Spalart et al. [26] for incompressible highly vortical flows, add-ons to the energy method by Sato et al. [27], Sanders et al. [28], and Arnts et al. [29], and finally, hybrid near-field/far-field methods by Zucrow et al. [30], Hill et al. [31], and Kerrebrock et al. [32].

2.1.3 Comparison of Industry Methods and Theoretical Methods

The main difference between current industry-standard practices and theoretical methods is that the industry relies on "on-engine" measurements and theoretical models largely rely on "off-engine" measurements. "On-engine" measurements refer to point/plane measurements taken on or in the engine and various stations like what is shown in Figs. 2.2, 2.3, and 2.4. "Off-engine" measurements refer to point/plane measurements taken downstream of the engine in the near or far-field. "On-engine" measurements are generally tried and true and can currently be done in-flight at a substantial cost. "Off-engine" measurements are generally reserved for wind tunnel or ground test experimentation and can be achieved at a much lower cost.

An ideal validation experiment with little interaction would make use of both the ”on-engine” and ”off-engine” methodologies. For example, combining the gas-path/nozzle method and Jones/Young method would lead to two independent force results at the same time. The data needed for both is completely different and of different complexity levels. This Ph.D. dissertation will have a large focus on technique development allowing the Jones/Young method to extend past theory and CFD simulations into a real, in-flight force diagnostic technique.

2.1.4 Simulation and Experimental In-Flight Force Examples

This section will give brief descriptions of the literature involving simulated and experimental applications of the techniques discussed thus far. The simulation examples will come first which will be followed by the experimental examples.

Simulations

Shirazi et al. [33] investigated a simple axisymmetric configuration that models a simplified submarine shape (DARPA SUBOFF model) using the wake integration method (method described by Drela [22]). This kind of method is widely deployed in many wind tunnels. Shirazi completed many simulations at varying angles of attack using the more common surface integration technique and compared that to the wake integration method in a simulated domain. A schematic of the model, control volume and equations used can be seen in Fig. 2.13 from Ref [33].

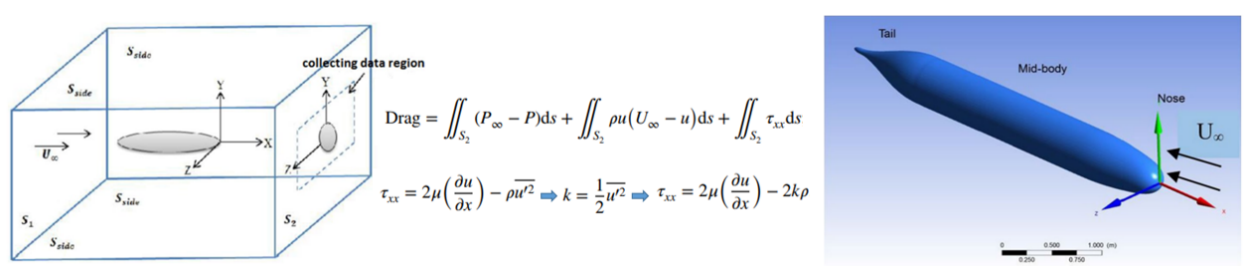

Figure 2.13: Drawn control volume, drag equations, and SUBOFF configuration.

As discussed previously in the energy control volume method [11], the dissipation terms are hard to measure. Instead, Shirzai uses an isotropic turbulence disturbance assumption to neglect the $2\mu(\partial u/\partial x)$ term seen in Fig. 2.13 since it is very small relative to the Reynolds

stress component. While this is a simplifying method for CFD simulations, it is still a challenge to measure the turbulence kinetic energy (k) experimentally. However, the results are still highly applicable and informative. The results can be seen in Fig. 2.14 from Ref. [33]. The left side of this figure shows the comparison of the surface integral to the wake integral method for different aspect ratios of the length-to-diameter. The results line up very well validating that the wake integral method is viable. The right side of the figure is highly informative about what is important to measure downstream of the model. In this case, turbulence has very little effect on the total drag far downstream of the model. Near the model, pressure and momentum dominate while pressure falls off relatively quickly. Therefore, far downstream, momentum is the dominant contributor to drag. This finding is incredibly important for situations where turbulence may not be able to be measured or pressure measurements may not be as accurate. These results can inform experimental applications.

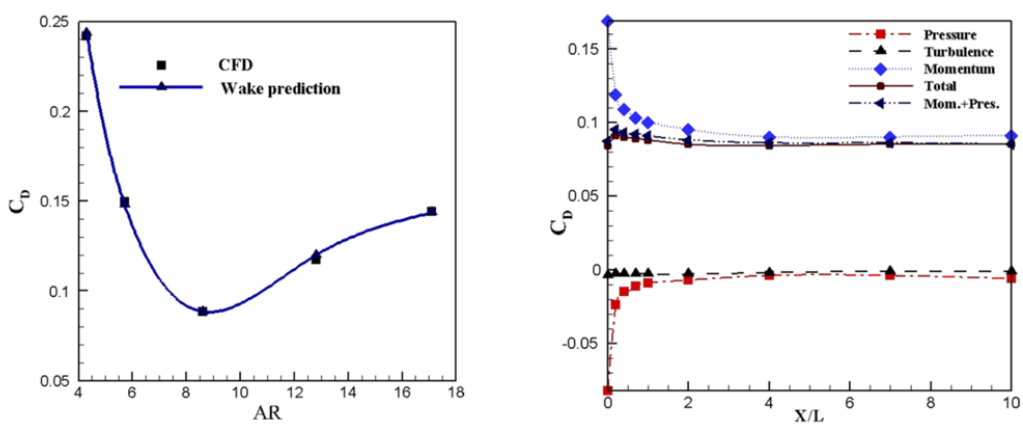

Figure 2.14: Left: Comparison of the surface integral and the wake integral results. Right: Contribution of pressure and momentum fluctuation terms.

It should be noted that the next step up from Shirzai in fidelity, is the work by Ueno et al. [34]. No figures/results will be shown here to save space but Ueno investigated the far-field drag analysis of NASA's common research model [35] in the simulated domain. No engine was modeled in these simulations but key insight was gained into how one might perform CFD on such a model and the associated techniques needed to get the drag. In particular, Ueno used Maskell's techniques [15] to derive induced drag from the far-field data.

Again taking a step up in fidelity, Blaesser [36] looked at the interference drag due to the engine nacelle location on transonic aircraft. This includes full CFD modeling of the

plane as well as the nacelle/engine. However, the pylon connecting the engine to the plane was not modeled. Blaesser did not use far-field techniques to determine drag. Instead, the interest was local, and drag counts (0.0001 of a drag coefficient) were used to report the results. However, the modeling methodology and mesh constraints/boundary conditions are noteworthy to inform future CFD ventures. Some examples of the meshing techniques used can be seen in Fig. 2.15 from Ref. [36].

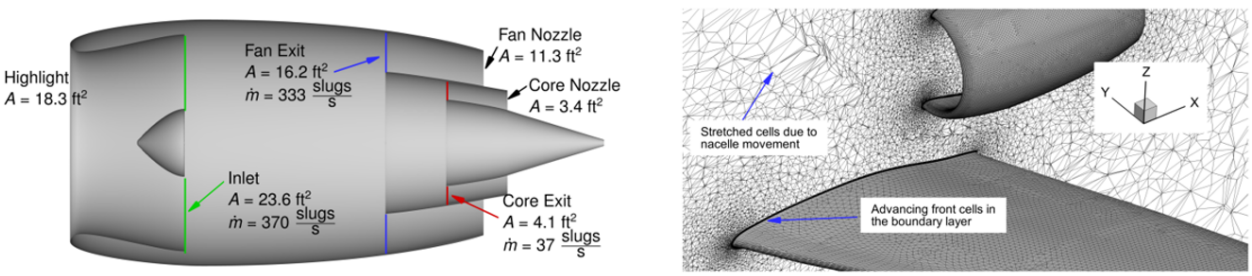

Figure 2.15: Left: Example engine boundary conditions w/o modeling engine internals. Right: Engine/wing combination meshing.

Similar to Blaesser, Destarac et al. [37] investigated drag on transonic aircraft. However, Destarac looked at more drag components than just interference drag including the wing-body-pylon-nacelle model. A brief venture into drawing a control volume for drag/thrust bookkeeping was introduced but the thrust was later dropped in favor of separate, more detailed, control volumes for viscous and wave drag. These concepts as well as some preliminary results can be seen in Fig. 2.16 from [37].

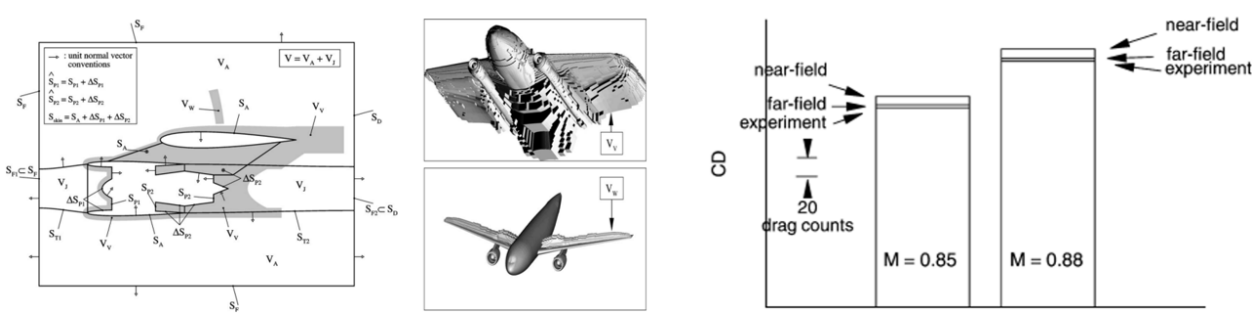

Figure 2.16: Left: Jet-propelled aircraft; control volumes/boundaries. Middle: Integration volumes V_V and V_W for viscous drag and wave drag. Right: Drag bar chart.

Looking at Fig. 2.16, the left side shows a potential control volume for the wing-pylon-nacelle configuration. To separate thrust and drag, Destarac et al. [37] have separated the volume into two sub-volumes. The first is labeled V_V which encompasses all of the drag-producing components outside of the engine. The second is labeled V_J which is for the jet

inlet and exhaust only. Drawing a control volume like this is still ambiguous due to the uncertainty in shear layer bounds, as previously touched upon.

Destarac et al. [37] fall short of actually modeling thrust. Instead, a through-flow nacelle is opted for so that only drag needs to be accounted for. This simplification allows for easier separation of the control volume for viscous and wave drag calculations. Since the model is 3D, the control volume becomes complicated as seen in the middle of Fig. 2.16. The control volume was iteratively solved and changed using automatic mesh refinement and is based on flow velocity values compared to the known freestream velocity.

Destarac et al. [37] end by comparing near-field and far-field simulated results to experimental drag results. This can be seen on the right side of Fig. 2.16. The far-field method works better than the near-field method. This validates Drela's assumptions [11, 22].

Finally, the highest-fidelity simulations were done by Goulos et al. [38]. Goulos et al. simulated both thrust and drag on an entire model. However, only surface integration and a near-field approach were applied. Goulos et al.'s work is still applicable given the high detail of mesh and domain generation that were used and proven to be accurate. These insights must be used in any future simulation computations.

Experiments

Building off the theoretical ONERA wake drag methods [10], Meheut [39] experimentally tested a KH3Y half-model in the Airbus Deutschland low-speed wind tunnel of Bremen at a Mach number of 0.174 with and without the nacelle. A variety of wake force methodologies were applied and tested. The results of this test can be seen in Fig. 2.17 from Ref. [39].

	ΔC_L	ΔC_D(dc)	ΔC_{Dp}(dc)	ΔC_{Di}(dc)
Balance measurements	0.02	170		
Wake measurements				
Betz	0.06		64	
ONERA2	0.06	169	64	105
Jones	0.06		69	
Van der Vooren et al.	0.06		70	
ONERA3	0.06	162	71	91
Kusunose	0.06	170	79	91
ONERA1	0.06	169	79	90

Figure 2.17: Left: Half-model KH3Y. Right: Methodology comparisons.

The KH3Y half-model is in a high-lift configuration meaning that the induced drag will not be negligible. This is clear when examining the table on the right side of Fig. 2.17 where dc stands for drag counts (0.0001 of a drag coefficient). The only methods capable of measuring induced drag by themselves are ONERA 1-3 and Kusunose. All four of these methods align well with the balance measurements taken. Meheut also shows that the addition of the nacelle complicates the flow with changes in the wake vortex structure. These changes need to be accounted for by expanding the control surface at the wake plane. These findings are consistent with Drela [22].

Other examples of experimentation, especially those involving in-flight software can be found in the report by Mei et al. [40]. This report details the information provided by the Aerial Instrumentation Workshop that is put on by the U.S. Department of Energy. Although much of the information is not applicable here, several examples of wing and fuselage-mounted instrumentation packages are pictures and detailed. This type of information will be needed when designing where and how to mount the hardware needed for a near/far-field measurement of an in-flight vehicle.

The in-flight force measurements just discussed all require field measurements of flow properties at low uncertainties for evaluation. Laser and imaging technologies offer an opportunity for making such measurements for aircraft using non-intrusive techniques. In the case of my work, filtered Rayleigh scattering is targeted due to the breadth of information available from this measurement such as static density, pressure, and temperature as well as three-component velocity.

2.2 Filtered Rayleigh Scattering

The following subsections are intended to give a detailed description of what filtered Rayleigh scattering is, how it is processed, what the current applications are, and what some of the hardest challenges look like. This is done through extensive discussion and presentation of current and past works by the broader community that has continually improved and expanded the technique. Many of the details discussed have been covered by Cutler and Lowe in the AIAA book titled "*Optical Diagnostics for Reacting and Non-Reacting Flows: Theory and Practice*", specifically in Chapter 3 titled "*Laser Rayleigh Scattering, Filtered Rayleigh Scattering, and Interferometric Rayleigh Scattering*" [41].

2.2.1 Fundamental Description

To understand filtered Rayleigh scattering (FRS), the fundamental phenomenon of Rayleigh scattering must be understood. In the nineteenth century Lord Rayleigh described what is now known as Rayleigh scattering, as a general wave scattering phenomenon that results from the interaction of light and matter on a scale much smaller than the wavelength of the incident light [42, 43, 44, 45, 46, 47]. The background and impact of Rayleigh's work have been outlined in detail by Twersky [48] and Young [49]. This impact continues today through the experimental aerodynamics community as the characteristics of Rayleigh scattering directly relate to the aero/thermodynamic properties of air. These properties have been extensively outlined by Miles et al. [50]. The general characteristics of laser Rayleigh scattering (LRS) have been outlined by Boyda et al. [51] and in Fig. 2.18 as follows:

1. Rayleigh scattering occurs down to molecular levels.
2. The Rayleigh scattering resulting from the interaction between light and matter is elastic; meaning there is no energy transfer between them.
3. The probability of photons scattering from a gas molecule (scattering intensity) increases with the amount of matter in the volume and the scattering cross-section of the gas. (Static Density)
4. Light scattered off matter in motion is Doppler shifted in frequency proportional to its bulk velocity. (Velocity)
5. In a stagnant gas, individual molecules are always in motion, (kinetic theory of gases) imparting a Doppler shift proportional to the speed of the individual molecules. (Static Temperature)

Items 1 & 2 are what allow for truly non-intrusive measurement of the scattering from the gas molecules. Item 3 defines that Rayleigh scattering is linearly dependent on the number density of molecules and therefore, can be used to find the static density of the flow. Items 4 and 5 allow for the measurement of velocity and static temperature, respectively. Finally, static pressure can then be derived using the state equation. Figure 2.18 gives a visual representation of these points. The lineshapes in this figure were generated using the Tenti S6 model [52, 53] which will be reviewed in more detail later.

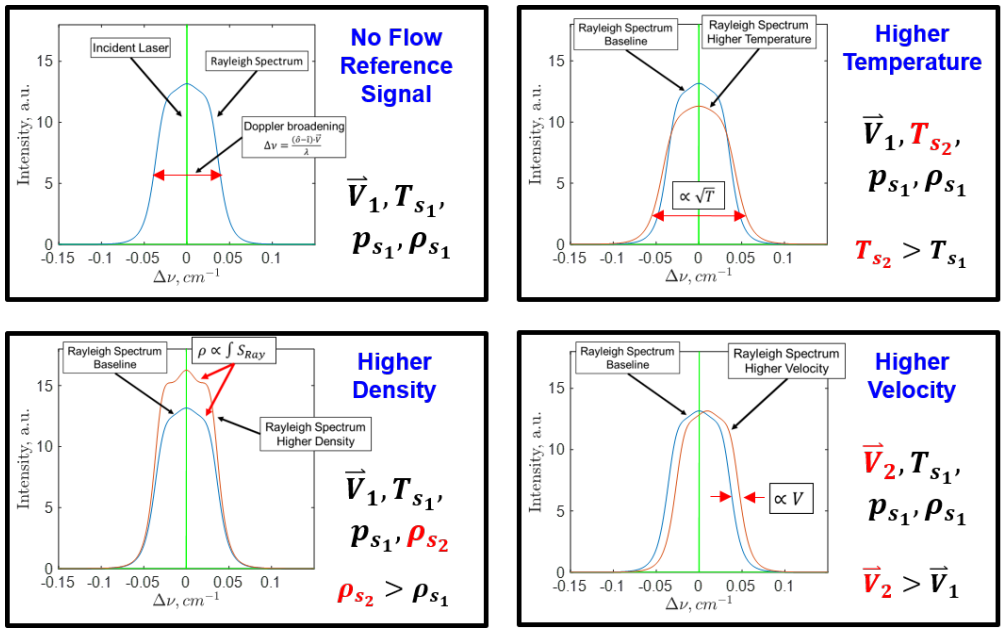

Figure 2.18: Upper left: No flow reference signal. Upper right: Higher temperature. Bottom left: Higher density. Bottom right: Higher velocity.

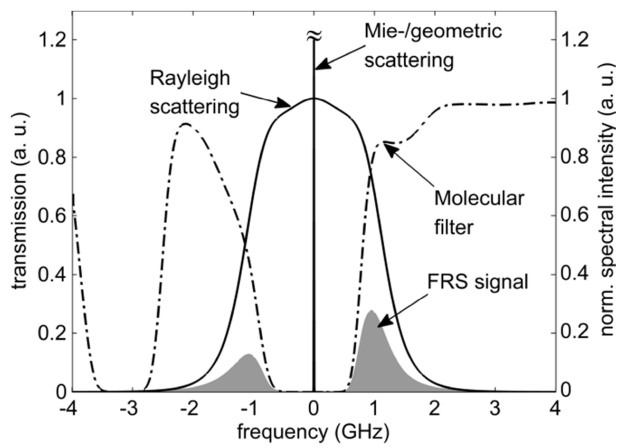

Figure 2.19: Rayleigh scattering after a molecular filter is used to attenuate the laser light.

Doll et al. [54] describe an important aspect of experimental Rayleigh scattering in that the flow environment will not be perfect. As Rayleigh scattering is an optical-based measurement, background scattering and/or Mie scattering [55] will affect the measurement. An example of background scattering would be when stray laser light bounces off of surfaces and then the resulting signal is superimposed onto the Rayleigh scattering signal. The same is true for Mie scattering which could occur with any sort of particles in the air. Therefore, a molecular filter can be used with known absorption levels to attenuate the scattering signals and leave behind just the Rayleigh scattering signal. This is known as filtered Rayleigh

scattering (FRS) and can be seen in Fig. 2.19 from Ref. [54].

Boyda et al. [56] describe that the actual signal received by the measurement device (camera) is the convolution of the transmission spectrum of the molecular filter and the Rayleigh, Mie, and background (geometric) spectrum. This can be seen in eq. 2.12.

$$S_{Signal}(\nu) = S_{Mie+Geo+Rayliegh} \otimes \tau_{iodine} = \int_{-\infty}^{\infty} S_{Mie+Geo+Rayleigh}(\eta)\tau_{iodine}(\nu - \eta)d\eta \quad (2.12)$$

$S_{Mie+Geo+Rayliegh}$ is the combined Mie, geometric, and Rayleigh spectrum that is centered on the incident laser frequency and τ_{iodine} is the transmission spectrum of the iodine vapor cell (used as the molecular filter). The iodine vapor cell works very well with 532nm (green) laser light [57] and is also shown in the molecular filter spectrum shown in Fig. 2.19. The specific iodine transmission spectrum model used at Virginia Tech with the 532nm green laser is the same as that developed by Forkey and colleagues [58, 59, 60]. However, alternative combinations of laser light and molecular filters do exist such as Mercury at 253.77nm [61], Cesium at 389, 852, and 894nm [62, 63], and Barium at 355nmm [64]. A generalized illustration of eq. 2.12 can be seen in Fig. 2.20 from Ref. [65] and represents the convolution of the Rayleigh scattering signal and a molecular absorption spectrum that could represent any of the aforementioned laser wavelength and gas pairs.

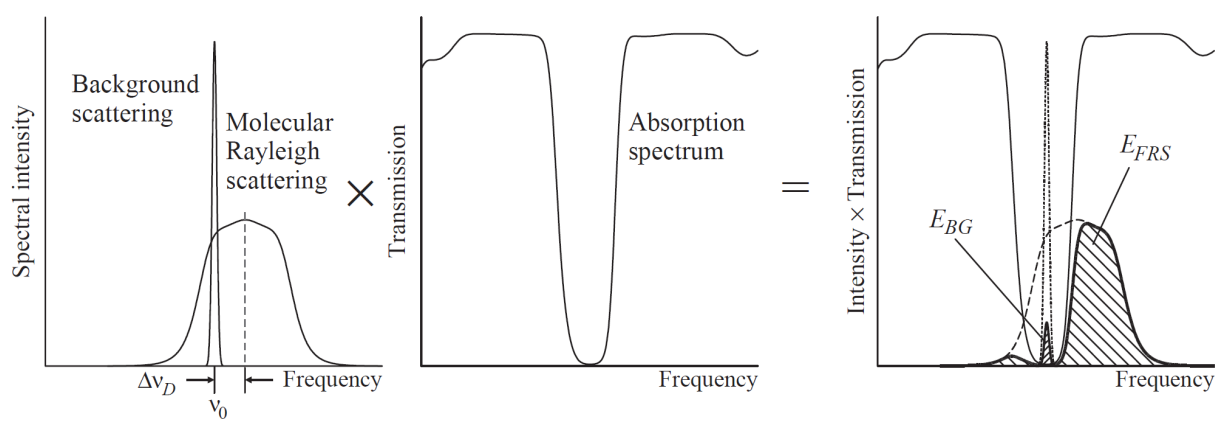

Figure 2.20: FRS signal created from molecular Rayleigh scattering and background scattering (from walls and/or windows). Left: Background and molecular Rayleigh scattering spectra. Middle: Transmission profile of the atomic/molecular filter. Right: Convolution of the scattered light spectrum and transmission profile resulting in the FRS signal.

In terms of velocity, the Doppler shift will be sensed in a direction that is likely not

orthogonal. This can be seen on the left side of Fig. 2.21 from Ref. [66]. The actual sensed velocity direction is defined by the difference between the camera vector and the laser propagation vector. Therefore, the matrix transformation from orthogonal velocities to sensed velocities can be seen on the right side of Fig. 2.21 from Ref. [67]. This matrix simply needs to be rearranged to go the other way. These components are known through camera calibration/registration. However, it is important to note that any error in the sensed velocities will carry into the transformation matrix. This will cause the resulting orthogonal velocities to always have more error. To mitigate this, the error in the sensed velocities must be minimized. This can be done by maximizing the sensitivity which means making the vector difference large to get as much Rayleigh scattering signal as possible. In practice, this cannot be optimized due to experimental constraints. It should also be noted that another major contributor is any error in computing the vectors themselves. This error will also propagate through. This has all been outlined in detail by Cadel et al. [66].

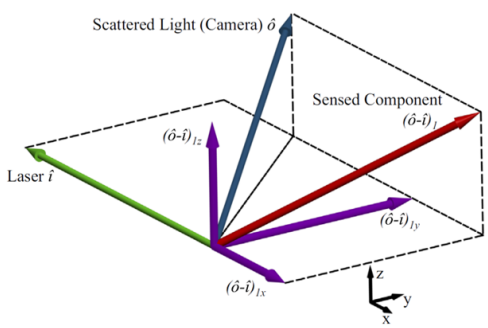

$$\begin{bmatrix} U_1 \\ U_2 \\ U_3 \end{bmatrix} = \begin{bmatrix} \left(\hat{o}-\hat{i}\right)_{1x} & \left(\hat{o}-\hat{i}\right)_{1y} & \left(\hat{o}-\hat{i}\right)_{1z} \\ \left(\hat{o}-\hat{i}\right)_{2x} & \left(\hat{o}-\hat{i}\right)_{2y} & \left(\hat{o}-\hat{i}\right)_{2z} \\ \left(\hat{o}-\hat{i}\right)_{3x} & \left(\hat{o}-\hat{i}\right)_{3y} & \left(\hat{o}-\hat{i}\right)_{3z} \end{bmatrix} \begin{bmatrix} U \\ V \\ W \end{bmatrix}$$

Figure 2.21: Left: FRS geometry and measured velocity components for a single camera/laser pair. Right: Transformation matrix of the velocity into a global, orthogonal system denoted U, V, and W in modified form for three cameras.

On the surface, FRS is not that complicated. However, details have been omitted here for explanation simplicity. A deep dive into the equations and theory is shown by Cutler et al. [41] and Boguszko et al. [65].

2.2.2 Data Processing Techniques

Current processing efforts by the author rely on fitting simulated spectrums to experimental spectrums by way of various iterative processes. This subsection aims to present a high-level overview of what the author and others currently do to post-process the raw FRS data. This includes FRS spectrum modeling, camera placement, and calibration, as well as final image processing techniques.

Step 1 is to take the raw images. Each image represents a specific laser frequency. As the frequency passes through the absorption region of the iodine cell, the intensity decreases. This is seen in the raw images provided. Step 2 is to use the camera calibration and known world coordinates and apply those coordinates to the raw images. Step 3 then uses these coordinates to warp the images such that they can be seen as if the viewer was head-on (perpendicular). These warped images are then cropped to the region of interest. These steps have been labeled as the global process since the image is being altered on a global basis instead of pixel by pixel (locally). Step 4 begins the local process. If a single pixel is considered, an experimental FRS spectrum can be generated by plotting the intensity of each image for that pixel against the known laser frequency or wavenumber. This step must be repeated for all pixels. A simulated spectrum is generated for each pixel. The simulated spectrum is iteratively matched to the experimental spectrum via a coded FRS model. A tolerance is set for the matching. Once matched, the next pixel undergoes the same process. Finally, in step 6, the individual pixels are recombined to show the measured planar values. Visual details will be shown later.

FRS Spectrum Modeling

As stated previously, the best current method to determine all of the parameters made available by an FRS measurement is to use an iterative method to fit a simulated spectrum to an experimental one [51, 68]. The first step is to find an accurate model for which the Rayleigh line shape can be modeled. The current best model is the Tenti S6 model [52, 69]. This model is a slight correction to the original Hanson-Morse model [70, 71] where the correction is done to an approximation that had been made. The model is a set of six linear equations that must be solved making it simpler than previous models.

The numerical Tenti S6 model has been looked at specifically for FRS purposes by Mcmanus et al. [69]. Specifically, Mcmanus investigated the Tenti S6 model for combustion-relevant gases using an experimental setup. This was done by comparing measured FRS signals to simulated FRS signals that were generated by combining the Tenti S6 model and an experimentally verified iodine absorption model. It was experimentally shown that over a temperature range of 300K to 2400K, with representative exhaust gases from a combustion cycle, the Tenti S6 model was sufficiently accurate (less than 4% average difference). It was also shown that the combined FRS signal from a gas mixture can be treated as the mole fraction-weighted average of the FRS signals from each component. This statement will be

important later in this document when talking about experiments performed.

A newer, simpler, Rayleigh line shape model was introduced by Witschas et al. [72]. This model is an easily processable, analytical alternative to the highly complex Tenti S6 model. The author does acknowledge that the Tenti S6 model is still the best. However, in limited applications, the Witschas model can be faster and with an error smaller than 0.85%. The application is limited to the ratio of the acoustic wavelength to the mean free path between collisions. This ratio must be between 0 and 1.027. Such a model may be useful if processing time or computation power is limited.

Hunt et al. [73] assert that the Tenti S6 model can be computationally expensive, especially when using it in an iterative scheme. Again, an iterative scheme is being used to match simulated data to experimental data. This assertion is not unlike that made by Witschas. Instead of an analytical model like Witschas, Hunt opts for a machine learning approach. This method is called the support vector spectrum approximation (SVSA). This uses vector regression and singular value decomposition to create an efficient, accurate, and well-conditioned approximation of any existing spectral lineshape. In practice, the author has noted that the SVSA method is approximately four orders of magnitude faster than the original Tenti S6 model with less than 1% error (see Fig. 2.22 from Ref. [73]). Specifically, this method was developed to optimize the design of an FRS experiment of a complex flow.

Early indications show that the SVSA model can be used to cut the timing process into a quarter of what it has traditionally been with the Tenti S6 model. This is off from four orders of magnitude as previously stated as it was found that more points were needed in the SVSA model to get the desired uncertainty. Slight errors arise at the peak of the transmissions if not enough points are used. This is not easy to see in Fig. 2.22 but small wiggles near the peak transmissions can be seen in the top two plots if examined closely. Overall, the author has noted the time savings of the SVSA model and will explore its usefulness in chapter 3.

Finally, Doll et al. [74] experimentally calculated the Rayleigh lineshape from a highly controlled experiment. The experimentally found, analytic, Rayleigh lineshape model has limitations based on the experimental conditions. An analytical model was built around the experimental data as well as the original Tenti S6 model. This analytical model is more complex than that by Witschas due to the number of coefficients used. All of these models will be investigated in detail within chapter 3.

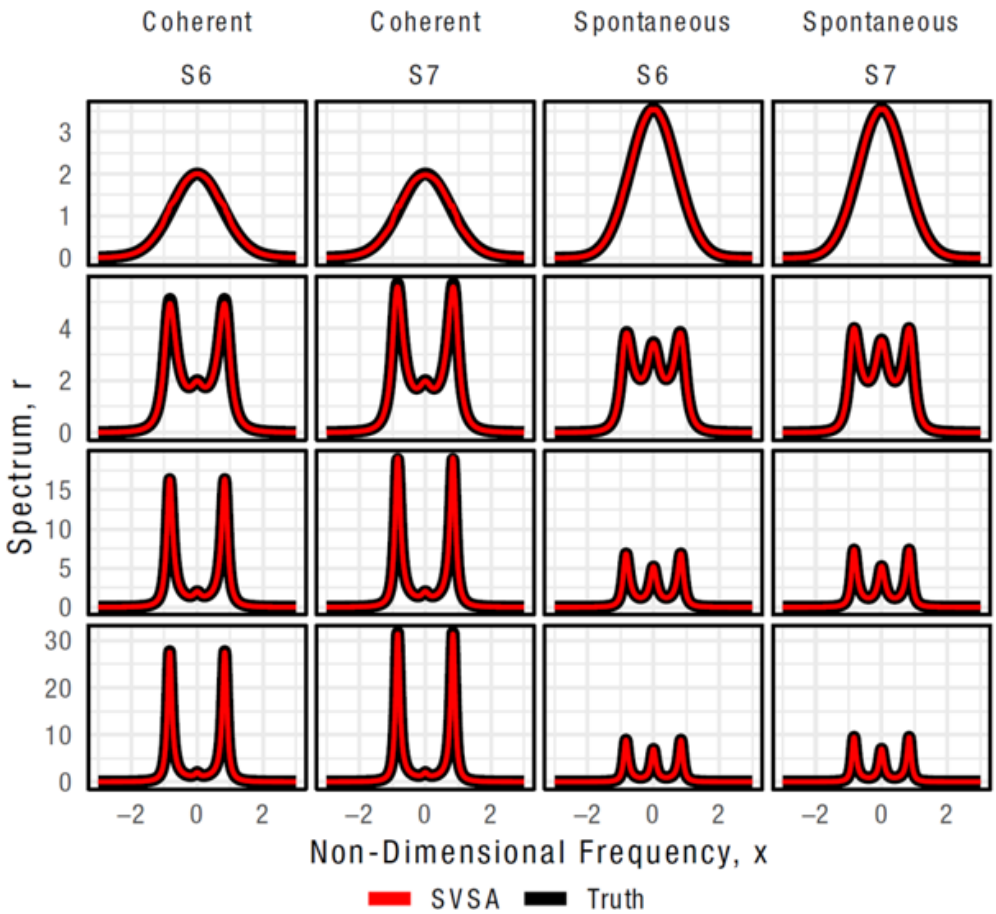

Figure 2.22: Examples of Rayleigh scattering lineshapes. The black lines are modeled by the S6 model. The red lines are the SVSA approximation.

Camera Placement and Calibration

Currently, the author and groups like Doll [54] choose camera positions based on physical room, experimental applicability, and FRS sensitivities. However, techniques do exist to help with camera placement with the intent to minimize errors in 3D measurements. This will not be talked about extensively here. It is worth mentioning a paper by Olague et al. [75] which uses a multi-cellular genetic algorithm to produce optimal camera locations. This is done by defining a criterion on which error propagation may be analyzed (FRS sensitivity in the context of this document) and then using a global optimization process to minimize the criterion. This is something to keep in mind as the fidelity of FRS measurements keeps increasing.

Camera calibration to find the camera locations and map grid corners is of the utmost importance in an FRS measurement. The camera locations are used to determine the camera

viewing vectors and the grid corners are later used to warp the images so that all of the images line up with one another. If this is not done correctly, 3-component velocity and mapping back to world coordinates is not possible.

Many camera calibration methods and codes exist. Only a few will be highlighted here as codes that are currently in use or are closely related to codes in use by the author. The first is the CalTech camera calibration toolbox for MATLAB [76]. This is an open-source toolbox built for MATLAB that allows for the intrinsic and extrinsic parameters to be found for any number of cameras. It is very simple to use but does require manual user intervention to select the region of interest. It has been found by the author that anything less than using three cameras at a time for calibration can lead to poor results. This is just a general rule as other variables such as how close the cameras are to each other and what angle they are viewing the calibration plate also play a role. An example calibration using real data can be seen in Fig. 2.23. It should be noted that in this case, two cameras were placed side-by-side to achieve three sets of two cameras. This is exactly what is seen.

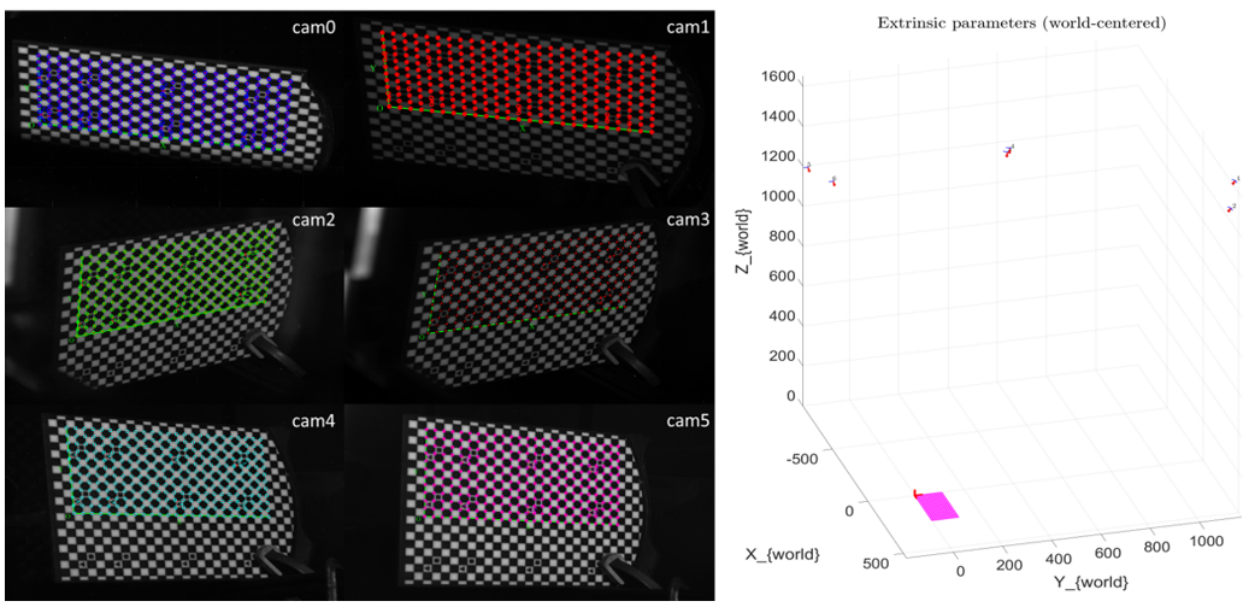

Figure 2.23: Left: Example images using a calibration plate with six different cameras. Right: Calibration results show all six cameras in 3D space compared to the calibration plate.

To get around the issue of high error with a low camera number using the CalTech code, a single-camera calibration method by Tsai [77] was implemented as a check. This method is less accurate when a high number of cameras are present and the CalTech code is used but it is much more accurate when only calibrating a single image. If the results

from the Tsai calibration and the CalTech calibration are reasonably close, the calibration is deemed a success. It is still important to have a physically measured idea of where the cameras are in space to compare back to the calibration results.

Image Processing and Meshing

Image processing and meshing are of growing importance as the time it takes to process each pixel of data increases. Processing time increases as the technique fidelity increases. For example, processing for velocity (one parameter) versus velocity and static temperature (two parameters) versus the full-fidelity, multi-parameter fit of velocity, static temperature, pressure, and density. Each variable added significantly increases the time needed to fit the experimental and simulated spectrums. On top of this, each pixel is relatively noisy. Therefore, an averaging/denoising technique is of interest to decrease both the time it takes to process the raw data as well as increase the signal-to-noise ratio.

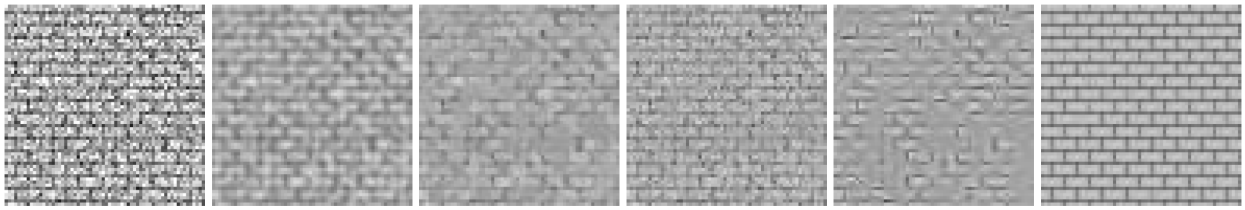

Figure 2.24: From left to right: noisy image, Gauss filtering, Total variation, Neighborhood filter, translation invariant wavelet thresholding, and NL-means algorithm.

Since FRS is an optical-based measurement of relatively low-intensity light, the noise in an image can be a hard challenge. Applying an image-denoising technique such as that presented in Buades et al. [78] could have a large impact on the final results. This work is called the NL-means algorithm and is based on a non-local averaging of all pixels in an image. Without going into too much detail, weighted averaging is used to find large structures and differences in an image. This method is compared to many different methods as seen in Fig. 2.24 from Ref. [78]. Figure 2.24 shows the power of the NL-means algorithm. Although it works well for a brick wall, it is yet to be seen if the small differences in FRS images would be enough to make this algorithm worthwhile when compared to Gauss filtering or some other easier method.

The results of the averaging techniques are important so that accurate structures can be examined and then a secondary, much larger, averaging scheme applied. The reason

for the two averaging schemes is the same as mentioned in the Tenti S6 discussion. The sheer number of pixels in an image along with the number of iterations needed per pixel becomes impossible to manage. Therefore, a scheme that keeps the major structures from the raw image but produces a highly averaged image would be hugely advantageous. Since the first scheme described by Buades keeps the major structures, another scheme that sees the structures and averages elsewhere is needed.

This is where shape-based image meshing techniques like the one seen in Goksel et al. [79] could be implemented. Goksel applies the method to CT images in the medical world but got inspiration from finite element method (FEM) meshing techniques. In these images, the size, shape, and placement of the elements for which the pixels will be averaged are important factors in determining the final results. An iterative meshing scheme is used starting with a standard grid mesh which is then iterated upon to minimize an objective function by which intra-element intensity variations and poor element geometry are penalized for the entire mesh. Trade-offs between the objective function are made by changing the weights of each variable. This scheme minimizes the number of elements needed while retaining the major structures of the image. This can be seen in Fig. 2.25 from Ref. [79].

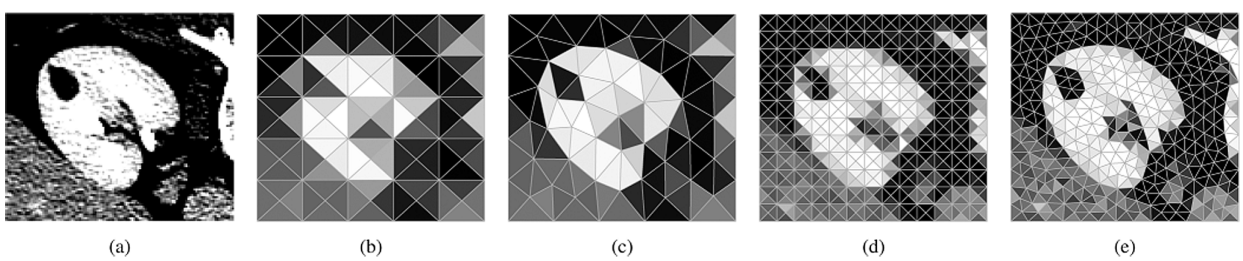

Figure 2.25: Mesh optimization on a 2-D CT image slice (a) of the kidney. Initial (b) and optimized (c) discretizations with 61 nodes; and initial (d) and optimized (e) discretizations.

This derived technique is simpler than the one shown by Goksel. It is possible to include the optimization scheme by Goksel in the meshing technique derived by the author. Although this has not been done yet. The scheme shown is referred to as "multi-level processing". This is a simple and relatively crude way to examine the effects of pixel averaging that is popular in many PIV applications. The first layer consists of averaging the entire data set to get one data point. Each subsequent layer (n) grows according to 4^n data points until no averaging is done. The optimal answer that balances processing time and acceptable accuracy will be one of the solved layers. These considerations are not a major part of the work in this dissertation but have been included for future references and probable processing directions. This will be discussed again in Section 7.

2.2.3 Applications and Challenges

Currently, two major authors (Boyda and Doll) are driving the most relevant literature regarding this Ph.D. work. This work will be focused upon. Other relevant works will also be mentioned.

Major Relevant Literature

This section will start by examining the work done by Boyda et al. [51, 56, 80, 81, 82, 83] (start of work on FRS at Virginia Tech) followed by an examination of the work done by Doll et al. [54, 68, 84, 85, 86, 87], concluding with error estimation literature by Ireland [88, 89].

Boyda [80] starts by extending the cross-correlation Doppler global velocimetry (CC-DGV) (described by Cadel [90]) technique to unseeded flows, relying only on the signals from Rayleigh scattering to get a mean velocity measurement on a well-characterized air jet. The application of CC-DGV to unseeded flows can also be termed cross-correlation-filtered Rayleigh scattering (CC-FRS). The cross-correlation is used to improve the robustness of the FRS method. In this method, two iodine absorption spectra are recorded simultaneously. The first spectrum is measured using a split in the laser path that lets the beam pass through an iodine filter and into the camera without passing through the flow. This is the reference signal which has no Doppler shift. The second is the scattered light that passes through a different iodine cell and camera. These two signals can then be cross-correlated to find the frequency shift between them. This frequency shift is the Doppler shift and can therefore be related to mean velocity. The results of this work can be seen in Fig. 2.26 from Ref. [80]. The root mean square errors (RMSEs) at Mach numbers of 0.5, 0.7, and 0.9 are 0.038 U/U_∞, 0.053 U/U_∞, and 0.05 U/U_∞, respectively. For the distorted case, the RMSE was 0.026 U/U_∞. These values are obtained by comparison to pitot-probe measurements taken at the same locations.

Boyda [81] investigates the uncertainty in a CC-FRS measurement using Monte Carlo simulations and the Cramér-Rao lower bound (CRLB) [88, 89] focusing on uncertainty and signal-to-noise ratios. The CRLB was determined using the method presented by Fischer et al. [62], and the Monte Carlo simulations were performed using the same technique presented by Cadel et al. [66]. The figures are omitted here but for the given conditions of a Mach number of 0.7 and temperature of 268K, it was found that the velocity bias error estimate is

approximately 1% with random errors of approximately ±0.6 m/s at signal-to-noise ratios achievable in a real-world experiment.

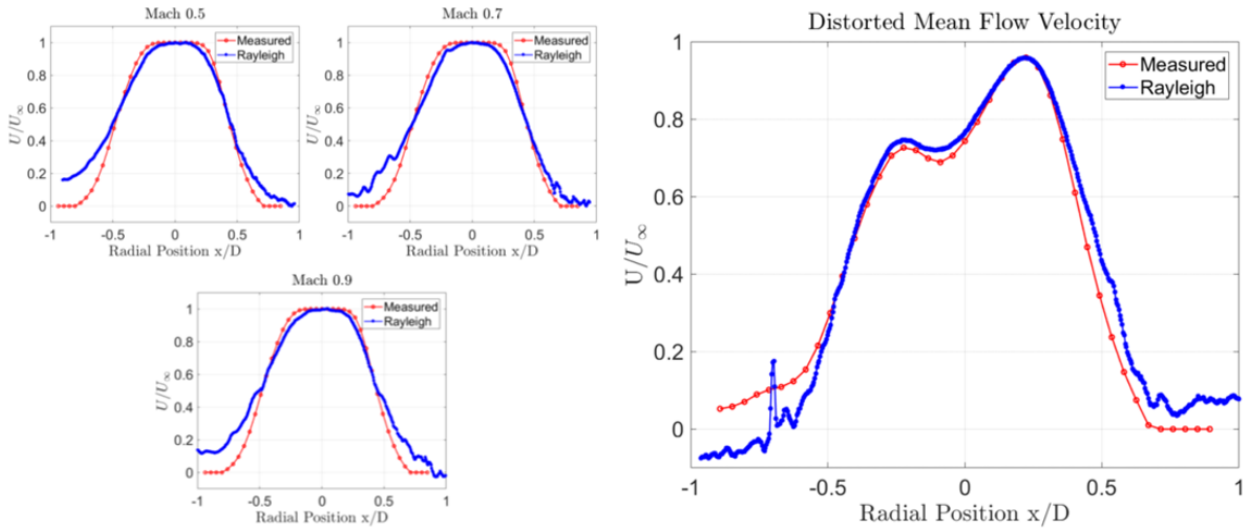

Figure 2.26: Flow characterization for axisymmetric flow (left three figures) and distorted flow (right figure). Measured = pitot-probe. Rayleigh = FRS.

Boyda [56] then extends the previous work on Mie and background scattering rejection using a molecular filter by noting that not all of the scattering effects can be removed. Again, this can be a result of particles in the air causing Mie scattering or scattering off of background objects such as wind tunnel walls or internal ducts. To account for this Boyda developed a comprehensive scattering model including Rayleigh scattering (using Tenti's S6 model [52]), Mie scattering, and background scattering. The resulting signal equation can be seen in eq. 2.12. The intensity ratio (IR) of Rayleigh scattering compared to Mie and background scattering is used to estimate their contributions to the final measured signal. This is defined by Fig. 2.27 from Ref. [56] which also shows the resulting composite Rayleigh scattering signal.

When the flow is non-zero, a Doppler shift is applied to the entire measured spectrum which shifts both the Rayleigh and Mie scattering spectrums horizontally. This horizontal shift moves away from the molecular filter scattering rejection region (near $\Delta\nu = 0$). This means that the Mie scattering will be superimposed onto the Rayleigh scattering signal causing the Rayleigh line shape and intensity to be different. This shift makes the cross-correlation method to be invalid as the reference spectrum may not contain the same sort of Mie scattering in each pixel.

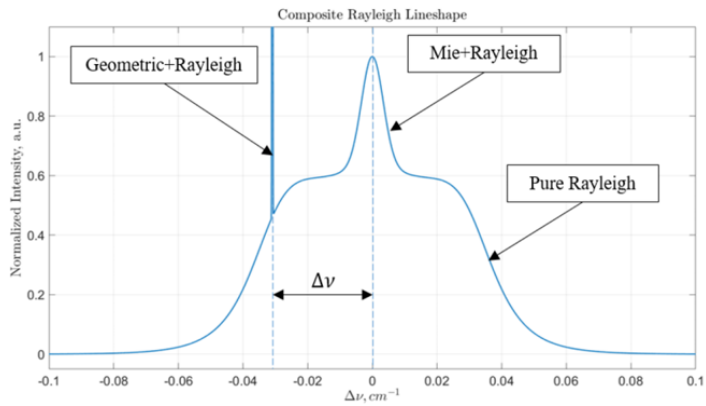

$$IR_{Mie} = \frac{\int(Mie)dv}{\int(Rayleigh)dv}$$

$$IR_{Bknd} = \frac{\int(Background)dv}{\int(Rayleigh)dv}$$

Figure 2.27: Composite Rayleigh spectral lineshape.

Unlike Mie scattering, background scattering does not change with the flow velocity. Therefore, the background scattering region of influence is uniquely defined by the frequency of the laser and the associated transmission through the iodine vapor cell. Again, the cross-correlation method cannot be used anymore as a negative bias in the velocity magnitude will occur as a result of the increasing background intensity bias. Therefore, a least-squares fit of the experimental data to the newly derived composite model has to be used to back-out FRS measurement values.

Boyda [82] attempts to rectify the biases introduced by background light contributions in planar FRS measurements by applying structured laser illumination planar imaging (SLIPI). This method results in a large reduction of the background light coming from stationary objects such as walls or jet nozzles. This will not be reviewed in detail here as none of the measurements in this Ph.D. work will use this method. However, high-quality FRS measurements by Boyda [51] do use this SLIPI technique with great comparison to five-hole probe measurements. Boyda's latest paper [83] provides evidence that FRS can be used to determine inlet distortion with high accuracy.

Doll [54, 68, 84, 85, 86, 87] uses much of the same techniques as discussed using Boyda's work. However, the applications are very unique as well as the way FRS is used. Instead of the FRS technique previously discussed, Doll generally uses frequency scanning FRS (FSM-FRS). This method involves frequency tuning a narrow line-width continuous wave laser source along the absorption filter's transmission profile. The Rayleigh scattering's spectral distribution will be preserved for each scanning frequency. The FRS signal will not be preserved as the spectral components passing the iodine filter are altered. As images are acquired at each frequency step, spectra are generated for each pixel. In theory, this

should allow for much faster FRS measurements. However, the resulting variables will still be averaged over the time it takes to frequency scan and how many scans (resolution) are needed. Without going into too much detail Doll has used this method to take measurements behind an annular cascade ([54]), an endoscopic fiber-based measurement of gas flows ([84]), a compressed air jet ([85]), a McKenna type premixed flame combustor ([86]), and a Ranque-Hilsch vortex tube ([87]).

Finally, it is important to note that spectroscopic measurement errors can be hard to quantify given the number of variables involved. Ireland [88] attempts to quantify this by using the Cramér-Rao lower bound. This defines the best achievable precision for any given method. This was done by Boyda [80]. Ireland [89] then goes on to prove this method through experimentation.

Minor Relevant Literature

This section will serve to document relevant FRS literature for documentation purposes but for which may not directly apply to this Ph.D. work. This includes both experimentation and other expanded FRS techniques.

It is important to quickly note that FRS has grown to such popularity that a US patent has been awarded to Bivolaru [91] for an interferometric Rayleigh scattering system. This system is capable of simultaneous measurements of temperature, bulk velocity, and density at nanosecond time scales. This is done using a pulsed laser source and a Fabry-Perot interferometer. While highly capable, the system has limited applications outside of a lab.

Yeaton et al. [92] attempt to show a more applicable technique to broader flow regions than Bivolaru by introducing the spatiotemporally resolved filtered Rayleigh scattering (STRFRS) technique which uses an array of solid-state photo-multipliers instead of Fabry-Perot interferometers. The drawback to this technique is the measurement region. Given sixteen photo-multipliers are used to create the array, only 16 locations can be measured at once. This system is capable of 250 MSamples/s. This kind of sampling rate is high above what traditional FRS measurements are capable of at several seconds minimum. It is important to note that this was a proof-of-concept and would need extensive work to get working as a generalized system.

Several other interferometric, time-resolved FRS experiments are worth noting. The first is by Estevadeordal et al. [93] which describes a high-repetition-rate interferometric-

Rayleigh-scattering (IRS) technique capable of high-speed flow-velocity measurements at 10-100 kHz. The drawback is that density and temperature measurements are not possible but planar measurements are. Next, Mielke et al. [94] developed a Rayleigh scattering technique capable of a 32 kHz sampling rate using a continuous-wave-laser focused on a point. Planar measurements are not possible but temperature and density are. Finally, Cutler et al. [95] describe a 100 kHz sampling rate IRS technique capable of planar/multivariable measurements using a burst-mode laser. This technique was specifically designed for large-scale wind tunnels for the study of unsteady and turbulent flows.

Apart from temporally resolved methods as discussed before, time-averaged FRS techniques have large sweeping applications as long as the flow being measured can be considered steady-state. These kinds of measurements have been done for a long time now. For example, Miles et al. [96] in 1992 used FRS to measure flow in supersonic/hypersonic facilities such as the Princeton University Gas Dynamics Laboratory. Shortly after in 1993, Zhao et al. [97] published an article outlining how laser Rayleigh scattering could be applied to combustion techniques and the associated uncertainties.

More recently, Lowe [98] published an article about modern laser velocimetry including FRS and particle image velocimetry (PIV) as it applies to the distortion in the inlets of the engines and future flight applications. However, this paper is just an introduction and largely just covers theory. This leads to the most recent and most applicable published data by the Virginia Tech FRS group (Saltzman et al. [99]). Saltzman applied FRS to a heated supersonic jet with a thermal non-uniformity measuring velocity and temperature. Saltzman compared the FRS results to PIV measurements where the root-mean-square error between the two was 10 m/s and 11 K. This Ph.D. work intends to continue this work and move towards in-flight FRS measurements.

2.3 Knowledge Gaps

This section intends to first outline the knowledge gaps in the in-flight force literature as it pertains to control volume methodology. Secondly, knowledge gaps in the filtered Rayleigh scattering technique will be discussed. Finally, the gap in knowledge of combining the two techniques will be introduced. It should be noted that little to no literature has bridged this specific gap. Instead, related techniques will be presented.

2.3.1 In-Flight Control Volume

As described by the SAEAIR documents [1, 2, 3, 4, 5, 6], industry standards are well-known, albeit, complicated. These methods rely on correlations determined in expensive ground tests to measure correlated ”in-flight” forces. Not only do these methods not measure in-flight forces directly, but they also are not capable of providing flow visualization. Therefore, flow properties have to be inferred. In contrast to industry techniques, Drela [11, 22] describes force decomposition techniques that can be extended to measurement techniques mostly used by experimentalists in wind tunnels (large opportunity to be proven either by experiments and/or simulations). However, these techniques do not rely on complicated correlations and measure thrust and drag forces directly.

The major gap in this literature is bridging the gap between current industry standards and experimental methods. The ultimate technique would replace the current industry standards with a control volume technique that measures flow properties directly with the same/similar uncertainty to current practices. There are two major hurdles to overcome. The first is how to draw a proper control volume that can be used to differentiate between thrust/drag and how individual components get accounted for. All of the control volume methods so far have had one common flaw, the ambiguity of drawing the control volume/surface bounds. Ideas for bounding these control volumes include vorticity, turbulence kinetic energy, velocity, and/or temperature. Regardless of which one(s) is employed, the shear layer remains ambiguous. However, depending on the required uncertainty, the very small shear layer region in a near-field measurement plane will not have a large impact on the final result. For example, including 50% or 75% of the shear layer in the force calculation will not have a large impact since a very large majority of the mass flow will be included regardless of what percentage of the very small shear layer is used. It should be noted that convincing the industry to switch to these new methods is not the scale for which success will be measured. Shifting the industry will take more time and evidence than this work can provide. However, one of the main objectives of this work is to provide the foundation from which an industry shift can start.

Secondly, a measurement technique to pair with the CV methodology is needed. As discussed, this cannot be based on physical probe rakes. Instead, an optical technique will be needed. The proposed technique for this Ph.D. work is filtered Rayleigh scattering paired with an extended Jones/Young method. This will allow for direct measurement of forces (decomposed forces) and flow visualization simultaneously.

2.3.2 Filtered Rayleigh Scattering

Filtered Rayleigh scattering has broad-reaching applications. Major gaps in knowledge remain to get the FRS technique ready for an in-flight application. The Mie and background scattering cannot be ignored and must be accounted for. These can be harsh in-flight given clouds, water vapor, and the plane geometry itself. While Boyda [82] has contributed significantly to this, user input of Mie and background values are still needed. These values are manually iterated based on user inputs to match a simulated spectrum to an experimental spectrum. This needs to be a process in which the results are reproducible, robust, and fundamentally developed. An automatic process can meet these objectives with current modeling techniques. This will require the use of non-linear fitting algorithms that can be broadly applied to highly varying application spaces.

The next major gap is in the post-processing of the raw data. Since each pixel contains its own spectrum and each spectrum must be least-squares fit to a simulated spectrum using an iterative process. Traditionally, hand-fitting high-resolution spectra from each pixel or pixel bin in an image takes weeks or months to accomplish. This is unacceptable given the high cost of in-flight or ground-based measurements on full-scale hardware. Therefore, the post-processing algorithm must be efficient to drive down the processing time to acceptable levels such as hours while retaining accuracy. It should be noted that this work focuses on quantitative measurements. For simple flow visualization and qualitative FRS measurements in near-real time, the work by Saltzman et al. [100] can be used.

In summary, two gaps exist that require an algorithm:

1. An algorithm that can efficiently and robustly post-process raw FRS data into usable variables such as velocity, static temperature, and static density. This fitting algorithm must be quick to provide information close to near-real-time as possible.

2. The algorithm must be capable of processing unwanted effects such as Mie and background scattering values. Measured spectra will have these effects. Without accounting for these effects, the final values for velocity, static temperature, and static density will be biased.

Overall, filling this knowledge gap leads to a large step forward in the fundamental understanding and capability of filtered Rayleigh scattering measurements. Currently, no literature outside of Virginia Tech has attempted to address these issues.

2.3.3 In-Flight Control Volume and Filtered Rayleigh Scattering Technique Combination

Very little literature spans both in-flight force and laser-based techniques. Currently, no FRS-based in-flight force measurements have been published. Therefore, the closest literature to fill this gap will be presented. This includes particle image velocimetry (PIV) and laser-based optical mass flux sensors.

Guimarães et al. [101] look at nonuniform flows ingested by turbofan engines that advanced aircraft concepts with engine/airframe integration must account for. This is done by using particle image velocimetry. This experiment was performed on the Pratt & Whitney JT15D at Virginia Tech's TurboLab. This experiment proved that laser-based optical techniques are a valid way to measure full-scale engine flow parameters.

Cressall et al. [102] performed an experiment looking at the accuracy of volumetric inflow/outflow rates using integrated PIV velocity fields. This kind of measurement is exactly like the one that would be needed for an in-flight measurement using FRS. Cressall showed that this kind of technique measures the volumetric flow rate accurately to within 2% giving good credence that FRS could be used in the same way.

Bridges et al. [103] performed a model-scale test using the NASA Glenn Research Center Aero-Acoustic Propulsion Laboratory (AAPL). Twelve PIV planes were taken in the exhaust which was supplied with heated air delivered from the facility's compressed air system. This air had to be seeded. Although this study was done to measure noise determination methods, it also measured the velocity out of the exhaust. This information is not enough to calculate mass flow. However, it could be envisioned that FRS could have been used for the same test which could have supplied mass flow results. This is another example of how FRS could be used to improve propulsion measurements.

Miller et al. [104] designed and flight-qualified a diode laser-based optical mass flux sensor. This mass flux sensor is specifically for an inlet that is designed to improve propulsion systems for advanced flight vehicles. The sensor works based on the Doppler-shifted absorption of oxygen using a fiber-coupled diode laser source to simultaneously measure density and velocity. This technique is only a point measurement and many points must be taken to get a good average of the air mass flux into an engine. Even though it's limited, the sensor was successfully tested on P&W F-100 gas turbine engines at NASA Dryden. This work was continued much later by Lyle et al. [105, 106], where a modern version of the sensor

was introduced with much lower uncertainty. Even though it is only a point measurement of something FRS could deliver as a planar measurement, it is temporally resolved.

Finally, Lowe [107] presents a completely different approach to measuring in-flight forces with a non-intrusive technique. This method is acoustics based and relies on sonic anemometry and thermometry. This technique is capable of measuring simultaneous temperature and velocity. It has also been applied to ground-based measurements which show promising results for applications like in-flight forces. Since the technique relies on a separate, distinct sound source, efforts are being applied toward the inlet and not necessarily to the exhaust at the time due to poor signal-to-noise ratios. Again, FRS does not have this issue as it is optically based and can be applied to the inlet and exhaust without issue.

Chapter 3 - Processing Techniques and Algorithms for Filtered Rayleigh Scattering Images Including Mie and Background Scattering Contributions

The post-processing of filtered Rayleigh scattering (FRS) data for non-intrusive measurements of 3-component velocity, static temperature, static pressure, background scattering, and Mie scattering is a non-trivial task. Mie and background scattering must be included as they can cause biases in velocity, static temperature, and static density in non-ideal environments. These effects will be present in most practical, real-environment cases outside of highly controlled experiments. This is especially true in exhaust flow cases of turbomachinery (Mie scattering with unburnt propellant) and internal flow cases (background scattering off of walls and other structures).

With the ever-increasing interest in non-intrusive measurements, it is clear that a fast and robust method for evaluating the raw data is needed. The ability of FRS to measure vector and scalar quantities without seed introduction sets it apart from well-known techniques such as particle image velocimetry (PIV) and Doppler global velocimetry (DGV). The algorithm developed in this work is capable of automatically processing images from experiments with Mie and background scattering contributions. This algorithm is applied to FRS in which clear examples are given both in simulation as well as experimentation.

Rayleigh scattering (specifically, Rayleigh-Brillouin scattering or RBS) is a wave optics phenomenon resulting from the interaction of light and matter on the scale of, or smaller than, the wavelength of the laser light. This eliminates the need for seeding flows. The ability to take planar measurements of scalar and vector quantities simultaneously with Rayleigh scattering makes this measurement technique extremely attractive. To do this, the key attributes of the Rayleigh scattering signal must be understood:

1. The Rayleigh scattering resulting from the interaction between light and matter is elastic, meaning there is no energy transfer between them.

2. Rayleigh scattering occurs down to molecular levels.

3. The probability of photons scattering from a gas molecule (scattering intensity) increases with the amount of matter in the volume and the scattering cross-section of the gas (static density/pressure).

4. Light scattered off matter in motion is Doppler shifted in frequency proportional to its bulk velocity (velocity).

5. In a stagnant gas, individual molecules are always in motion, (kinetic theory of gases) imparting a Doppler shift proportional to the speed of the individual molecules (static temperature).

Items 3 through 5 yield the measurement principles, namely that direct measurements of static pressure (3) and static temperature (4) can be used to get static density from the state equation, while the mean Doppler shifted signal yields flow velocity. These effects are all observed through the use of a molecular absorption filter, in this case, an iodine vapor cell is used. Greater details can be found in Miles et al. [50, 96].

The rest of this chapter will be organized into three main sections followed by a conclusions section. The first main section (Section 3.1) is titled "Modeling and Simulation". Section 3.1.1 contains information pertaining to the theoretical modeling of RBS lineshapes, the addition of Mie and background scattering effects, iodine transmission spectra modeling, convolution modeling, and nonlinear fitting algorithms. Section 3.1.2 contains uncertainty analysis information such as Monte Carlo results and multi-level processing schemes. Finally, Section 3.1.3 walks through the results of a simulated experiment.

The second main section (Section 3.2) is titled "Experimental Investigation Techniques". Section 3.2.1 walks through the camera calibration process and expected uncertainties. It should be noted that this is included to provide evidence for bounding the scattering angle variable tightly with high confidence. Section 3.2.2 looks at camera registration and some developments to make this easier in post-processing. Section 3.2.3 goes through the process of finding the discrete wavenumbers that the laser was tuned to using a particle swarm algorithm. Finally, Section 3.2.4 describes how to find the laser vectors over the entire image in an easy and efficient way.

The third main section (Section 3.3) is titled "Final Experimental Data Processing". Section 3.3.1 details a benchtop freejet experiment as an "ideal" case for testing and validation of the entire FRS process. This section includes multi-level processing results as well as FRS and probe data comparisons with the associated uncertainties. Section 3.3.2

details a ”non-ideal” experiment using a JetCat P100-RX turbojet [108]. This experiment was conducted to show the robustness of the processing algorithms and FRS process as a whole. FRS and probe data are also compared with associated uncertainties.

The conclusion will summarize the major findings as well as give some final remarks on future work possibilities. Finally, the appendix will include figures that were not used in the main manuscript but that are considered relevant.

3.1 Modeling and Simulation

The current processing code, developed at Virginia Tech, determines the scattering angle, static temperature, velocity, Mie scattering intensity ratio, background scattering intensity ratio, and static density using a non-linear least-squares fitting algorithm. The least-squares fit compares the measured scattering spectrum to a simulated theoretical spectral model. The theoretical model comes from the convolution of the RBS spectral model with a theoretical transmission spectral model for an iodine vapor cell in the vicinity of 532nm light. This specific wavelength is typical for frequency-doubled, diode-pumped lasers using gain media such as Nd:YVO_4 or Nd:YAG lasers. Doll et al. use similar techniques [54, 84, 85]. The addition of Mie and background scattering into the theoretical model has been covered extensively by [80, 81, 109] and [99]. However, the user must manually iterate to get the theoretical spectrum to match the measured spectrum. This is laborsome and often results in different outcomes based on the user. Therefore, an automatic, iteratively solved scheme has been developed. This method will be covered in detail within this section.

3.1.1 Theoretical Modeling

This subsection will cover five different RBS models- the creation of a hybrid theoretical and experimentally found iodine transmission spectra, and the convolution of these two to create the foundation for the Filtered Rayleigh Scattering technique. From there, this section will end by detailing the non-linear least-squares fitting of the convolution spectra to back out the six fitting parameters of scattering angle, static temperature, velocity, Mie intensity ratio, background intensity ratio, and static density. For an in-depth look at the fundamental theoretical modeling of laser Rayleigh scattering and filtered Rayleigh scattering, the author refers the reader to reference [41].

Rayleigh-Brillouin Scattering Models

Traditionally, RBS spectra have been generated using the numerical Tenti-S6 model [52, 53, 69]. This model has widely been accepted as the current best approximation and is a slight correction to the original Hanson-Morse model [70, 71]. This correction was needed due to an approximation that was made and subsequently proven incorrect by Tenti et al. [52]. Specifically, the Tenti-S6 model is a set of six linear equations that are solved simultaneously to form the RBS lineshape given the dimensionless frequency variable relative to the laser line center (X), the ratio of the acoustic wavelength to the mean free path between collisions (Y), internal heat capacity (c_{int}), internal relaxation number (R_{int}), and Euken factor (f_u) (much simpler than previous models, yet still complex). Y, R_{int}, and f_u are dependent on static flow properties and their relationship can be seen below [53].

$$X = \frac{\nu - \nu_{laser}}{k\nu_0} \tag{3.1}$$

$$Y = \frac{p}{\eta k v_0} = \frac{n_0 k_b T}{\eta k v_0} \tag{3.2}$$

$$R_{int} = \frac{3\eta_b}{2\eta}\frac{(3/2 + c_{int})}{c_{int}} \tag{3.3}$$

$$f_u = \frac{m\sigma}{\eta k_b (3/2 + c_{int})} \tag{3.4}$$

In the equations above, ν is the associated frequency, n_0 is the number density (amount of molecules in a given volume), k_b is the Boltzmann constant, η is the dynamic viscosity, k is the wave vector magnitude defined as $k = 4\pi \sin(\theta/2)/\lambda$ with θ being the scattering angle and λ the wavelength of the incident light, v_0 is the most probable gas kinetic velocity which is defined as $v_0 = \sqrt{2k_b T/m}$ with m being the molecular mass of the gas, η_b is the bulk viscosity, and σ is the thermal conductivity. The reader is encouraged to refer to references [52, 53, 69] for a more in-depth discussion and derivation behind this model lineshape.

A nominal flow case (standard sea level conditions with a velocity of 100 m/s) was chosen to investigate the effects of the number of nodes versus generation time where a wavenumber of zero is the laser frequency. Nodes represent the number of points to include

in the generation of the Rayleigh line shape. The model will have to iteratively generate a large number of these spectra for each pixel in an image. Therefore, it is of the utmost importance that this run as fast as possible. Ten-thousand nodes were used as the "true" case and then compared. Five hundred nodes were decided to be used in the model due to its low error and fast computation time relative to the "true" case (Fig. 3.1). The difference plots show that the error oscillates between nodal points. At each node, the error is zero. However, the error between each node can reach several percent. At higher nodal levels, the oscillations get closer together and have less magnitude error which causes the charts to look solid. It should also be noted that the error in the higher nodal levels is symmetric about the center wavenumber whereas, for 50 nodes, a non-symmetric pattern can be seen.

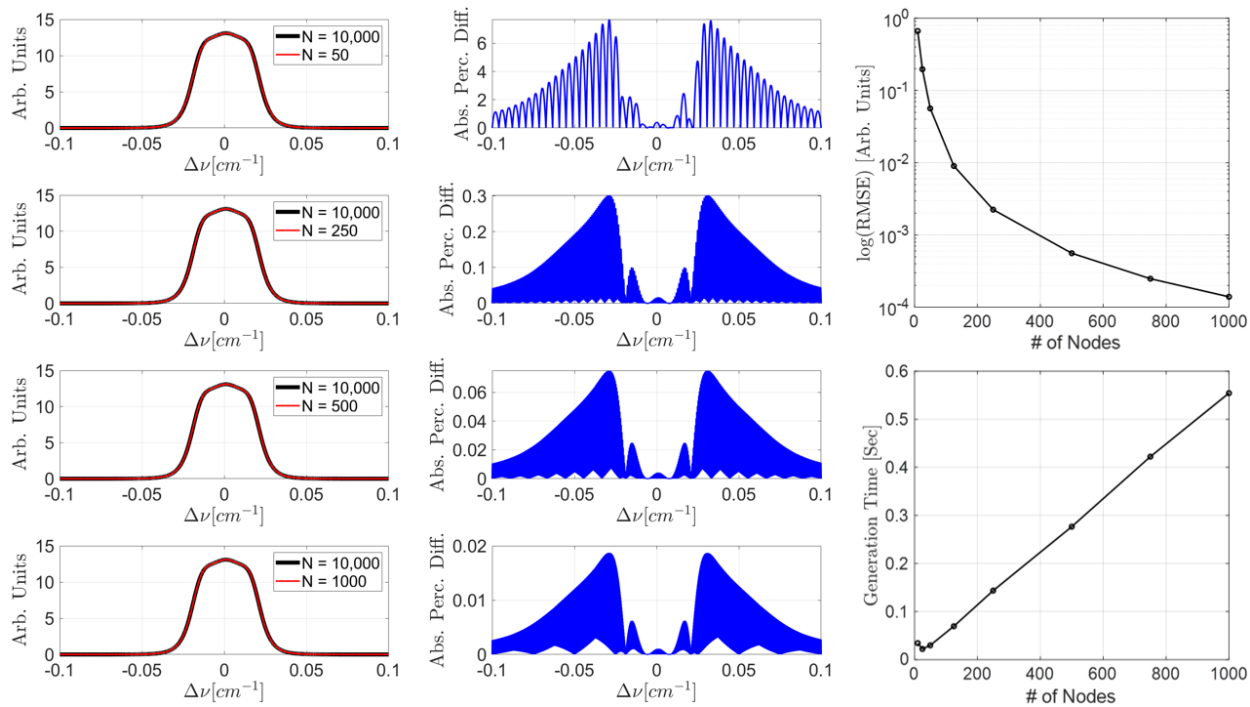

Figure 3.1: Tenti S6 model results using various numbers of nodes. RMSE and generation time are also included. The right side shows the normalized percent difference between the "true spectra" and the different nodal levels.

The Tenti-S6 model has been examined specifically for FRS purposes by McManus et al. [69]. Specifically, McManus investigated the Tenti-S6 model for combustion-relevant gases using an experimental setup. This was done by comparing the measured FRS signals to the simulated FRS signals generated by convolving the Tenti-S6 model and an experimentally verified iodine absorption model. It was experimentally shown that over a temperature range of 300K to 2400K, with representative exhaust gases from a combustion cycle, the Tenti-S6

model was accurate to less than a 4% average difference. However, Doll et al. [68] challenge this standard by using high signal-to-noise ratio FRS spectra to calibrate the RBS lineshape based on their derived analytical model. This will be discussed further later.

Alternative numerical models were pursued such as a newer, simpler, RBS lineshape model that was introduced by Witschas [72]. This model is an easily processable, analytical alternative to the highly complex Tenti-S6 model. The model is made up of three Gaussian lineshape equations. One for the central Rayleigh peak and two for the red and blue-shifted Brillouin side lobes. In limited applications, the Witschas model can be faster and has an error smaller than 0.85% compared to the Tenti-S6 model. The application is limited to a defined range for Y between 0 and 1.027. Such a model is useful if processing time or computation power is limited. The Witschas model will be used for comparison later.

Two other analytic models by Doll et al. [74] were investigated. Both models are made up of eleven parameter functions consisting of sixty-eight coefficients. The eleven parameter functions are then used in three functions that are superimposed to create the central Rayleigh peak followed by the red and blue (stokes and anti-stokes) shifted Brillouin side lobes. The sixty-eight coefficients are found via fitting to a provided lineshape. In the first case, the provided lineshape is just the Tenti-S6 model making this analytic model analogous to the Witschas model (with more equations allowing for a better fit). In the second case, the provided lineshape is an experimentally found RBS lineshape. The second case is limited in the Y range due to experimental limitations. Values outside of this range will be shown for investigation purposes only.

Finally, Hunt et al. [73] assert that the Tenti-S6 model can be computationally expensive, especially when using it in an iterative scheme. Again, an iterative scheme is being used to match simulated FRS data to experimental FRS data. This assertion is not unlike that made by Witschas and Doll. Instead of an analytical model like Witschas or Doll, Hunt opts for a machine-learning approach. This method is called the support vector spectrum approximation (SVSA). This uses vector regression and singular value decomposition to create an efficient, accurate, and well-conditioned approximation of any existing spectral lineshape. Therefore, its limitations are largely based on the model used for training.

The SVSA results seen in Fig. 3.2 are compared against the chosen Tenti-S6 model with five-hundred nodal points. It should be mentioned that this implementation of SVSA was trained using the Tenti-S6 model. It is possible to use the SVSA method to decrease the nodal points even further which drives down the computation time without significantly

increasing error. These results show that error does not decrease much despite increasing the number of SVSA nodal points. However, the computation time increases significantly. Generally, the author has used at most 180 individual wavenumbers in an experiment. To keep the number of nodal points above that number, two-hundred nodal points are used with the SVSA method. In an experiment, the data will not be taken exactly at the nodal wavenumbers. Therefore, the simulated Rayleigh scattering spectrum needs to be interpolated to match the wavenumbers used in the experiment. Using more nodal points than experimental wavenumbers allows the interpolation error to stay low. In practice, the author has noted that the SVSA method is approximately four times as fast compared to the original Tenti-S6 model with an accuracy of a few percent (see Fig. 3.2). Specifically, this method was developed to optimize the design of an FRS experiment of a complex flow. It is important to note that the SVSA approximation results in a slight deviation near the peak of the Rayleigh scattering spectrum (can be seen if closely examining Fig. 3.2). This is shown to be negligible as the deviation in peak behavior is essentially "filtered out" during the convolution operation with the theoretical iodine transmission spectrum (discussed later).

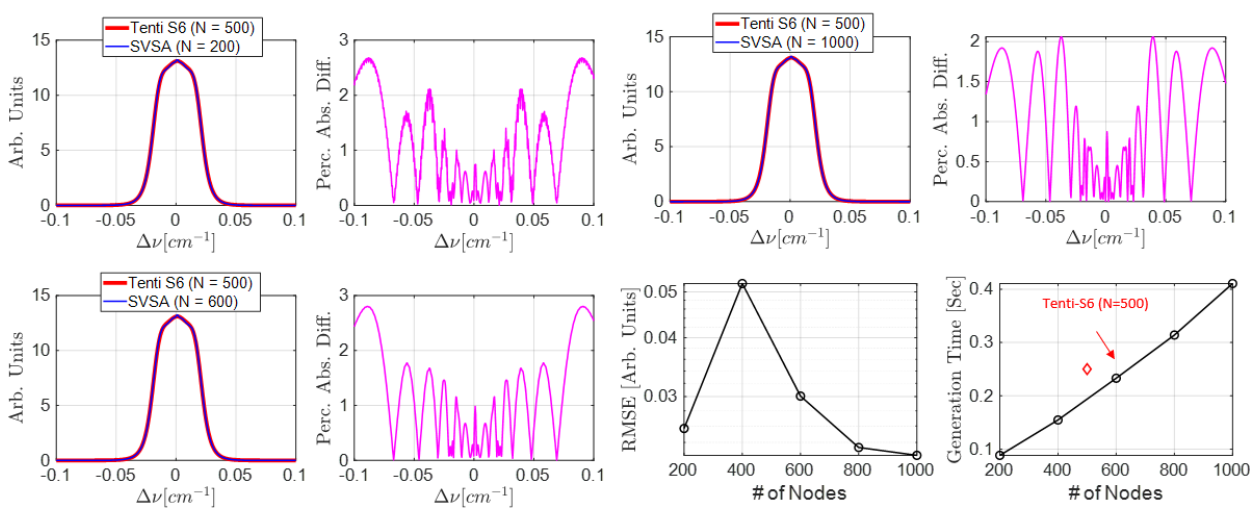

Figure 3.2: Support vector spectrum approximation (SVSA) comparison to the Tenti S6 model with a different number of nodes. RMSE and generation time are also included. The pink charts on the right represent the normalized percent difference between the Tenti S6 model and SVSA model at different nodal levels.

Now that all five models have been introduced, they can be compared. From this point forward the original Tenti-S6 model will be referred to as "$RBS-S6$", the Witschas model as "$RBS-W$", Doll's Tenti-S6-based model as "$RBS-D$", Doll's experimentally calibrated based model as "$RBS-DC$", and the SVSA model as "$RBS-ML$". The first thing all of the newer models are aimed at is computational efficiency. An overview comparison, as well

as an order of magnitude time comparison, are in Table 3.1.

Table 3.1: Overview of Rayleigh-Brillouin scattering models, spectrum generation time, type of model, and the operation limits for each model. ML = Machine Learned.

Model	Time [S]	Type	Limits
$RBS - S6$	10^{-1}	Numerical	$T < 2400K$
$RBS - W$	10^{-4}	Analytic	$0 < Y < 1.027$
$RBS - D$	10^{-4}	Analytic	$0.32 < Y < 2.4$
$RBS - DC$	10^{-4}	Analytic	$0.68 < Y < 1.17$
$RBS - ML$	10^{-2}	ML	Conditional

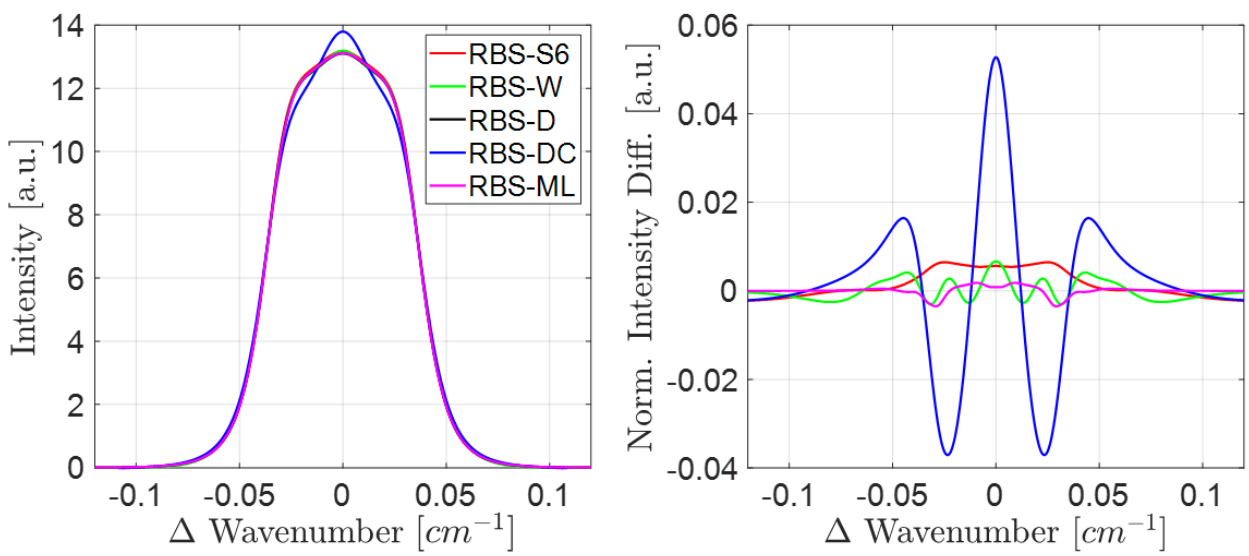

Figure 3.3: Normalized Rayleigh-Brillouin scattering lineshape model comparison. Similar to that shown by Doll et al. Left: Rayleigh-Brillouin scattering lineshape comparison. Right: Max normalized difference to $RBS - S6$. Plotted for $\theta = 90°$, $T_s = 300\ K$, and $\rho_s = 1.225\ kg/m^3$

Table 3.1 does not, however, show the accuracy of these models. For accuracy, Fig. 3.3 is needed. The left Fig. 3.3 shows an example RBS lineshape from each model (all models valid) while the right shows the normalized percent difference to the $RBS - S6$ model (assumed correct). The easiest difference to see is that of the $RBS - DC$ model. It has a larger central Rayleigh peak and smaller Brillouin side lobes. This difference results in a max difference to the $RBS - S6$ model of 5%. The reasoning for the difference in shape can be found in Doll et al. [68] but can be simply explained by the difference between experimental data and theoretical data for this particular range of scattering angles. The rest of the models, based on the $RBS - S6$ model, line up very closely and are within a 1% difference. These differences will all result in slightly different values for scattering angle, static temperature, velocity,

Mie intensity ratio, background intensity ratio, and static density even when given the same data set. Therefore, the trade-off between time and accuracy must be made appropriately. It is important to note that all RBS lineshapes have been normalized by Eq. 3.5 such that the integral intensity is unity.

$$S_{RBS_{Norm}} = \frac{S_{RBS}}{\int_{-\infty}^{\infty} S_{RBS} d\nu} \qquad \text{where,} \qquad \int_{-\infty}^{\infty} S_{RBS_{Norm}} d\nu = 1 \tag{3.5}$$

To help inform the impact of the model differences, the effect of the measured parameters on the RBS spectral lineshape needs to be well understood. Figure 3.4 is an example of the Rayleigh lineshape dependencies using the $RBS - S6$ model. The same figure can be found for the other models in Fig. 3.5.

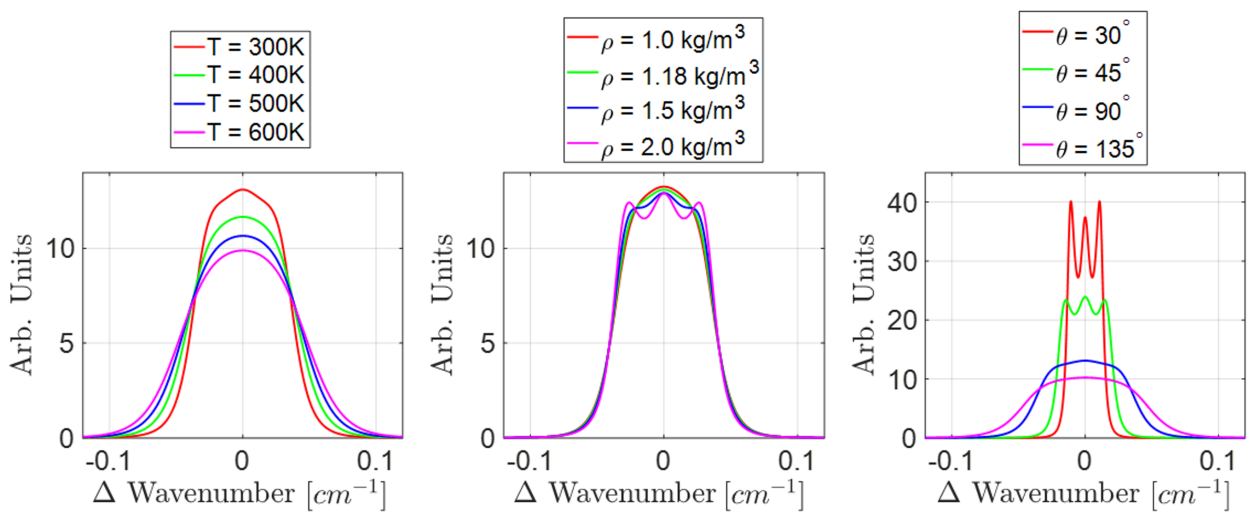

Figure 3.4: Normalized $RBS - S6$ Rayleigh-Brillouin scattering lineshape dependencies. Left: Static temperature. Middle: Static density. Right: Scattering angle.

The left chart of Fig. 3.4 shows the static temperature dependency of the RBS lineshape. As the static temperature increases, the RBS lineshape is broadened while the peak intensity decreases. The spectral full-width half-maximum scales approximately with the square root of static temperature [65]. These characteristics of static temperature dependency hold for all models being investigated. The middle chart of Fig. 3.4 shows the static density dependency of the RBS lineshape. As the static density increases, the Brillouin side lobes become more pronounced. This also leads to variations in peak intensity. Finally, the right chart of Fig. 3.4 shows the scattering angle dependency of the RBS lineshape.

The scattering angle is defined by the angle between the laser propagation vector ($\hat{i}$)

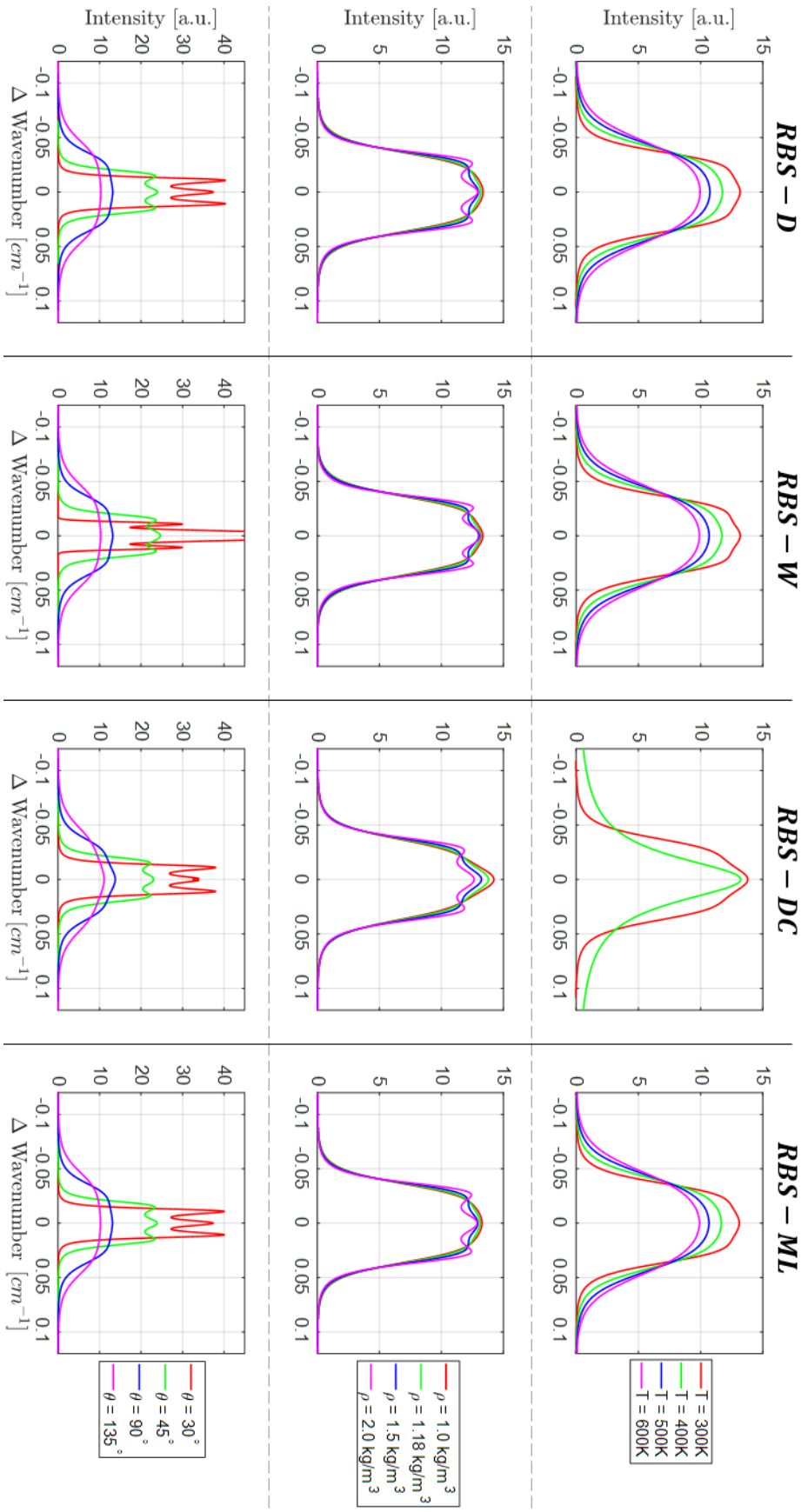

Figure 3.5: Rayleigh model dependencies on static temperature, static density, and scattering angle.

and the observation vector ($\hat{o}$). See Fig. 3.6 for a visual description. As the scattering angle is decreased, Brillouin side lobes become very pronounced and the peak intensity becomes very large. Forward scattering ($\theta < 90°$) results in lower intensity RBS signals compared to backward scattering ($\theta > 90°$). Figure 3.4 has been normalized in such a way that it makes it difficult to see this. It should be noted that all models follow the same characteristics as listed above. However, limits seen in Table 3.1 limit the application of the models to some of the examples seen in Fig. 3.4.

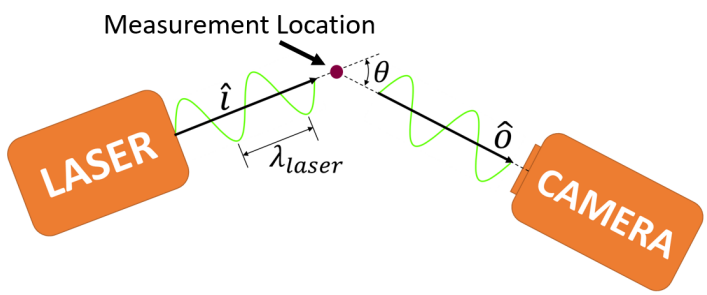

Figure 3.6: Simplified scattering angle visual.

Not included in Fig. 3.4 or Fig. 3.5 are the effects of velocity. The bulk velocity of the flow will Doppler shift the entire RBS spectrum to the left or right on the wavenumber spectrum depending on the sign of the velocity measured. This velocity can be computed using the Doppler shift equation (Eq. 3.6) as long as the laser propagation and observation vector are known as described in Fig. 3.6. Note that the velocity is measured (sensed) in the direction of the difference between the scattered light direction and the laser propagation direction. See Cadel et al. [90] for an in-depth explanation.

$$\Delta\nu_D = \frac{(\hat{o} - \hat{i}) \cdot \overrightarrow{V}}{\lambda} \tag{3.6}$$

Addition of Mie and Background Scattering

Mie scattering is the scattering of the incident light (laser light) off of particles in the air that are of the same size or larger than that of the wavelength of light. Since the Mie scattering is due to particles moving with the flow, the scattered light will Doppler shift along with the rest of the RBS spectrum. For the present work, the author has defined the width of the Mie scattering spectrum using 200 MHz corresponding to 5 - 18% turbulence intensity of the flow - representative of flow cases generated from Virginia Tech facilities

[81]. One-half of this width becomes the standard deviation input to the normal probability density function used to produce the Mie scattering spectrum. This spectrum can be seen in Fig. 3.7.

Background scattering can also be called geometric scattering as it is the scattering of the incident light off of objects that can be seen with the camera. This scattering will not be Doppler-shifted with the flow since the background is (generally) not moving. This can be seen in Fig. 3.7 as the resulting intensity increase is offset from the Doppler-shifted frequency (located at the nominal center frequency of the laser). The background spectrum is also generated using a normal probability density function; however, the mean is placed at the offset wavenumber due to the velocity of the flow, and the laser frequency variation defines the standard deviation. The current work makes use of a Coherent Verdi-V18 laser with a stated laser frequency stability of 5 MHz. Compared to Mie scattering, background scattering is much narrower, but the resulting intensity peak is much greater in magnitude.

Finally, all three scattering contributions (S_{Mie}, S_{Bknd}, and S_{RBS}) can be added together to give the total scattering spectrum (S_{Tot}) which can be seen at the right of Fig. 3.7. This figure clearly shows that when a bulk velocity is applied to the flow, background and Mie scattering will have different effects on the final spectrum. Just like with RBS, the Mie and background scattering equations need to be normalized (Eqs.3.7 through (3.11)). The only difference is that the normalized spectrum is multiplied by an integral intensity ratio (IR). Finally, the three spectra can be combined via Eq. 3.11 to find the conglomerate spectrum. The integral of the combined spectrum ($S_{Tot_{Norm}}$) is 1. It is important to note that Mie and background scattering effects are unwanted and must be mitigated. The following subsection will discuss how to filter most of their influence out of the final signal.

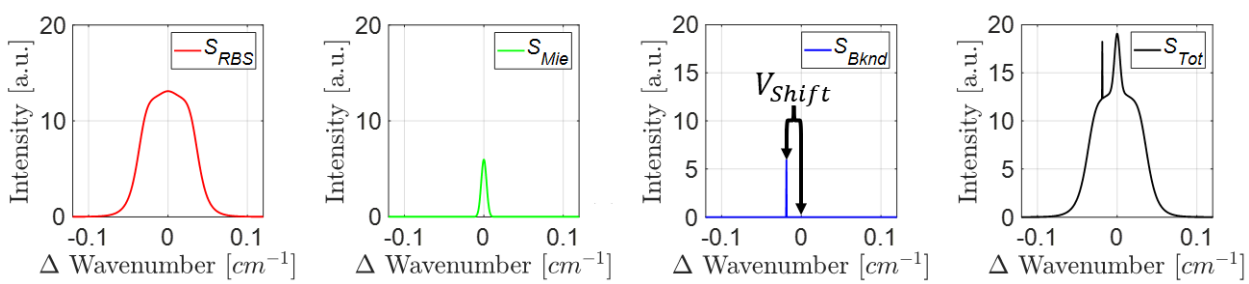

Figure 3.7: Effect of Mie and background scattering on final scattering signal. Generation parameters: T_s of 300K, θ of 90°, ρ_s of 1.1 kg/m^3, Mie_{IR} and $Bknd_{IR}$ of 0.1 and 0.01, and V of 100 m/s. Note: Background scattering shown shifted relative to other scattering due to non-zero velocity.

$$S_{Mie_{Norm}} = \frac{S_{Mie}}{\int_{-\infty}^{\infty} S_{Mie} d\nu} * IR_{Mie} \tag{3.7}$$

where,

$$IR_{Mie} = \frac{I_{Mie}}{I_{RBS}} = \frac{\int_{-\infty}^{\infty} S_{Mie} d\nu}{\int_{-\infty}^{\infty} S_{RBS} d\nu} \tag{3.8}$$

$$S_{Bknd_{Norm}} = \frac{S_{Bknd}}{\int_{-\infty}^{\infty} S_{Bknd} d\nu} * IR_{Bknd} \tag{3.9}$$

where,

$$IR_{Bknd} = \frac{I_{Background}}{I_{RBS}} = \frac{\int_{-\infty}^{\infty} S_{Bknd} d\nu}{\int_{-\infty}^{\infty} S_{RBS} d\nu} \tag{3.10}$$

$$S_{Tot_{Norm}} = S_{Mie_{Norm}} + S_{Bknd_{Norm}} + S_{RBS_{Norm}} \tag{3.11}$$

Iodine Transmission Spectra Modeling

A molecular vapor filter can be used with known absorption levels to attenuate the unwanted scattering signals such that the RBS signal may be interrogated. An iodine vapor cell works well with 532nm (green) laser light (Shimizu et al. [57]) due to several deep transitions that occur in the spectral region around this wavelength. The specific iodine transmission spectrum model used in the current work with the 532nm laser is the same as that developed by Forkey and colleagues ([58, 59]). However, alternative combinations of laser light and molecular filters do exist such as Mercury at 253.77nm (Yalin et al. [61]), Cesium at 389, 852, and 894nm (Fischer et al. [62]), and Barium at 355nm (Hetlage et al. [64]).

The iodine absorption spectrum can be seen in Fig. 3.8 for a wide range of wavenumbers. The red box outlines the wavenumber range to which the simulated and experimental results will use. This box has been zoomed in to show the sharp features that will be used to attenuate the total RBS signal. Finally, the total RBS signal has been plotted on top of the iodine absorption spectrum. Note that the Mie and background scattering contributions rise above a normalized intensity of one. Leveraging the sharp absorption features of iodine, one aims to filter out these undesirable contributions as much as possible.

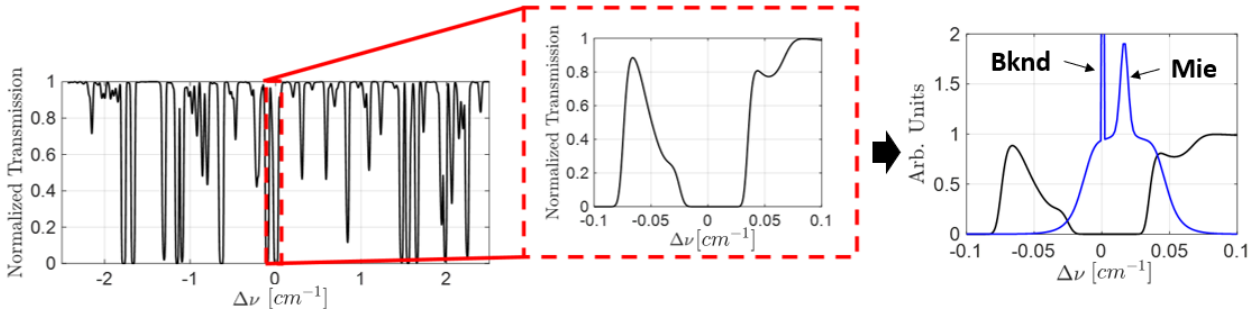

Figure 3.8: Iodine transmission spectrum (Forkey spectrum) for an iodine vapor cell. Representative RBS signal is also included.

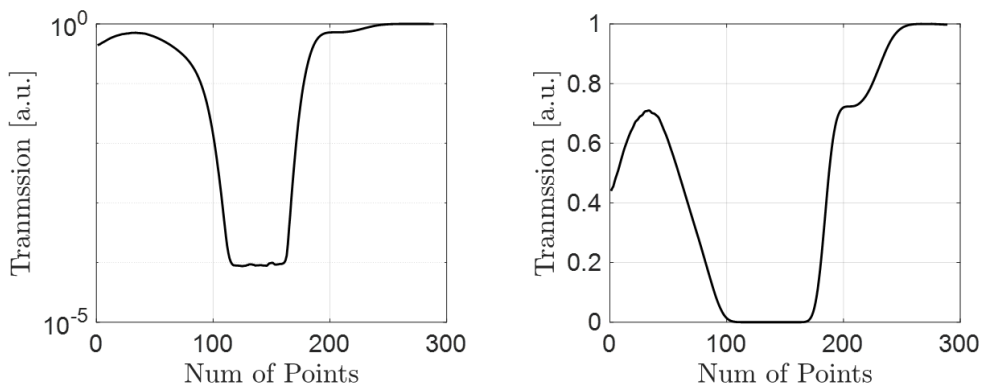

Figure 3.9: Experimentally found iodine transmission spectrum. Note that the flat line of the transmission is sensor-dependent. Left: Log scale. Right: Linear scale.

The iodine transmission spectrum developed by Forkey et al. [58, 59] is purely theoretical. While accurate, it does not exactly give what the camera is seeing. Therefore, the transmission spectra must be found experimentally using the same camera that would be used in an actual filtered Rayleigh scattering experiment. This must also be done at the time of each experiment so that camera drift and degradation can be accounted for. To do this, the laser beam must be spread out and directed onto the wall such that the camera and iodine cell pair can see it. The larger the laser spot on the wall the better. This is because the pixels can be averaged together to generate high signal-to-noise ratios. Shining the laser on the wall allows for high counts within the camera while tracking the intensity of the light while the laser is scanned over the correct wavenumber range. Scanning refers to investigating a set of discrete wavenumbers that have a predefined range that can be controlled via voltage input to a PZT motor within the laser head. The data is then compiled in Fig. 3.9.

Photodiodes were used along with a split-off section of the laser and another iodine cell to track the transmission level. These values were then fit via particle swarm [110, 111, 112]

to the theoretical transmission spectrum to back out the wavenumbers. This can be seen in Fig. 3.10. This will incur some error since the theoretical transmission spectrum is not what the actual transmission spectrum is. However, this error is assumed small over the scanning range.

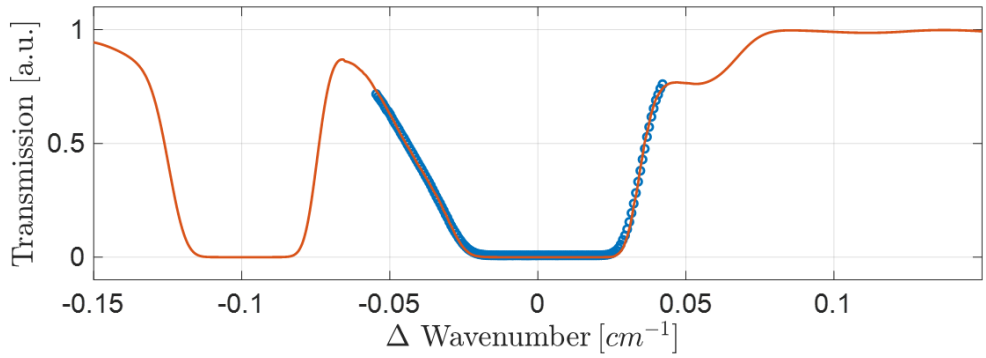

Figure 3.10: PD fit (blue circles) to theoretical transmission spectrum (red line) to back out scanned wavenumbers.

Now that the wavenumber and experimentally found transmission values are available, they can be plotted on top of the theoretical transmission spectrum. This can be seen in Fig. 3.11. The measured transmission spectrum has been smoothed using a moving average filter to get rid of any erroneous points. The difference between the two curves is quite large. Especially on the left side of the trough. In the log-scaled figure, it can be seen that the bottom of the trough is flat in the measured spectrum. This is where the camera could no longer see anything. Since the transmission is so low, leaving it flat will not affect the result.

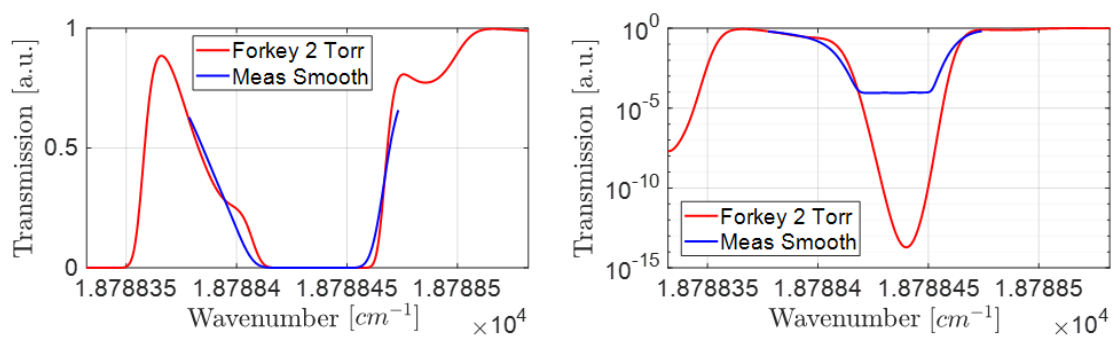

Figure 3.11: Spectra comparison between the theoretical transmission spectrum as well as the experimentally found iodine transmission spectrum.

The last problem to overcome is that the experimentally found iodine transmission spectrum does not cover all available wavenumbers in the theoretical Forkey spectrum. Therefore, a hybrid transmission spectrum must be made. The hybrid spectrum consists of splicing the

experimentally found results into the theoretical results (see Fig. 3.12). Since the experimentally found data is significantly different from the theoretical spectrum, it is intended that the FRS experiment will only scan over the discrete set of wavenumbers that were predefined during the experimental transmission spectra scans. If the theoretical spectrum or wavenumbers outside of the discrete set were used then the final resulting values of scattering angle, static temperature, velocity, Mie and background intensity ratio, and static density would have some inherent bias. This bias comes from the ability of the iterative model to fit any spectra well. However, the variables used to create the fitted spectra may not be correct if the simulated spectra are using models not indicative of the actual setup. Therefore, the bias may change depending on what is being measured so no bias estimates will be given here. In other words, the models applied to simulate the spectra must be representative of the experimental setup. Otherwise, bias will be incurred.

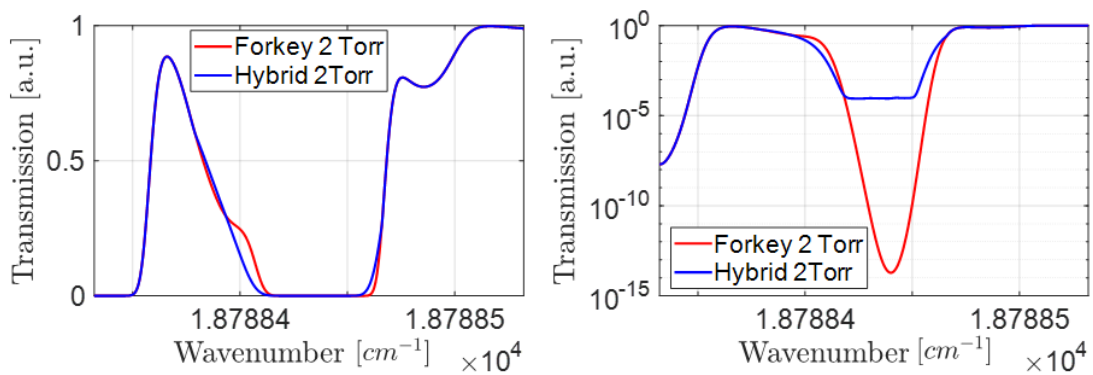

Figure 3.12: Comparison of hybrid iodine transmission model and theoretical transmission model.

Convolution Modeling of Rayleigh Scattering and Iodine Transmission Spectra

Boyda et al. [56] describe that the actual signal received by the measurement device (camera) is the convolution of the transmission spectrum of the molecular filter and the Rayleigh, Mie, and background (geometric) scattering spectrum. This can be seen in Eq. 3.12 where the transmission spectrum of the iodine cell is defined by τ_{I_2}.

$$S_{FRS}(v) = S_{Tot} \otimes \tau_{I_2}$$

$$S_{FRS}(v) = \int_{-\infty}^{\infty} S_{Tot}(\eta)\tau_{I_2}(\nu - \eta)d\eta \tag{3.12}$$

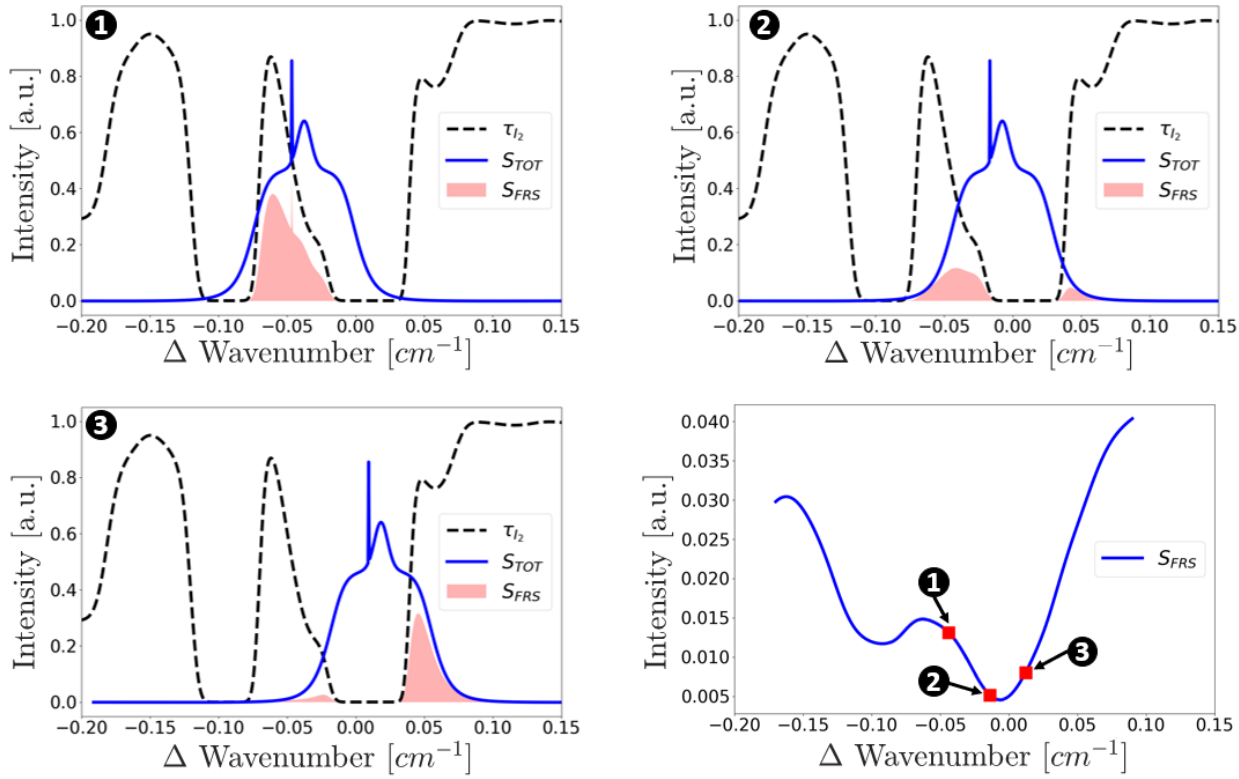

Figure 3.13: 1-3: Example convolutions with the I_2 transmission spectrum in black, the total scattering spectrum in blue, and the FRS signal in red. Bottom Right: Final convolved spectrum in blue plotted with the individual contributions from the three example frequencies. The center wavenumber is approximately 18788.4 cm^{-1}. Printed with permission from Warner et al.

Since the laser is scanned over a wavenumber range, a RBS signal is produced at each wavenumber. This wavenumber corresponds to a specific absorptivity level in the iodine transmission spectrum. Therefore, the convolution must be calculated at each wavenumber and then reconstructed to form the final convoluted spectrum. Figure 3.13 shows this process as charts 1-3 show the iodine transmission spectrum in black and the RBS spectrum in blue on the center laser frequency. The remaining FRS signal is shown in red as a majority of the RBS signal is filtered out. The shape of this red-shaded region contains information about the velocity, temperature, density, and Mie and background scattering of the flow. Finally, on the bottom right, the full convolution signal is shown in blue. Notice the differences between this spectrum and the iodine transmission spectrum. This blue line is what can be compared to the experimental data as the camera looks through an iodine cell. In other words, the camera measures the convolved spectrum, not the pure RBS signal.

Instead of using the combined Rayleigh-Brillouin, Mie, and background scattering spectra and then taking the convolution (as seen in Fig. 3.13), each piece can also be

convolved separately and then added together. This can be seen in Fig. 3.14. Looking at it broken up, it is much easier to see where the components are affecting the overall transmission. Inside the deep troughs, almost no Mie or background scattering influence is present. However, in the high transmission regions, the Mie and background scattering greatly affect the final convolved spectrum. This effect is evident in the bottom right chart of Fig. 3.14 as the combined convolution matches well to the RSB signal only convolution in the troughs but not in the higher transmission region. This will be discussed in detail later.

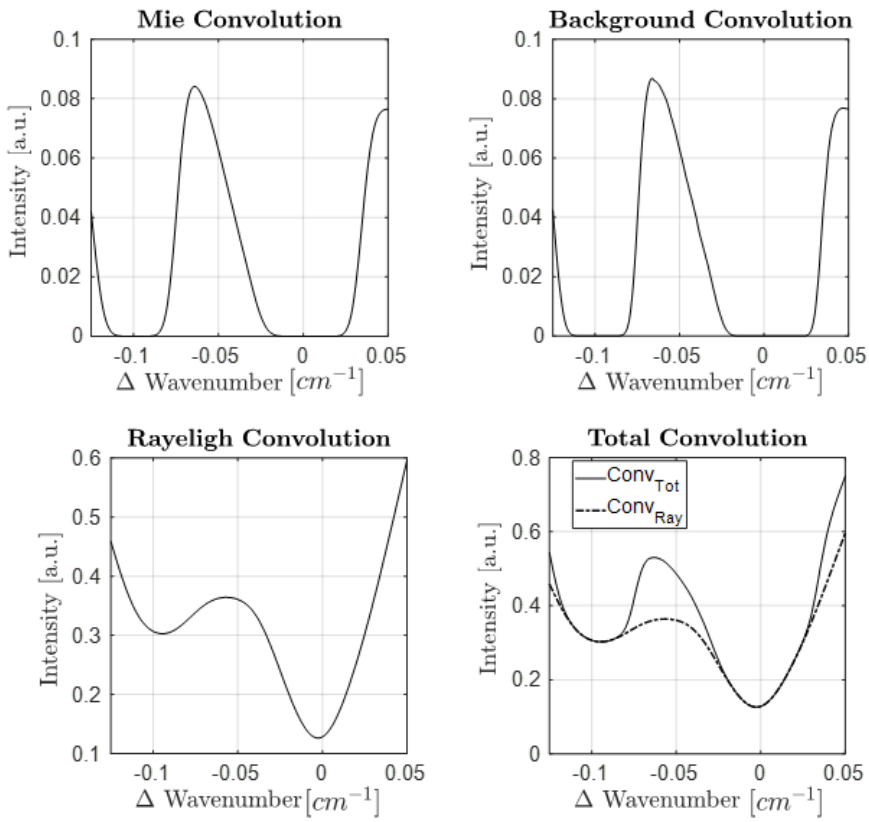

Figure 3.14: Calculating the convolved signal. Top left: Pure Mie scattering convolution. Top right: Pure background scattering convolution. Bottom left: Pure Rayleigh-Brillouin scattering convolution. Bottom right: Total convolution and pure Rayleigh-Brillouin scattering convolution.

The total convolution seen in Fig. 3.15, includes the static density influence on the RBS spectra seen previously. However, this influence comes mostly from using the ideal gas equation to find static pressure to feed into Eq. 3.2. It does not account for the overall intensity increase of the convolution spectra will see with a higher static density. The following formulation will walk through incorporating this effect into the convolution model.

To get a density-dependent convolution spectrum, Yeaton et al. [92] identified that

the statistical expectation of the total number of Rayleigh scattered photons incident on the camera sensor can be written as Eq. 3.13 where P_o is the incident laser power, n is the molecular number density, L_x is the length of the measurement volume along the propagation direction, λ is the wavelength of the incident light, Ω is the light collection angle, Δt is the time integration (camera exposure time), ϵ is the efficiency of the optical measurement system, h is the Planck constant, c is the speed of light, $\frac{d\sigma}{d\Omega}$ is the differential scattering cross-section, and β is the angle between the laser polarization and the scattering direction which is different from the scattering angle, θ.

$$N_r = \frac{P_o n L_x \lambda \Omega \Delta t \epsilon}{hc} \left(\frac{d\sigma}{d\Omega} \right) sin^2 \beta \tag{3.13}$$

$$n = \left(\frac{N_A}{M} \right) \rho_s \tag{3.14}$$

The molecular number density, n, is related to the static density by Avagadro's constant, N_A, and the molar mass, M. This can be seen in Eq. 3.14.

For constant imaging position, gas composition, laser properties, interrogation volume, and exposure time the terms relevant to the constant values can be grouped as the photon constant, C_p in number of photons per unit density as seen in Eq. 3.15. With the integration of the photon constant, C_p, Eq. 3.13 can be transformed into Eq. 3.16. This equation shows that the incident Rayleigh scattered photons are directly proportional to the static density. Therefore, the convolution intensity is proportional to the number of photons incident on the camera sensor.

$$C_p = \frac{P_o L_x \lambda \Omega \Delta t \epsilon N_A}{Mhc} \left(\frac{d\sigma}{d\Omega} \right) sin^2 \beta \tag{3.15}$$

$$N_r = C_p \rho_s \tag{3.16}$$

The conversion from photons to intensity involves a conversion from photons to electrons then an analog to digital conversion from electrons to intensity count. These conversions will each have noise but will be ignored for now and put aside for future investigation. Therefore, these conversions can be lumped into a single intensity constant, C_I, in units of counts per photon. With this constant, the convolution equation becomes Eq. 3.17. Where, the integral

intensity is defined in terms of two parameters, density and an intensity scaling factor, which contains all the dependencies of the physical setup. Therefore, Eq. 3.17 can be rewritten with Eq. 3.12 in mind as Eq. 3.18 where S_{Tot} contains all the gas property-dependent shape changes and, after combining the photon coefficient and the intensity coefficient into a single intensity scaling constant, $C_{IS}\rho_s$ is responsible for the integral intensity scaling.

$$C_p C_I \rho_s = \left(\frac{P_o L_x \lambda \Omega \Delta t \epsilon N_A}{Mhc} \left(\frac{d\sigma}{d\Omega} \right) sin^2\beta \right) C_I \rho_s \tag{3.17}$$

$$S_{FRS}(\nu) = (C_{IS}\rho_s S_{Tot}) \otimes \tau_{I_2} \tag{3.18}$$

Since associative properties hold in the convolution, the scalar multiple $C_{IS}\rho_s$ can be brought outside of the convolution to result in the final convolution equation as Eq. 3.19. This is the signal model that will be used for all results from here on.

$$S_{FRS}(\nu) = C_{IS}\rho_s \int_{-\infty}^{\infty} S_{Tot}(\eta)\tau_{I_2}(\nu - \eta)d\eta \tag{3.19}$$

In practice, C_{IS} may be determined explicitly with the experimental observation of the convolution spectrum if scattering angle, static temperature, sensed velocity, and static density are all known. This is only true during a flow-off case where ambient measurements of each are highly reliable. This methodology will be used and presented in detail later on when discussing experimental processing.

Now that the method to get the convolved spectra has been defined, the results from Fig. 3.4 can be repeated. This time it will be done with the convolved spectrum instead of the pure RBS signal. The results of this convolution can be seen in Fig. 3.15 (the convolution spectra of the other four RBS models are in Fig. 3.16). Starting with the top left chart, as the velocity increases, the spectrum has a bulk wavenumber shift to the left of the center wavenumber value. Consequently, as the velocity decreases, the spectrum shifts to the right. No other changes are caused by velocity. Now, looking at the top middle chart, as the static temperature rises, the troughs become lower and the peaks become higher. At high static temperatures, the first dip on the left starts to disappear as the RBS spectrum becomes wider and wider. Just like in Fig. 3.4 the spectra have been normalized so the static density change (top right chart) is not as clear. An increase in static density bulk shifts the entire spectrum up in intensity. The peak RBS values are also altered slightly which is what is

causing the slight differences in the higher transmission regions. Velocity, static temperature, and static density can then be used to derive static pressure as well as many total values.

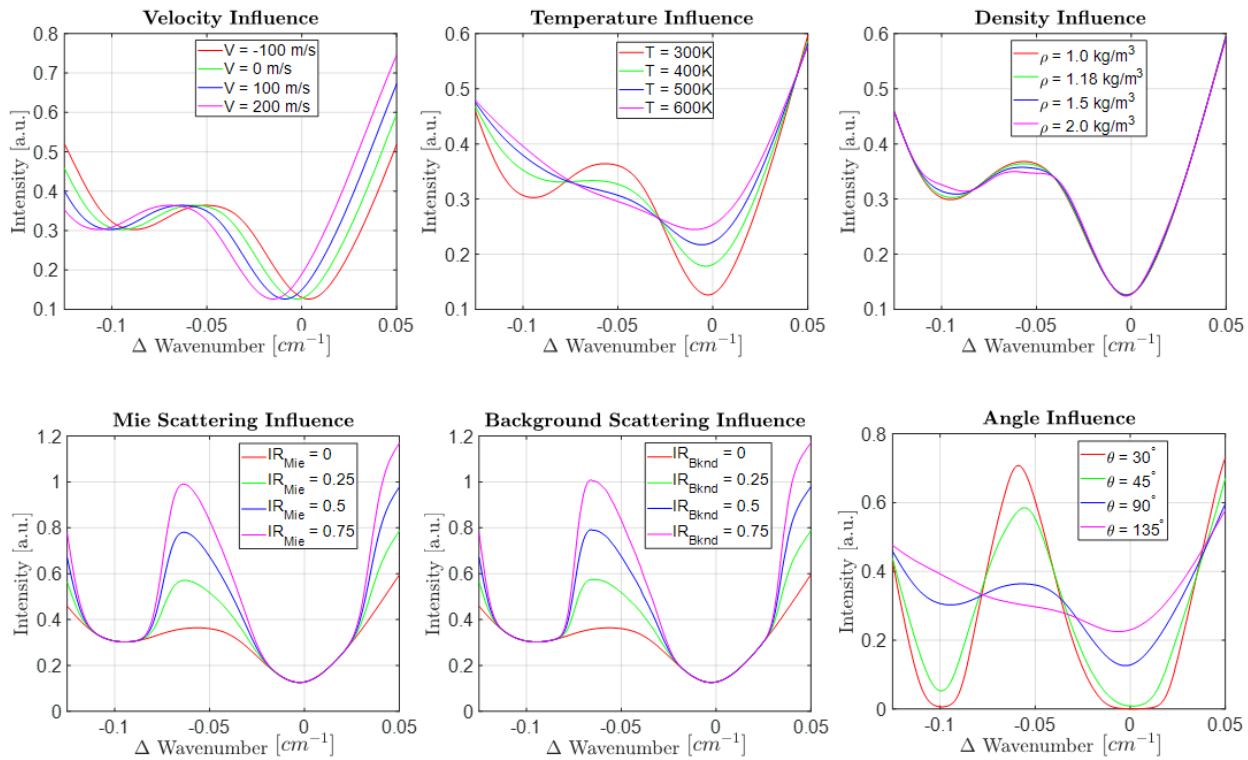

Figure 3.15: Convolution spectra dependencies on flow properties. X-axis is $\Delta Wavenumber$ ($\Delta\nu$) and Y-Axis is intensity in arbitrary units. Shown using the $RBS - S6$ Rayleigh-Brillouin scattering model. Constants when variable is not being varied: $V = 0\ m/s$, $T = 300\ K$, $\rho = 1.18\ kg/m^3$, $\theta = 90°$, $Mie_{IR} = 0.25$, and $Bknd_{IR} = 0.5$.

Looking at the bottom right chart, the scattering angle variation has a major impact on the spectra shape, as expected. In the forward scattering regime, the Doppler broadening effect becomes less prominent as the scattering angle approaches 0°, yielding less Rayleigh scattered light. Looking at Fig. 3.4, even though the intensity is greater, the width of the Rayleigh lineshape is smaller. When the light is filtered by the convolution with the molecular filter, most of it gets filtered out compared to the backward scattering regime which is much broader even though it has less overall intensity. This decrease in sensed Rayleigh scattered light in the forward scattering regime results in the convoluted spectrum appearing much like the iodine absorption spectrum. Finally, the bottom left and bottom middle charts in Fig. 3.15 describe the Mie and background influences on the final convolution. In this case, since velocity is held constant at zero, the effects look almost the same.

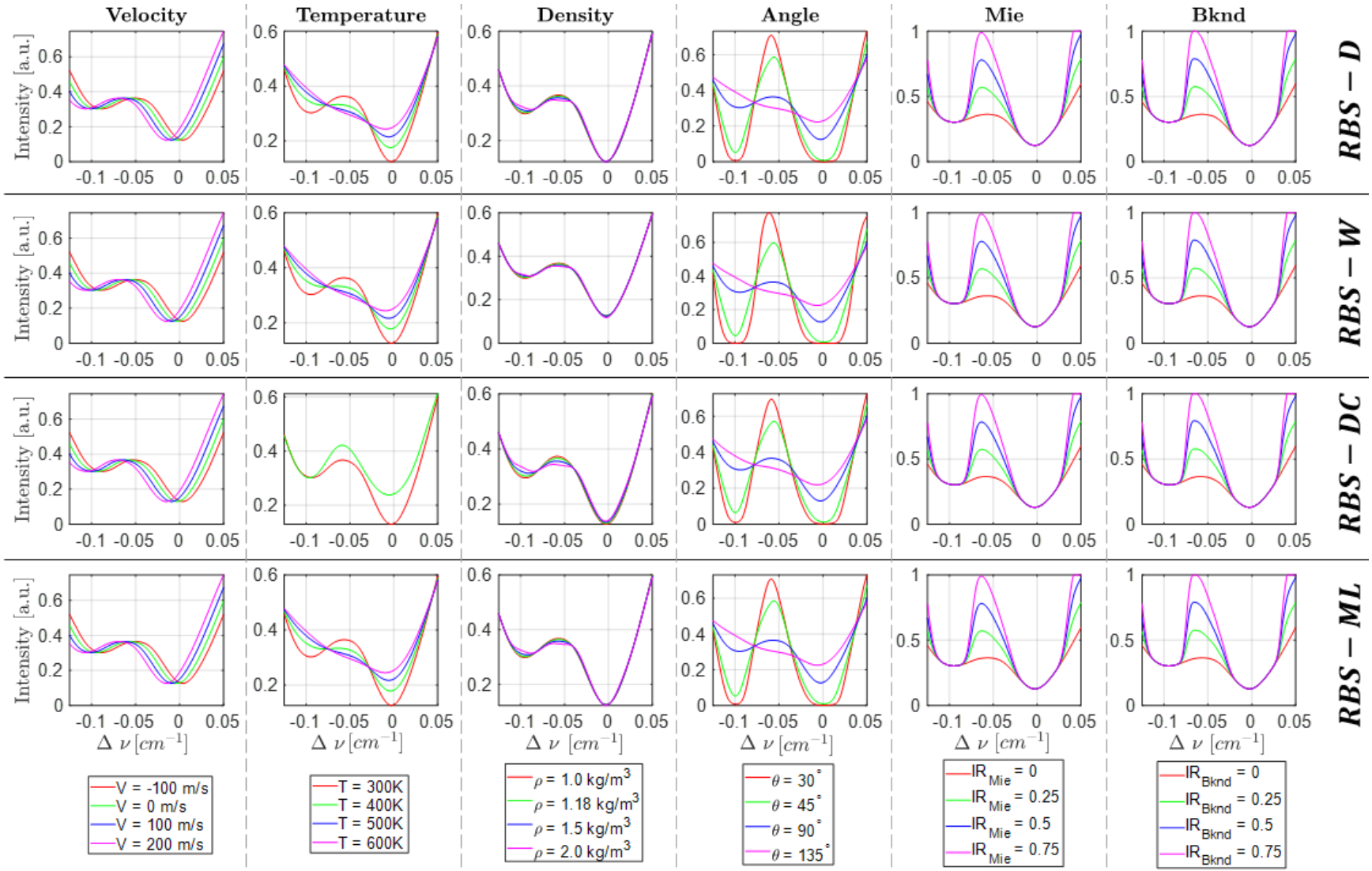

Figure 3.16: Convolution spectra using other Rayleigh models. Showing dependence on velocity, static temperature, static density, scattering angle, Mie scattering and background scattering.

To view the differences in more detail, Fig. 3.17 is needed. The top two charts show that outside of the low transmission region, Mie and background scattering greatly increase the convolved intensity. However, the chart with the velocity shift shows the effect of the bulk velocity on the background intensity ratio. The bottom two charts show the combined effects of both the Mie and background scattering on the convolution spectrum. The very bottom chart shows that when combined with a velocity shift, the high transmission regions become slightly narrower when compared to the no velocity shift case. This is because the overall intensity is no longer as high. In other words, the effects of Mie and background scattering are more spread out and therefore the filter is applied to less light at each wavenumber.

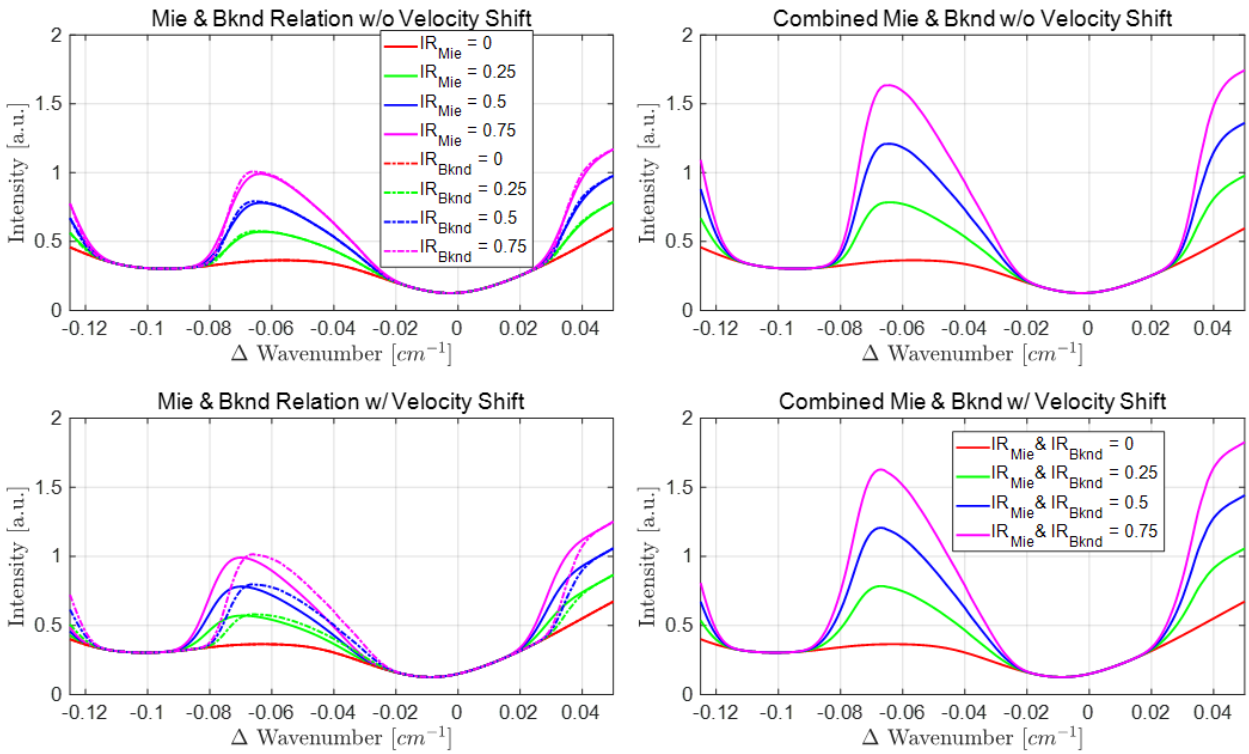

Figure 3.17: Top two charts: Mie and background scattering effects with and without a velocity of 100 m/s. Bottom two charts: Mie and background combined scattering effects with and without a velocity of 100 m/s.

Traditionally, predicting Mie and background scattering values requires some sort of knowledge from the experimental setup or can be found via manual iteration to match the simulated spectrum to the experimental spectrum (examples in Boyda et al. [56]). Either way, this process is inaccurate and prolongs the processing time required. These costs are what motivated the development of an automatic processing scheme in which the unique spectrum generated for one pixel during an experiment is processed through an automatic

process that iteratively varies variables like velocity, static temperature, static density, Mie scattering, and background scattering values until the simulated spectrum best matches the experimental spectrum. At present, variables such as shot noise are not accounted for but are part of future work. The automatic processing scheme will be defined in detail in the next subsection.

Nonlinear Fitting of Convolved Spectra — "Automatic Processing"

Automatic processing, in this case, refers to an iteratively solved minimum error problem using a nonlinear least-squares curve fitting algorithm of the form seen in Eq. 3.20 [113, 114, 115, 116, 117, 118, 119, 120]. Rather than computing the sum of the squares as seen in Eq. 3.20, this particular solver requires the user-defined function to compute the vector-valued function as seen in Eq. 3.21. The user-defined objective function (Φ) can be seen in Eq. 3.22 and is simply a least-squares error between the experimental data (measured) and the simulated data based on the models derived in the previous sections. The objective function (Φ) will return a function value $f(x)$ at each point (x) along the spectrum.

$$min\|f(x)\|_2^2 = min\left(f_1(x)^2 + f_2(x)^2 + ... + f_n(x)^2\right) \tag{3.20}$$

$$f(x) = [f_1(x) \quad f_2(x) \quad ... \quad f_n(x)]^T \tag{3.21}$$

$$\Phi = 0.5 * (S_{FRS_{Sim}} - S_{FRS_{Meas}})^2 \tag{3.22}$$

To minimize Eq. 3.22, scattering angle, static temperature, velocity, Mie, and background scattering intensity ratios, as well as static density must be iterated upon. To make sure these values remain physical and within the scope of the model, a lower bound was placed on each variable. For example, intensity ratios for Mie and background scattering cannot be below zero. Additionally, the scattering angle must be between 0°and 180°. These are the only physical variable constraints placed on the solver. An example of the solver through time is shown in Fig. 3.18.

Instead of a threshold value placed upon the objective function as a stopping criterion, stopping criteria are placed on all six solved variables. Figure 3.19 shows an example of this

process using a scattering angle (θ) of 90°, static temperature (T_s) of $300K$, sensed velocity (V_{Sens}) of $0m/s$, Mie intensity ratio of 0.25, background intensity ratio of 0.5, and static density (ρ_s) of 1.11 kg/m^3. In this case, the solution is stopped when the average difference of the last 250 iterations for each variable is less than a predefined threshold. Example threshold values can be seen in Table 3.2. Smaller threshold values mean longer processing times but greater accuracy can be achieved.

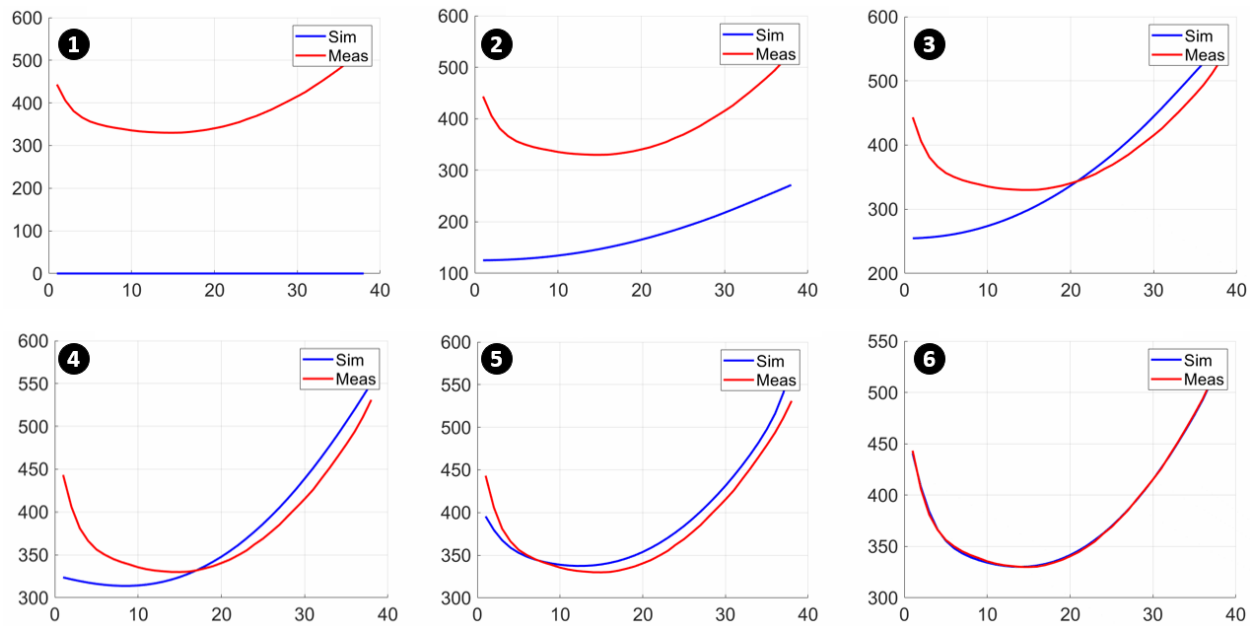

Figure 3.18: Non-linear least-squares model fitting. Picture one is the start and picture six is the best-fit case. Y-axis is intensity in arbitrary units while the X-axis is the number of points along the spectra.

Table 3.2: Threshold value for each solved variable.

θ [°]	T_s $[K]$	V $[\frac{m}{s}]$	Mie_{IR}	$Bknd_{IR}$	ρ_s $[\frac{kg}{m^2}]$
0.1	0.1	0.1	0.01	0.01	0.01

Looking at Fig. 3.19, it can be seen that the solved variables are not independent. This means that the uncertainty in both variables must be low to enable accurate solutions. In other words, if the scattering angle is off by several degrees then so too will static temperature (see Fig. 3.4 for a detailed look at these effects). Sensed velocity, Mie scattering intensity ratio, and background scattering intensity ratio are also not independent of one another due to how Mie and background scattering effects are modeled (see Fig. 3.7). These uncertainties will be explored in the next subsection.

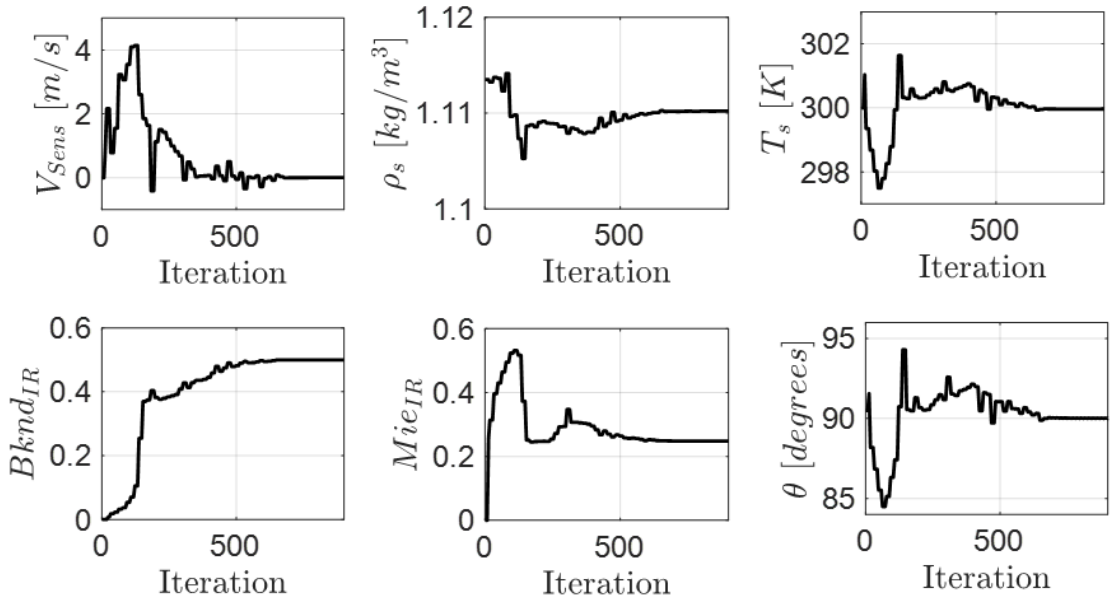

Figure 3.19: Convergence of solved variables over 900 iterations.

3.1.2 Uncertainty Analysis

The results thus far have been calculated on the assumption of "perfect" data. This means that the signal-to-noise ratio (SNR) (defined in Eq. 3.23 where σ_S^2 is the signal variance and σ_N^2 is the noise power) is infinite. In other words, no noise is present in the signal. In practice, this is known not to be true. Noise will always exist in the signal. This noise can consist of both random Gaussian noise as well as shot/Poisson noise. This section will show results from applying the automatic iterative process to spectra that contain random Gaussian noise. Shot noise remains of interest but has been left for future work.

$$SNR(dB) = 10log_{10}\left(\frac{\sigma_S^2}{\sigma_N^2}\right) \tag{3.23}$$

Monte Carlo Uncertainty Analysis

The error of the final result from the iteration process varies largely with SNR. Each variable also has different SNR levels that must be achieved in the measured spectrum to achieve the same kind of uncertainty due to the availability of information in a given signal corresponding to each flow property of interest. To determine these values, Monte Carlo simulations of modeled spectra were generated over 1000 times at each SNR level with a scattering angle of 90°, static temperature of 300 K, sensed velocity of 100 m/s, Mie

scattering intensity ratio of 0.25, background scattering intensity ratio of 0.5, and a static density of 1.11 kg/m^3 for each SNR level (Fig. 3.20). These values are representative of what will be seen in the ideal experiment.

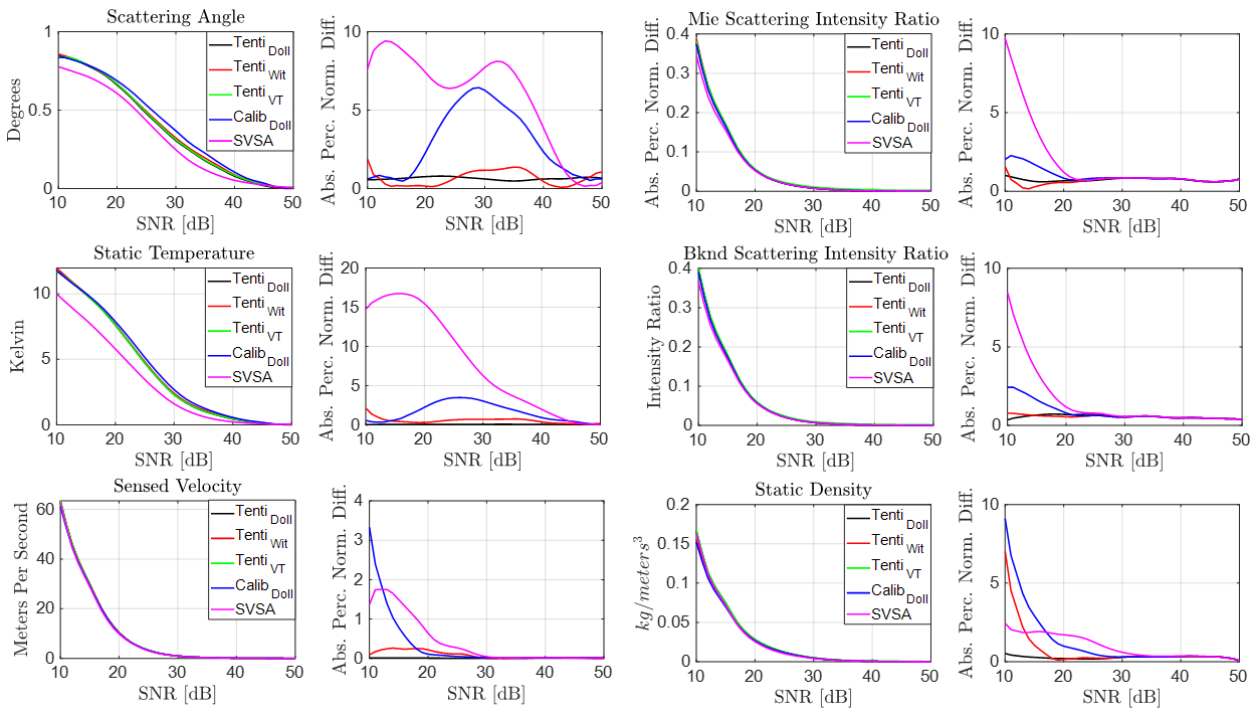

Figure 3.20: Monte Carlo results at various SNR levels with each Rayleigh scattering model using a 95% confidence interval.

These Monte Carlo simulations were run at SNR levels of 10 dB to 50 dB at 2.5 dB increments. These generated spectra can be considered as "measured" spectra and run through the iterative processing code which will match the simulated spectra from the models discussed previously. Looking back at Fig. 3.17, the entire wavenumber range has been considered for these calculations. Note, that increasing the number of measured points within this wavenumber region is advantageous as the model will have more points to fit. In other words, erroneous points are less likely to have an impact on the final solution. In this case, 50 wavenumbers have been used as a representative number of what can be achieved experimentally. See Fig. 3.20 for graphical results of the Monte Carlo simulations.

An experimentally achievable SNR value seen at Virginia Tech is at max around 30 dB. At this SNR level, the expected uncertainty for the scattering angle is approximately 0.35°, for the static temperature it is approximately 3.2 K, for the sensed velocity it is approximately 1 m/s, for Mie and background scattering intensity ratio it is approximately 0.01, and finally, for static density, the uncertainty is approximately 0.01 kg/m^3. These

uncertainty values represent the 95% confidence interval. Figure 3.21 shows a representation of various SNR levels using Eq. 3.23. At this stage, it is unclear why the SVSA model has lower uncertainty concerning scattering angle and static temperature. One possibility is that the slight variation in RBS lineshape compared to the Tenti models makes it easier to distinguish between scattering angle and static temperature variations. This will need to be examined in detail in the future. For Cramér-Rao lower bound (CRLB) uncertainty results refer to Pitt et al. [121].

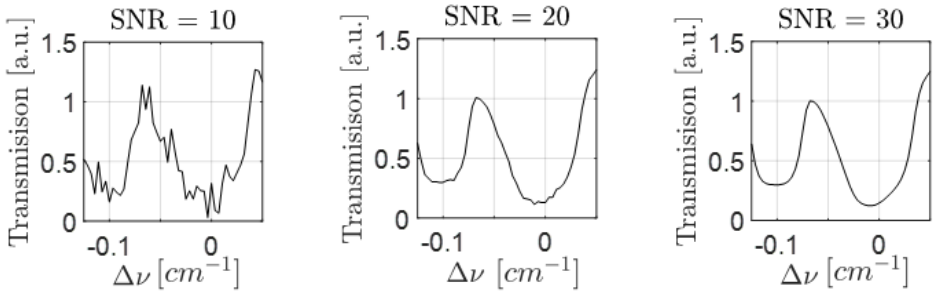

Figure 3.21: Examples of various SNR levels (in dB) using the FRS curve.

Multi-Level Processing Scheme to Increase SNR and Decrease Uncertainty

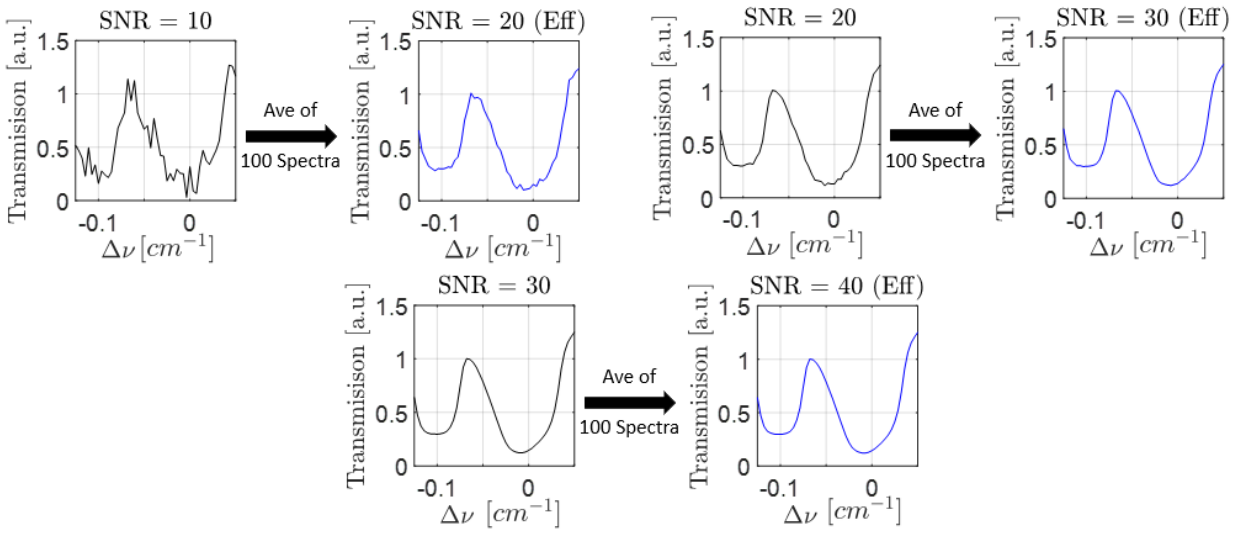

Figure 3.22: Averaging lower SNR spectra to create an effectively higher SNR averaged spectrum.

Due to the assumption that the noise is fully random, averaging spectra together will decrease the random noise and in turn, increase the SNR. Equation 3.23 shows that to double the SNR, the ratio of signal to noise must be ten times higher. In other words, an SNR of 10

means that the ratio of the noise to the signal is 0.1 whereas an SNR of 20 leads to a ratio of 0.01. Therefore, one hundred spectra at an SNR of 10 dB can be averaged to produce an effective (eff) SNR of 20 dB. This is proven in Fig. 3.22. Figure 3.22 shows effective SNR levels of 20 dB, 30 dB, and 40 dB. This leads to the assumption that the more spectra that can be averaged the more accurate the result will be.

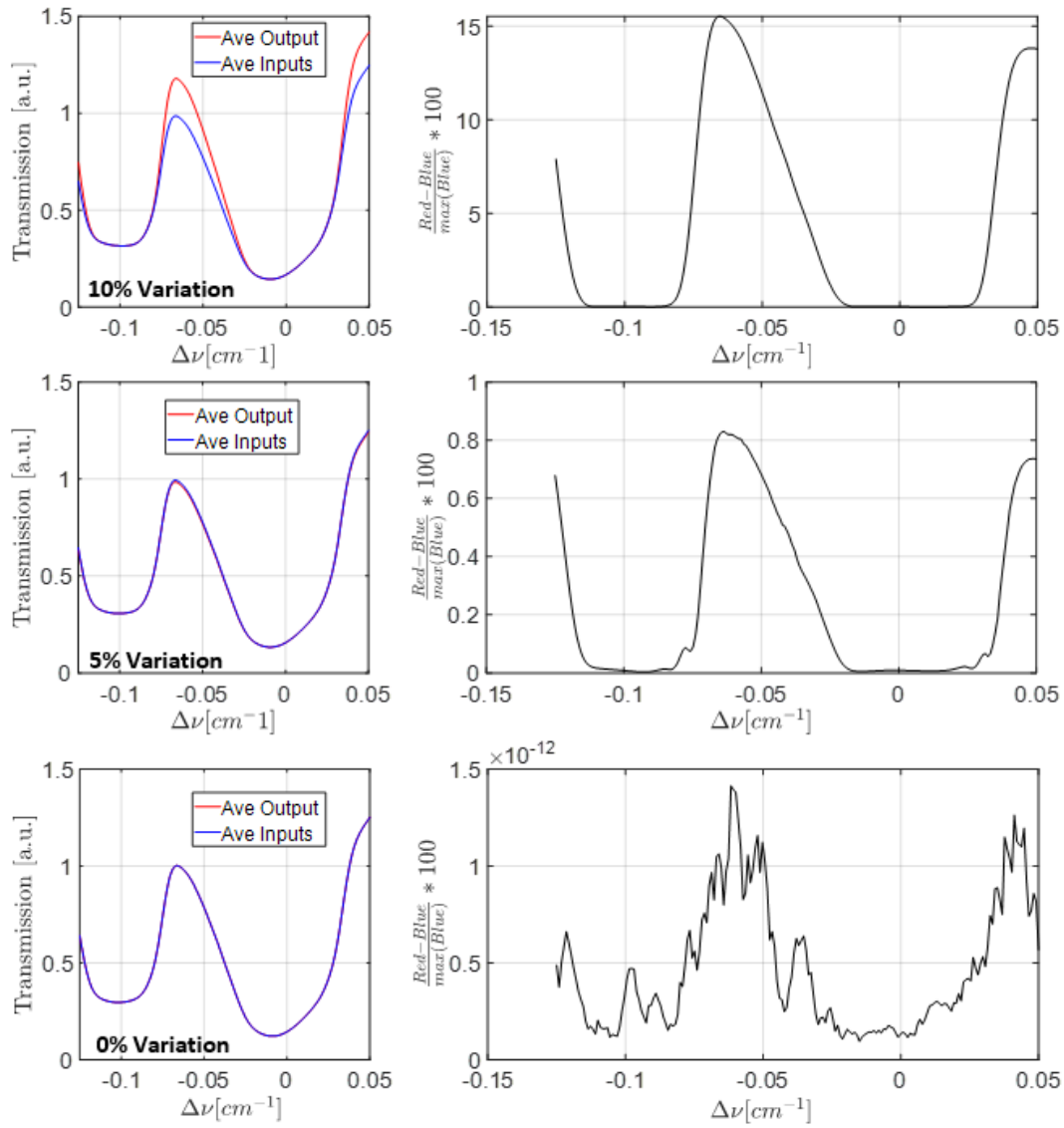

Figure 3.23: Examination of the effect of averaging schemes and non-linearity effect. The right side charts represent the normalized percent difference between the average output and average input curves.

In contrast, Fig. 3.23 provides evidence that the averaging scheme fails in areas where the solved variables have a high gradient. It does this by looking at two different averaging schemes over 1000 different flow simulations. The first, "Ave Output", means that the 1000

flow simulation spectra have been run through the iterative solver code to produce the six output variables for each of the flow simulations and then each solved variable is averaged to produce one averaged spectrum. The second, "Ave Inputs", simulates the six output variables over 1000 cases averages them, and then uses the averaged variables to produce one spectrum. Essentially, in the first case, the spectra are averaged and in the second case, the variables used to produce the spectra are averaged.

The top chart in Fig. 3.23 is an example of a 10% variation in the input variables. The middle chart is an example of a 5% variation in input variables. Finally, the bottom chart is an example of a 0% variation in the input variables. This shows that the first averaging scheme, which is the only one out of the two that can be done with experimental data, does not give a good final result compared to the blue "Ave Inputs" scheme in which the average of the data set is represented correctly in the averaged spectra. It is believed that the nonlinearity of the models has a large impact on these results. However, a deeper investigation is left for future work. It is also important to note that the normalized percent difference charts on the right side of Fig. 3.23 look very similar to the iodine transmission spectrum. This makes sense given that the RBS spectrum has the most influence outside of the trough regions. In other words, the RBS spectrum influences changes with the iodine transmission spectrum.

To answer how much averaging is too much or too little, another approach is needed. To do this, multi-level processing is used. This is a hierarchical way of determining the limit on how many spectra (pixels) can be averaged to produce a usable result. The first level is an average of the entire plane of data to create one averaged spectrum. This spectrum will then be run through the iterative code as normal. The second level will then increase the number of averaging bins from one to four. This process is repeated at each level with the number of bins in the X and Y direction increasing by powers of two at each level. Of course, the maximum level will not be averaged at all. However, one of the levels in between the first and last will be the optimal averaging scheme that balances resolution, error, and time to process. This decision will have to be set by acceptable processing times and allowable errors. A graphical description of this process will be given later. Simulated results will not be shown here but will be shown for the experimental data later.

3.1.3 Simulated Experiment

To ensure the models and processes described previously are working as expected, a simulated experiment was conducted at various SNR levels. This experiment could be run with all of the different RBS scattering models. However, keeping in mind all of the results shown thus far, with time, accuracy, and range of validity in mind, only the $RBS - D$ RBS scattering model will be shown. The data fields simulated can be seen in Fig. 3.24 and are of a freejet with no added temperature and very little angle variation. This means that all of the data fields should be planar constant except for the sensed velocity field. The data has been simulated over 64 x 64 pixels at a resolution of 1 mm per pixel for simplicity. It is also important to note that the intensity scaling constant, C_{IS}, has been set to 1 for simplicity. This will not be the case for the experimental data analysis.

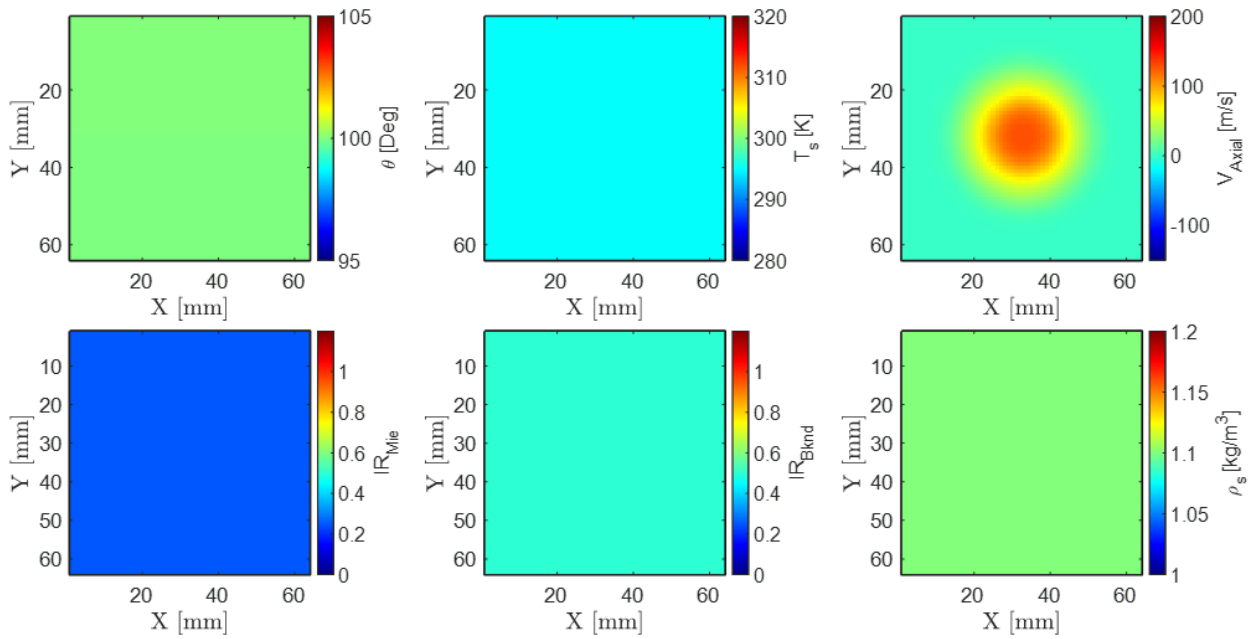

Figure 3.24: Simulated planar data of a non-heated freejet.

Figure 3.25 shows two different iteratively solved outputs at an SNR of 20 dB and 30 dB, respectively. Starting with the 20 dB case, the scattering angle and static temperature have the largest variation. This is consistent with the Monte Carlo findings in Fig. 3.20. Next, the Mie and background scattering intensity ratios have some connection with the sensed velocity as in the area of high velocity, the variance of the data decreases. This is consistent with the findings from Fig. 3.19 that these three variables are not independent of one another. The SNR of the 30 dB case largely follows the same characteristics as the SNR of 20 dB case but the variance has decreased as expected. It is important to note

that no median filtering was applied to these outputs. This type of filter would work to decrease the variation in the final outputs. This will be expanded upon further later when the experimental data is shown.

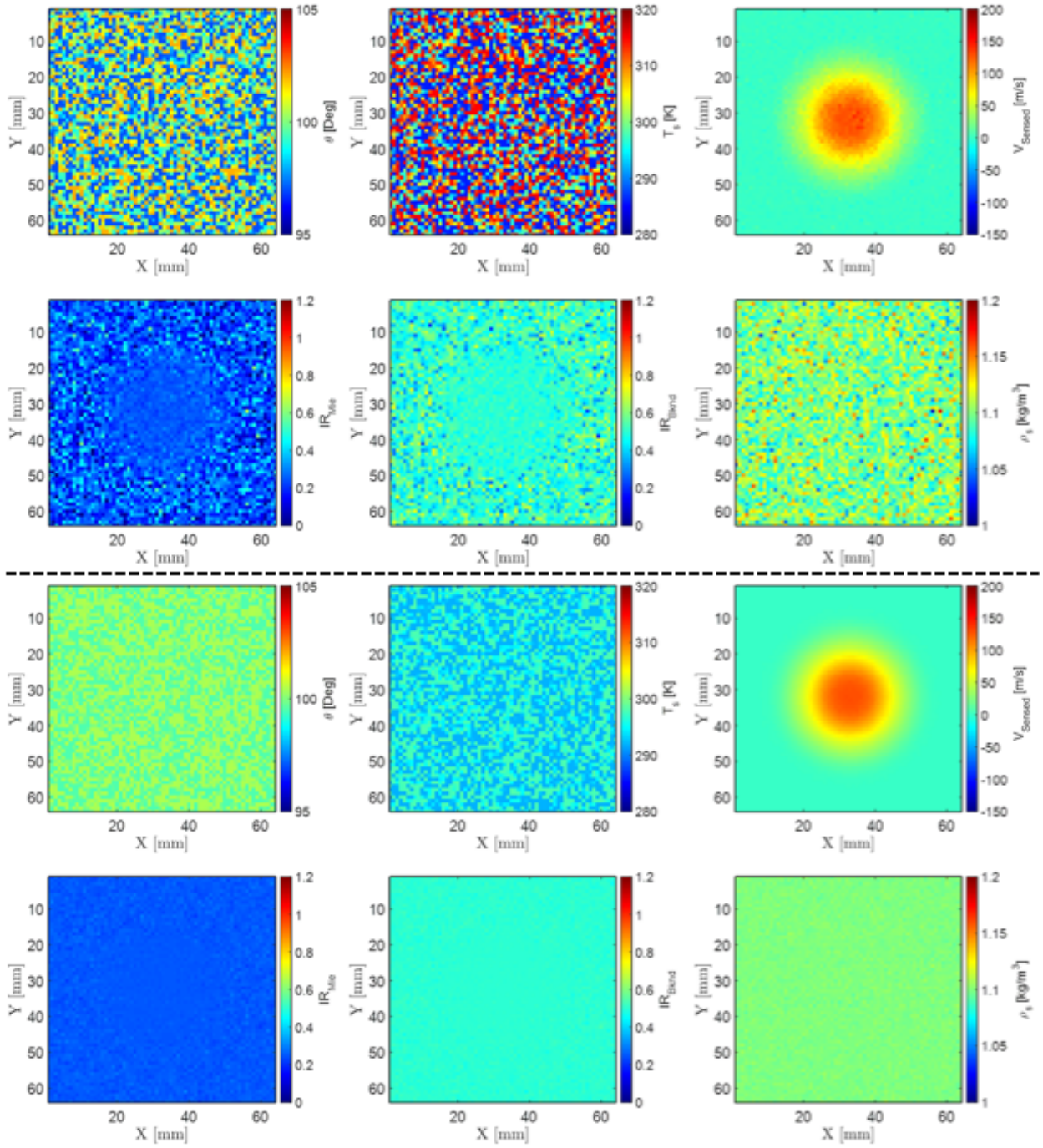

Figure 3.25: Processed simulated data of a non-heated freejet. Top: SNR = 20 dB. Bottom: SNR = 30 dB.

3.2 Experimental Investigation Techniques

To validate the findings of the models and simulations, two experiments were carried out. The first was on a highly controlled benchtop freejet and the second was performed on the exhaust of a small, RC plane-sized, turbojet [108]. The following subsections will walk through all of the processing steps outlining the major findings and reasoning behind each one. The subsections have been written in the order in which processing takes place.

3.2.1 Camera Calibration

Camera calibration refers to finding the world coordinates of the camera(s) in 3D space relative to the target area calibration plate. The current camera calibration algorithm employed is written by Bouguet et al. [122]. From this point on, this algorithm will be referred to as the CalTech calibration code. Without going into much detail, this code allows images taken of the calibration plate (taken from the camera) to be read into MATLAB and processed to find the necessary coordinates of each camera. However, in use, the author has noted special geometric locations relative to the calibration plate in which a good or bad calibration can or cannot be performed. These locations change slightly with the number of cameras being calibrated at one time.

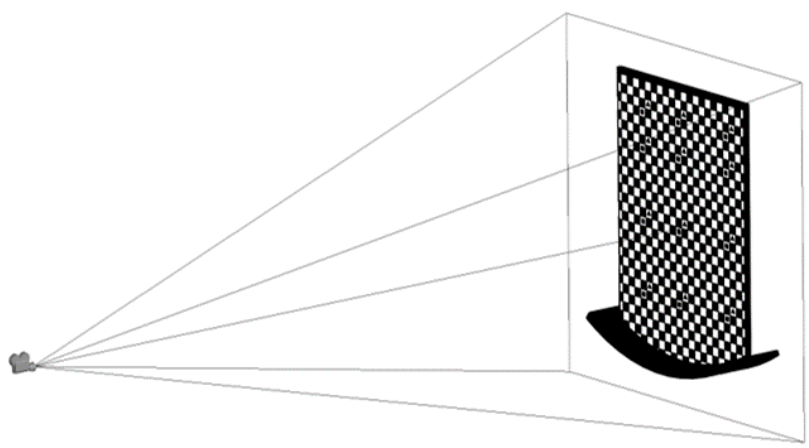

Figure 3.26: Example of one camera simulated calibration using SolidWorks. Pictured are the camera location, the camera field-of-view, and the calibration plate itself.

To best figure out these locations, an example calibration plate was loaded into SolidWorks in which the special camera settings allow for photos to be taken and rendered with input camera settings. The camera settings that will be used from here on are those of the

pco.edge 4.2 bi UV sCMOS cameras [123]. An example of this sort of ”simulated” camera location can be seen in Fig. 3.26. It is important to simulate a calibration in CAD software such as SolidWorks so that the camera location is known with no uncertainty.

Figure 3.26 is an example of only one camera calibration. In actuality, over thirty camera locations were simulated along a sphere surrounding the camera calibration plate. A sphere was used so that all three coordinate axis as well as combinations of each could be tested. In other words, a camera could be placed exactly on the three coordinate axes and anywhere in between. One camera-only calibration, two cameras-only, and three-plus camera calibration will be shown. It should be noted that after three cameras were included, no additional cameras increased the accuracy of the resulting world coordinates. The results of this investigation can be seen in Fig. 3.27.

Referring to the left chart in Fig. 3.27, using only one camera in the calibration process can result in significant errors. The red ”non-calibratable” areas are approximately $\pm 5°$around any coordinate axes. In this region, along the X and Y planes, the calibration squares become very skewed and the algorithm struggles to find the right corner points. Along the Z plane, the rotation matrices become singular and the algorithm loses depth information. For the same reasons, the yellow areas (potentially considerable error) extend to $\pm 10°$around the coordinate axes. In the green areas, the user would expect less than a 1% error in the final X, Y, and Z coordinates compared to the known values.

The two-camera calibration result follows closely with the one-camera calibration results. However, some of the red ”non-calibratable” regions have disappeared. The two along the X-Y plane have remained and the red circle near the top due to the skewness of the calibration squares. This will remain regardless of how many cameras are added. The yellow regions have largely remained but have shrunk to $\pm 5°$around the coordinate axes. The addition of the second camera has allowed for the retention of the depth information. Given two cameras, a planar coordinate can be held constant as seen on the top right chart in Fig. 3.27. If the X-coordinate is held constant then it is expected that the Z and Y coordinates will have significant errors. This is indicated by the red arrows. If the Y-coordinate is held constant, the X-coordinate will have a significant error. Finally, if the Z-coordinate is held constant, then all three coordinates will have less than a 1% error.

Finally, the three-plus camera calibration results yield almost entirely green areas except for the red regions where the skewness is still too high. These red areas have not changed from the two-camera calibration results. All yellow areas have disappeared. Holding

coordinates constant no longer matters as the results will always be within 1% error outside of the red regions. It should be noted that these results do not reflect the results of camera blurriness or distortion. That sort of investigation has been left for future work.

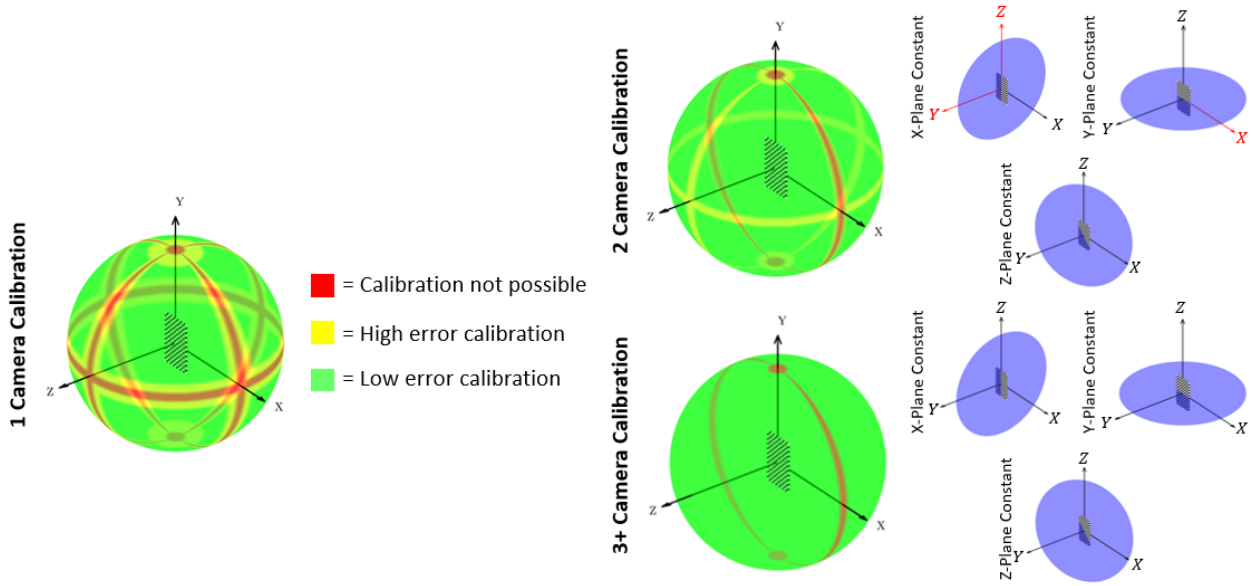

Figure 3.27: Left: One-camera calibration. Top right: Two-camera calibration. Bottom right: Three-plus camera calibration. Green areas represent less than a 1% error in X, Y, and Z world coordinates, yellow represents a potentially significant error, and red represents not calibratable. Charts to the side show planar constant results with the red coordinate axes having a significant error.

Low-error camera calibration is extremely important when taking into account the relationship between scattering angle and static temperature as seen in Fig. 3.19. If the camera calibration has a low error, then bounds can be set on acceptable scattering angle results from the iterative code. Without bounding on scattering angle, and low SNR levels, the iterative code could produce high error results for both scattering angle and static temperature. In other words, if the error in scattering angle is high, the error in static temperature will also be high. Other calibration processes such as camera registration (discussed in the next subsection) will impact outputs such as three-component velocity and increased error from laser instability.

3.2.2 Camera Registration

Camera registration is the second step in the calibration process. This step takes the camera calibration results to warp, crop, and overlay all of the calibration images on top

of one another. Essentially, this is an alignment process so that all of the images look like they've been taken from a head-on point-of-view with the same zoom level. This process will become clear by the end of this subsection. This subsection will only use two cameras as an example. However, the methodology is not limited by camera number.

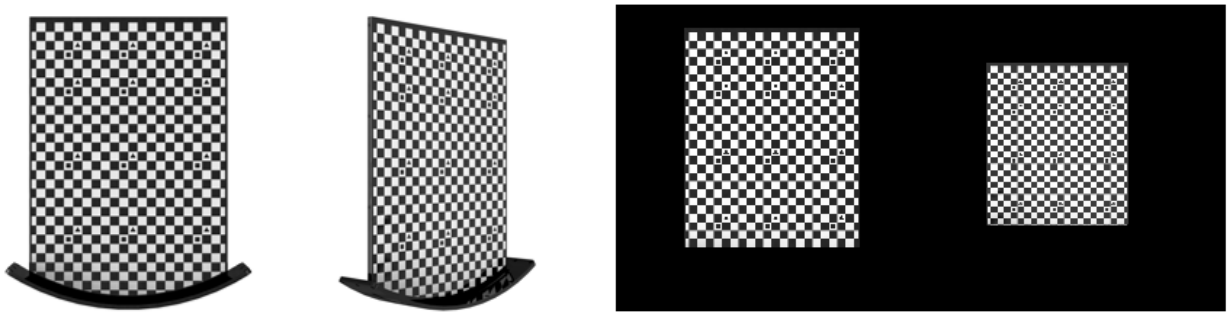

Figure 3.28: Left: Original calibration plate images. Right: Cropped and warped images. Viewed as if both images were taken from a head-on perspective.

Figure 3.28 illustrates the first step in the camera registration process. The original images should be cropped to just the region of interest on the calibration plate. This must be done as a preparation stage for later in this subsection. The images will be correlated to lie over the top of one another during the alignment process. Any background remaining in the image would also be correlated and could lead to error. Therefore, only the region of interest should remain. Finally, the results from the camera calibration stage are applied in a warping process such that the images look like they are being viewed from the same head-on orientation.

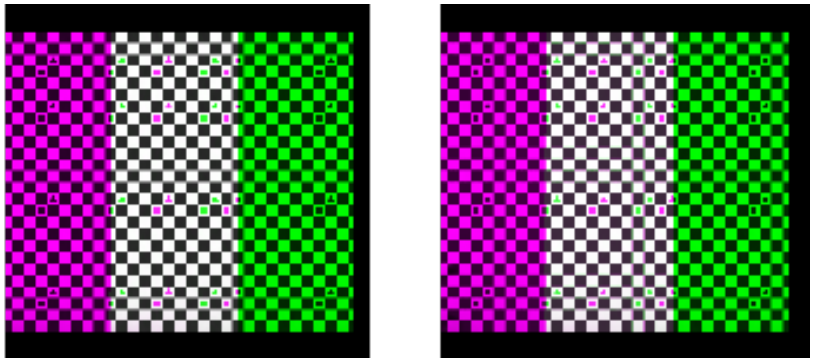

Figure 3.29: Left: Camera one bad registration. Right: Camera two bad registration.

The second step of the camera registration process overlays and aligns the images on top of one another. This step is crucial for two reasons that will be discussed in detail later. The first is three-component velocity which requires three cameras. If the images

aren't aligned, then a significant error will be incurred when rotating the sensed velocity to orthogonal components. The second has to do with laser stability. During the measurement process, a filtered image (light passes through the I2 absorption cell) and an unfiltered image (no filter) can be divided to get rid of any effects laser stability has on the measured spectra. To do this, an image correlation algorithm is applied (see ref. [124] for more information). The results of this correlation can be seen in Fig. 3.29.

Figure 3.29 is a good representation of a failed correlation. The zoom and orientation are correct except the horizontal translation is not. The algorithm has found a local minimum by lining up some of the squares and triangles (the images will be black and white if lined up properly). Just in the wrong place. This is due to the pattern on the calibration plate being relatively symmetric. Too many local minima exist that the algorithm has a hard time finding the global minimum (maximum correlation). Therefore, the author recommends creating a sort of spiral pattern instead. That way the correlation and orientation are unique at the global minimum.

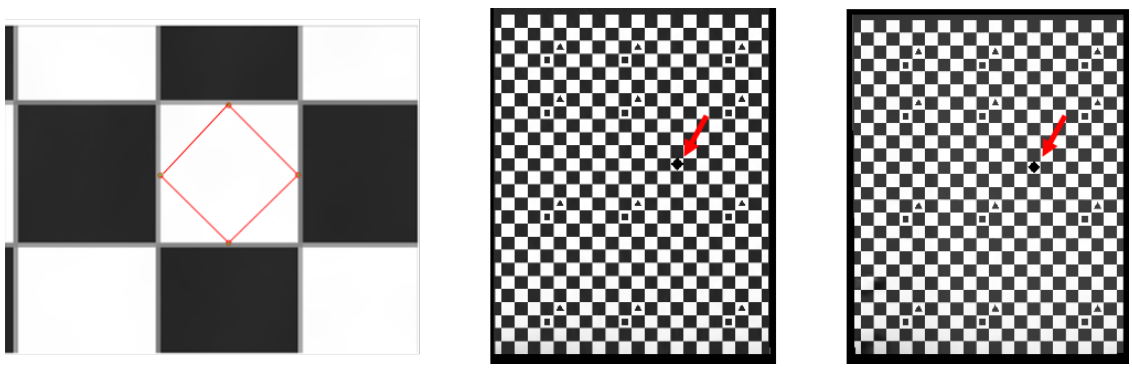

Figure 3.30: Addition of a shape on the calibration images to help with image registration.

To remedy this issue in post-processing, a shape must be added to each calibration plate. A diamond shape will be used as it is unique compared to the other squares and triangles already on the calibration plate. The additional shape is used as an anchoring point so that the correlation algorithm can find the correct solution much easier. The shape must be placed in the same location on the calibration plate in each image. The drawing of the shape must be similar but does not need to be exact. An example of this process can be seen in Fig. 3.30 where the left chart shows the drawing of the shape and the two charts to the right are the calibration images with the additional shape drawn. The red arrows indicate where the additional shape was added. The correlation can then be rerun where the results are shown in Fig. 3.31. Minimal pink and green areas are seen after the image registration is completed meaning that the two images have been warped and overlaid

correctly. The final step (not shown) is to select the origin of the coordinate axes created in camera calibration on each image. This will then set the X and Y coordinates for each pixel in the image and image registration/calibration can be considered complete.

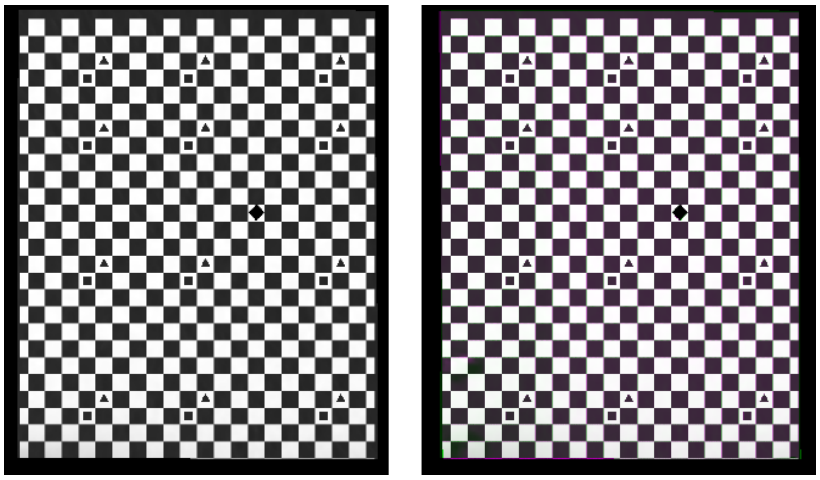

Figure 3.31: Correct correlation and registration of the calibration images.

3.2.3 Wavenumber Finding

As briefly touched on previously, a wavemeter is not part of the experimental setup. Instead, the experimental data from the PDs within the laser cart is fitted to the theoretical Forkey spectrum or created hybrid absorption spectra via the particle swarm algorithm [110, 111, 112]. Figure 3.32 [125] does a good job of visually representing this algorithm. The algorithm was inspired by nature as a way to simulate the social behavior of a flock of birds or a school of fish. Put simply, it solves a problem by creating a population of candidate solutions (particles) and moving these particles around within the domain created by the objective function. This movement is governed by the particle's current position and velocity. These parameters are then influenced by the local best-known position and guided towards better-known positions found by other particles. The advantage is that no initial guess or bounds are needed meaning that the algorithm works well when the wavenumber of the laser is not known. The downside to this algorithm is the time it takes to solve. While fast for a simple problem such as wavenumber finding, it is much too slow to apply to the overall problem of fitting six different parameters. This is why the nonlinear least-squares solver was chosen as the overall solver, as discussed previously.

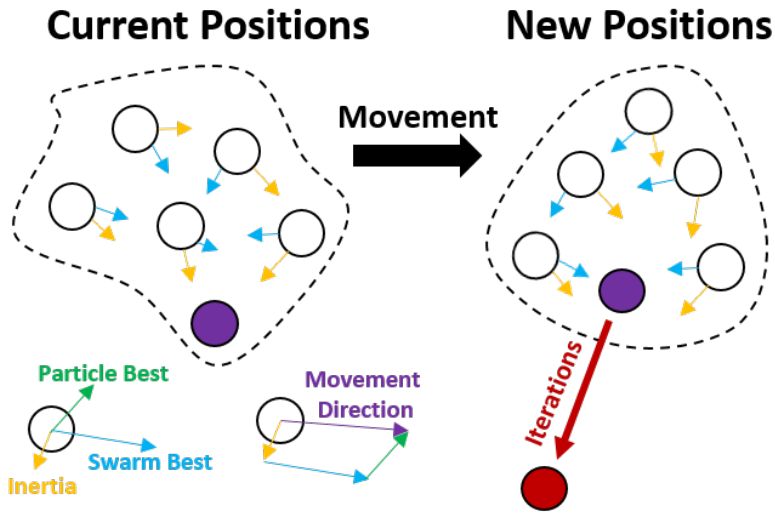

Figure 3.32: Graphical representation of the particle swarm algorithm. Modified from Chen et al.

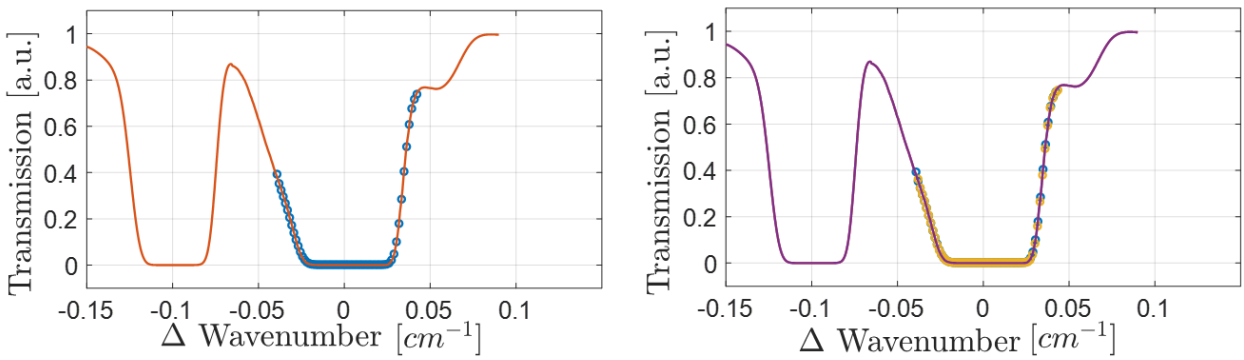

Figure 3.33: Experimentally found wavenumber. Left: Flow-on wavenumber fitting. Right: Flow-off wavenumber fitting (purple circles) overlaid onto the flow-on (blue circles) fitting result.

Examples of this algorithm applied to real data are shown in Fig. 3.33. The top chart shows the hybrid Forkey transmission line in red with the fitted experimental PD data in blue. The PD data is fitted via the particle swarm algorithm. The result is a very nice fit data set to back out the wavenumbers that were scanned over. The bottom chart shows the flow-off PD data fit in yellow with the flow-on in blue. If the laser was exactly stable, the flow-on and flow-off cases would be scanned at the exact same discrete wavenumber. This is because the PDs are inside the laser cart and should not be affected by the flow whatsoever. However, in this case, the laser was not exactly stable so the wavenumbers scanned are slightly different. This is okay as long as the wavenumbers are captured correctly as shown here.

3.2.4 Laser Vector Finding

Now that the wavenumbers have been found, the last step before actual processing can be conducted. This is a laser calibration process to find the direction vectors that the laser is propagating in. If using a line, this process is fairly simple as the laser propagation direction vector will be constant. However, if using a laser plane, the direction vector will change across the image. This must be accounted for to produce the right orthogonal velocities. In this case, a scanning mirror is used to produce an even laser power across the laser sheet. This can also be done with optical lenses but the resulting laser sheet will not have a constant intensity. The laser plane is then aligned with the calibration plate such that both edges of the sheet can be seen (see the far left chart in Fig. 3.34). The same image transformation, warping, and registration are applied to these images as was applied to the previous calibration images. If two lines are drawn using both edges of the laser sheet, they will intersect at the origin point (scanning mirror). To produce these two lines, two points are selected along each edge and a straight line is drawn between the two (middle chart in Fig. 3.34). The lines are followed back to the point of intersection at which point the lines can be used to draw the laser propagation vector over the entire image. This is shown via the small blue arrows on the far right chart in Fig. 3.34. This completes the final step before the iterative processing begins.

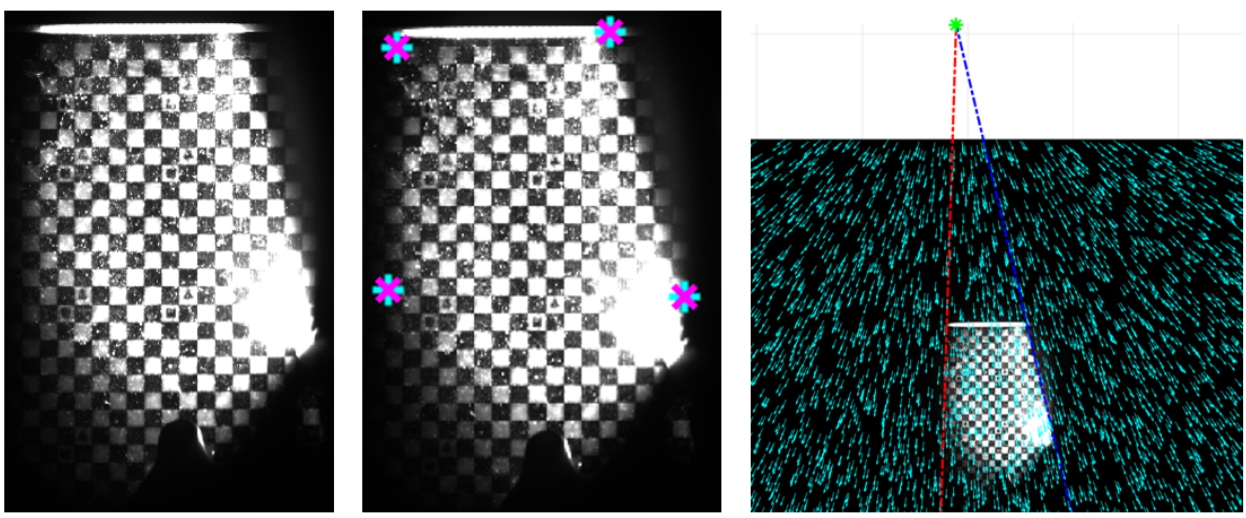

Figure 3.34: Example of the laser calibration process.

3.3 Final Experimental Data Processing

It is important to show that this processing technique works in many different environments and has not been tailor-made for one flow case. In other words, this technique must be general. To show this, two experiments were set up. The first was on a non-heated benchtop freejet under relatively ideal conditions. This test will mimic the conditions that most of the simulated data was processed on and will only show axial velocity as opposed to three-component velocity. The second data set was conducted in the exhaust of a small RC plane-sized turbojet. This test includes soot as well as high gradient changes in static temperature, three-component velocity, and static density. Any additional processing steps needed will be called out and specified.

3.3.1 Benchtop Freejet

As stated, FRS data was collected using a free jet (Fig. 3.35) with approximately the same operating conditions as the simulations. The free jet has a diameter-based Reynolds number of approximately 2.3×10^5. The jet allows for Mach numbers approaching $M = 0.4$ and can be adjusted via nozzle shape. A co-flow can be used to approach speeds of $M = 0.05$, however, it was not used in this experiment. Plenum total pressure and total temperature are measured. The air coming into the jet is filtered at the bottom and then straightened via internal honeycomb structures. The entire system is then attached to a series of traverses allowing for 3-axis control for alignment purposes.

The laser sheet was made via a scanning mirror and placed approximately four inches above the exhaust plane of the nozzle. Given the proximity of the pco.edge bi UV camera, the pixel resolution is about 1mm/pixel. This allowed for approximately 40 pixels across the nozzle exit. Figure 3.36 shows the approximate camera view of the laser plane and jet exhaust with the flow off. The laser sheet has a power of approximately six watts evenly distributed across the laser sheet. If looked at closely, the edges of the laser sheet are brighter because the amount of time spent at the edge is double that of anywhere else. This is solely a function of how the scanning mirror works. Therefore, the laser sheet was made wide enough to fully capture the region of interest without getting near the sides. Finally, the laser sheet is terminated inside a beam dump towards the right side of the image.

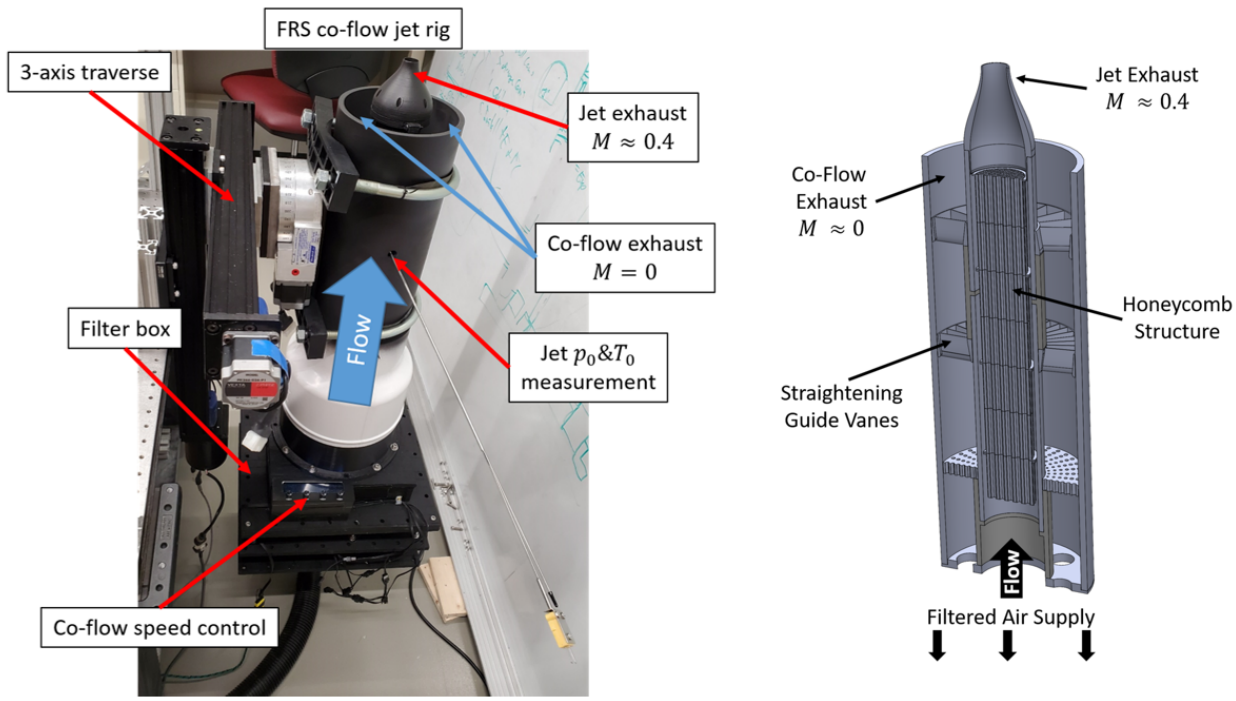

Figure 3.35: Benchtop non-heated freejet.

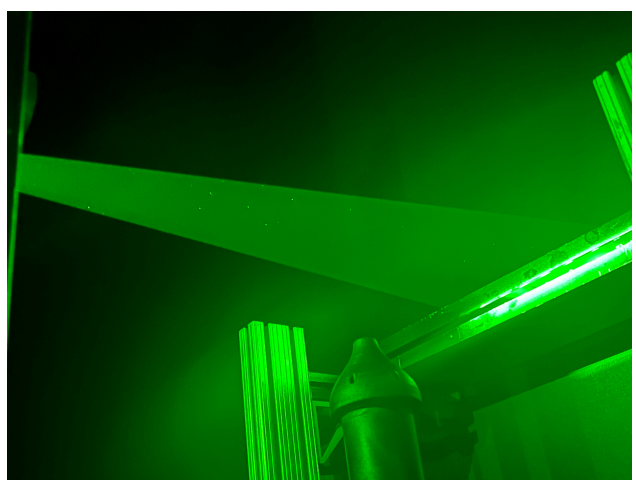

Figure 3.36: Approximate view from the camera of the laser plane above the jet exhaust.

Following the steps as described by the simulation and modeling section, a no-flow scan was first performed to back out the geometric scattering intensity constant C_{IS}. This is done by assuming known values for scattering angle, static temperature, zero velocity, and static density. The iterative code can then match the simulated spectra to the experimental spectra by iterating upon C_{IS} values as well as Mie and background scattering values. These three values are allowed to change in each pixel or averaged bin. This is in contrast to manual iteration which assumes that these values are constant over the entire image. The effect of

this will be seen when the manually iterated results are discussed later.

Once C_{IS} is found experimentally, the flow-on scan can be performed. This time, C_{IS} is considered known but the other flow properties are not. Therefore, the iterative solver is used to iterate over values of scattering angle, static temperature, sensed velocity, Mie and background scattering intensity ratio, as well as static density. Mie and background scattering intensity ratio must be iterated over in both the flow-on and flow-off case as particles in the flow will likely change as well as the velocity will shift the wavenumber via the Doppler shift and therefore, could change the background intensity in different parts of the image. Figure 3.37 captures the processing steps graphically to help with understanding.

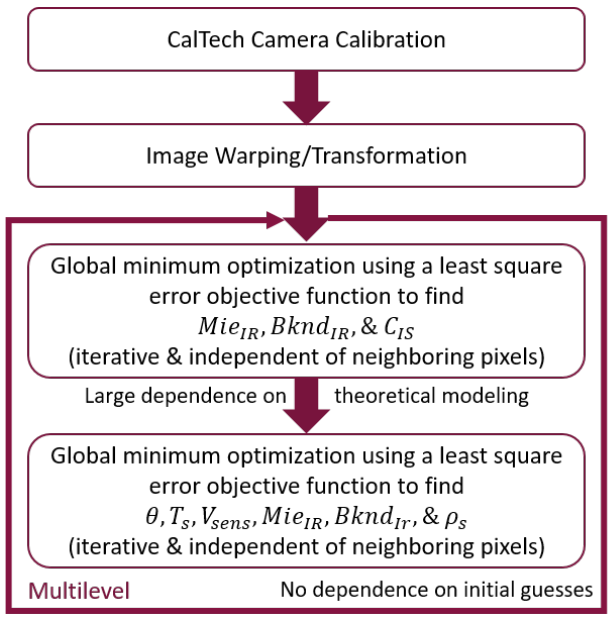

Figure 3.37: Post-processing flow chart to achieve the six output variables.

Figure 3.37 also points out that this methodology has a large assumption that the theoretical modeling is accurately predicting what is happening within the experiment. The trade-off to this assumption is that initial guesses are not required. Another thing Fig. 3.37 points out is the multi-level processing. As described previously, this will be done to determine the maximum binning size that can be used while maintaining accuracy and cutting processing time. Once the multi-level processing is run and a binning level is selected, it no longer needs to be run for repeated scans or data that have similar geometric properties as well as flow properties.

Figure 3.39 shows the experimental results of multi-level processing from the entire image averaged to the top level at which point no averaging is being done. It is important to

note that the raw image has been cropped to a square and then fed through the code to save processing time. The $RBS - D$ model was used to produce these results and was chosen for its large validity range and quick spectrum generation time. The scattering angles of this data set are outside the range of the $RBS - DC$ Rayleigh scattering lineshape model. It should also be noted that the sensed velocity has been transformed into one-component axial velocity through Fig. 3.38 where θ_{Axial} is the angle from the sensed velocity direction to the axial component. In this case, it is assumed that all of the flow is moving in the axial direction. For the next experimental case using the turbojet, this cannot be assumed due to the flow swirl and therefore will have to use a three-component transformation.

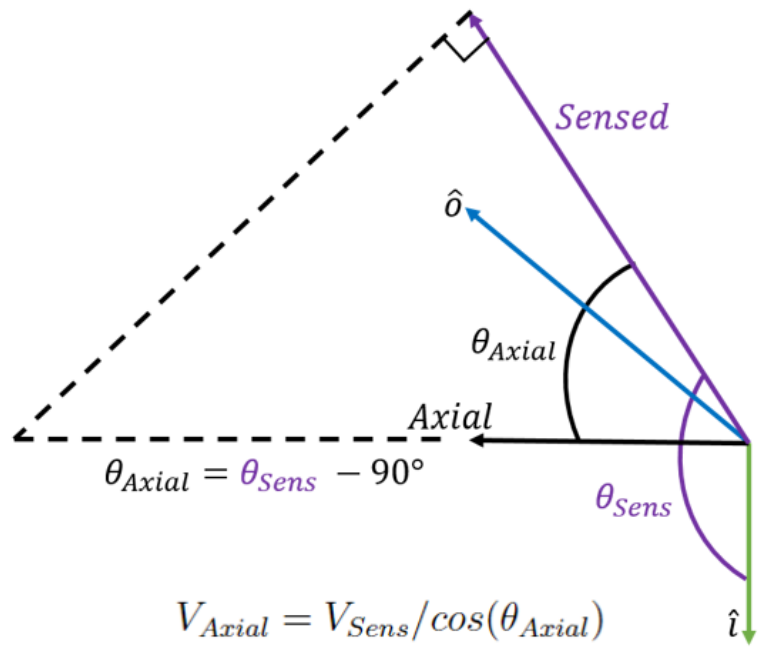

Figure 3.38: One-component axial velocity rotation.

As discussed earlier in Fig. 3.23, averaging too much will lead to a wrong answer. Referring to level one, most values start low compared to level six, but the Mie and background intensity ratio values are almost flipped. The Mie intensity ratio starts very low and ends up higher whereas the background intensity ratio starts high and ends much lower. Level six values correspond to what was expected given that the background is a flat black wall. Looking at the axial velocity, the jet profile does not start appearing with anything useful until level five. Level five appears to be the first useful level in the case of all the variables having a minimal averaging error. However, level six looks even better. For this case, the total six levels only took approximately two hours to compute using parallel processing using six cores on an Intel(R) Xeon(R) CPU E5-1650 at a speed of 3.6 GHz. At that speed and

time to process, it is acceptable to take the highest fidelity level. Each level takes exponentially more time to solve. For example, ten levels would take days. Of course, ten levels were not possible in this case because of the camera resolution used. In future experiments, FRS data will be taken on much larger flow paths and ten or more levels might be needed. Since the algorithm is written in parallel, more cores will be used to get the processing time down to acceptable levels.

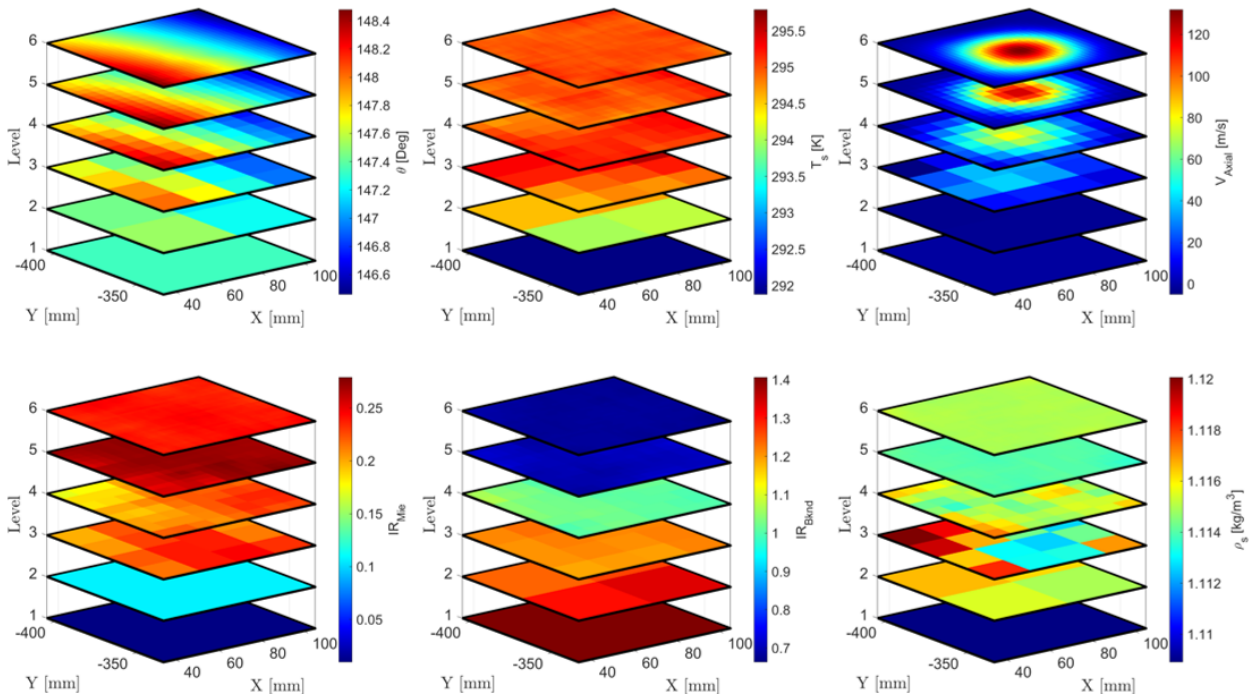

Figure 3.39: Multi-level processing on the benchtop freejet. Top left: Scattering angle. Top middle: Static temperature. Top right: Axial velocity. Bottom left: Mie intensity ratio. Bottom middle: Background intensity ratio. Bottom right: Static density.

Probe measurements of total temperature and total pressure were taken to validate the final FRS results. The comparison between these data sets can be seen in Fig. 3.40. The error bars on each are calculated using a 95% confidence interval. The FRS error bars match closely with an SNR of 30 dB in Fig. 3.20. This is because the SNR of the experimental data is very close to 30 dB. The static values of the FRS results seen in Fig. 3.39 were taken and converted into total values through the isentropic equations. A line was taken through the center of the jet horizontally (the same line as the probe data was taken over). Overall, the probe results have much less uncertainty, as expected. The agreement between the FRS data and the probe data is very good and thus the ”simple” flow case can be processed well by the iterative solver.

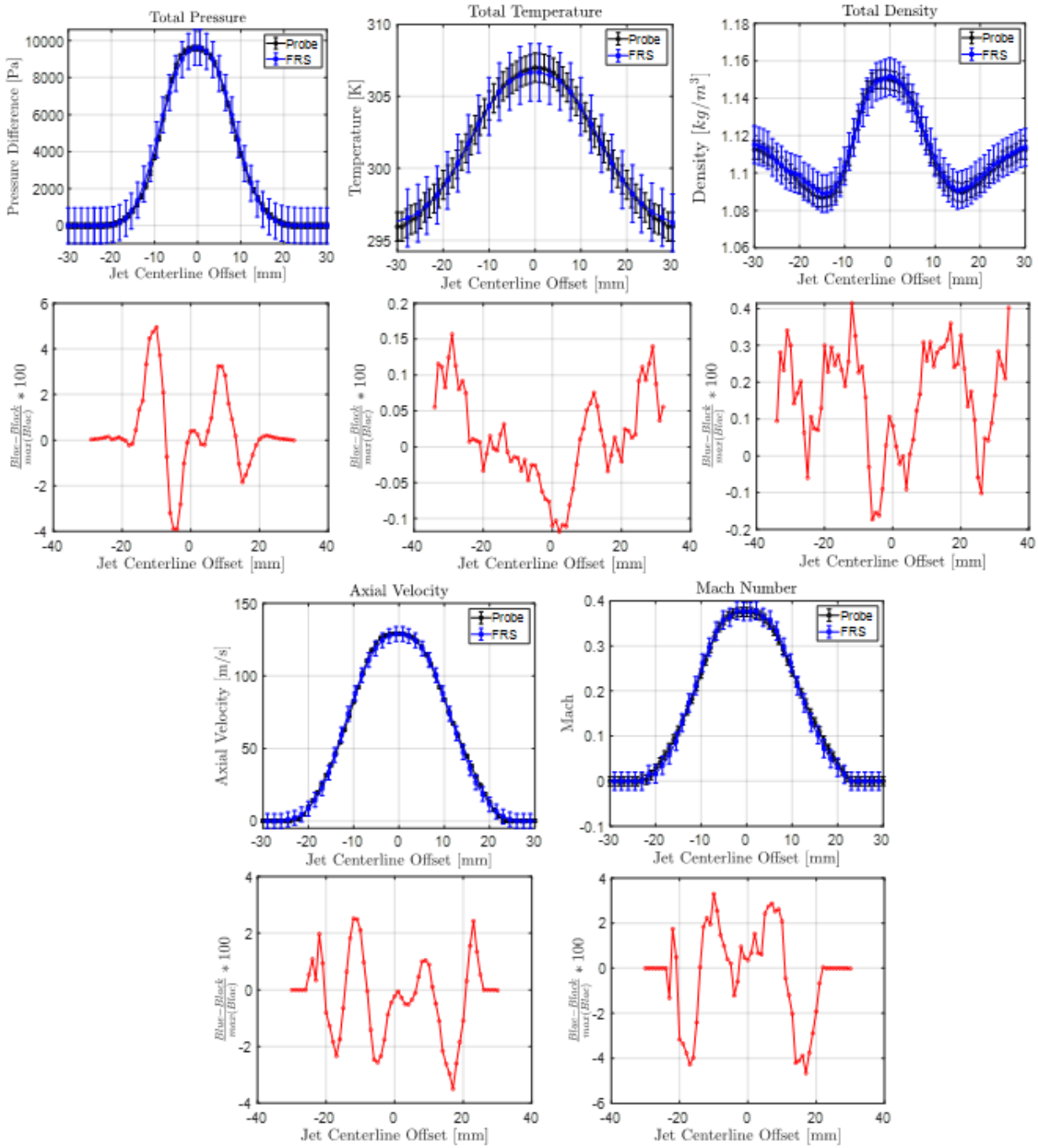

Figure 3.40: Blue and black: FRS results transformed into total results to compare with the total measurements made by the probe. Red: Normalized percent difference between probe data and FRS data.

Figure 3.41 illustrates the improvements in processing time and technique in FRS data post-processing. Using a manual iteration technique means that the user must manually iterate on values to try and match the experimental and simulated spectra. This takes

on the order of a few months to come to the best-fit result. Even then, the final result will contain some amount of human bias. In this case, the final velocity result was not correct even though the spectra matched decently well. To overcome this challenge, the auto-processing code went through many iterations and solver algorithms. This can be seen as the time to process continued to decrease until the present point of approximately two hours to go from raw data to well-understood and highly accurate results. Although much faster, the post-processing is not in real-time. Instead, it can be considered near real-time. Now that the auto-processing code has been proven to work on data that looks much like the simulated data the algorithms were tested on, much more complex data will be processed by using the exhaust of a small turbojet that burns Jet A.

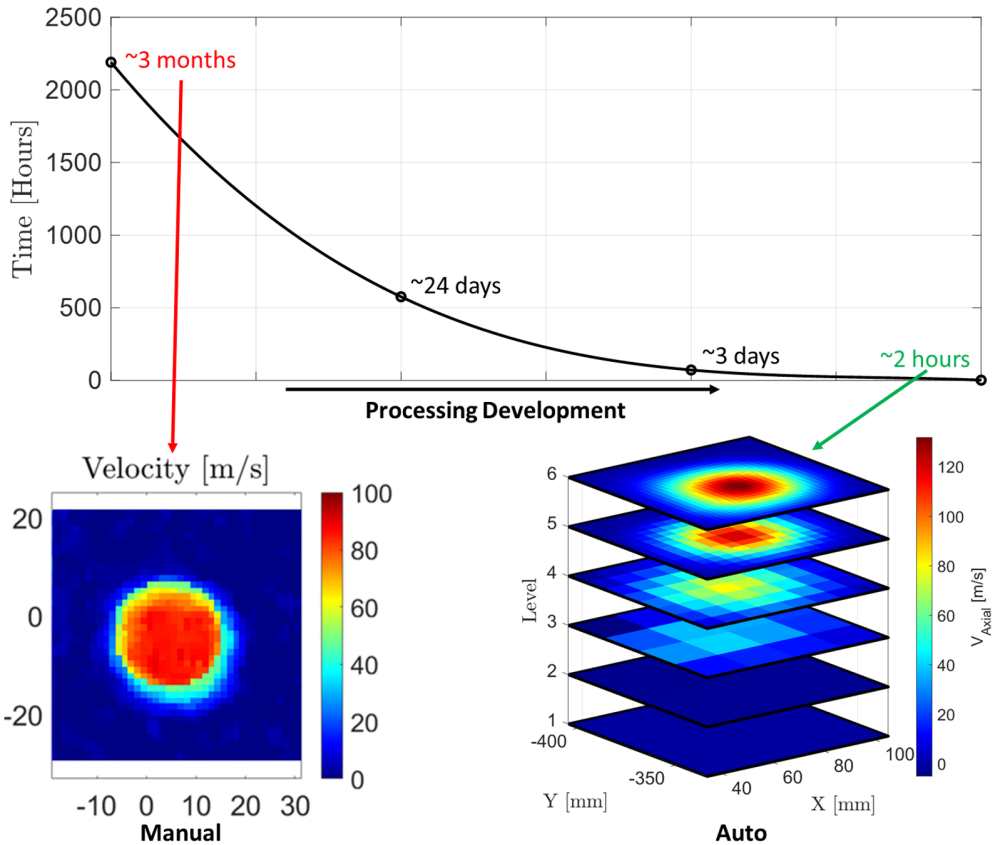

Figure 3.41: Post-processing development and comparisons.

3.3.2 JetCat P100-RX TurboJet

The goal of this experiment was to provide a non-ideal environment to test the robustness of the aforementioned automatic process. The JetCat exhaust provides a reliable

and continuous non-ideal environment. This environment includes contributions from vibrations, combustion gases, and unburnt fuel. The next few subsections will introduce the JetCat system, detail the influences of the combustion products, show the experimental setup, and present the fully processed planar results with comparisons to traditional probe measurements.

JetCat Setup and Combustion Product Modeling

The JetCat P100-RX [108] is a small, approximately 4-inch diameter turbojet that runs on a 95% JetA/kerosene and 5% turbine oil fuel mixture. This turbojet is capable of pressure ratios of up to 2.9, a mass flow of up to 0.23 kg/s, 100 N of thrust, exhaust velocities of 435 m/s, and exhaust total temperatures of 800 K. Typically these engines are meant to provide thrust for RC planes with electrical power coming from LiPo battery banks. In this case, the JetCat has been fitted with a continuous power supply as well as large amounts of fuel to run for up to one hour at a time. See Fig. 3.42 to view the JetCat 80/20 mounting system and simple wiring.

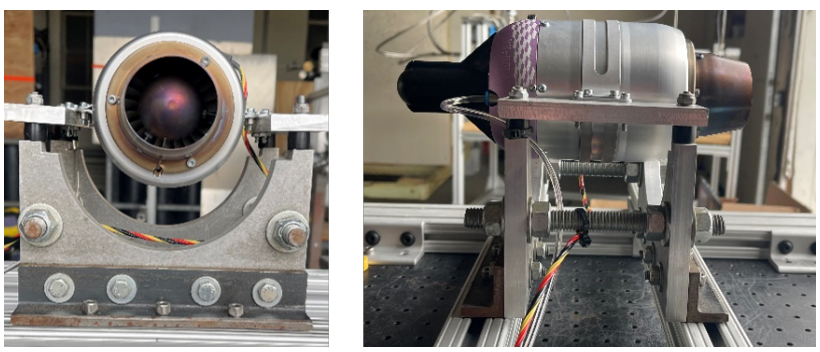

Figure 3.42: Simple JetCat mounting and wiring at Virginia Tech's turbo-machinery lab (TurboLab).

Until this point, standard air gas properties have been assumed to create the RBS lineshape. However, because the JetCat burns kerosene, the exhaust gas properties will be a mixture of kerosene and air. To account for this, the effect of kerosene combustion products on the Rayleigh scattering lineshape must be known. To start, the stoichiometric equation must be written out (see Eq. 3.24) where, $\alpha, \beta, \gamma, \sigma$, and δ are all numbers of moles. The kerosene model used is $C_{12}H_{26}$ while the air model used is $0_2 + 3.76N_2$.

$$C_{12}H_{26} + \alpha\left(O_2 + 3.76N_2\right) \rightarrow \beta CO_2 + \gamma H_2O + \sigma N_2 + \delta O_2 \tag{3.24}$$

The number of moles is obtained using mass conservation with known air-fuel ratios that have been transformed into a molar basis. The molar constant α in Eq. 3.24 can be considered the molar basis air-fuel ratio. The JetCat was run at 75% throttle (125,000 RPM) as this power level was found to be the most stable (most complete combustion). Figure 3.43 (Davis et al. [126]) can be used along with Eq. 3.25 to determine the mass-based fuel-air ratio (f).

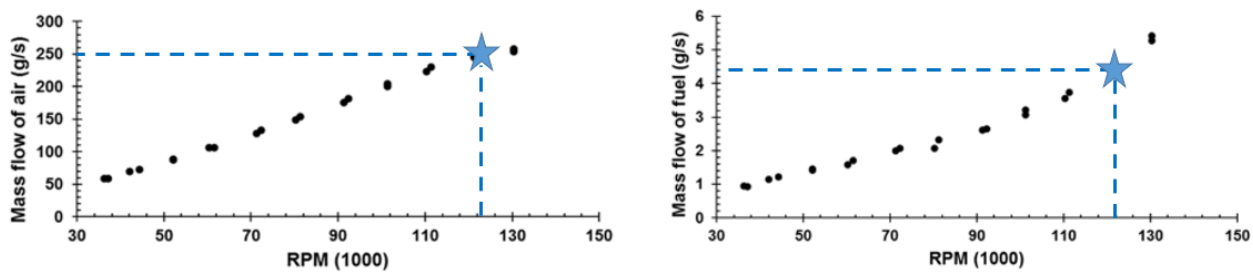

Figure 3.43: Left: JetCat P100-Rx mass flow of air. Right: JetCat P100-RX mass flow of fuel from Davis et al.

$$f = \frac{\text{fuel flow rate}}{\text{air flow rate}} \approx \frac{4g/s}{250g/s} = 0.016 \tag{3.25}$$

Since the mass-based fuel-air ratio has been solved, it can be transformed into the molar-based air-fuel ratio ($\overline{AF}$) by solving Eq. 3.26 for α. The solved stoichiometric equation can be seen in Eq. 3.27.

$$\overline{AF} = f^{-1}\frac{M_{fuel}}{M_{air}} = 62.5 * \frac{170.34g/mol}{28.97g/mol} = 4.76\alpha \tag{3.26}$$

$$C_{12}H_{26} + 77.2\,(O_2 + 3.76N_2) \rightarrow 12CO_2 + 13H_2O + 290.3N_2 + 58.7O_2 \tag{3.27}$$

Given the stoichiometric coefficients and the molecular weight of $CO_2 = 44\ g/mol$, $H_2O = 18\ g/mol$, $N_2 = 28\ g/mol$, and $O_2 = 32\ g/mol$, the mole fractions of each product can be found. These are found as $X_{CO_2} = 0.05$, $X_{H_2O} = 0.02$, $X_{O_2} = 0.18$, and $X_{N_2} = 0.75$. These values are similar to air with mole fractions of $X_{O_2} = 0.2$ and $X_{N_2} = 0.78$. The different mole fractions of the combustion products will change the RBS cross-section. The exact equations and values will for the RBS cross-section (and differential cross-section) are not given here but the author invites the reader to look at references [53, 69, 127, 128, 129, 130, 131] for further details.

Looking at just the second trough region shown in Fig. 3.13, the convolved RBS spectra can be calculated using the new RBS cross-sections. These are plotted in Fig. 3.44. The top left chart in this figure shows the individual contributions of each combustion product to the filtered Rayleigh scattering signal. Given the mole fractions of each gas, the result that N_2 and O_2 are the highest contributors to the signal is expected. Therefore, the top right chart also makes sense as the combustion product mixture signal and the air-only signal are fairly close. The bottom and final chart of Fig. 3.44 shows that for a majority of the region-of-interest, the difference between the two signals is less than a 1%. This 1% difference is approximately equivalent to the variation of a signal that has an SNR of 26 dB. The data collected from the JetCat has an approximate SNR of 24 dB, therefore in this case, modeling the combustion products has little to no effect. However, it has been done for completeness.

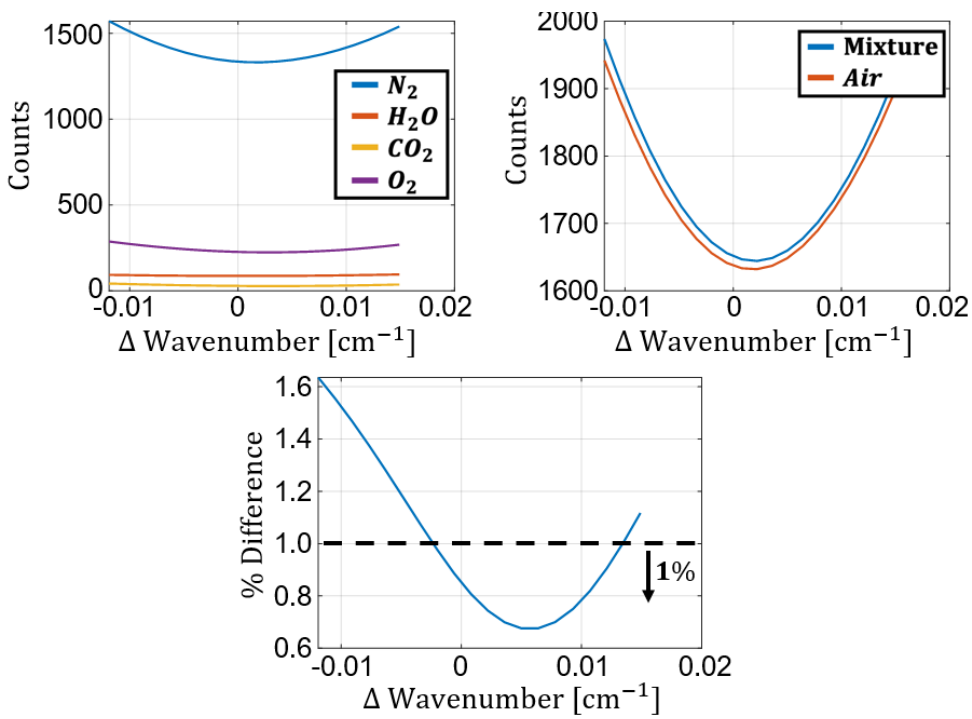

Figure 3.44: Top left: Filtered Rayleigh scattering signal from each product individually. Top right: Comparison of combustion product mixture to air. Bottom: Percent difference in the filtered Rayleigh scattering signal over the wavenumbers investigated.

Experimental Setup and Other Processing Techniques

The experimental setup seen in Fig. 3.42 where sidewalls and roof panels have been added to minimize background scattering. The laser sheet is made from a free-space laser beam shining onto a scanning mirror. The laser passes through a small slit in the roof and is

then terminated inside of the beam dump well below the region of interest to minimize any stray scattered laser light. The components to run the JetCat such as a power supply and fuel were stored beneath a large metal plate. The fuel stored was approximately 20 liters which allowed for a continuous run time at full power of about forty-five minutes or about one hour at 75% power. Once the fuel was used, the JetCat would be stopped and a new fuel tank could be swapped in for repeatable long-duration testing.

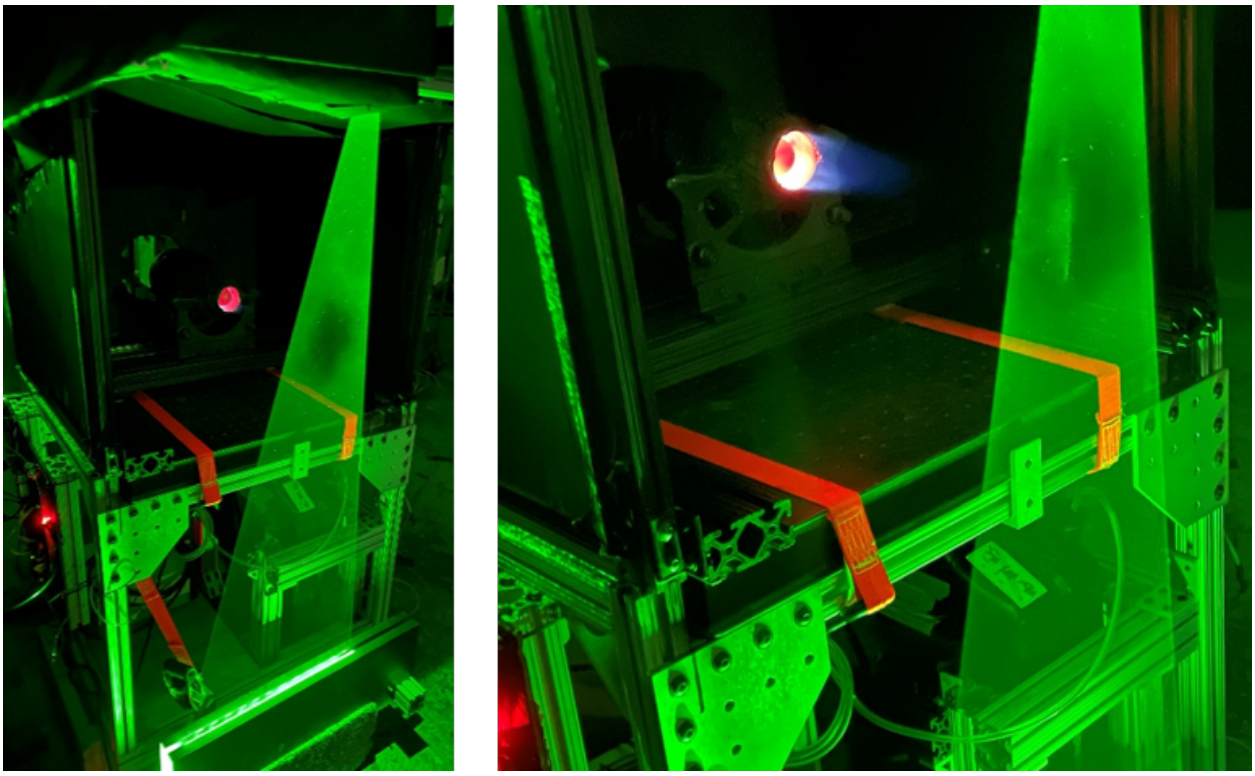

Figure 3.45: Left: Zoomed-out view of the JetCat in flow-on conditions with the beam dump near the bottom of the image. Right: Zoomed-in view of the JetCat in flow-on conditions with a long exposure time to see the jet plume. Jet plume in laser sheet visible in both images.

Just like in the previous experiment with the freejet, total temperature and total pressure measurements were taken of the jet plume making use of a linear traverse. The setup can be seen in Fig. 3.46. Looking at the JetCat itself, the JetCat was wrapped with black foil for this experiment so that the laser did not reflect off of the metallic surface easily. The black foil also blocked the light emitting from the glowing nozzle during the long-duration tests. Now, the probe traverse can be seen towards the bottom of the image. The traverse is long enough to get a complete jet profile plus some distance in the no-flow regions. The probe was traversed vertically and horizontally along the centerline at 12 x/D

downstream of the exhaust. The results of this data will be shown in the next section as comparison/validation data for the FRS results. It should be noted that the probe was mounted in such a way that it traverses the same plane as the laser sheet.

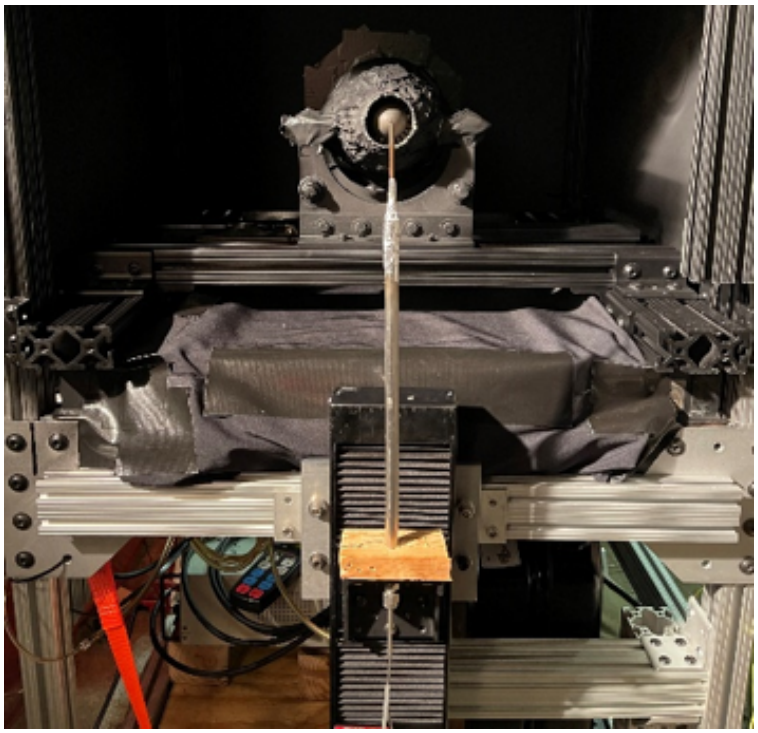

Figure 3.46: Total temperature and total pressure traverse setup in the exhaust of the JetCat.

While the experiment was running, it was noticed that incomplete combustion was common and the exhaust of the JetCat contained large amounts of soot. This can be seen on the left-hand side of Fig. 3.47. An example of a clean image can be seen on the right-hand side of Fig. 3.47. The images in Fig. 3.47 were taken one frame apart with an exposure of approximately 0.5 seconds.

To get around this issue, three images were taken at each laser frequency as the laser was scanned over the entire frequency range. The three images were then filtered for the lowest soot content by looking at the intensity count in the jet plume region. If the intensity was high, the image would be considered not good enough and thrown out. If more than one image remained, a single random image from the image set was used. If no images remained, the set would be flagged and the user would manually select the best image. The data set that was used for processing never had a data set that was flagged for no remaining images. However, some data sets had image sets that were flagged and this process would need to be automated to reduce processing time further.

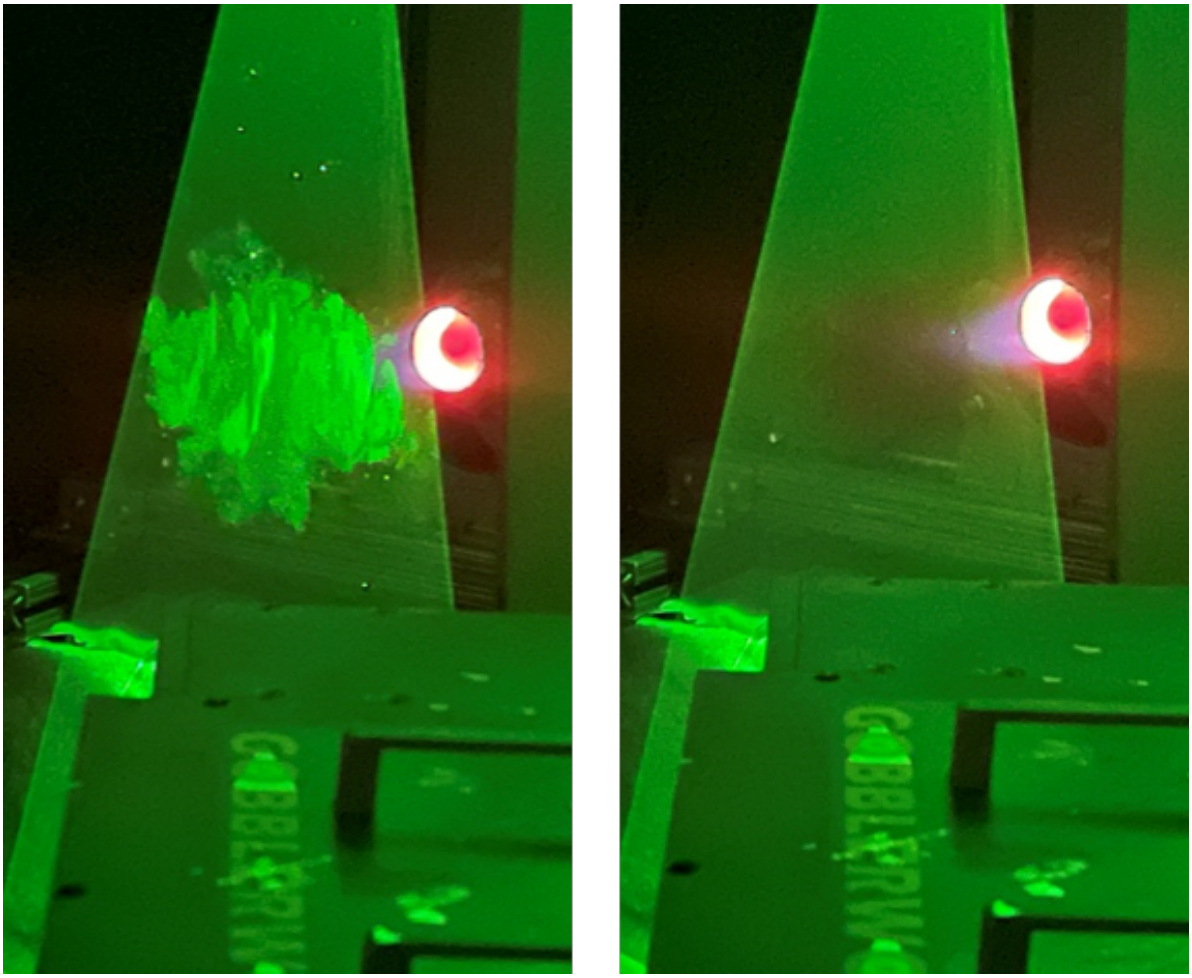

Figure 3.47: Left: Example image of incomplete combustion leading to large amounts of soot in the exhaust. Right: Complete combustion with a clean laser sheet.

Unlike all of the previous data that used the double trough centered at 18788.4321 $cm^{-}1$ (see Fig. 3.8), the JetCat exhaust data was taken at the triple trough region centered around 18789.9835 $cm^{-}1$ (see Fig. 3.48). This was done due to laser instabilities at the double trough region. Laser instabilities were mostly caused by the loud noise produced by the JetCat. The average noise level at the laser cart was 110 dB. The side effect of doing this is that it will test the iterative code solver on a completely different-looking convolution spectrum. The downside is that the uncertainty values found through the Monte Carlo simulations (see Fig. 3.20) are no longer valid.

To quantify the uncertainty of the JetCat exhaust data, the Monte Carlo simulations were run again. Only this time the triple trough will be used and representative conditions in the JetCat exhaust were used. The same procedures were followed as previously described. The results of this analysis can be seen in Fig. 3.49.

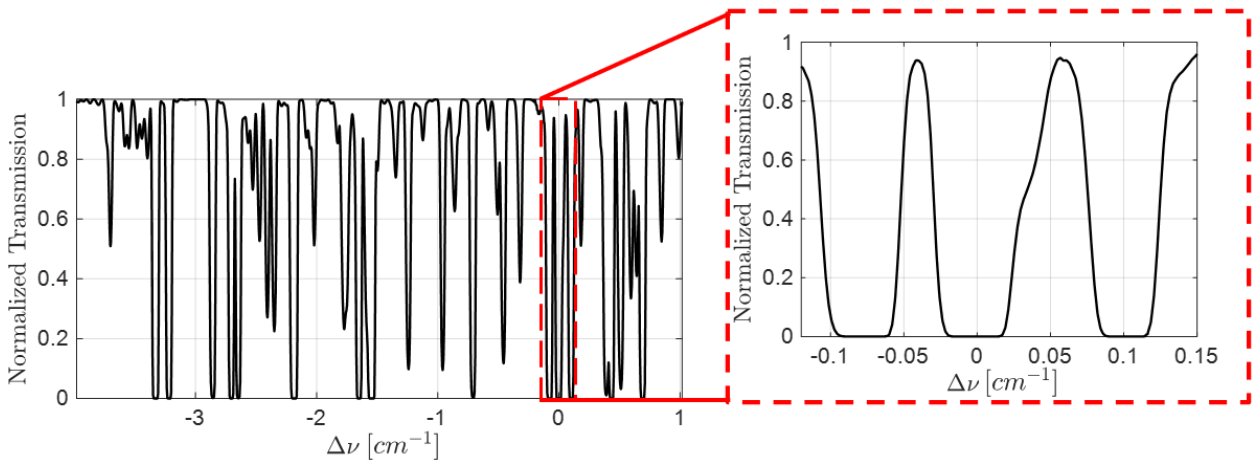

Figure 3.48: Iodine transmission spectrum (Forkey spectrum) with a zoomed-in view of the tripe-trough region.

Comparing Fig. 3.49 to Fig. 3.20, the overall trend is comparable. Each value is less than that of those computed in Fig. 3.20 except for static temperature. This overall decrease in uncertainty is caused by using the entire triple trough region instead of just down in the trough like was used in the double trough region. Having more points to compare to (150 in the triple trough versus 50 in the double trough) greatly reduces the fit error. The entire triple trough region had to be used because of the narrowness of the individual troughs and the overall filtered area. Most of the Rayleigh signal is filtered out so the iterative code needs more points to be able to solve with low uncertainty. This narrowing also makes it much more difficult to solve for temperature as the steepness of the troughs makes the difference in the full-width-half-maximum very small as temperature changes. This is especially true at low SNR levels. This kind of processing is only possible when Mie and background scattering effects are accounted for. Otherwise, the high transmission regions would throw the fitting scheme off and the final fitted values would have high error.

Finally, the last step that is needed to process the JetCat exhaust data is the rotation of the three sensed velocities to orthogonal U, V, and W velocities. Three cameras were used for this test to get three sensed velocities. To do this, a procedure similar to the one shown in Fig. 3.38 will be shown. Except for this time, a rotation matrix will be used which can be seen in Fig. 3.50 from Cadel et al. [90]. The variable U_s refers to the sensed velocity while θ refers to the sensed velocity direction found by $\hat{o} - \hat{i}$ as defined by Fig. 3.50. For more information and derivation of the final velocity uncertainty once rotated to orthogonal components the author refers the reader to Cadel et al. [90] as this will not be covered here but will be used in the final results later.

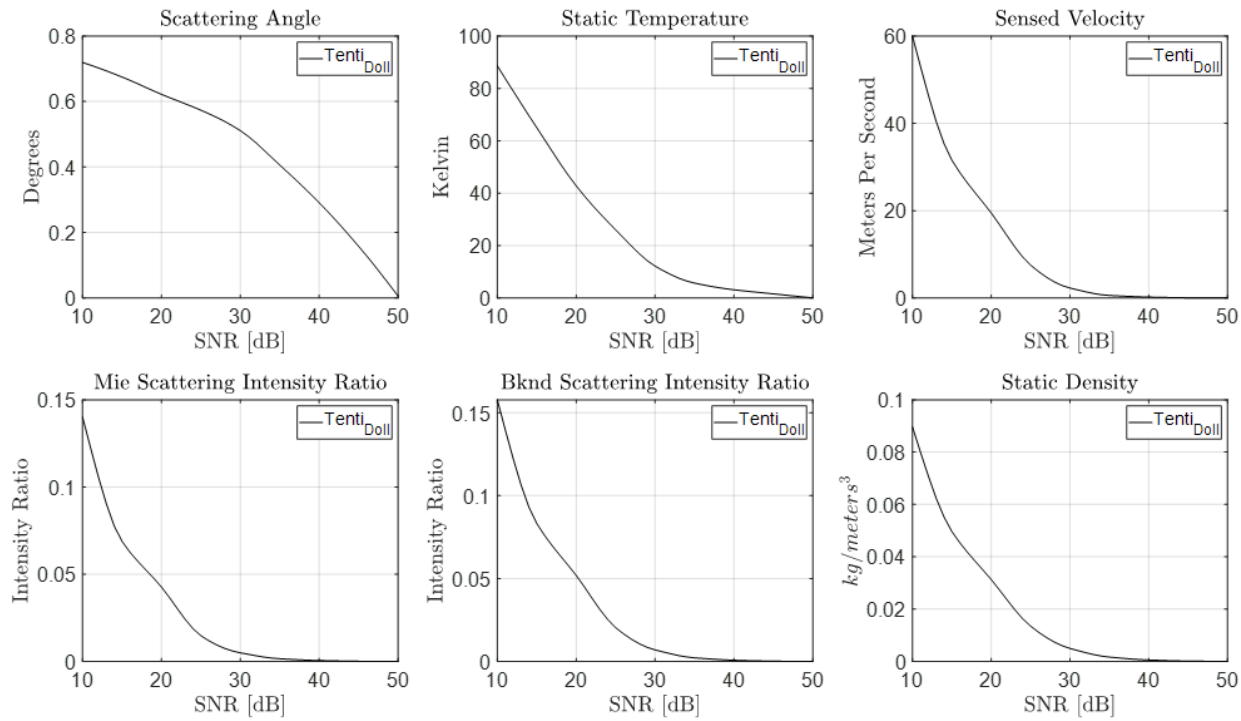

Figure 3.49: Monte Carlo results at various SNR levels with the $RBS-D$ Rayleigh scattering model using a 95% confidence interval.

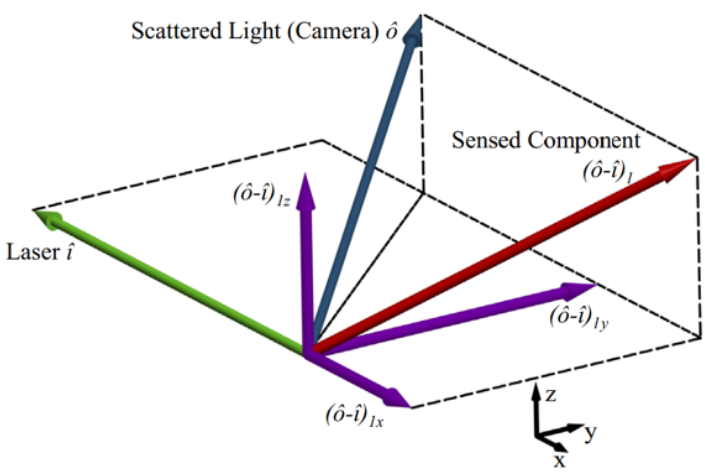

$$\begin{bmatrix} U_{S_1} \\ U_{S_2} \\ U_{S_3} \end{bmatrix} = \begin{bmatrix} \theta_{1x} & \theta_{1y} & \theta_{1z} \\ \theta_{2x} & \theta_{2y} & \theta_{2z} \\ \theta_{3x} & \theta_{3y} & \theta_{3z} \end{bmatrix} \begin{bmatrix} U \\ V \\ W \end{bmatrix}$$

Figure 3.50: Geometry and measured velocity components for a single camera/laser pair from Cadel et al.

Results

The laser plane of the JetCat exhaust was taken approximately at 12 x/D downstream of the exhaust. This was done to minimize the amount of background scattering as seen from the cameras in addition to terminating the laser plane a distance away from the measurement

region. As such, the laser sheet was spread wide enough to capture the entire JetCat exhaust at this distance. Although capable, the laser sheet was kept at this width to maximize the amount of laser power available and minimize the exposure times of the cameras.

Following the same procedure as in the freejet case (specifically Fig. 3.37), the planar FRS results (excluding velocity) can be seen in Fig. 3.51. Note that the results have been cropped to the entire laser sheet. This is in contrast to the freejet results seen in Fig. 3.39 as the laser sheet in those results was many times wider than the region of interest and so the cropping could be done inside of the laser sheet region. Also, since three independent measurements were made from the three cameras, the static density and static temperature results have been averaged together to decrease the uncertainty in the final result by the $\sqrt{3}$. Scattering angle and Mie and background scattering intensity ratios are camera specific. The ones shown in Fig. 3.51 are from the camera seen at the bottom of Fig. 3.47.

The top chart in Fig. 3.51 shows the solved scattering angle which was bounded tightly within a few degrees to the solved camera calibration result as all of the cameras were in the green zone as defined by 3.27. Again, in this green region, it is known that the X, Y, and Z camera coordinates have less than a 1% error, therefore, the bounds on scattering angle can be tight to get a good static temperature measurement.

The second row of charts in Fig. 3.51 shows the static density on the left and static temperature on the right. The lower static density and higher static temperature seen towards the bottom of these contours are due to the asymmetry of the jet where the flow on the right side of the jet is being forced down more so than the flow on the left side is being forced up. Evidence for this can be seen in Fig. 3.52 which will be discussed in detail later.

Finally, the bottom row of charts in Fig. 3.51 shows the Mie scattering intensity ratio on the left and the background scattering intensity ratio on the right. Note the contour color level differences. The Mie scattering intensity ratio is much higher than that of the background scattering intensity ratio, as expected. However, the background scattering intensity ratio was expected to be relatively constant across the plane. Due to the dependence of all six solved variables on one another (as evident in Fig. 3.19) and such low background scattering intensity ratios, the dependence effect can be seen. The Mie scattering intensity ratios are much higher due to the incomplete combustion as seen in the left image in Fig. 3.47. Although multiple images were taken at each laser frequency to mitigate this issue, the technique was not perfect. However, the iterative code handled it well and good results were still achieved.

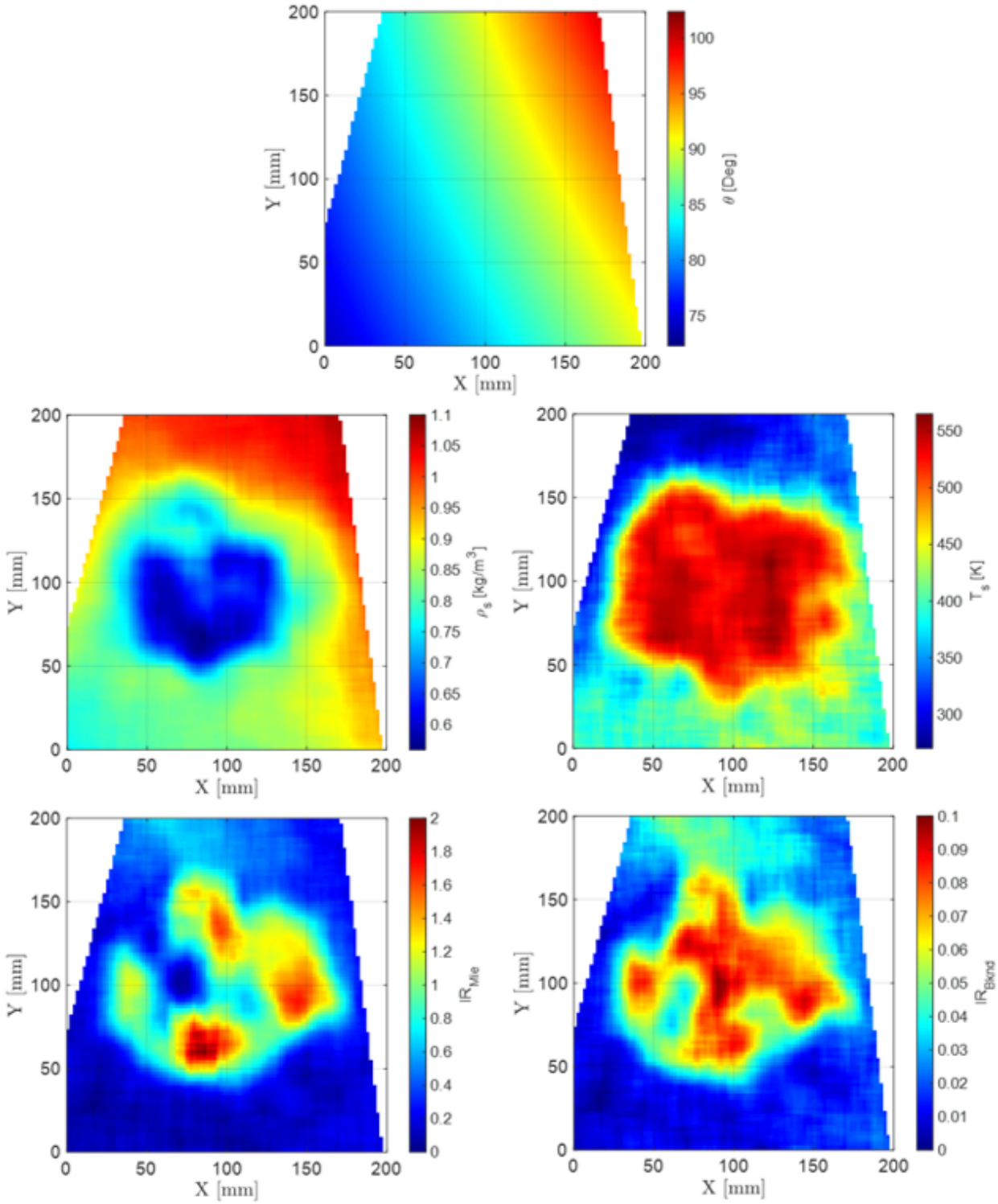

Figure 3.51: Auto-processed results for scattering angle, static density, static temperature, And Mie and background intensity ratio.

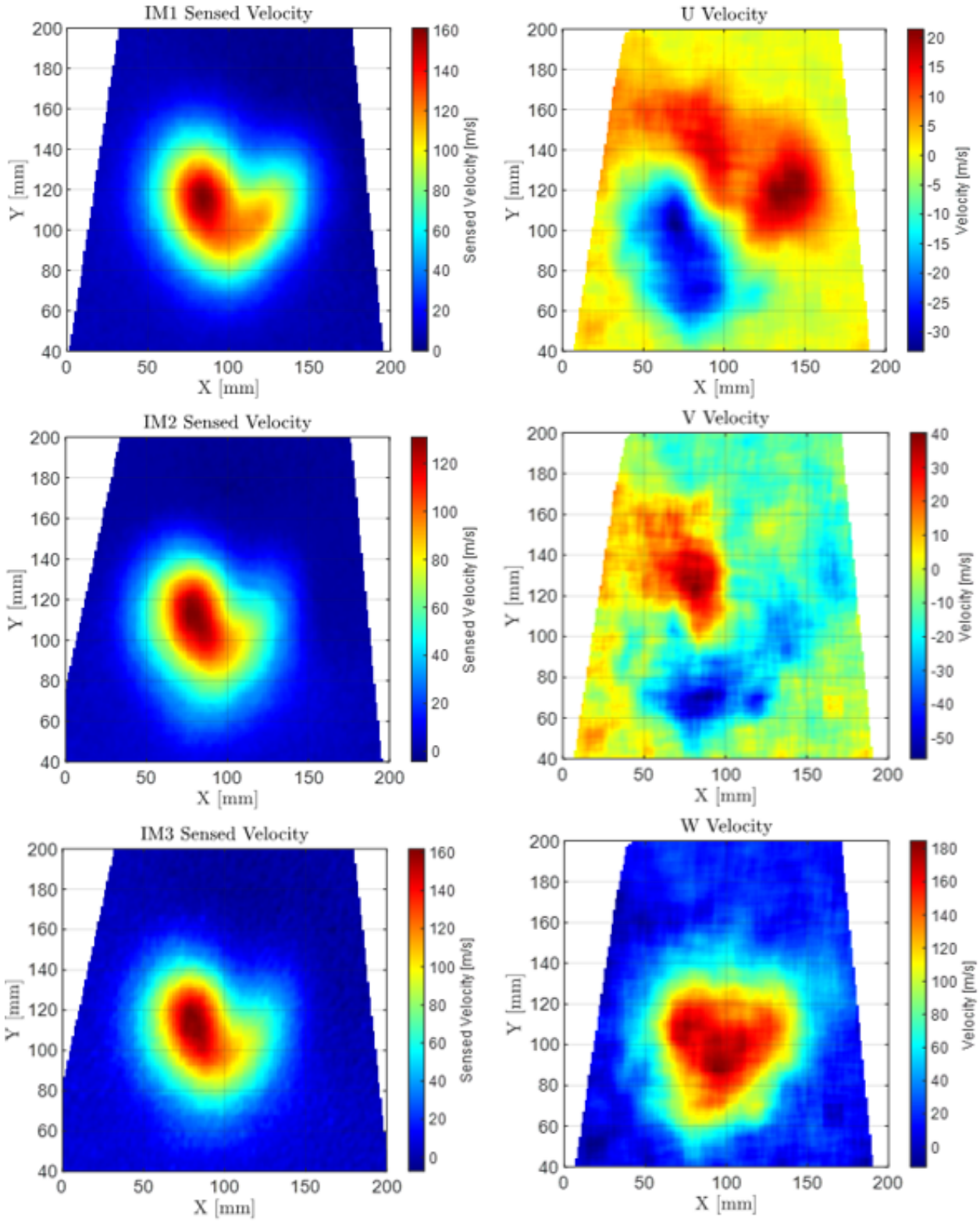

Figure 3.52: Left: Sensed velocity charts from each camera. Right: Sensed velocity converted to orthogonal velocity components.

Figure 3.52 shows the sensed velocity results from the three cameras on the left and the transformed/rotated three-component orthogonal results on the right. The top chart on the right is the U-velocity which corresponds to a positive velocity to the right and a negative velocity to the left. The middle right chart is the V-velocity which corresponds to a positive velocity upwards and a negative velocity downwards. This was done so that the W-velocity in the bottom right chart would correspond to a positive velocity out of the page. Figure 3.52 shows a clear swirling pattern that is positive in the clockwise direction of motion. This motion will be discussed in more detail later along with Fig. 3.53.

The asymmetry of the JetCat exhaust is especially prevalent in the bottom right chart of Fig. 3.52. The axial velocity is no longer the expected circular shape. It is longer in the vertical direction than it is wide in the horizontal direction. The flow has also had enough time to collapse and fill in the low-velocity zone that would have been expected from the plug located in the JetCat nozzle (see Fig. 3.42). However, the U and V velocity components do decrease, on average, to close to zero velocity in between the areas of high swirl, as expected.

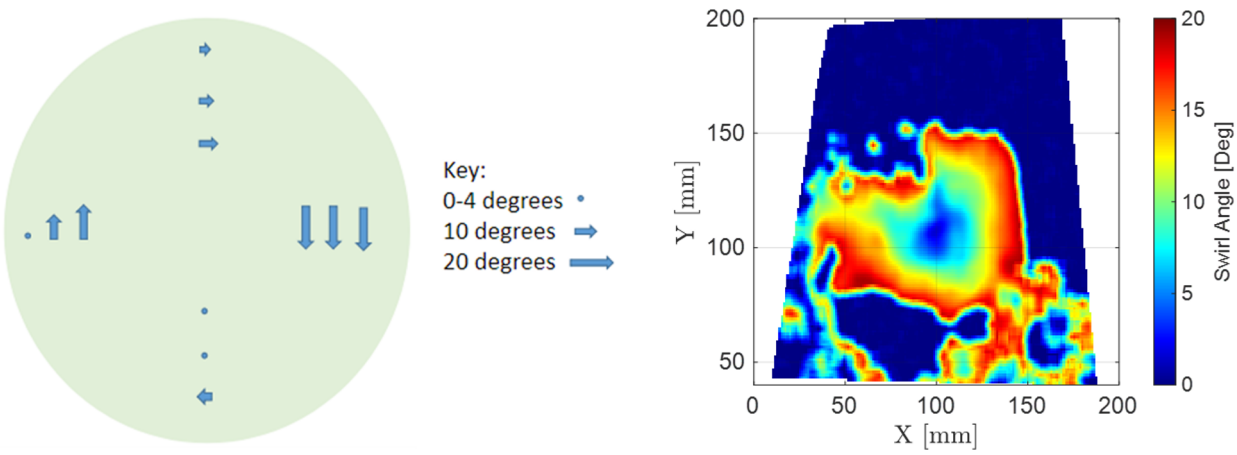

Figure 3.53: Swirl angle. Positive is clockwise. Left: 5-hole probe measurement data from Coulon et al. Right: FRS results.

Using Eq. 3.28, the swirl angle of the flow can be calculated, where *atan* represents the four-quadrant inverse tangent. A positive swirl angle is in the clockwise direction. The FRS results of this analysis can be seen on the right side of Fig. 3.53. Since the measurement was taken so far back from the JetCat exhaust plane, most of the identifiable shape in the swirl has dissipated. However, the center of the JetCat is still visible around the 100 mm mark in both the X and Y direction. To validate these results, the chart on the left side in Fig. 3.53 has been included which are five-hole probe results from Coulon et al. [132]. Coulon et al. do not mention the axial location of the five-hole probe. However, based on the images

provided, it looks to be at an axial location of approximately an x/D of 6. This is about half the distance the FRS results were taken at. This makes sense given their assumed swirl profile to be circular. Although not a perfect comparison, the two charts in Fig. 3.53 do match up well.

$$\text{Swirl Angle} = atan(\sqrt{U^2 + V^2}, \sqrt{W^2}) \tag{3.28}$$

Finally, as validation, probe data was taken in the vertical and horizontal directions (Fig. 3.54) using a total temperature and total pressure probe along the centerline of the JetCat (see Fig. 3.46). Referring to Figs. 3.51 and 3.52, the data was taken at approximately the 100 mm mark in both the X and Y direction. Two probe lines were taken and compared due to the asymmetry of the jet. The blue and black charts correspond to the FRS and probe data while the red charts correspond to the normalized percent difference between the FRS data and the probe data. The static results from FRS have been converted into total results using isentropic equations. Overall, the FRS results line up well with the probe results in both the vertical and horizontal cases.

Starting with the top charts in Fig. 3.54, the total pressure probe measurements and FRS results line up very well with minimal differences between the two data sets. The second row, corresponding to total temperature lines up well within the JetCat exhaust but diverges slightly towards the edges. This is likely due to the minimal space corresponding to the freestream as seen in Fig. 3.51 and the interaction with the edge of the laser sheet which has higher intensity as seen in Fig. 3.47. Future experiments should widen the laser sheet to avoid this issue.

The next two rows, corresponding to Mach number and axial velocity align well with the probe results. However, velocity diverges slightly in some locations. In almost all cases the probe data is within the uncertainty bounds of the FRS results. Therefore, this divergence will not be explored more here but is likely due to large particle scattering effects in these regions.

Finally, the total density is shown in the bottom two charts of Fig. 3.54. These results vary the most compared to the other variables even though the probe data is almost always within the bounds of uncertainty for the FRS results. This is likely due to the low SNR as well as large magnitude changes of total and static density from the ambient conditions to the JetCat exhaust.

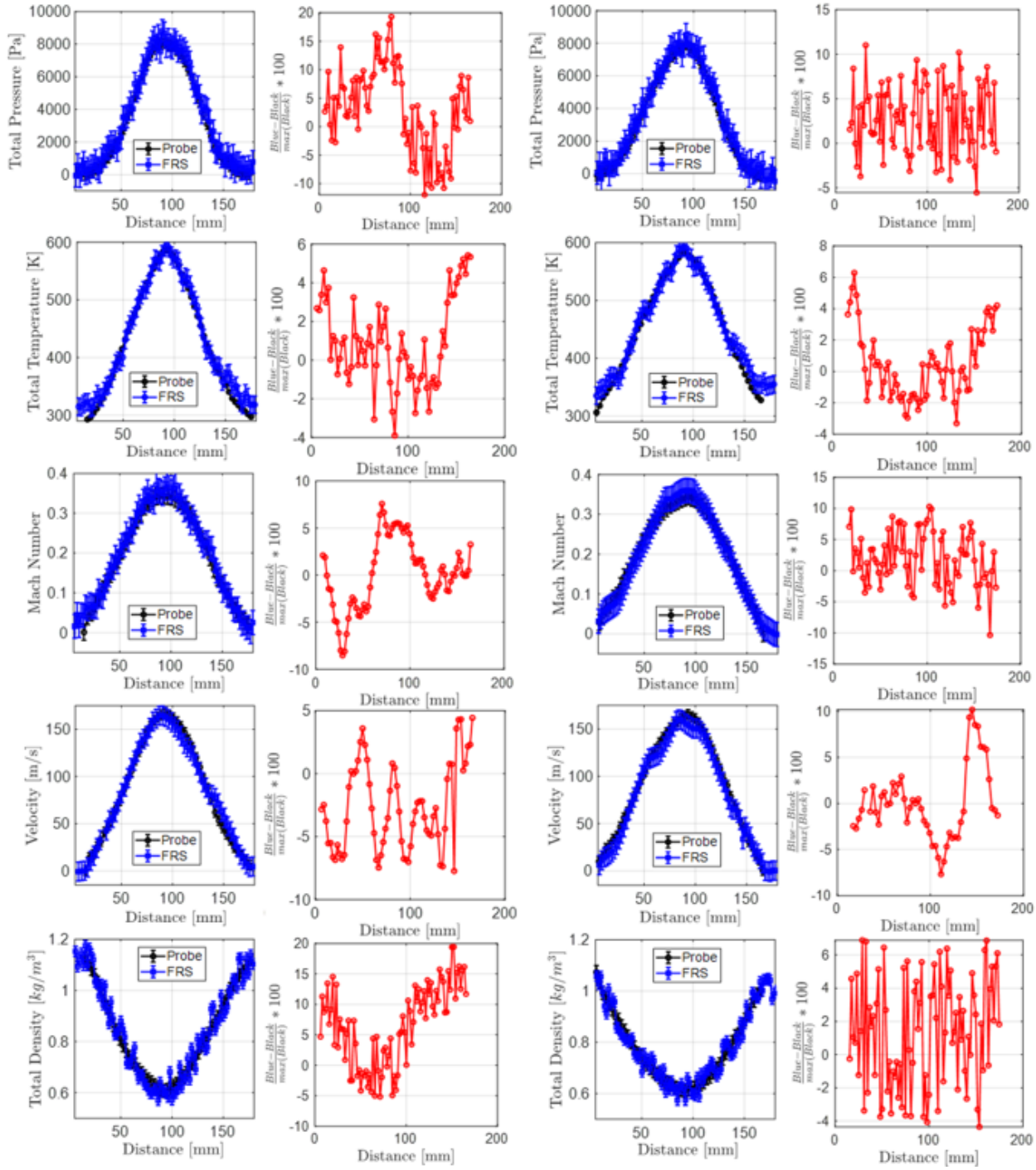

Figure 3.54: Blue: Vertical (left) and horizontal (right) probe line and FRS data taken at approximately 100 mm. Error bars are shown with 95% confidence bounds. Right: Normalized percent difference between the probe data and FRS data in red.

3.4 Final Remarks and Discussion

The post-processing of filtered Rayleigh scattering data for non-intrusive measurements of 3-component velocity, static temperature, static density, and Mie and background scattering intensity ratios is a non-trivial task. It was shown that an auto-processing iterative scheme using a non-linear least-squares model can be used to quickly and accurately determine flow variables. This was shown using five different Rayleigh-Brillouin scattering models where ultimately, the $RBS - D$ model was selected for its wide range of validity and quick spectra generation times. This kind of analysis shows the potential for minimal user input and large time/cost savings in the post-processing of raw FRS data. The new algorithm allows users to quickly and accurately take non-intrusive measurements with the FRS technique and make adjustments day-to-day based on the previous day's data. This was previously impossible due to the amount of manual post-processing needed by the user.

Overall, this chapter described the entire FRS modeling technique to generate simulated signals. The equations were presented as well as evidence of what trade-offs were made between accuracy and overall processing time. Many of these trade-offs have a compromise where sufficient accuracy and minimal time are required. These processing methods were first applied to simulated data where different signal-to-noise ratios were compared using Monte Carlo simulations. It was shown that to reach less than a 1% error in all six variables examined, an SNR level of 40 dB would be needed. This is not practical in an experiment. Practical SNR levels are achievable around the 30 dB mark using the pco.edge 4.2 bi UV cameras and 20 dB using the FLIR BFS-U3-31S4 cameras. To validate the processing code, two experiments were performed both with background and Mie scattering present. The first was with a bench top freejet. The results were compared to manually processed FRS results as well as total temperature and total pressure probe results. The second experiment was conducted in the exhaust plume of a JetCat P100-RX. Again, these results were compared to total temperature and total pressure results as well as five-hole probe results for swirl angle. In both cases, the probe results and FRS results aligned well with 95% confidence interval bounds for all variables. The auto-processing method was shown to have advantages over the manual methods used in the past for both time and accuracy based on these experimental results. It is now clear that the algorithm developed in this work is capable of automatically processing images from experiments with Mie and background scattering contributions with little error.

3.5 Nomenclature

AF	mass-based air-fuel ratio
$\overline{AF}$	molar-based air-fuel ratio
C_I	intensity constant
C_{IS}	intensity scaling constant
C_p	photon constant
c	speed of light
c_{int}	internal heat capacity
DGV	Doppler global velocimetry
$RBS - DC$	Doll's experimentally calibrated Rayleigh scattering model
dB	decibels
FRS	filtered Rayleigh scattering
$FWHM$	full width half maximum
f_u	Euken factor
FRS	filtered Rayleigh scattering
h	Planck constant
$\hat{i}$	laser propagation vector
$I_{Background}$	background scattering intensity
I_{Mie}	Mie scattering intensity
I_{RBS}	Rayleigh-Brillouin scattering intensity
IR_{Bknd}	background scattering intensity ratio
IR_{Mie}	Mie scattering intensity ratio
k	wave vector magnitude
k_b	Boltzmann constant
L_x	length of the measurement volume along the propagation direction
M	molar mass
M_{air}	molar mass of air
M_{fuel}	molar mass of fuel
m	molecular mass
N_A	Avagadro's constant
N_r	total number of Rayleigh scattered photons incident on the camera sensor
n	molecular number density
n_o	number density

$\hat{o}$	observation vector
P_N	noise power
P_o	incident laser power
P_S	signal power
PIV	particle image velocimetry
PD	Photodiode
p	static pressure
R_{int}	internal relaxation number
RPM	revolutions per minute
S_{Bknd}	background scattering spectrum
$S_{Bknd_{Norm}}$	normalized background scattering spectrum
S_{Mie}	Mie scattering spectrum
$S_{Mie_{Norm}}$	normalized Mie spectrum
S_{RBS}	Rayleigh-Brillouin scattering spectrum
$S_{RBS_{Norm}}$	normalized Rayleigh-Brillouin scattering spectrum
S_S	convoluted spectrum
S_{Tot}	total scattering spectrum
SNR	signal-to-noise ratio
$S_{FRS_{Meas}}$	measured spectrum
$S_{FRS_{Sim}}$	simulated spectrum
$SVSA$	support vector spectrum approximation
T	static temperature
$RBS-D$	Doll's Tenti-S6 based analytical model
T_{iodine}	iodine transmission spectrum
$RBS-S6$	original Tenti-S6 model
$RBS-W$	Witschas model for Rayleigh-Brillouin scattering spectrum
U, V, W	orthogonal velocity components
$\overrightarrow{V}$	total velocity
V_{Axial}	axial velocity
V_{Sens}	sensed velocity
v_o	gas kinetic velocity
X	non-dimensional Rayleigh scattering lineshape modeling parameter
x	non-dimensional modeling parameter for SVSA
Y	non-dimensional Rayleigh scattering lineshape modeling parameter

y	non-dimensional modeling parameter for SVSA
α	stoichiometric coefficient
β	angle between the laser polarization and the scattering direction
β	stoichiometric coefficient
γ	stoichiometric coefficient
$\Delta\nu$	wavenumber difference
$\Delta\nu_D$	frequency shift to to Doppler effect
Δt	time integration or camera exposure time
δ	stoichiometric coefficient
ϵ	efficiency of the optical measurement system
η	dynamic viscosity
η_b	bulk viscosity
θ	scattering angle
θ_{Axial}	angle between sensed velocity direction and axial axis
θ_{Sens}	angle between sensed velocity direction and laser propagation direction
λ	wavelength
ρ_s	static density
σ	thermal conductivity or stoichiometric coefficient
σ_N^2	noise variance
σ_S^2	signal variance
Φ	objective function to minimize error
Ω	light collection angle
$\frac{d\sigma}{d\Omega}$	differential scattering cross-section

Chapter 4 - Filtered Rayleigh Scattering Measurement Technique Validation in Engine Applications and Boundary Layers

The contents of this chapter will be published in *Turbo Expo Proceedings 2023* (Sean W. Powers, Gwibo Byun, and K. Todd Lowe. "Validation of Filtered Rayleigh Scattering Optical Rake Measurement Techniques in Turbomachinery Applications and Boundary Layers"). This manuscript was recommended for journal publication by all reviewers and the session chair. It was also recommended for the best paper award.

Significant portions were previously discussed in *"Filtered Rayleigh Scattering Measurement Technique Validation in Engine Applications"* (Sean W. Powers, Gwibo Byun, and K. Todd Lowe) which was presented at the AIDCAT 2022 conference.

The objective of this chapter is to provide evidence that the FRS technique can be applied to non-ideal environments, measure near-wall phenomena such as boundary layers, and replace physical probe rakes with the same magnitude in uncertainty. This chapter starts to address non-ideal applications for control volume analysis where the data is investigated from a statistical point of view. These knowledge gaps were discussed in subsection 2.3.3

Proceedings of the ASME 2023 Turbomachinery Technical Conference and Exposition (GT2023)
June 26 – June 30, 2023, Boston, MA

GT2023-102014

VALIDATION OF FILTERED RAYLEIGH SCATTERING OPTICAL RAKE MEASUREMENT TECHNIQUES IN TURBOMACHINERY APPLICATIONS AND BOUNDARY LAYERS

Sean W. Powers[1], Gwibo Byun[1], K. Todd Lowe[1,*]

[1]Kevin T. Crofton Dept. Aerospace and Ocean Engineering, Virginia Polytechnic Institute and State University, Blacksburg, VA, USA

ABSTRACT

Filtered Rayleigh scattering (FRS) is a non-intrusive, laser-based optical technique for measuring 3-component velocity, static temperature, and static density with high spatial resolution and low uncertainty. FRS can be used to derive total values as well as turbomachinery efficiencies. The Virginia Tech team has been developing this seedless technique for simultaneous planar (or line) measurements to overcome the limitations associated with seed-based laser measurement techniques such as laser Doppler velocimetry (LDV), particle image velocimetry (PIV), and Doppler global velocimetry (DGV) as well as limitations with physical probe rakes such as blockage and wake production. This technique is especially attractive in flow cases or environments where the aforementioned seed-based laser measurement techniques are limited or not possible. A combination of specially designed boundary layer total pressure probe rake measurements, FRS optical rake measurements, and computational fluid dynamics (CFD) results in the inlet of a Honeywell TFE731-2 turbofan are presented. Results show that all three techniques (FRS, probe, and CFD) match within approximately 2% root-mean-square error (RMSE). Inlet efficiency was derived and found to be within 2.3% difference for all three techniques.

Keywords: CFD, Experimental, Inlets, Measurement Techniques, Sensors, Turbomachinery

NOMENCLATURE

Roman letters

C_p	Specific heat capacity
FRS	Filtered Rayleigh scattering
f_D	Doppler shifted frequency
H, h	Enthalpy, specific enthalpy
I	Intensity
$\hat{i}$	Laser propagation unit vector
M	Mach number
n	Number of data points
OTS	Optical test section
$\hat{o}$	Camera observation unit vector
P	Pressure
PRB	Probe
R	Gas constant
r	radius
RDI	Radial distortion index
S	Signal intensity
SG	Strain gauge
T	Temperature
V	Axial velocity unless otherwise stated
Y^+	Viscous wall distance from wall to first simulation node

Greek letters

γ	Ratio of specific heats
$\Delta\nu$	Detuning wavenumber
δ, δ_T	Boundary layer thickness, thermal thickness
η_{inlet}	Inlet efficiency
λ	Wavelength
μ	Mean
ρ	Density
σ, σ^2	Standard deviation, Variance
τ_{I_2}	Iodine transmission spectrum

Superscripts and subscripts

a	ambient
e	edge
FRS	Optical rake derived
$Probe$	Physical probe rake derived
Sim	Simulation derived
s	static values or isentropic values
TOT	total
t	total values

1. INTRODUCTION

Aerothermodynamic measurements on turbine engines are typically carried out with physical probe rakes, and oftentimes the most important measurements are near surfaces. This is due to the significant efficiency losses that can be incurred by the presence of boundary layers and distortion fields. However, the design and implementation of such rakes can be costly and in some locations, impossible. Even further, the presence of the rake can change the flow being measured in undesirable ways, especially if multi-

*Corresponding author: kelowe@vt.edu

stage measurements are needed. Advanced probe rakes have been devised in an attempt to solve these issues through the use of complex geometric shapes but are application-specific (see Bui et al. [1]). To overcome intrusiveness, optical sensing may be used. A typical example of a laser-based non-intrusive optical technique is laser Doppler velocimetry (LDV) [2]. LDV makes use of frequency modulation to determine velocity over a very small area where the results are often reported at a single point. However, because of this small measurement area, LDV is impractical for large planar or line measurements and is only used in special cases for turbomachinery. Although not immediately related, a more common application of a non-intrusive measurement in turbomachinery is the Non-intrusive Stress Measurement System (NSMS) probes which are typically used for fan blade vibrational investigations [3]. In application, NSMS work has been done under simple or ideal assumptions leading to successful high technology readiness levels (TRL) but field measurements remain at lower TRL levels and are not routinely used for engine (or advanced rig) applications (see Chen et al. [4]).

The current work applies the filtered Rayleigh scattering (FRS) technique to create an optical rake capable of planar measurements of 3-component velocity, static temperature, and static density in turbine engine environments as well as produce the first successful quantitative FRS boundary layer measurement in an internal flow. However, the authors do wish to acknowledge the work done by Williams et al. [5] for their work using FRS in hypersonic boundary layers as a flow visualization technique. It is important to note that the optical rake in the current work is made of a laser line and a camera to view the laser line (no physical setup in the flow). The results are consistent with physical probe rake results and simulation results. The FRS technique makes use of Rayleigh scattering coming from a laser line or plane which is then viewed by cameras or fiber optics. Several works have explored similar topics in turbomachinery applications such as Doll et al. [6, 7] and Schroll et al. [8]. Previous measurements relevant to those presented in this manuscript include those from Boyda et al. [9] and Saltzman et al. [10].

This work starts with a brief overview of the theory behind Rayleigh scattering and filtered Rayleigh scattering in Section 2. Next, the test setup is presented in Section 3 which includes the simulation setup as well as the physical experimental setup. Section 4 presents the three-pronged comparison results between the physical probe rake, the FRS optical rake, and the simulation results. These include a statistical averaging investigation to decrease the uncertainty in the FRS optical rake data. Finally, Section 5 provides a brief conclusion and summary of the results.

2. FILTERED RAYLEIGH SCATTERING

The following subsections serve to provide a brief fundamental overview of Rayleigh scattering and filtered Rayleigh scattering. The effects of velocity, static temperature, and static density on the Rayleigh scattering spectrum will be introduced along with unwanted effects such as Mie (particle) and background (geometric) scattering. The importance of filtering as a means of interrogating the spectral content of the Rayleigh scattering lineshape and ridding the data of unwanted signals will also be described. The readers are referred to Powers et al. [11] for fundamental, in-depth descriptions of filtered Rayleigh scattering and related processing techniques that will be used to post-process the data in this manuscript.

2.1 Rayleigh Scattering Theory

Rayleigh scattering is a wave optics phenomenon resulting from the interaction of light and matter on the scale of, or smaller than, the wavelength of the incident light source (typically a laser). The scattering intensity of the Rayleigh scattered light is proportional to one over the wavelength to the fourth power. Therefore, the shorter the wavelength, the higher the scattering intensity in proportion to the incident light intensity. A simple example of Rayleigh scattering is why the sky is blue. When examining the visible light spectrum (~400nm - ~700nm), violet light (~400nm) scatters almost ten times more than red light (~700nm). Violet light is scattered much more quickly than longer wavelengths. Therefore, by the time the light gets near the surface to be observed, most of the violet light has already been scattered leaving the blue light as the shortest and therefore the highest scattering intensity of the remaining light.

The natural phenomenon of Rayleigh scattering off of gas molecules can be leveraged to eliminate the need for seeding flows with tracer particles. This is in contrast to measurement techniques such as particle image velocimetry (PIV), Doppler global velocimetry (DGV), and laser Doppler velocimetry (LDV). On top of this, in their conventional and common implementations, these techniques can only be used to measure velocity. However, Rayleigh scattering can be used to simultaneously measure scalar quantities of static temperature and static density as well as scalar/vector quantities of velocity. To do this, the key attributes of the Rayleigh scattering signal must be understood: 1) The probability of photons scattering off of a gas molecule increases with the amount of matter which allows for a static density measurement. 2) Light scattered off of matter in motion is Doppler shifted in frequency proportional to its bulk velocity (this velocity is the sensed velocity and will be explained in more detail later). 3) Since individual molecules are always in motion, a Doppler shift is imparted proportional to the speed of the individual molecules allowing for static temperature measurements. Items 1 through 3 yield the measurement principles, namely that direct measurements of static density (1) and static temperature (3) can be used to compute static pressure from the state equation, while the mean Doppler shifted signal yields flow velocity (2). These effects are all observed through a molecular absorption filter; in this case, an iodine vapor cell is used which will be described in Subsection 2.2.

Referring Fig. 1.A, the technique used hereafter will not concern ambient light from the sun but rather laser light (specifically, continuous 532 nm wavelength light from a Coherent Verdi-V18, frequency-doubled Nd:YVO_4 diode-pumped solid-state laser) which is shown as the green line. The Rayleigh scattering spectrum is then produced by Doppler broadening and shown as the blue curve. This chart is referred to as the "no flow reference signal" so that the influence of changes in static temperature, static density, and velocity can be easily examined.

Figure 1.B shows the influence of increasing static temperature. The full-width-half-maximum (FWHM) is proportional

to the square root of static temperature. Therefore, as the static temperature increases, the Rayleigh scattering signal width increases. However, the peak intensity decreases. Figure 1.C shows the influence of static density. Static density is proportional to an increase in the overall intensity of the entire Rayleigh scattering signal. Therefore, a higher static density means that the overall intensity of the signal will increase. Finally, Fig. 1.D shows the influence of velocity. Velocity does not change the Rayleigh scattering signal shape or intensity. Velocity shifts the Rayleigh scattering signal left or right in frequency (depending on the sign) through the Doppler frequency shift equation shown in Eq. 1 where, f_D is the Doppler shifted frequency of the incident laser light, $\hat{o}$ is the unit vector pointing from the measurement location to the observer (camera), $\hat{i}$ is the unit vector of the laser propagation direction, λ is the wavelength of the incident laser light, and $\vec{V}$ is the three-component velocity vector.

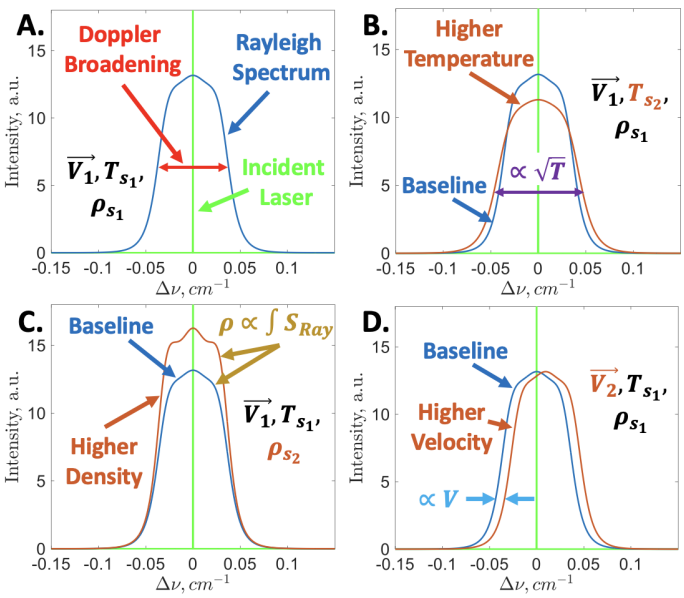

FIGURE 1: A: LASER RAYLEIGH SCATTERING SIGNAL (LRS). B: T_s INFLUENCE. C: ρ_s INFLUENCE. D: $\vec{V}$ INFLUENCE.

$$f_D = \left(\hat{o} - \hat{i}\right) \lambda^{-1} \cdot \vec{V} \tag{1}$$

2.2 Filtered Rayleigh Scattering Theory

A perfect Rayleigh scattering signal is rarely achieved outside of a highly controlled experiment. Undesirable scattering contributions often take the form of Mie (particle) scattering and background (geometric) scattering. Mie scattering is the scattering of light off of particles that are on the order of or larger than the wavelength of light that hits them. Background scattering is the scattering of light off of stationary physical objects within the field-of-view of the camera/observer.

Figure 2.A1 and Fig. 2.B1 show these undesirable contributions. The background scattering intensity can be very large and will always be at the same frequency as the laser; this is why it is at a wavenumber difference of zero ($\Delta\nu = 0$). Mie scattering can also have a large intensity but is Doppler shifted in frequency along with the Rayleigh scattering spectrum. This means it remains centered on the Rayleigh spectrum as shown. In this case, the background and Mie contributions do not align because the velocity is some non-zero value that has Doppler shifted the spectrum. At zero velocity, the Mie and background contributions would culminate in one large central peak.

To mitigate these undesirable scattering contributions a molecular vapor filter (iodine in this case) can be used. This is where the "filtered" part of filtered Rayleigh scattering (FRS) gets its namesake. FRS leverages sharp features present in the absorptivity spectrum of iodine vapor to interrogate the spectral content of the Rayleigh scattering signal while decreasing the contributions of Mie and background scattering. A snapshot of this process can be seen in Fig. 2.A1 and Fig. 2.B1 and is explained in depth by Powers et al. [11] and Warner et al. [12]. The result of this convolution is shown in Fig. 2.A2 and Fig. 2.B2 where the red dot corresponds to the result of the convolution from Fig. 2.A1 and Fig. 2.B1. This convolution is what is experimentally measured by a camera that looks through a molecular iodine cell.

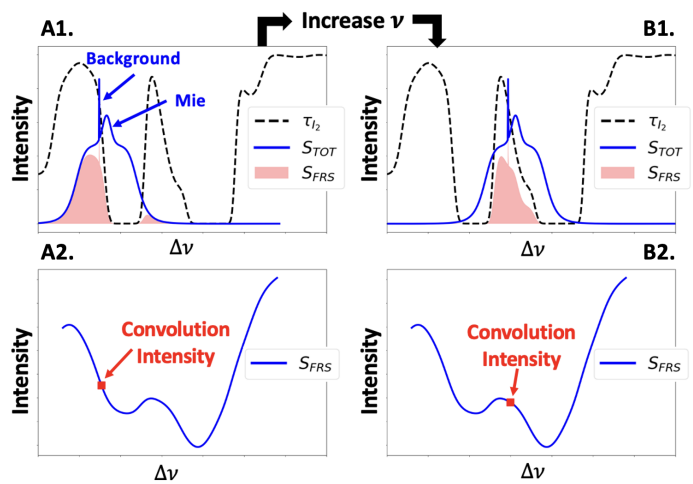

FIGURE 2: FRS TECHNIQUE. THE IODINE TRANSMISSION (τ_{I_2}) SPECTRUM IN A1 AND B1 IS CONVOLVED WITH THE TOTAL RAYLEIGH SCATTERING SPECTRUM (S_{TOT}) TO PRODUCE THE FINAL FRS SPECTRUM (S_{FRS}) IN A2 AND B2. PRINTED WITH PERMISSION AND MODIFIED FROM WARNER ET AL. [12].

Fundamental theory and equations on FRS theory are detailed in Powers et al. [11]. The processing technique to convert raw Rayleigh scattering signals to direct planar, line, or point measurements of static temperature, static density, or velocity can also be found in the same resource. This methodology will be used for the results shown here but will not be reviewed. It is worth noting that the FRS technique employed here is limited in its frequency response by the exposure time of the cameras (~ 2.5 seconds) and the number of discrete wavenumbers measured (~ 90). Therefore, the time to get one data set of results is approximately 3 minutes. Therefore, all of the data contained in this work is considered time-averaged.

3. TEST SETUP

Detailed documentation and validation of FRS for engine applications require not only FRS data but also physical probe data

and simulation data. The following subsections walk through the simulation setup and design of a high-speed inlet for the Honeywell TFE731-2 turbofan and the experimental setup at Virginia Tech's Advanced Propulsion and Power Laboratory. This experimental setup will explore why the high-speed inlet was needed and a comparison will be drawn between the physical probe rake as well as the FRS optical rake.

3.1 Simulation Setup

The Honeywell TFE731-2 is a 15,500 N (3,500 lbf) class turbofan engine with a bypass ratio of approximately 2.6 [13]. This engine can produce an inlet Mach number of approximately 0.3 at full throttle. However, modern engines can produce an inlet Mach number of approximately 0.5 at full throttle. Therefore, a high-speed inlet was needed to match modern capabilities. The design process started with computational fluid dynamics (CFD) simulations conducted in ANSYS Fluent with a corrected fan speed (CFS) level of 75% (the target operating point for the experiment) with a minimum Y^+ value of 50. This Y^+ value required standard wall functions in ANSYS Fluent that are based on the work by Launder et al [14]. This 2D-axisymmetric RANS simulation was comprised of 350,000 elements and 1.7 million nodes and made use of the SST $k-\omega$ turbulence model [15].

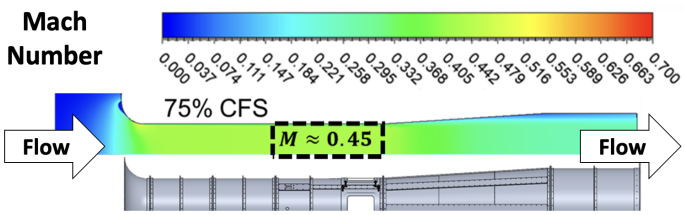

FIGURE 3: ANSYS FLUENT SIMULATION RESULTS AT 75% CORRECTED FAN SPEED (CFS).

A CFS of 75% leads to a Mach number of approximately 0.45 within the optical test section (OTS) which is outlined by a black box in Fig. 3 (Mach numbers above 0.75 possible at 100% CFS). The boundary layer in the optical test section (OTS) is approximately 29 mm in height, whereas the boundary layer near the exit into the engine is approximately 60 mm. Note that all boundary layer heights in this work refer to the $0.99V_e$ thickness definition. The fluid flow simulation results will be used for comparison to both the FRS optical rake data and physical probe rake data. This three-pronged approach is helpful to the validation of the FRS technique. If all three techniques align well, the flow and techniques used can be considered to be well understood (simulations and measurement results agree) and consistent (comparator measurements agree with quantified uncertainties).

3.2 Experimental Setup

3.2.1 Honeywell TFE731-2 and High-Speed Inlet. Figure 4 shows the CAD model on the left as well as photographs of the fully assembled setup on the right. At the front of the CAD model, an inlet ramp was placed such that the air sucked from the ground was diverted into the bellmouth of the inlet without creating vortices, thus preserving the flow quality. The bellmouth is followed by a long straight section that leads into the OTS. This was done to give the flow the required length for reaching equilibrium boundary layer conditions (see Fig. 3). After exiting the OTS the flow was diffused at an approximate angle of 2.5° to the larger diameter of the TFE731-2. The shallow diffusion angle minimizes flow separation, thus minimizing the boundary layer that the TFE731-2 must ingest.

The optical test section (OTS) was specially designed to house the physical probe rakes as well as the FRS optical rake (laser line). More information on these rakes is given in Subsection 3.2.2. The primary feature of the OTS is the four optical viewing windows. These were made of quarter-inch thick acrylic that was sanded and polished to optical quality. These windows were anti-reflective (AR) coated and were used to allow the cameras to see the laser line. Only three were used but a redundant fourth was added for possible future measurements. The camera stand was placed around the OTS window locations for camera mounting. This stand was intentionally connected to the engine mount so that the cameras would be subject to the engine's vibrational environment. The TFE731-2 hangs from an engine mount, which is mobile and is positioned such that the bellmouth operates sufficiently far from laboratory walls, thus avoiding unwanted interactions.

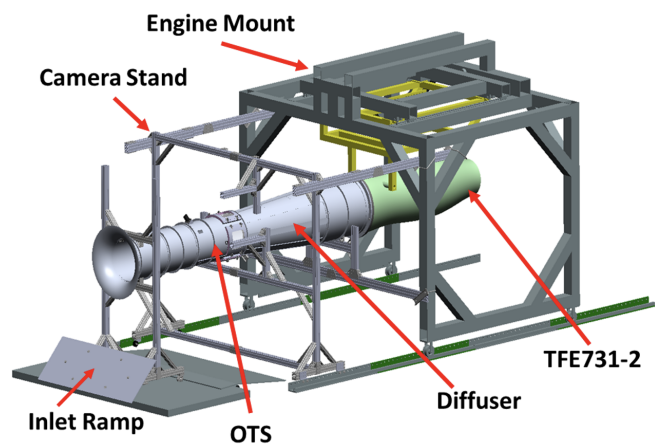

FIGURE 4: TFE731-2 EXPERIMENTAL SETUP CAD.

The high-speed inlet is made of several sections that are bolted together. These sections are sealed with rubber gaskets and held together with 16 bolts and nylon locking nuts at each interface. Due to manufacturing imperfections, a lip (max 2.5 mm) is present which may be either forward or backward-facing between each section. This causes the boundary layer to grow larger than expected compared to the simulation results. This will be discussed further in Section 4.

3.2.2 Physical/Optical Rakes and Other Measurements. As stated previously, safety monitoring measurements were taken using static pressure and strain gauge measurements at different locations as seen in Fig. 5.A. The static pressure measurements monitored the flow speed. The four static pressure taps in the OTS were placed at the same axial location and 90° degrees apart to measure the axisymmetry of the flow. It should be noted that strain gauges were placed along the high-speed inlet to monitor structural safety.

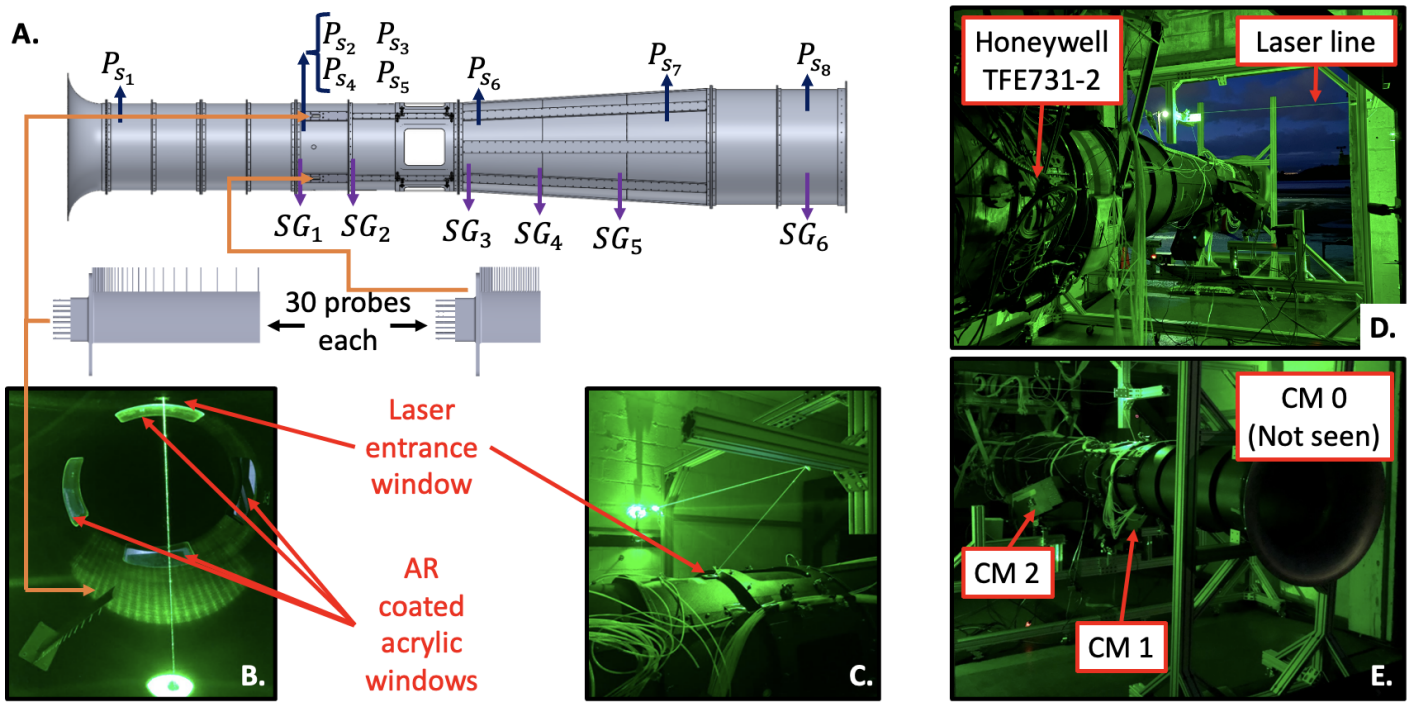

FIGURE 5: A: HIGH-SPEED INLET WITH ASSOCIATED STATIC PRESSURE AND STRAIN GAUGE MEASUREMENT LOCATIONS AS WELL AS THE TWO BOUNDARY LAYER PROBES. B: VIEW INSIDE THE OTS. C: VIEW OUTSIDE THE OTS. D: ENTIRE SETUP LOOKING FROM THE ENGINE UPSTREAM. E: ENTIRE SETUP LOOKING FROM THE BELLMOUTH DOWNSTREAM.

The two physical boundary layer probe rakes can be seen in Fig. 5.A. These rakes are custom-made boundary layer measurement rakes from Vectoflow [16]. They were manufactured with 3D-printed aluminum and each contain 30 total pressure probes. The total pressure probes are spaced such that near-wall measurements have a higher resolution than the tips of the rakes. The larger rake is approximately three times the size of the smaller rake. The rakes are sized such that the smaller rake is slightly taller than the edge of the boundary layer in the OTS. The larger rake reaches about halfway to the centerline of the OTS. Both rakes were used at the same time to characterize the boundary layer with high resolution. They were placed at the same axial location but 180° apart from each other.

The optical rake can be seen in Fig. 5.B as the green (532nm) laser line. The laser line passed through several test cells from the control room into the TFE731-2 test cell where it was redirected at an approximately 45° angle down into the OTS as been in Fig. 5.C. The angle was used to increase the spatial resolution of the FRS measurement inside the boundary layer. In other words, shooting the laser beam at an angle increases the distance that the laser travels through the boundary layer which means more pixels and thus more measurements in that region. This can only be done assuming that the boundary layer growth is negligible and that the freestream flow is constant. Given the results in Fig. 3, this is the case. It should be noted that the camera's field-of-view was from the centerline up to the laser entrance at the top of the OTS (more to come later). This was done to avoid the relatively intense background scattering caused by terminating the laser line at the bottom of the OTS. Figure 3.E and Fig. 3.F show the experimental setup in its entirety.

It is also worth noting that a total temperature probe rake was set up several feet upstream and laterally to the high-speed inlet. This rake was composed of six type K thermocouples placed approximately 30 0mm apart starting at the ground and ending at a height of approximately 1.5 m. This height extended beyond the height of the high-speed inlet. The results of this rake were averaged and are used in Section 4.

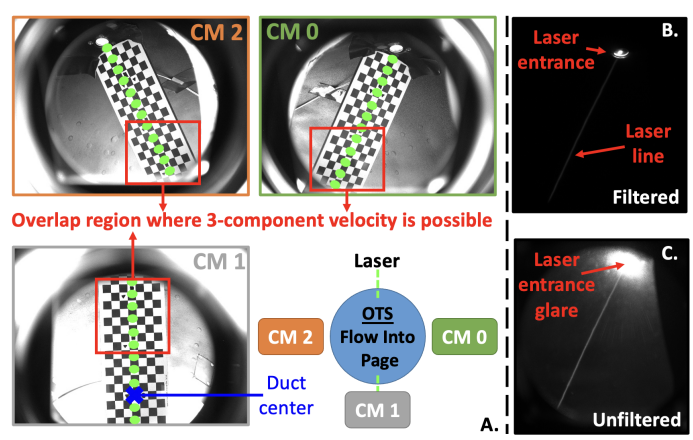

FIGURE 6: A: CAMERA MODULE (CAM MOD OR CM) LOCATIONS AND FIELDS-OF-VIEW. B: FILTERED IMAGE OF OPTICAL RAKE. C: UNFILTERED IMAGE OF OPTICAL RAKE.

Finally, Fig. 6.A shows the camera configuration around the OTS. Three camera modules were used, each containing two FLIR Blackfly BFS-U3-31S4 cameras. One camera viewed the laser line through the iodine vapor cell and is referred to as the fil-

tered camera (Fig. 6.B). The second camera did not look through the iodine vapor cell and is referred to as the unfiltered camera (Fig. 6.C). The path length of light was kept approximately constant between the two cameras. This is done so that the unfiltered camera can be used to normalize the intensity of the filtered camera. For more information see Powers et al. [11].

Camera module (CM) 0 was placed to the right of the OTS, CM 1 was directly below the OTS, and CM 2 was placed to the left of the OTS. The fourth redundant window at the top of the OTS was covered with black cloth to reduce the scattering of stray laser light. Figure 6.A shows example calibration images from each camera module. CM 0 and CM 2 were the only camera modules that could see the wall. CM 1 was tilted to get a view of the centerline. The red box region in each image is the region shared by all cameras' fields-of-view. This is the only region in which 3-component velocity measurements are possible. Static temperature, static density, and axial velocity measurements are possible throughout each region. It is also important to note that the results shown in Section 4 combine the results from each camera module into one "run" or data set. Three total runs were completed in this experiment; the results shown are from a 2 by 2 pixel averaged bin for an approximate signal-to-noise ratio (SNR) of 26. The pixel averaging results in a spatial resolution of approximately 0.75 mm by 0.75 mm.

4. FRS RESULT COMPARISON TO PROBE AND CFD RESULTS

The following subsections will first present non-binned results. The second subsection will present binned results which make use of the high spatial resolution of the FRS data to drive down the uncertainty in the final result. A statistical investigation will also be presented that examines the effect of different averaging schemes and the potential for introducing bias into the data set. It should be noted that the closest physical probe rake measurement to the wall was approximately 2.5 mm above the inlet wall compared to 4.5 mm for the FRS optical rake. The following figures will present and compare simulated data, physical probe rake data, and FRS optical rake data in the range of 2.5 mm to 300 mm from the wall, which extends just beyond the centerline of the inlet. Again, only data taken for the 75% CFS operating point will be shown which represents a centerline Mach number of approximately 0.45. All values were corrected to standard day conditions at sea level. All primary uncertainty values were calculated using Monte-Carlo simulations as shown in Powers et al. [11]. Spatial uncertainty was considered negligible as the camera calibration uncertainty stemming from the Caltech calibration algorithm [17] was approximately 0.1 pixels (0.05 mm) in any direction.

4.1 Non-Binned Results

Static and total values were measured/derived for temperature, pressure, and density along with 3-component velocity. In all charts, the black line represents the simulation data, the filled circles the physical probe rake data, and the hollow circles the FRS optical rake data. The red and cyan circles represent data from run 1, the green and yellow circles from run 2, and the blue and magenta circles from run 3. This holds for all figures.

Figure 7 shows the single-component axial velocity results. The axial velocity was determined by rotating the FRS-measured sensed velocity (velocity direction corresponding to the difference in the observation vector of the camera and the laser propagation vector) to the axial direction assuming that all of the sensed velocity is the result of pure axial velocity. This is approximately true given the results in Table 1. Figure 7.A has a linear scaling on the y-axis to see the majority of the data points outside of the boundary layer while Fig.7.B has a logarithmic y-axis scale for easier investigation of the data points inside the boundary layer. The axial velocity from the FRS optical rake was directly measured using equation Eq. 1 and has a 95% confidence uncertainty of $\pm 3\ m/s$. The axial velocity from the physical probe data was derived using Eqs. 2 through 4. Equation 2 uses the total pressure measurements from the physical probe rake and static pressure measurements made on the wall to calculate the Mach number. It is assumed that the static pressure is constant across the duct (proven later in Fig. 10). Equation 3 is used to calculate the static temperature across the duct using a total temperature probe measurement that was taken in ambient air upstream of the inlet. It is assumed that the total temperature is constant across the duct (proven later in Fig. 8). The probe-derived static temperature and Mach number are then used in Eq. 4 to derive the axial velocity of the flow.

$$\frac{P_{s_{wall}}}{P_{t_{probe}}} = \left(1 + \frac{\gamma+1}{2} M_{probe}^2\right)^{\frac{-\gamma}{\gamma-1}} \tag{2}$$

$$\frac{P_{s_{wall}}}{P_{t_{probe}}} = \left(\frac{T_{s_{probe}}}{T_{t_{probe}}}\right)^{\frac{\gamma}{\gamma-1}} \tag{3}$$

$$V_{probe} = M_{probe}\sqrt{\gamma R T_{s_{probe}}} \tag{4}$$

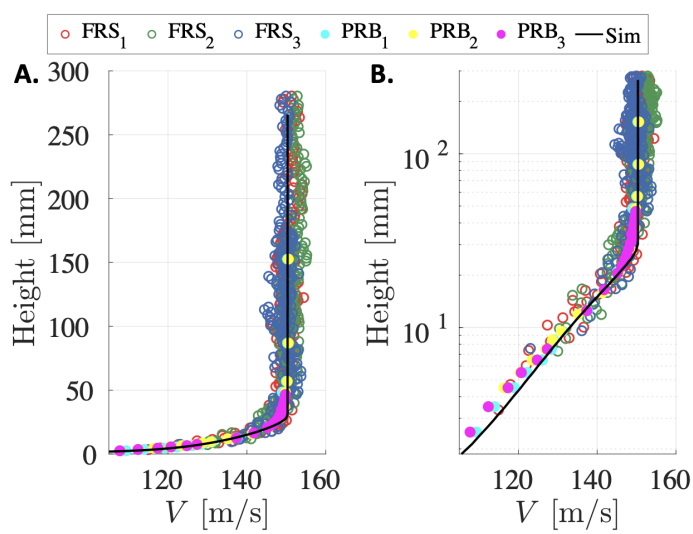

FIGURE 7: AXIAL VELOCITY COMPARISON BETWEEN ALL THREE TECHNIQUES. A: LINEAR Y-SCALE. B: LOG Y-SCALE.

The FRS optical rake measurements, physical probe rake measurements, and simulation data align well deep into the boundary layer. Compared to the simulation, the boundary layer

in the measured data is slightly thicker (δ_{Sim} = 29 mm, δ_{Probe} = 48 mm, and δ_{FRS} = 50 mm). This is due to the imperfect manufacturing as described previously. A disparity in the spatial resolution between probe rake data and FRS optical rake data is also apparent. The resolution of the physical probe rake data in the boundary layer (1 mm x 1 mm max) does not match that of the FRS optical rake data (0.75 mm x 0.75 mm). The difference in spatial resolution grows larger closer to the centerline. The highest probe measurement occurs around 150 mm while the last FRS measurement occurs near 280 mm. The spatial resolution advantage of the FRS data will be explored further in Section 4.2. Finally, the physical probe rake acquired data as close as 2.5 mm from the wall (limited by the rake's physical geometry), while the FRS optical rake data extended to within 4.5 mm from the wall. The FRS data was limited by the glare of the laser light on the entrance window. Future work will use a higher-pressure iodine cell to filter more of the scattered light to get closer to the wall.

Sensed velocity (direction corresponding to the difference in the observation vector and the laser propagation vector) or the velocity in which the FRS technique directly measured, was rotated back to three-component orthogonal components using a rotation matrix as defined by Cadel et al.[18]. However, it was only captured in the camera field-of-view overlap among all three camera modules as described in Fig. 6.A. The results of this can be seen in Table 1. The physical probe rake was incapable of measuring multi-component velocity and the simulation resulted in zero velocity for any non-axial velocity components outside the boundary layer. The values shown are the average values over the entire overlap region indicating near-zero velocity for non-axial velocity and axial velocity values matching Fig. 7. It should be noted that while multi-hole pressure probes could be used to validate the FRS optical rake values in Table 1, they were not used here due to the expected low in-plane velocity components.

TABLE 1: FRS 3-COMPONENT VELOCITY RESULTS WITHIN THE CAMERA MODULE FIELD-OF-VIEW OVERLAP REGION WITH APPROXIMATE 95% CONFIDENCE UNCERTAINTY BOUNDS.

Run	V_x [m/s] (+Right)	V_y [m/s] (+Up)	V_z [m/s] (Axial)
1	-0.04 ± 3.3	-0.99 ± 3.4	150.4 ± 4.2
2	-0.34 ± 3.3	0.75 ± 3.4	150.7 ± 4.2
3	0.29 ± 3.3	-0.60 ± 3.4	150.2 ± 4.2

Figure 8 shows the comparison between the FRS optical rake data and simulation data for static temperature (Fig. 8.A) and total temperature (Fig. 8.B). The FRS Mach number was found using Eq. 5 and the total temperature was found using Eq. 6.

$$M_{FRS} = \frac{V_{FRS}}{\sqrt{\gamma R T_{s_{FRS}}}} \tag{5}$$

$$T_{t_{FRS}} = T_{s_{FRS}} / \left(1 + \frac{\gamma + 1}{2} M_{FRS}^2\right)^{-1} \tag{6}$$

Physical probe rake data was not included in Fig. 8 since the rake did not directly measure temperature. The probe-measured total temperature in front of the inlet was approximately 288 K while the derived static temperature using Eq. 3 was approximately 276 K. These values align well with the values of the FRS optical rake (measured static values and derived total values) and simulation data outside the boundary layer. The simulation data shows a clear thermal boundary layer with a thickness of 32 mm ($\delta_{T_{Sim}}$). This compares well to the FRS optical rake derived thermal boundary layer thickness of 35 mm ($\delta_{T_{FRS}}$). The FRS thermal boundary layer was derived by averaging all runs together, conducting a 5 mm x 5 mm spatial averaging, and fitting a curve to the data. The 95% confidence uncertainty of the FRS static and temperature values is approximately ±6 K and ±7 K, respectively. The total value increases because of the uncertainty in the derived Mach number.

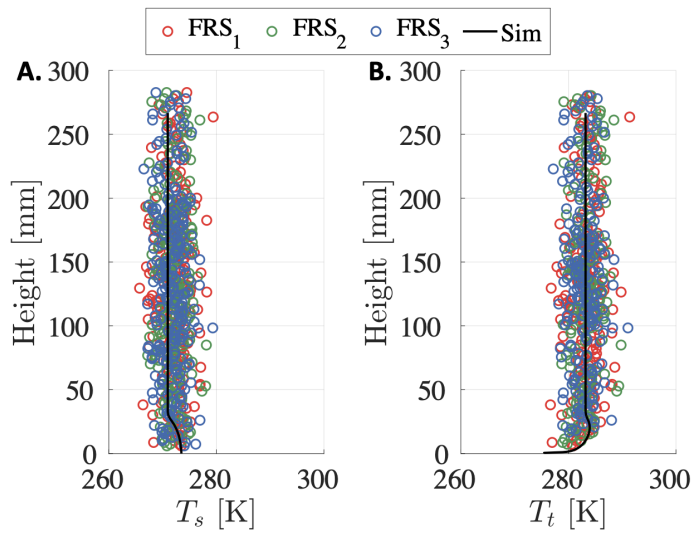

FIGURE 8: TEMPERATURE COMPARISON BETWEEN FRS AND CFD. A: STATIC TEMPERATURE. B: TOTAL TEMPERATURE.

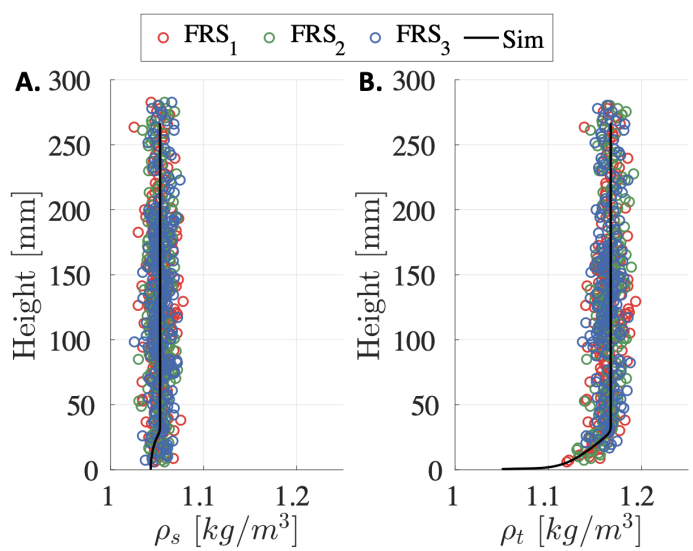

FIGURE 9: DENSITY COMPARISON BETWEEN FRS AND CFD. A: STATIC DENSITY. B: TOTAL DENSITY.

$$\rho_{t_{FRS}} = \rho_{s_{FRS}} / \left(1 + \frac{\gamma+1}{2} M_{FRS}^2\right)^{\frac{-1}{\gamma-1}} \tag{7}$$

Figure 9 shows the comparison between the FRS optical rake data and the simulation data for static density (Fig. 9.A) and total density (Fig. 9.B). The FRS optical rake total density was found using Eq. 7. Again, physical probe rake data was not included since the rake did not directly measure density. The physical probe-derived static density and total density were derived using the ideal gas equation and have values of 1.105 kg/m^3 and 1.225 kg/m^3, respectively which match well with the FRS optical rake and simulation data. The FRS optical rake and simulation data match well down into the boundary layer. The slight shift in static density within the boundary layer is not captured as well in the FRS optical rake data compared to the static temperature shift seen in Fig. 8.A. This is likely due to the static density 95% confidence uncertainty of ±0.02 kg/m^3 which is on the same order as the static density shift seen in the simulation. However, the total density shift is seen well in the FRS optical rake data where the FRS total density 95% confidence uncertainty is ±0.04 kg/m^3. Again, the total value increases because of the uncertainty in the derived Mach number.

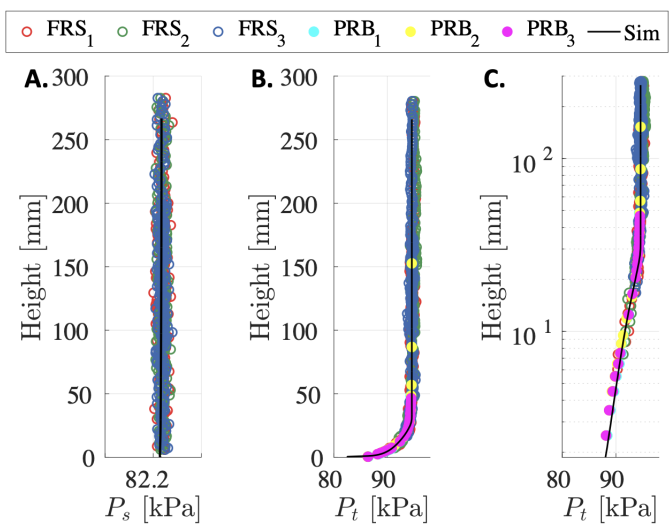

FIGURE 10: PRESSURE COMPARISON BETWEEN ALL THREE TECHNIQUES. A: STATIC PRESSURE. B: TOTAL PRESSURE W/ LINEAR Y-SCALE. C: TOTAL PRESSURE W/ LOG Y-SCALE.

Finally, Fig. 10 shows the comparison between all three data types for static pressure (Fig. 10.A) and total pressure (Fig. 10.B and Fig. 10.C). It is important to note that the FRS optical rake values have all been found using the ideal gas equation. No FRS optical rake static pressure or total pressure measurement was made directly. The total pressure physical probe rake measurements are direct measurements. The physical probe static pressure measurement was taken at the wall with a value of 87.9 kPa which was assumed constant across the entire duct. Similar to static density, the static pressure boundary layer dependence does not appear well in the FRS optical rake data. This is likely due to the very small magnitude shift where the FRS optical rake static pressure 95% confidence uncertainty of ±0.1 kPa is insufficient to resolve this feature. However, the total pressure curve is very well matched between all three techniques. As stated previously, the physical probe data extends closer to the wall at 2.5 mm while the closest FRS optical rake measurement was at 4.5 mm due to the severe glare on the glass entrance window located right at the wall. The 95% confidence uncertainty in the FRS optical rake total pressure measurements was approximately ±0.8 kPa.

Overall, the above results show that the FRS optical rake results are as good as the physical probe rake but offer benefits by not producing wakes or blockage. A summary of the uncertainties associated with each measurement can be seen in Table 2. The FRS optical rake has a distinct spatial resolution advantage over the more traditional physical probe rake albeit with higher uncertainty in individual measurements. The following subsection makes use of the high FRS spatial resolution through spatial averaging to decrease the uncertainty in the FRS optical rake measurement.

TABLE 2: UNCERTAINTY SUMMARY FOR ALL FRS OPTICAL RAKE MEASURED VARIABLES. 95% CONFIDENCE.

Type	V [m/s]	T [K]	ρ [kg/m^3]	P [kPa]
Static	±3	±6	±0.02	±0.1
Total		±7	±0.04	±0.8

4.2 Binning Statistics and Results

This subsection examines the effects of spatial binning on the FRS optical rake data and provides a more direct comparison to the physical probe rake data. The statistical analysis examines several averaging techniques and how those affect the randomness and bias of the resulting averaged data compared to the original, non-averaged data. A hybrid averaging technique is then applied to the original FRS data to match the spatial resolution of the physical probe rake data. The uncertainties are then compared.

4.2.1 Statistical Binning Effects. As previously stated, spatial averaging can be used along with the FRS optical rake data to decrease uncertainty. The uncertainty in each measurement scales with the inverse of the square root of N where N is the number of samples used to obtain the averaged point. However, this implies that the data being averaged are distributed randomly across the mean. If the data is not purely random, some averaging schemes will introduce bias into the final result. Therefore, the statistics of the original datasets must be known as well as the effects of different averaging schemes.

TABLE 3: DATASET STATISTICAL ANALYSIS RESULTS.

Scheme	$\overline{V}$ [$\frac{m}{s}$]	σ [$\frac{m}{s}$]	Skew	Kurt
Run 1	150.3	1.54	-0.08	3.11
Run 2	151.1	1.71	0.09	2.87
Run 3	149.7	1.60	-0.37	3.67

For this investigation, only data outside of the boundary layer was used as the mean in this region can be assumed constant. Table 3 shows the statistical analysis results. It can be seen that

runs 1 and 2 are approximately Gaussian while having non-zero skewness (positive to the left and negative to the right) and having slightly non-normal kurtosis (>3 means narrow and <3 means broader compared to a normal distribution). Run 3 is the farthest away from a normal distribution of all the runs and is skewed to the right while being more narrow than a normal distribution. Run 3 will be used for the averaging scheme analysis (and repeated in Table 4) as the effects of averaging will be much more apparent than in runs 1 and 2 since it is further from a normal distribution. In other words, if the data was perfectly normally distributed, averaging would not bias the final result.

Four averaging schemes were investigated. These included a moving average, 10 averaging bins, 20 averaging bins, and run averaging. The moving average used a sliding 10-point average in which 5 points each were averaged from below and above the data point. This technique retained the full original spatial resolution. The two bin-averaging schemes simply separated the data evenly into a different number of bins and averaged everything within that bin. This resulted in lower spatial resolution than the original data. The lower the number of bins, the lower the final spatial resolution. Finally, the run-averaging scheme simply averaged the three runs together to retain the same spatial resolution. Since all three runs had the same data point locations, no potential bias from the data point location is present in this data. The findings of this investigation can be seen in Table 4.

TABLE 4: AVERAGING SCHEME COMPARISONS. "SKEW" IS SKEWNESS. "KURT" IS KURTOSIS. "RES" IS RESOLUTION.

Scheme	$\overline{V}$ [$\frac{m}{s}$]	σ [$\frac{m}{s}$]	Skew	Kurt	Res [mm]
Run 3	149.7	1.60	-0.37	3.67	0.75 x 0.75
Mov. Ave.	149.5	0.62	-0.55	2.30	0.75 x 0.75
20 Bins	149.0	1.57	-0.05	2.23	10 x 0.75
10 Bins	148.9	2.92	-0.07	1.77	20 x 0.75
Run Ave.	150.2	0.85	-0.12	3.16	0.75 x 0.75

Table 4 shows that regardless of the averaging scheme, the average axial velocity changes only slightly. However, other values can change drastically. The standard deviation (σ) decreases with the 10-point moving average but increases drastically with a decreasing number of averaging bins. Averaging the three different runs together results in a standard deviation of approximately half that of the standard deviation of only run 3. The skewness of the data shows a large negative growth with the moving average but a large decrease in overall skewness with every other averaging scheme when compared to solely run 3. The kurtosis of the data is highly sensitive to the selection of averaging scheme. Each averaging scheme has a worse kurtosis compared to run 3 except for the case of averaging all three runs together. Overall, if the aim is to use an averaging scheme that preserves the randomness of the datasets and has the highest resolution, multiple datasets with matching data locations should be averaged together. In this case, averaging three runs together (dividing the uncertainty by $\sqrt{3}$) lead to 95% confidence uncertainty values of $\pm 1.7\ m/s$ for axial velocity, $\pm 3.5\ K$ for static temperature, and $\pm 0.01\ kg/m^3$ for static density. Therefore, assuming the run conditions are constant, more datasets drive the uncertainty down.

4.2.2 Spatial Binning Results. Now that the effects of the different averaging schemes are understood, a "hybrid" averaging scheme can be used to match the spatial resolution of the FRS data to that of the physical probe rake (see Fig. 11). The averaging schemes in the previous section only focused on the data outside of the boundary layer. Excessive averaging in the boundary layer will not be "shape-preserving". In other words, the boundary layer shape will not be conserved if averaged excessively. Run averaging is still the preferred method since it is also shape-preserving. However, this will not be used here to show the repeatability from run to run.

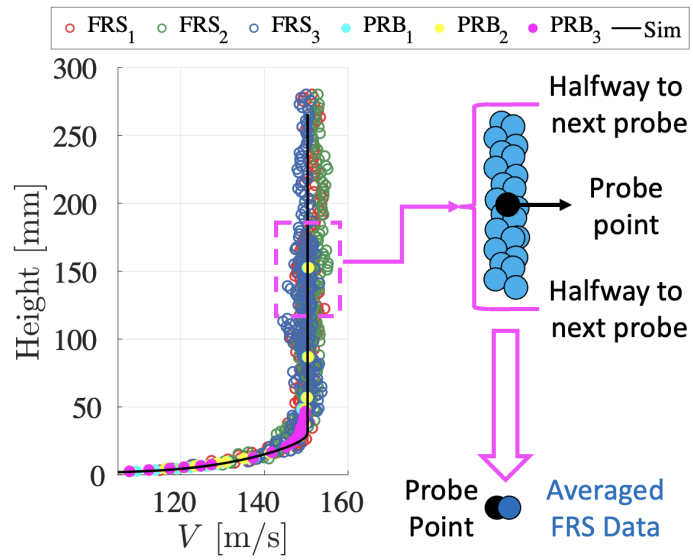

FIGURE 11: HYBRID SPATIAL AVERAGING SCHEME USING THE PHYSICAL PROBE DATA AS AVERAGING BIN BOUNDS.

Figure 11 shows the hybrid averaging scheme used. The physical probe points are used as center points for the FRS optical rake data averaging bins. There are approximately 40 unique bins that result from this technique. Each bin is a different size and therefore has a different resulting uncertainty. Because it uses the physical probe points as bin bounds (noting that more bins are used in the boundary layers seen in Fig. 5.A), this method is shape-preserving. Near the centerline of the duct, approximately 100 FRS data points are averaged, whereas, at the bottom of the boundary layer, just 2 are averaged.

Figure 12 compares the measurement of axial velocity from the FRS optical rake (direct) and the physical probe rake (derived). The maximum 95% confidence uncertainty in axial velocity for the FRS optical rake data occurs at the bottom of the boundary layer and is approximately $\pm 3.5\ m/s$. The minimum 95% confidence uncertainty in axial velocity for the FRS optical rake data occurs near the centerline of the duct and is approximately $\pm 0.3\ m/s$. The 95% confidence uncertainty for the physical probe data is relatively constant at approximately $\pm 0.2\ m/s$. Therefore, this hybrid averaging technique can result in FRS data that has approximately the same magnitude of uncertainty as the physical probe rake. Averaging the runs together would further drop the uncertainty. These uncertainty values show that the FRS technique cannot yet rival probe point measurement uncertainty. However,

the FRS technique has a vast advantage in spatial resolution.

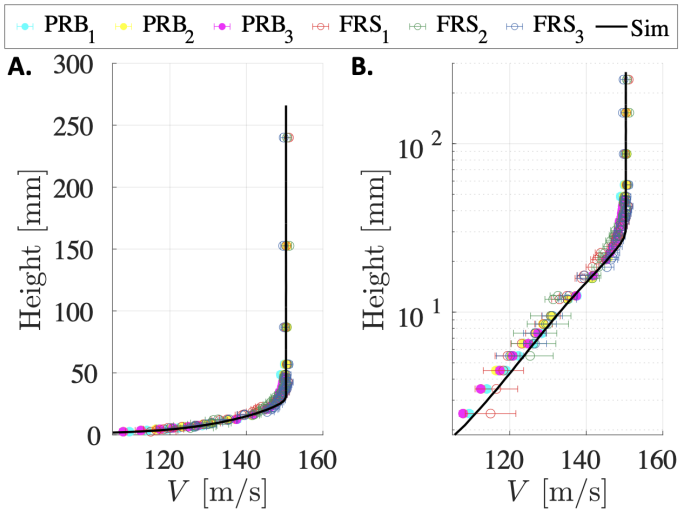

FIGURE 12: SPATIALLY AVERAGED FRS OPTICAL RAKE AXIAL VELOCITY FOR DIRECT COMPARISON W/ PHYSICAL PROBE DATA W/ 95% CONFIDENCE UNCERTAINTY BOUNDS. A: LINEAR Y-SCALE. B: LOG Y-SCALE.

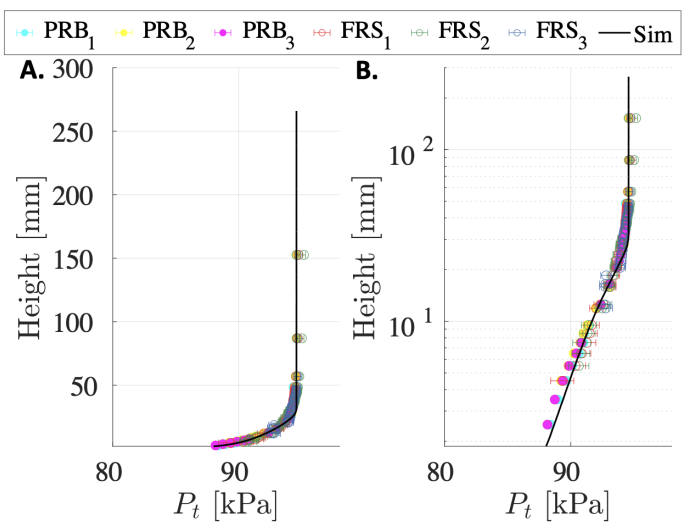

FIGURE 13: SPATIALLY AVERAGED FRS OPTICAL RAKE TOTAL PRESSURE FOR DIRECT COMPARISON W/ PHYSICAL PROBE DATA W/ 95% CONFIDENCE UNCERTAINTY BOUNDS. A: LINEAR Y-SCALE. B: LOG Y-SCALE.

Figure 13 compares the measurement of total pressure from the FRS optical rake (derived) and the physical probe rake (direct). Again, the maximum 95% confidence uncertainty in total pressure for the FRS optical rake data occurs at the bottom of the boundary layer and is approximately $\pm 0.06\ kPa$. The minimum 95% confidence uncertainty in total pressure for the FRS optical rake data occurs near the centerline of the duct and is approximately $\pm 0.81\ kPa$. The 95% confidence uncertainty for the physical probe data is relatively constant at approximately $\pm 0.05\ kPa$. Therefore, the averaging scheme still holds if the physical rake data is a direct measurement and the FRS optical rake data is a derived measurement. This is important as the FRS optical rake and physical probe rake offer varying direct and indirect measurement capabilities.

To combine all results into one, the inlet efficiency has been calculated and directly compared between the physical probe rake, the FRS optical rake, and the simulation using mass-averaged results. The results can be seen in Table 5 and were computed using Eq. 8 through 14. Equations 8 through 11 derive the basic inlet efficiency equations. Equation 8 describes the efficiency as the ratio between the average difference in isentropic enthalpy and the average difference in the actual enthalpy. The average is needed since these values change radially across the cross-section of the inlet. Equations 9 and 10 expand the numerator and denominator by writing the enthalpy in terms of the specific heat at constant pressure, temperature, and pressure. Equation 9 specifically transforms the isentropic total temperature ratio into the actual total pressure ratio such that the inlet efficiency can be rewritten in Eq. 11 in terms of measured values only.

TABLE 5: INLET EFFICIENCY COMPARISON OF ALL THREE TECHNIQUES USING MASS-AVERAGED DATA. 95% CONFIDENCE.

Run	Physical Rake	Optical Rake	Simulation
1	93.6% ± 0.16%	93.5% ± 0.44%	95.7%
2	93.5% ± 0.16%	93.4% ± 0.44%	95.7%
3	93.6% ± 0.16%	93.7% ± 0.44%	95.7%

$$\eta_i = \frac{\overline{h_{t_{OTS_s}} - h_a}}{\overline{h_{t_{OTS}} - h_a}} = \frac{\overline{H_{t_{OTS_s}} - H_a}}{\overline{H_{t_{OTS}} - H_a}} \tag{8}$$

$$\overline{H_{t_{OTS_s}} - H_a} = \frac{C_p}{T_a}\left(\frac{\overline{T_{t_{OTS_s}}}}{T_a} - 1\right) = \frac{C_p}{T_a}\left[\left(\frac{\overline{P_{t_{OTS}}}}{P_a}\right)^{\frac{\gamma-1}{\gamma}} - 1\right] \tag{9}$$

$$\overline{H_{t_{OTS}} - H_a} = C_p(\overline{T_{t_{OTS}}} - T_a) = \frac{C_p}{T_a}\left(\frac{\overline{T_{t_{OTS}}}}{T_a} - 1\right) \tag{10}$$

$$\eta_i = \frac{\frac{C_p}{T_a}\left[\left(\frac{\overline{P_{t_{OTS}}}}{P_a}\right)^{\frac{\gamma-1}{\gamma}} - 1\right]}{\frac{C_p}{T_a}\left(\frac{\overline{T_{t_{OTS}}}}{T_a} - 1\right)} = \frac{\left[\left(\frac{\overline{P_{t_{OTS}}}}{P_a}\right)^{\frac{\gamma-1}{\gamma}} - 1\right]}{\left(\frac{\overline{T_{t_{OTS}}}}{T_a} - 1\right)} \tag{11}$$

Equations 12 through 14 derive the mass-averaged inlet efficiency by assuming a perfectly circular cross-section and that the line of data accurately represents the entire plane. Equation 12 represents the mass averaging in integral form whereas Eq. 13 represents the summation form of the mass averaging technique while rotating the line of data around the circular inlet to complete the area. Finally, Eq. 14 represents the final form of the discrete mass-averaged inlet efficiency in percent.

$$\eta_i = \frac{\left[\left(\frac{P_{t_{OTS}}}{P_a}\right)^{\frac{\gamma-1}{\gamma}} - 1\right]}{\left(\frac{T_{t_{OTS}}}{T_a} - 1\right)} = \frac{\iint \rho V \frac{\left[\left(\frac{P_{t_{OTS}}}{P_a}\right)^{\frac{\gamma-1}{\gamma}} - 1\right]}{\left(\frac{T_{t_{OTS}}}{T_a} - 1\right)} dA}{\iint \rho V dA} \tag{12}$$

$$\eta_i = \frac{\pi \sum_{i=1}^{n-1} \rho_i V_i \left[\frac{\left(\frac{P_{t_{OTS_i}}}{P_a}\right)^{\frac{\gamma-1}{\gamma}} - 1}{\frac{T_{t_{OTS_i}}}{T_a} - 1}\right] r_i \left(r_{i+1} - r_i\right)}{\pi \sum_{i=1}^{n-1} \rho_i V_i r_i \left(r_{i+1} - r_i\right)} \tag{13}$$

$$\eta_i(\%) = \frac{\sum_{i=1}^{n-1} \rho_i V_i \left[\frac{\left(\frac{P_{t_{OTS_i}}}{P_a}\right)^{\frac{\gamma-1}{\gamma}} - 1}{\frac{T_{t_{OTS_i}}}{T_a} - 1}\right] r_i \left(r_{i+1} - r_i\right)}{\sum_{i=1}^{n-1} \rho_i V_i r_i \left(r_{i+1} - r_i\right)} * 100\% \tag{14}$$

Overall, the usefulness of the hybrid averaging scheme to reduce the uncertainty in each measurement while being shape-preserving has been shown. It can be used to produce FRS optical rake data that rivals the magnitude and uncertainty of traditional physical probe rakes in both direct and derived measurements. To drive the uncertainty down further, more datasets should be taken and then averaged together which would retain the FRS optical rake spatial resolution while matching the physical probe rake uncertainty. Finally, the inlet efficiency calculated by the three different techniques varies by approximately 2% regardless of the data set used. The CFD simulation resulted in higher efficiency values since the boundary layer was slightly smaller than the experimental boundary layer. The uncertainties of the experimental data were calculated using the propagation of uncertainty equation [19] and Eq. 14. This formulation has been omitted here for conciseness.

5. CONCLUSIONS

Overall, the FRS optical rake was shown to operate well in turbomachinery applications and provide high-quality data that would have been impossible with a physical probe rake all the while resulting in low error and uncertainty. The major conclusions from this work are as follows:

1. Physical probe rakes offer lower pointwise uncertainty (0.8% RMSE) compared to FRS optical rake measurements (2% RMSE).

2. The spatial resolution of the FRS optical rake can be used with bin averaging to decrease the uncertainty to levels comparable to physical probe rakes.

3. The information gained from precise measurements at a few locations (physical probe rake) cannot compete with approximately the same uncertainty measurement at many different locations (FRS optical rake). Especially since the FRS optical rake technique can be extended to planar measurements.

4. FRS optical rake data is approximately normally distributed. Spatial binning can lead to biasing away from a normal distribution. Run averaging should be used instead.

5. Mass-averaged inlet efficiency can be computed accurately with an FRS optical rake to within 0.1% of physical probe rake data.

6. An FRS optical rake can be used with confidence on non-ideal (vibration and sound) rigs such as turbine engines.

Note, the FRS optical technique has been validated over this specific application space. More work is needed to fully validate and optimize the technique over a large range of conditions and applications. However, the FRS technique is expected to perform similarly well in different conditions (e.g., in a compressor or turbine rig) as the uncertainties largely scale with signal-to-noise ratio and to a much lesser extent, flow conditions as described by Powers et al. [11].

ACKNOWLEDGMENTS

The authors wish to acknowledge the Science, Mathematics, and Research for Transformation (SMART) scholarship, the Aerospace and Ocean Engineering department at Virginia Tech, and Pratt & Whitney for supporting the authors in the development of the filtered Rayleigh scattering optical rake technique.

REFERENCES

[1] Bui, T., Oates, D. and Gonsalez, J. "Design and evaluation of a new boundary-layer rake for flight testing." *38th Aerospace Sciences Meeting and Exhibit* (2000)DOI 10.2514/6.2000-503.

[2] (2023). URL https://web.mit.edu/fluids-modules/www/exper_techniques/LDA.text.pdf.

[3] Lou, F., Harrison, H. M., Fabian, J. C., Key, N. L., James, D. K. and Srivastava, R. "Development of a centrifugal compressor facility for performance and Aeromechanics Research." *Volume 2D: Turbomachinery* (2016)DOI 10.1115/gt2016-56188.

[4] Chen, Zhongsheng, Sheng, Hao, Xia, Yemei, Wang, Weimin and He, Jing. "A comprehensive review on Blade Tip Timing-based health monitoring: Status and future." *Mechanical Systems and Signal Processing* Vol. 149 (2021): p. 107330. DOI 10.1016/j.ymssp.2020.107330.

[5] Williams, Owen J., Sahoo, Dipankar, Baumgartner, Mark L. and Smits, Alexander J. "Experiments on the structure and scaling of hypersonic turbulent boundary layers." *Journal of Fluid Mechanics* Vol. 834 (2017): p. 237–270. DOI 10.1017/jfm.2017.712.

[6] Doll, U., Dues, M., Bacci, T., Picchi, A., Stockhausen, G. and Willert, C. "Aero-thermal flow characterization downstream of an NGV cascade by five-hole probe and filtered Rayleigh scattering measurements." *Experiments in Fluids* Vol. 59 No. 10 (2018). DOI 10.1007/s00348-018-2607-z.

[7] Doll, U., Stockhausen, G. and Willert, C. "Endoscopic filtered Rayleigh scattering for the analysis of ducted gas flows." *Experiments in Fluids* Vol. 55 No. 3 (2014). DOI 10.1007/s00348-014-1690-z.

[8] Schroll, M., Doll, U., Stockhausen, G., Meier, U., Willert, C., Hassa, C. and Bagchi, I. "Flow Field Characterization at the outlet of a lean burn single sector combustor by laser-optical methods." *Volume 6: Ceramics; Controls, Diagnostics and Instrumentation; Education; Manufacturing Materials and Metallurgy* (2016)DOI 10.1115/gt2016-56365.

[9] Boyda, M. T., Byun, G., Saltzman, A. J. and Lowe, K. T. "Influence of mie and geometric scattering contributions on temperature and density measurements in filtered Rayleigh scattering." *AIAA Scitech 2020 Forum* (2020)DOI 10.2514/6.2020-1516.

[10] Saltzman, A. J., Boyda, M. T., Lowe, K. T. and Ng, W. "Filtered rayleigh scattering for velocity and temperature measurements of a heated supersonic jet with thermal non-uniformity." *25th AIAA/CEAS Aeroacoustics Conference* (2019)DOI 10.2514/6.2019-2677.

[11] Powers, S. W., Byun, G. and Lowe, K. T. "Auto-Processing of Filtered Rayleigh Scattering Images Including Mie and Background Scattering Contributions." *Experiments in Fluids* (2023)[Submitted].

[12] Warner, E. P. and Lowe, K. T. "Machine-Learned Background Quantification for Filtered Rayleigh Scattering Measurement Processing." *Submitted to AIAA SciTech 2023* (2023).

[13] "TFE731 turbofan engine." URL https://aerospace.honeywell.com/us/en/products-and-services/product/hardware-and-systems/engines/tfe731.

[14] Launder, B.E. and Spalding, D.B. "The numerical computation of turbulent flows." *Numerical Prediction of Flow, Heat Transfer, Turbulence and Combustion* (1983): p. 96–116DOI 10.1016/b978-0-08-030937-8.50016-7.

[15] Kannan, B. T., Karthikeyan, S. and Sundararaj, Senthilkumar. "Comparison of turbulence models in simulating axisymmetric jet flow." *Lecture Notes in Mechanical Engineering* (2016): p. 401–407DOI 10.1007/978-981-10-1771-1_43.

[16] "Vectoflow." URL https://www.vectoflow.de/en/.

[17] "Camera calibration toolbox for Matlab." (2023). URL https://doi.org/10.22002/D1.20164.

[18] Cadel, Daniel R. and Lowe, K. Todd. "Cross-correlation Doppler Global Velocimetry (CC-DGV)." *Optics and Lasers in Engineering* Vol. 71 (2015): p. 51–61. DOI 10.1016/j.optlaseng.2015.03.012.

[19] Witkovsky, V., Wimmer, G., Durisova, Z., Duris, S. and Palencar, R. "Brief overview of methods for measurement uncertainty analysis: Gum Uncertainty Framework, Monte Carlo method, characteristic function approach." *2017 11th International Conference on Measurement* (2017)DOI 10.23919/measurement.2017.7983530.

Chapter 5 - Control Volume Analysis for Experimental Force Accounting

The contents of this chapter will be submitted to the *AIAA Journal* (Sean Powers, Keaton Hanley, K. Todd Lowe, and Joseph Schetz. "Control Volume Analysis for Experimental Force Accounting"). No significant portions have been discussed outside of this manuscript.

The objective of this chapter is to provide evidence that a derived control volume combined with filtered Rayleigh scattering shows promise for in-flight force measurements. The techniques developed in this paper paved the path for force calculation and decomposition using control volume analysis around turbomachinery and address the knowledge gaps as discussed in subsection 2.3.2.

Control Volume Analysis for Experimental Force Accounting

Sean Powers *, Keaton Hanley†, K. Todd Lowe‡, and Joseph Schetz §
Virginia Polytechnic Institute and State University, Blacksburg, VA, 24060, United States

A control volume framework is derived to decompose forces produced by a turbofan with special considerations for application to experimental measurements. The rich history of aerodynamic force decomposition is reviewed and compared. The parallel expanded streamtube method (PES) of Drela was chosen as the best fit for application to experimental data as it allows for realistic measurement types and locations, especially for optical methods. The PES method is then extended using a combination of the Townsend criterion and Prandtl's turbulent mixing length model to decompose the exhaust stream into the core and bypass flow of a turbofan engine. The uncertainty of this methodology including random error, bias error, and control volume error is derived using the propagation of uncertainty technique. Finally, a simple simulated data set is used to test the extended PES method (EPES) as well as compute the uncertainty given known random, bias, and CV uncertainty. The total error is then presented along with the error influence coefficients assuming uncertain variables of axial velocity, specific heat ratio, specific gas constant, static temperature, static density, freestream static pressure, freestream velocity, and measurement area. The largest sources of uncertainty were found to be static temperature and density. A comparison paper to this presents the application of the new method to experimental measurements on a Honeywell TFE731-2 turbofan engine.

Nomenclature

A	=	bin area in m^2
CV	=	control volume
EIC	=	error influence coefficient in N^2
$EPES$	=	extended parallel expanded streamtube method
$\mathcal{F}$	=	force in N

*SMART Fellow, Kevin T. Crofton Department of Aerospace and Ocean Engineering, 460 Old Turner St, Blacksburg, VA 24060, AIAA Student Member.

†Graduate Research Assistant, Kevin T. Crofton Department of Aerospace and Ocean Engineering, 460 Old Turner St, Blacksburg, VA 24060, AIAA Student Member.

‡Professor, Kevin T. Crofton Department of Aerospace and Ocean Engineering, 460 Old Turner St, Blacksburg, VA 24060, and AIAA Associate Fellow.

§Fred D. Durham Endowed Chair Emeritus, Kevin T. Crofton Department of Aerospace and Ocean Engineering, 460 Old Turner St, Blacksburg, VA 24060, and AIAA Life Fellow.

h	=	enthalpy in J/kg
ℓ	=	length in m
$\dot{m}$	=	mass flow rate in kg/s
N	=	number of bins
PES	=	parallel expanded streamtube method
p	=	pressure in Pa
S	=	control volume surface
T	=	Temperature in K
U	=	axial velocity in m/s
$\overline{V}$	=	expanded velocity in m/s
γ	=	specific heat ratio
δ	=	uncertainty
∇	=	gradient
ρ	=	density in kg/m^3
τ	=	shear stress in Pa
$\mathcal{X}$	=	uncertainty variable placeholder
ψ	=	squared velocity gradient in m^2/s^2

Superscripts

$-$	=	expanded value or mean
$'$	=	fluctuating value

Subscripts

B	=	bypass or bias
C	=	core
R	=	random
s	=	static
t	=	total or turbulent
TP	=	Trefftz plane
x	=	x-direction
y	=	y-direction
∞	=	freestream

I. Introduction

Aerodynamic force decomposition has a rich history that considers a wide range of topics such as airframe/engine interactions, surface properties, and measurement capabilities. These considerations have been addressed in many different techniques using numerous assumptions. Drela [1, 2] gives an overview of such techniques. Figure 1 gives an overview of techniques used throughout history. Each milestone (numbers) relaxed the required assumptions and expanded the capability of what could be calculated.

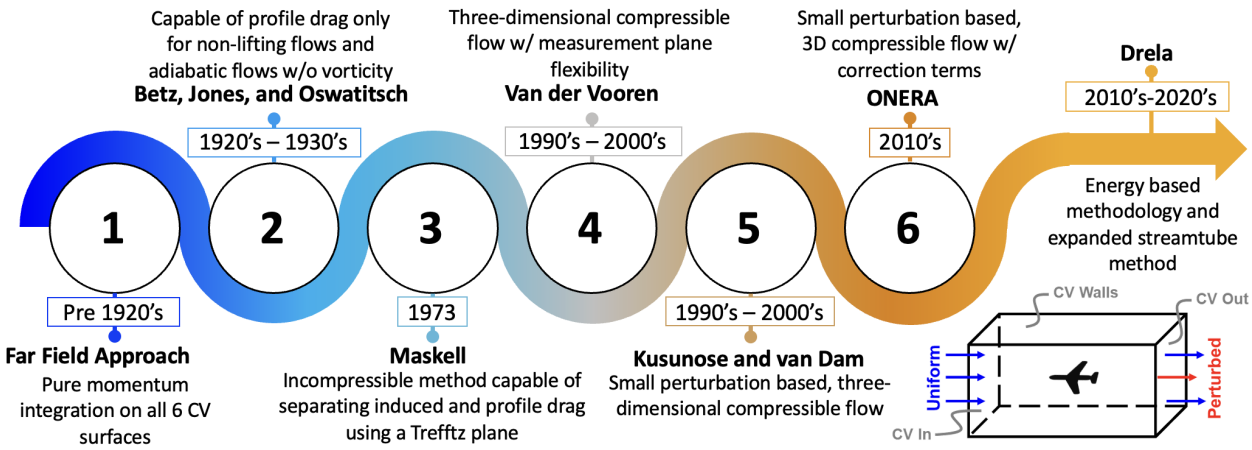

Fig. 1 Overview of aerodynamic force decomposition methods throughout history. An example six-sided control volume is included in the bottom right.

The far-field approach outlined in Méheut et al. [3] is the simplest control volume approach, and it is directly comparable to the balance measurements that can be determined inside a wind tunnel. It is based on the integration of the momentum equation inside a closed volume, however only the total drag can be found. Simplifications to the far-field approach were undertaken by Betz et al. [4], Jones et al. [5], and Oswatitsch et al. [6], which allow for simple drag calculations in non-lifting flows and adiabatic flows without vorticity. Maskell et al. [7] introduced the general incompressible method capable of separating parasite and induced drag into distinct components using a Trefftz plane. The Trefftz plane is located far downstream such that motion by trailing vortices becomes 2D with no induced velocity in the axial direction [8].

The Van der Vooren formulation [9, 10] builds on the work by Maskell et al. to deal with three-dimensional, compressible flow. It uses only a wake survey and the assumption that the flow is isentropic and adiabatic from the wake survey plane location to the Trefftz plane. However, the Van der Vooren method can only be used when the entire flow field stagnation pressure remains higher than the upstream static pressure. The Kusunose [11] and Van Dam [12] methods, based on the small-perturbation assumption, can be used to get around this. Méheut et al. [3] compared all the previous control volume methods to their methods called the ONERA formulations [13, 14]. Upon comparison with numerical simulations, the various force methods led to different results.

This development continues today with Drela's work using energy-based methods [1] and the introduction of the

parallel expanded streamtube (PES) method [2]. This method takes inspiration from many of the major milestones listed, but it makes specific use of Jones's incompressible formulation [5]. However, PES can be used with both incompressible and compressible flows using ideas from Young et al. [15].

The current work focuses on turbomachinery applications, specifically, turbofan engines. A control volume methodology for force decomposition on turbomachinery can to reduce the complexity of current industry standards which can be seen in many SAE AIR standards documents[16–21]. The industry-standard methodology relies on a large number of probe measurements, empirical models, and assumptions to calculate the thrust of an engine on the ground and then correlate that to in-flight thrust. No methodology exists that can measure in-flight thrust let alone force decomposition such as thrust and drag components. This has been done on a "small scale" [17, 22] where probe rakes were used, however, this was far from creating a new industry standard.

Our work aims to extend Drela's PES method by providing the framework to separate forces in the exhaust of a turbofan engine to core and bypass flow contributions. Derivation of the framework gives special consideration to realistic measurement capabilities such as optical methods and probe rakes.

Section II details the existing control volume techniques and the extension of the PES method. Section III provides the derivation for the uncertainty equations including random, bias, and control volume uncertainty. Section IV describes the simple simulation of a turbofan engine and examines the force results as well as the uncertainty results. Section V provides conclusions and future directions.

II. Control Volume Techniques and Current Extension

A. Technique Selection

Near-field techniques such as the "Near-field force and decomposition" method (see Fig. 2.A) and the "Alternative near-field force decomposition" method (see Fig. 2.B) draw the control volume on the surface of the entire body being considered. The "Near-field force and decomposition" method calculates the resulting force based on the net result of the pressure and viscous forces acting on the body surface. In the "Alternative near-field force decomposition" momentum flux is allowed through the propulsor. This means the control volume is drawn on the inlet and outlet instead of on the machinery components. This difference makes the "Alternative near-field force decomposition" easier to use. Both of the near-field techniques apply to computational fluid dynamics (CFD) simulations, but they are impractical for experimental applications since the values for friction and pressure must be known at every point on the body surface.

The far-field technique presented as the "far-field force" method, uses the integral momentum theorem with a control volume that looks like the one seen in the bottom right of Fig. 1 and 2D format in Fig. 2.C. The momentum flux through all six control volume surfaces must be known to calculate force correctly. While difficult, this can be done by constraining the body in a wind tunnel, for example. The wind tunnel will only have an inlet and outlet surface on which

momentum is allowed to flow. However, the outlet plane must be located at the Trefftz plane. These requirements make experimental application of the "far-field force" technique outside of a wind tunnel difficult.

A hybrid near- and far-field technique known as the "Hybrid near-field/far-field streamwise force" method (see Fig. 2.D) combines a far-field approach to the inlet side of the control volume and a near-field approach to the exhaust. Many assumptions are needed, but the biggest in terms of experimental application is that the streamtubes of each force contribution must be known from the inlet to the outlet. This is difficult to know in an experimental application.

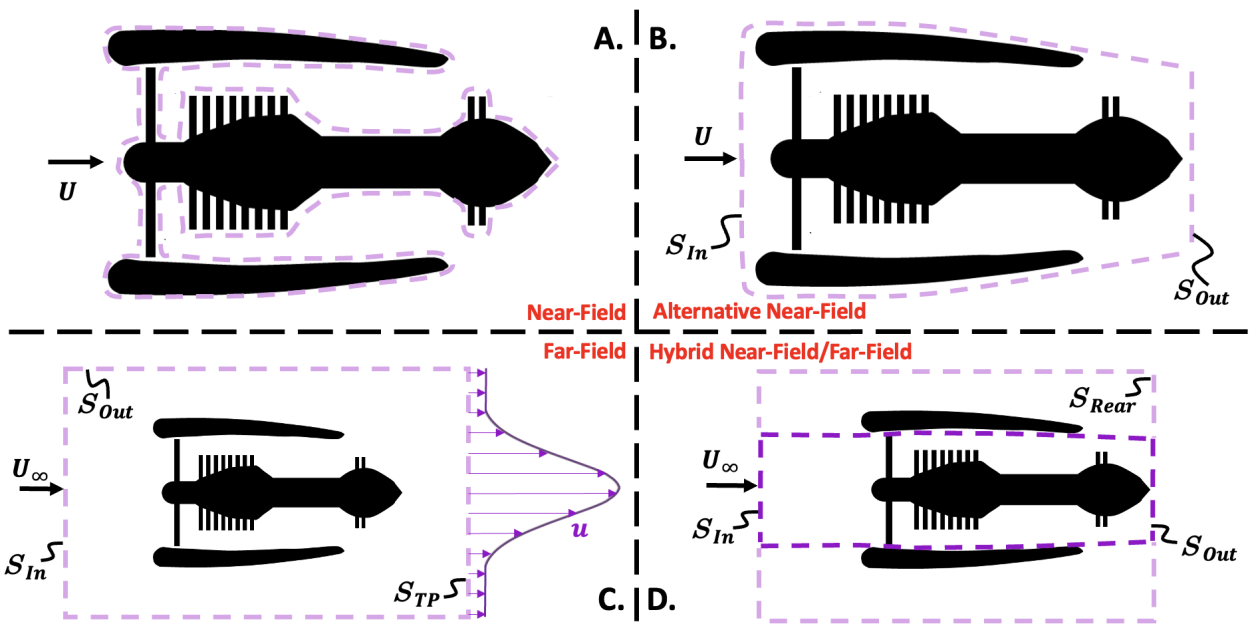

Fig. 2 Force decomposition methods. A: Near-field. B: Alternative near-field. C: Far-field. D: Hybrid near-field/far-field. Core cowling was removed for clarity. Reworked from Drela [2].

All methods so far have one thing in common, they are difficult to implement in an experiment outside of highly controlled environments. Therefore, Drela [2] derived the parallel expanded streamtube (PES) method which estimates the thrust of propulsive elements and the profile drag of the airframe elements by investigating the streamwise momentum in the Trefftz plane. However, to get around having to make measurements at the Trefftz plane, mass-conservation is used to produce $\overline{V}$ which is the "expanded" speed that a streamtube would have after it flows from the measurement plane to the expanded state at the Trefftz plane. The compressible $\overline{V}$ equation is shown in Eq. 1.

$$\overline{V}(p_t, h_t) = \sqrt{2h_t\left[1 - \left(\frac{p_\infty}{p_t}\right)^{\frac{\gamma-1}{\gamma}}\right]} \tag{1}$$

The PES method does not consider transverse velocities that would lead to induced drag and assumes that the streamtube from the local measurement plane to the Trefftz plane is isentropic such that the total pressure and specific enthalpy at the Trefftz plane and the local plane are the same. The Trefftz plane is taken to be at the freestream pressure. The control volume for the PES method as it pertains to turbofans can be seen in Fig. 3. It will be assumed that all

streamtubes exit through the Trefftz plane at the back and not through the sides of the control volume. As drawn for the simplified case, the engine will be massless and self-propelling to keep the control volume simple.

Drela defines the bounds of the streamtube by taking the S_{Out} plane to be right at the nozzle exit. Therefore, no mixing has occurred and the streamtube can be defined everywhere in the control volume due to mass conservation. However, in our work, as shown in Fig. 3, the S_{Out} plane is not located at the exit of the nozzle, so mixing has occurred. The combination of mixing and only one measurement plane makes it difficult to define a streamtube rigorously. If instead, the exhaust plume boundary is thought of as a boundary layer, a plume edge can be defined using the velocity profile and the freestream velocity. This plume boundary method then defines the purple dashed lines in Fig. 3 instead of defined by a streamtube.

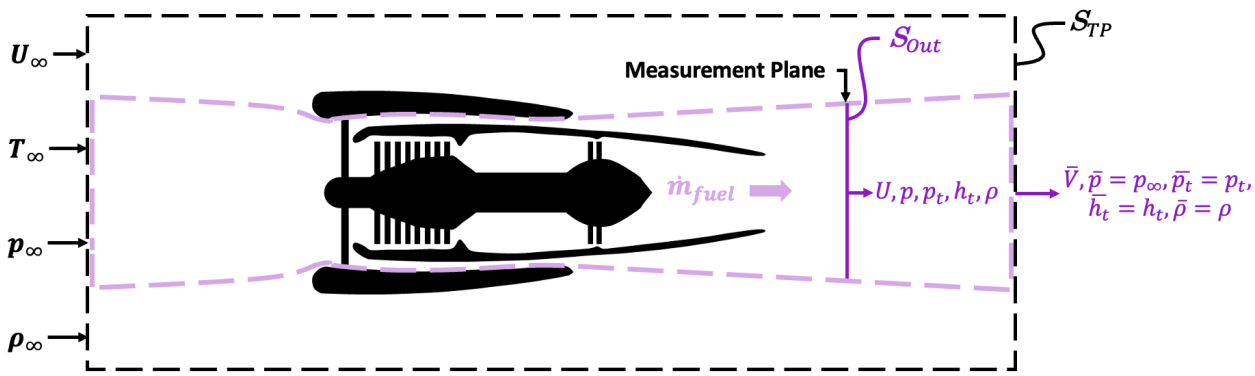

Fig. 3 Modified parallel expanded streamtube method applied to a turbofan engine where the bounds are defined by the exhaust plume edge instead of a mass-conserving streamtube. Exhaust expansion is exaggerated and is due to the growth of entrained freestream flow.

The final PES force equation is Eq. 2 where the sign will be positive for force-producing streams and negative for drag-producing streams. Due to the assumptions, the PES method breaks down in certain flow regimes with significant mixing and stagnation pressure losses as well as wall boundary layers which result in $\overline{V}$ becoming negative. However, typical propulsors have $p > p_\infty$ so this problem rarely emerges [2].

$$\mathcal{F}_{PES} \equiv \iint \left(\overline{V} - U_\infty\right) \rho U dS_{Out} + \dot{m}_{fuel} U_\infty \tag{2}$$

To simplify things further, the present work will focus only on total force components relating to a turbofan engine in free space. This means no consideration is given to the drag arising from the flow around the nacelle, the drag from the boundary layers on the nozzle components, or the structural components connecting the engine to the wing via a pylon. This has been left for future work.

B. Extended PES Method

The PES method allows for local exhaust planes to be measured and expanded back to the Trefftz plane, however, no guidelines have been previously published that describe how to draw the control volumes such that the forces in the exhaust of a turbofan may be decomposed into core and bypass forces as indicated by Fig. 4. The downstream core control surface is indicated by a vertical red line and is labeled as S_{Out_C}, while the bypass control surface is indicated by the blue vertical lines and is labeled as S_{Out_B}. These control surfaces have been drawn downstream at the same plane labeled as "measurement plane". Again, these values may be expanded to the Trefftz plane using the original PES method. The horizontal dashed lines denote the separation between each flow stream. See Fig. 5.

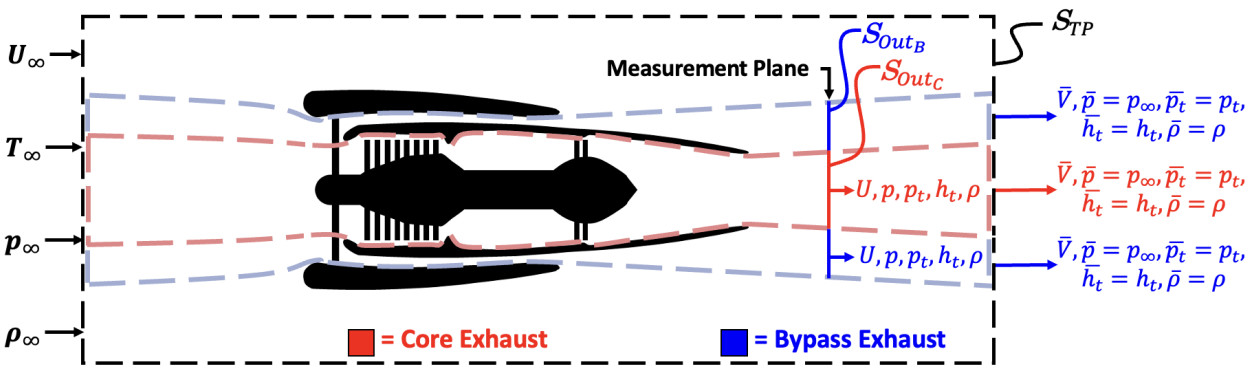

Fig. 4 Extended parallel expanded streamtube method control volumes where the exhaust stream has been decomposed into core and bypass streams. Exhaust expansion is exaggerated and is due to the growth of entrained freestream flow.

Figure 5 describes that a dividing streamsurface can be defined between the core and bypass flow. Townsend [23] observed that the maximum shear stress inside a constant pressure shear layer occurs approximately on the dividing streamsurface, and that has been used by Grazzini et al. [24]. This works well in subsonic flows but not in supersonic flows. The dividing streamsurface is defined here as one that divides two exhaust flow streams having the bypass flow stream above this surface and the core flow stream below this surface as depicted in Fig. 5. The location of the maximum shear stress is difficult to measure in a turbulent flow such as these mixing layers in practical situations. But, a turbulent mixing length model can be used to infer the location of the maximum shear stress at the location of the maximum velocity gradient.

Most all turbulence models represent turbulent stresses as proportional to the transverse gradient of the mean velocity. A simple example is the classic mixing length model for turbulent shear stress is shown in Eq. 3 [25], and it has been rewritten here with consideration for 2D planar data. This type of model assumes that the mixing length (ℓ_m) is not affected by wall effects and is constant in shear layers and the outer regions of boundary layer flow. While the turbulent shear stress can be approximated by measuring the density and mixing length ($\ell_m = 0.09\delta$ for mixing layers), the velocity gradient will dominate in high-gradient regions. Therefore, it can be assumed that the maximum shear stress location will be at the maximum velocity gradient location, and by applying the Townsend approximation, that

will locate the dividing streamsurface. To increase the difference to allow implementation into computer algorithms the square of the velocity gradient will be used here. These ideas are extended from the work of Grazzini et al. [24].

$$\tau_t(1D) = -\rho\overline{u'v'} = \rho\ell_m^2\left|\frac{\partial U}{\partial y}\right|\frac{\partial U}{\partial y} \rightarrow \nabla U(2D) = \sqrt{\left(\frac{\partial U}{\partial x}\right)^2 + \left(\frac{\partial U}{\partial y}\right)^2} \rightarrow \tau_t(2D) = \rho\ell_m^2(\nabla U)^2 \tag{3}$$

Note that the dividing streamsurface between the core and bypass must be used to divide the flows. However, the surface between the bypass and freestream will not be used as discussed in Subsection II.A. This can be explained by examining Eq. 2, where any force resulting below the dividing surface of the bypass and freestream (as depicted in Fig. 5) must be from the flow entrained by the bypass flow. Therefore, this force belongs to the bypass stream. Consequently, the boundary between the bypass and freestream is defined as the exhaust plume boundary. However, Eq. 2 includes the $\overline{V} - U_\infty$ term which subtracts the momentum from the freestream. Therefore, any freestream flow bounded inside the control volume will not have any force effect. This means that the plume boundary is not needed in a case like the one shown in Fig. 5 which simplifies the overall analysis. This kind of methodology can also be used to determine the approximate size of the mixing layer and quantify the amount of entrained air.

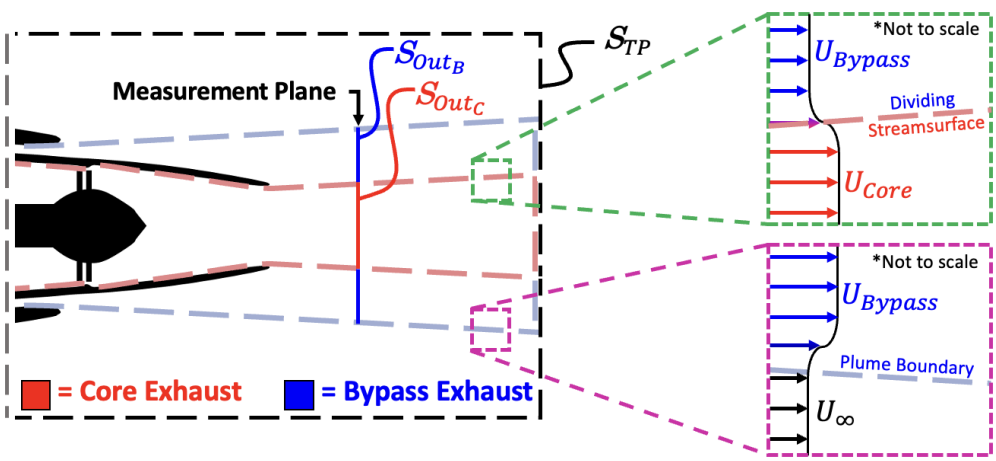

Fig. 5 Dividing streamsurface separating the core and bypass flow as well as the exhaust plume boundary dividing the bypass and freestream flow. Exhaust expansion is exaggerated and is due to the growth of entrained freestream flow.

In more complex scenarios, such as thrust and drag stream accounting, the dividing streamline approach would be needed to separate the additional flow streams. Accounting for the momentum transfer across the dividing streamline also becomes important. For the current work of force accounting and flow stream separation, the momentum transfer has been assumed negligible (in-plane velocity components are not considered). Future work will investigate this.

Now that the assumptions and control volumes have been presented, the final force equations can be written for the extended PES method which will be called the Extended PES (EPES) method. The integral force equations have been transformed into summations which is useful for discrete data such as that from experimentation. The total force equation can be seen in Eq. 4 which has three summations. Two of the summations sum over the x-direction and

y-direction, respectively. The third summation sums over the number of streams. In this simplified case, those streams will just be the core and bypass streams. However, this can be easily extended to include other streams.

$$\mathcal{F}_{EPES} = \sum_{k=1}^{N_{Streams}} \sum_{l=1}^{N_{x_k}} \sum_{m=1}^{N_{y_k}} \left[\rho_{s_{(l,m,k)}} \left(\overline{V}_{(l,m,k)} - U_\infty \right) U_{(l,m,k)} A_{(l,m,k)} \right] + \dot{m}_{fuel} U_\infty \tag{4}$$

III. Uncertainty Derivation

To complete the EPES method framework, the uncertainty in the derived forces must be estimated. This uncertainty consists of three major sources which can be seen in Fig. 6. The first is random uncertainty, which assumes that the variation in the data is distributed normally (Gaussian) around the mean. Figure 6.A visually shows this where the data is normally distributed between -1 and 1 with a mean of 0. The second uncertainty source is bias uncertainty, as shown in Fig. 6.B where the random uncertainty from the left chart has been bulk-shifted up by 0.25. Therefore, the mean has also shifted up by 0.25. This means that with the bias present, the measured mean is now significantly different than the known, unbiased mean. Finally, since the EPES method is a control volume method, uncertainty in the control volume boundaries exists. This is shown in Fig. 6.C where the nominal boundary is shown in solid black. However, the true boundary could be an expansion or contraction of the nominal. The control volume uncertainty will only impact the separation of the exhaust stream into core and bypass streams. No control volume uncertainty will exist in the total force calculation (for this simple example), since total force can be found without separating the exhaust components.

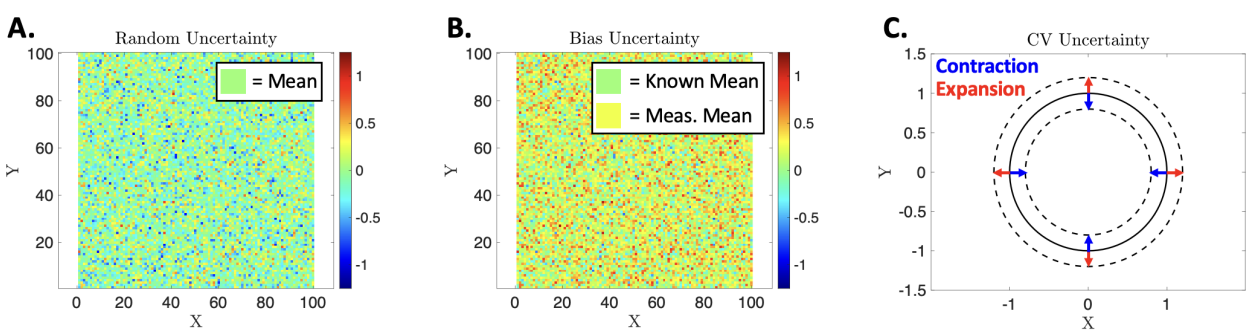

Fig. 6 Visuals for uncertainty sources. A: Planar random uncertainty. A Gaussian distribution between -1 and 1. B: Planar bias uncertainty. C: Control volume uncertainty.

The following subsections derive the analytic uncertainty equations using the propagation of errors formulation from Bendat and Piersol [26]. Finally, we combine all of the uncertainty sources into one final uncertainty equation.

Eight variables are assumed to be uncertain: static density, axial velocity, static temperature, specific heat ratio, specific gas constant, freestream static pressure, freestream velocity, and measurement area/resolution. These variables are assumed to be independent of one another such that the covariance is zero.

A. Random Uncertainty

The random uncertainty is defined by assuming a Gaussian distribution around the mean of the examined data. This random uncertainty implementation is shown in Eq. 5 and Eq. 6. Notice that the k summation only goes to the total number of streams (inlet and exhaust streams). The next two summations are in the x and y directions along each plane. These equations are written generally such that the random error in each bin may be different.

$$\delta_R \mathcal{F}_{EPES} = \sqrt{\sum_{k=1}^{N_{Streams}} \left[\frac{1}{N_{x_k} * N_{y_k}} \sum_{i=1}^{N_{x_k}} \sum_{j=1}^{N_{y_k}} \left(\delta_R \mathcal{F}^2_{EPES_{Bin_{(i,j,k)}}} \right) \right]} \tag{5}$$

$$\begin{aligned} \delta_R \mathcal{F}^2_{EPES_{Bin_{(i,j,k)}}} = & \left| \frac{\partial \mathcal{F}_{EPES}}{\partial \rho_s}^2 \right| \delta_R \rho^2_{s_{(i,j,k)}} + \left| \frac{\partial \mathcal{F}_{EPES}}{\partial U}^2 \right| \delta_R U^2_{(i,j,k)} + \left| \frac{\partial \mathcal{F}_{EPES}}{\partial T_s}^2 \right| \delta_R T^2_{s_{(i,j,k)}} + \left| \frac{\partial \mathcal{F}_{EPES}}{\partial P_{s_\infty}}^2 \right| \delta_R P^2_{s_{\infty(i,j,k)}} \\ & \ldots + \left| \frac{\partial \mathcal{F}_{EPES}}{\partial U_\infty}^2 \right| \delta_R U^2_{\infty(i,j,k)} + \left| \frac{\partial \mathcal{F}_{EPES}}{\partial \gamma}^2 \right| \delta_R \gamma^2_{(i,j,k)} + \left| \frac{\partial \mathcal{F}_{EPES}}{\partial R}^2 \right| \delta_R R^2_{(i,j,k)} + \left| \frac{\partial \mathcal{F}_{EPES}}{\partial A}^2 \right| \delta_R A^2_{(i,j,k)} \end{aligned} \tag{6}$$

Equation 6 shows that the partial differential equation is taken with respect to each uncertain variable and then multiplied by its standard deviation in that particular bin. The squares of this product are then added together to form the final total random uncertainty. The final standard deviation of the bin random uncertainty is the square root of the sum of the squares. This is extended in Eq. 5 where the bin uncertainties are summed under the square root to compute the final total force uncertainty in the entire plane. The more bins that can be used, the lower the random uncertainty will be.

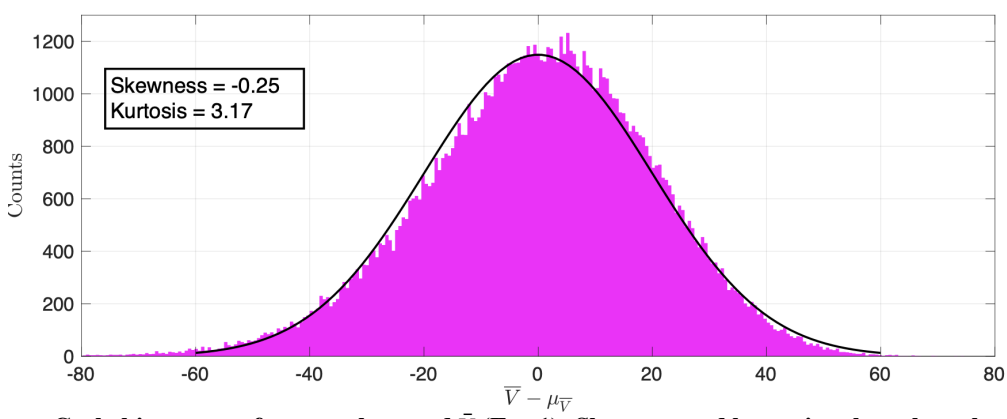

Fig. 7 Monte Carlo histogram of mean subtracted $\bar{V}$ (Eq. 1). Skewness and kurtosis values show the non-normal distribution of this equation. The black line plotted is a normal distribution for reference. The numbers used are from the simple simulation which is discussed later.

An important deficiency in employing the propagation of errors is that it assumes linearity by the Taylor series expansion. However, in the EPES method, Eq. 1 is a nonlinear, asymptotic function. Nonlinear functions of normally distributed parameters can give biased results, as seen in Box [27]. This was observed in a validation study between Monte Carlo simulations of EPES and the propagation of errors presented here. A Monte Carlo histogram of mean

subtracted $\bar{V}$ is shown in Fig. 7 which uses values from a simple simulation. The distribution is non-normal with right skewness. The propagation of uncertainty methodology is insufficient in capturing this behavior, but it can still closely predict the dispersion of the non-normal output distribution. Propagation of errors was chosen here due to its ease of implementation, its ability to perform quick sensitivity studies for design space applications, and a close approximation of the true 95% confidence interval. A Monte Carlo simulation was performed on the data seen in Fig. 7 which resulted in a difference of less than 0.5%. For more accurate assessments of the random uncertainty, the authors recommend Monte Carlo simulations or the methods in Witkovský et al. [28].

B. Bias Uncertainty

It is accepted practice to correct for a measurement bias before a measurement is taken, however, correcting for a bias in some measurements can be difficult and/or expensive. Therefore, an uncertainty framework must include bias uncertainty. The SUMU (algebraically sums the signed bias with the expanded uncertainty) method from Phillip et al. [29] was employed as Eq. 7. The SUMU method states that the confidence interval (Sig = 1.96 for 95%) only applies to the random uncertainty. The bias uncertainty is just an addition to that confidence interval. This means that the final 95% confidence interval can be asymmetric.

$$\mathcal{M}eas_{Error} = Meas_{NoError} \begin{cases} +Unc_{+} = +Sig * \delta Meas_{Rand} + \delta Meas_{Bias+} \\ +Unc_{+} = +Sig * \delta Meas_{Rand} + \delta Meas_{Bias-} \end{cases} \tag{7}$$

The positive bias equations can be seen in Eq. 8 and Eq. 9. The negative bias is the same as the positive bias but the primary bias values (δ_B) are all negative. So, Eq. 8 will have a negative sign. The propagation of errors equation for the bias uncertainty is very similar to the random uncertainty (Eq. 5). However, the random uncertainty is now a positive or negative bias uncertainty. The $1/\sqrt{N_{x_k} * N_{y_k}}$ reduction in uncertainty seen in the random equations is no longer in the bias equations so no amount of averaging will reduce that error.

$$\delta_{B+}\mathcal{F}_{EPES} = \sqrt{\sum_{k=1}^{N_{Streams}} \left[\sum_{l=1}^{N_{x_k}} \sum_{m=1}^{N_{y_k}} \left(\delta_{B+}\mathcal{F}^2_{EPES_{Bin_{(i,j,k)}}} \right) \right]} \tag{8}$$

$$\begin{aligned} \delta_{B+}\mathcal{F}^2_{EPES_{Bin_{(i,j,k)}}} = & \left| \frac{\partial \mathcal{F}_{EPES}}{\partial \rho_s}^2 \right| \delta_{B+}\rho^2_{s_{(i,j,k)}} + \left| \frac{\partial \mathcal{F}_{EPES}}{\partial U}^2 \right| \delta_{B+}U^2_{(i,j,k)} + \left| \frac{\partial \mathcal{F}_{EPES}}{\partial T_s}^2 \right| \delta_{B+}T^2_{s_{(i,j,k)}} + \left| \frac{\partial \mathcal{F}_{EPES}}{\partial P_{s_\infty}}^2 \right| \delta_{B+}P^2_{s_{\infty_{(i,j,k)}}} \\ \ldots + & \left| \frac{\partial \mathcal{F}_{EPES}}{\partial U_\infty}^2 \right| \delta_{B+}U^2_{\infty_{(i,j,k)}} + \left| \frac{\partial \mathcal{F}_{EPES}}{\partial \gamma}^2 \right| \delta_{B+}\gamma^2_{(i,j,k)} + \left| \frac{\partial \mathcal{F}_{EPES}}{\partial R}^2 \right| \delta_{B+}R^2_{(i,j,k)} + \left| \frac{\partial \mathcal{F}_{EPES}}{\partial A}^2 \right| \delta_{R}A^2_{(i,j,k)} \end{aligned} \tag{9}$$

A singular biased variable cannot be biased in both the positive and negative direction (if assumed constant over the entire field). However, when the bias is unknown, the worst-case scenario which results in the broadest confidence

bounds assumes that a variable could be biased in either direction.

C. Control Volume Uncertainty

Control volume uncertainty only pertains to the control bounds between the core and the bypass exhaust flows. A 95% confidence interval around the values of the max-squared velocity gradient is used to determine a bounding region from which the force through that region can be calculated. This calculated force is then the control volume uncertainty.

Since the maximum is used for the square of the velocity gradient, the confidence bounds will have to be one-sided. In other words, the positive and negative bounds cannot both be used, only the negative bound. This will create a bound inside of the core region as well as a bound in the bypass region. This bounded region is then applied to the force data after which the force is calculated. An example of this ring-shaped region was shown in Fig. 6.C.

The uncertainty in this methodology is calculated via a two-step process. The first step is to find the uncertainty in the square of the velocity gradient. The second step is to find the uncertainty in the confidence bounds of the squared velocity gradient. These two things will encompass both the uncertainty in the velocity gradient and spatial resolution uncertainty.

Step one is completed using the propagation of errors equation along with the equation for the square of the velocity gradient seen in Eq. 3 and recast below in Eq. 10. The propagation of errors equation is then derived in Eq. 11 assuming random uncertainty in axial velocity as well as in the spatial coordinates x and y. The components in Eq. 11 are described in Eq. 12 and 13. Putting it all together results in Eq. 14 which is the uncertainty in the velocity gradient.

The gradient at each point is taken as the square root of the sum of the squares of the gradient in both the x- and y-directions. This must be done since the data is a cartesian grid instead of a polar one. Also, since the data is discrete, the derivatives only exist at $N-1$ points in both directions. The derivatives are interpolated/extrapolated back to the original grid size to get around this. The error incurred is assumed to be small and not considered here. The "(i,j)" subscript has only been dropped from the partial derivatives in Eq.'s 12 through 14 to make them easier to read.

$$\psi_{(i,j)} = \nabla U^2_{(i,j)} = \left(\sqrt{\left[\left(\frac{\partial U}{\partial x}\right)^2 + \left(\frac{\partial U}{\partial y}\right)^2\right]_{(i,j)}}\right)^2 = \left[\left(\frac{\partial U}{\partial x}\right)^2 + \left(\frac{\partial U}{\partial y}\right)^2\right]_{(i,j)} \tag{10}$$

$$\delta\psi^2_{(i,j)} = \left|\frac{\partial \psi}{\partial U}_{(i,j)}\right|^2 \delta_R U^2_{(i,j)} + \left|\frac{\partial \psi}{\partial x}_{(i,j)}\right|^2 \delta_R x^2_{(i,j)} + \left|\frac{\partial \psi}{\partial y}_{(i,j)}\right|^2 \delta_R y^2_{(i,j)} \tag{11}$$

$$\frac{\partial \psi}{\partial U}_{(i,j)} = \frac{\partial}{\partial U}\left[\left(\frac{\partial U}{\partial x}\right)^2 + \left(\frac{\partial U}{\partial y}\right)^2\right] = \frac{\partial}{\partial U}\left[\left(\frac{\partial U}{\partial x}\right)^2\right] + \frac{\partial}{\partial U}\left[\left(\frac{\partial U}{\partial y}\right)^2\right] = 2\left[\frac{\partial^2 U}{\partial^2 x} + \frac{\partial^2 U}{\partial^2 y}\right] \tag{12}$$

$$\frac{\partial \psi}{\partial x}_{(i,j)} = \frac{\partial}{\partial x}\left[\left(\frac{\partial U}{\partial x}\right)^2 + \left(\frac{\partial U}{\partial y}\right)^2\right] = 2\left[\frac{\partial U}{\partial x}\frac{\partial^2 U}{\partial x^2} + \frac{\partial U}{\partial y}\frac{\partial^2 U}{\partial x \partial y}\right] \quad \text{similarly,} \quad \frac{\partial \psi}{\partial y}_{(i,j)} = 2\left[\frac{\partial U}{\partial x}\frac{\partial^2 U}{\partial y \partial x} + \frac{\partial U}{\partial y}\frac{\partial^2 U}{\partial y^2}\right] \tag{13}$$

$$\delta\psi^2_{(i,j)} = 4\left(\left[\frac{\partial^2 U}{\partial^2 x} + \frac{\partial^2 U}{\partial^2 y}\right]^2 \delta_R U^2_{(i,j)} + \left[\frac{\partial U}{\partial x}\frac{\partial^2 U}{\partial x^2} + \frac{\partial U}{\partial y}\frac{\partial^2 U}{\partial x \partial y}\right]^2 \delta_R x^2_{(i,j)} + 2\left[\frac{\partial U}{\partial x}\frac{\partial^2 U}{\partial y \partial x} + \frac{\partial U}{\partial y}\frac{\partial^2 U}{\partial y^2}\right]^2 \delta_R y^2_{(i,j)}\right) \tag{14}$$

Step two is to find the uncertainty in the confidence intervals, again through the propagation of errors. Equation 15 defines the standard deviation of the squared velocity gradient where N_x and N_y are the number of max points that are considered in the calculation. The squared uncertainty is then defined in the same line. Equation 16 is the partial derivative needed which is taken of the standard deviation with respect to the squared velocity gradient. The error in the velocity gradient is defined in Eq. 14. Finally, the entire control volume error is defined in Eq. 17.

$$\sigma_\psi = \sqrt{\frac{\sum_{i=1}^{N_x}\sum_{j=1}^{N_y}\left(\psi_{(i,j)} - \mu_\psi\right)^2}{N_x * N_y}} \quad \text{where,} \quad \delta\sigma^2_\psi = \left(\frac{\partial \sigma_\psi}{\partial \psi}\delta\psi_{(i,j)}\right)^2 \tag{15}$$

$$\frac{\partial \sigma_\psi}{\partial \psi} = \frac{1}{2 * N_x * N_y}\left(\frac{\sum_{i=1}^{N_x}\sum_{j=1}^{N_y}\left(\psi_{(i,j)} - \mu_\psi\right)^2}{N_x * N_y}\right)^{-\frac{1}{2}}\left(\sum_{i=1}^{N_x}\sum_{j=1}^{N_y} 2\left(\psi_{(i,j)} - \mu_\psi\right)\right) \tag{16}$$

$$\delta\sigma^2_\psi = \frac{\sum_{i=1}^{N_x}\sum_{j=1}^{N_y}\delta\psi^2_{(i,j)}}{(N_x * N_y)^2}\left(\frac{\left[\sum_{i=1}^{N_x}\sum_{j=1}^{N_y}\left(\psi_{(i,j)} - \mu_\psi\right)\right]^2}{\left[\sum_{i=1}^{N_x}\sum_{j=1}^{N_y}\left(\psi_{(i,j)} - \mu_\psi\right)^2\right]}\right) \tag{17}$$

D. Total Uncertainty

Now each source of uncertainty can be combined to form the final 95% confidence interval uncertainty force equations (Sig = 1.96). The first is the total force uncertainty which only includes random uncertainty and bias uncertainty. Control volume uncertainty is not included, since the force does not need to be decomposed. This is seen in Eq. 7 which has been rewritten here as Eq. 18 for conciseness.

$$\mathcal{F}_{EPES_{Total}} = \mathcal{F}_{EPES_{Total_{NoError}}} \begin{cases} +Unc_+ = +Sig * \delta\mathcal{F}_{EPES_{Rand}} + \delta\mathcal{F}_{EPES_{Bias+}} \\ -Unc_- = -Sig * \delta\mathcal{F}_{EPES_{Rand}} - \delta\mathcal{F}_{EPES_{Bias-}} \end{cases} \tag{18}$$

Then, the core and bypass force uncertainty can be written out which includes random uncertainty, control volume uncertainty, and bias uncertainty. The core force uncertainty can be seen in Eq. 19. The bypass force uncertainty can be

seen in Eq. 20. Note that the random and control volume uncertainties have been added with the root sum squared method following the methodology presented by Phillip et al. [29].

$$\mathcal{F}_{EPES_{Core}} = \mathcal{F}_{EPES_{Core_{NoError}}} \begin{cases} +Unc_{+} = +Sig\sqrt{\delta\mathcal{F}^2_{EPES_{Rand_C}} + \delta\mathcal{F}^2_{EPES_{CV}}} + \delta\mathcal{F}_{EPES_{Bias+C}} \\ -Unc_{-} = -Sig\sqrt{\delta\mathcal{F}^2_{EPES_{Rand_C}} + \delta\mathcal{F}^2_{EPES_{CV}}} - \delta\mathcal{F}_{EPES_{Bias-C}} \end{cases} \tag{19}$$

$$\mathcal{F}_{EPES_{Bypass}} = \mathcal{F}_{EPES_{Bypass_{NoError}}} \begin{cases} +Unc_{+} = +Sig\sqrt{\delta\mathcal{F}^2_{EPES_{Rand_B}} + \delta\mathcal{F}^2_{EPES_{CV}}} + \delta\mathcal{F}_{EPES_{Bias+B}} \\ -Unc_{-} = -Sig\sqrt{\delta\mathcal{F}^2_{EPES_{Rand_B}} + \delta\mathcal{F}^2_{EPES_{CV}}} - \delta\mathcal{F}_{EPES_{Bias-B}} \end{cases} \tag{20}$$

IV. Simulated Experiment as a Test Case of the EPES Method

A. Simple Simulation Setup

Neither experimental nor CFD-simulated data was readily available for implementation with the aforementioned EPES method. Instead, a simplified simulation was performed to provide a test case for the method and allow some analysis and visualization of the results. To start, 2D profiles were created by assuming radial distances at which the core and bypass flow streams were to be computed. It was then assumed that the measured planar values would be axial velocity, static temperature, and static density. These assumed values can be seen in Fig. 8.A in which the values have been non-dimensionalized by their maximum value to easily examine them on the same chart. The actual values are shown in Fig. 8.B. These values approximate those using a Honeywell TFE731-2 at Virginia Tech's TurboLab. The freestream values were set at a Mach number of 0.5 at relevant static temperature and density.

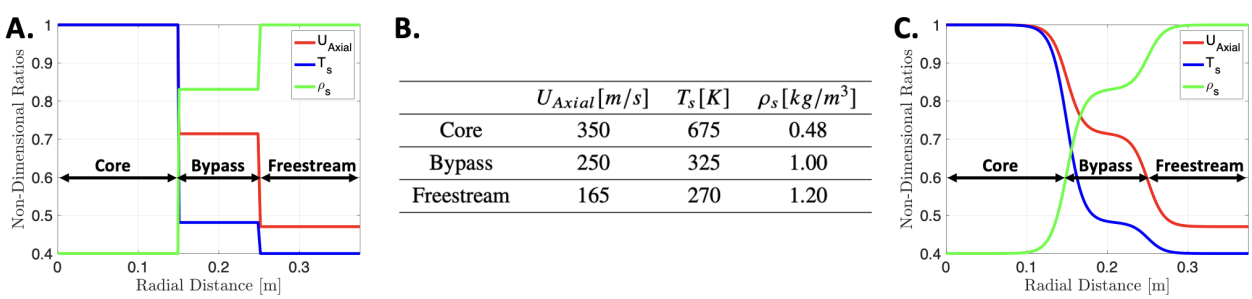

	$U_{Axial}[m/s]$	$T_s[K]$	$\rho_s[kg/m^3]$
Core	350	675	0.48
Bypass	250	325	1.00
Freestream	165	270	1.20

Fig. 8 A: Unblended profiles of measured variables. B: Measured variable values approximating a Honeywell TFE731-2 in-flight at Mach 0.5. C: Blended profiles of measured variables using hyperbolic tangent smoothing.

The next step in the simulation process was to assume that the measurements were taken downstream of the exhaust such that the profiles include mixing layers. These mixing layers were approximated using hyperbolic tangent smoothing [30] between the original step profiles. A blend distance of 0.02 m was chosen to replicate a measurement taken at several exhaust diameters downstream of the engine. See Fig. 8.C.

The final step in the simulation process is to rotate the radial 1D profiles to circular 2D profiles. Which are interpolated and extrapolated to cartesian coordinates that fill a square. The variables in Fig. 8 can also be used to produce the expanded velocity (Eq. 1) and the square of the velocity gradient (see Eq. 3 and Eq. 10) that are needed to use the EPES method. The contours of the planar values needed to compute the total and component forces are shown in Fig. 9. Which completes the simple simulated experiment.

Note that the final planar values seen in Fig. 9 are composed of a 500 by 500 array (corresponds to a bin area of approximately $2.23e^{-6}\ m^2$) of discrete measurement points equally spaced apart. This is experimentally achievable with an optical measurement where typical camera sensors have 2000 by 2000 points. However, this type of resolution would be difficult to achieve with probe measurements.

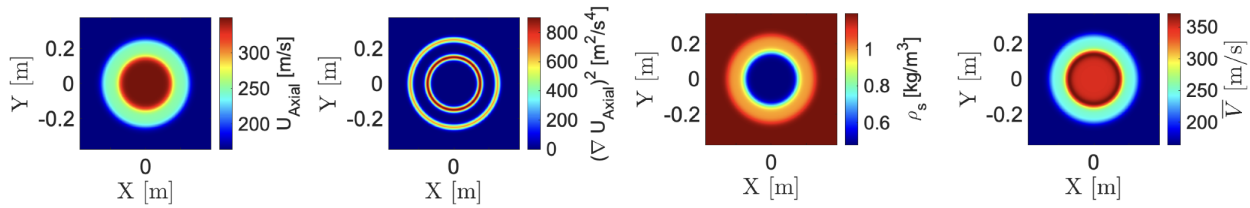

Fig. 9 Required planar values to compute the total and component forces using Eq. 4 and Eq. 10. A: Axial velocity. B: Square of the axial velocity gradient. C: Static density. D: Expanded velocity.

B. Simple Simulation Results

1. Total Force Results

To calculate the total force through the plane shown in Fig. 9, Eq. 4 must be used. However, no separation of streams is needed so N_{x_k} and N_{y_k} simply span the entire width and height of the plane, respectively. As a baseline case, the non-blended data (Fig. 8.A) which represent values taken in the near-field was used with the near-field approach and the EPES method. The total force results matched, as expected since no uncertainty has been introduced. The EPES method was then employed downstream with mixing (Fig. 8.C) and produced the final total force of 5535.705 N of force. Three decimal points of precision are given such that the impact of random uncertainty can be seen.

The total force is easy to achieve with this simple simulation data set since no control volume bounds are needed because the actual turbofan flow is bounded everywhere by freestream flow which produces no total force given the control volume defined in Fig 3. This is highly simplified compared to a real case in which the nacelle, structural pylon, wing, etc. are all involved.

2. Component Force Results

To decompose the total force into core and bypass force components the control volume defined in Fig. 4 is needed. The complexity is raised compared to the total force case because the flow streams must be separated in the mixing layer. This is done by finding the dividing streamsurface as shown in Fig 5 using the maximum velocity gradient criterion.

Therefore, Eq. 4 and Eq. 10 are needed to fully define the force from the core and bypass flow streams. Figure 10 provides a visual representation of the control volume definition process.

Figure 10.A is a visual representation of the separation of flow streams that was previously discussed in Subsection II.B. Where the max turbulent shear stress approximately follows the square of the velocity gradient. The max of the square of the velocity gradient can be found in the planar data which is shown as white points in Fig. 10.A. Any point inside this bounding circle is considered a part of the core flow stream, and any point outside of this bounding circle is considered part of the bypass flow stream as shown in Fig. 10.B. Note that the freestream can be included in the bypass stream since in Eq. 4 the $\overline{V} - U_\infty$ term subtracts the momentum from the freestream. Now that the flows have been separated, Eq. 4 can be used for each flow stream. For this simple simulation, the core flow stream has a force of 2445.010 N and the bypass flow stream has a force of 3090.695 N. The bypass ratio was also computed and has a value of around 2.2. Of course, with no assumed uncertainty, the total force is again exact.

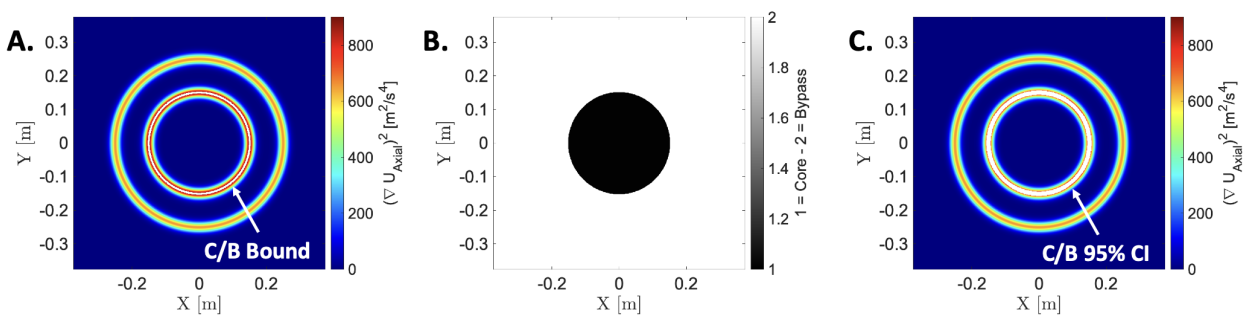

Fig. 10 A: Core and bypass bound using the max of the square of the velocity gradient. B: Separation of flow streams. C: 95% confidence interval in the CV bounds using the CV uncertainty quantification framework.

3. Uncertainty Results

Uncertainties for the EPES method were computed using the methodology presented in Section III. Table 1 shows the primary uncertainties chosen for this simple simulated experiment. These values are deemed representative of real experiments. To keep the analysis simple, the same uncertainty values were used for random, positive bias, and negative bias. The random uncertainty was normally distributed over the entire plane, and positive and negative biases were constant across the entire plane.

Table 1 Primary uncertainties for random, positive bias, and negative bias.

U	γ	R	T_s	ρ_s	P_{s_∞}	U_∞	A
5 m/s	0.02	3 J/kgK	5 K	0.015 kg/m^3	1000 Pa	2 m/s	2.25e-8 m^2

Table 2 shows a breakdown of the random, bias, and control volume uncertainties for total, core, and bypass force, respectively. The random uncertainty is small for all forces. This is due to the $1/\sqrt{N_{x_k} * N_{y_k}}$ scaling in Eq. 5. For example, 250,000 bins exist for the summation of the total force calculation, which leads to a 99.8% reduction in the

random uncertainty. To further illustrate this relationship, the core force is comprised of far fewer bins and has a 99.4% reduction (Table 2). The bypass force shows the same random uncertainty trend.

The bias uncertainty is not a function of the number of bins, since the mean of the biased data set is offset from the theoretical non-biased mean, and the bias uncertainty is orders of magnitude larger than the random uncertainty. In this case, symmetric bias uncertainty bounds were expected, since the positive and negative bias values tested were the same. If the bias directions were known, the bias uncertainty bounds would be asymmetric since, for example, velocity cannot be both positively and negatively biased. The overall bias magnitude would also be less. Without a chosen measurement technology and associated possible bias levels, the worst-case solution must be used.

As shown in Eq. 18, the total force uncertainty only contains random and bias errors. Looking at Table 2, the random and bias errors have been summed to produce a total uncertainty in the total force of ±11.964 N or 0.22%. For the component forces, the control volume uncertainty has the largest impact (see Fig6.C). As previously defined, the 95% confidence interval that was taken around the dividing line creates a ring-shaped area from which the grouping of the force through this area is uncertain. In this example, the ring-shaped area incorporates a portion of the mixing layer between the two streams of fluid. This is a non-negligible mass flow contribution that leads to higher magnitudes in uncertainty. In this simple simulation, this was calculated to be ±53.640 N or approximately 1.1% of the total force. The core force had a total uncertainty of 59.349 N or approximately 2.45%. The bypass force had a total uncertainty of 64.167 N or approximately 2.09%.

Table 2 95% Confidence interval force uncertainty breakdown.

	Total Force	Core Force	Bypass Force
$N_x * N_y$	250000	31548	218452
Force (N)	5535.705	2445.010	3090.695
Random (N)	±0.024	±0.032	±0.022
Positive Bias (N)	+11.941	+5.677	+10.504
Negative Bias (N)	-11.941	-5.677	-10.504
Control Volume (N)	–	±53.640	±53.640
Total Uncertainty (N)	+11.964, -11.964	+59.349, -59.349	+64.167, -64.167

Figure 11 shows the error influence coefficients (EIC), or the individual contributions to the propagation of uncertainty equations for random and bias uncertainty (Eqs. 6 and 9) since the uncertainty magnitudes were the same. Figure 11.A has a log y-scale while Fig 11.B has a linear y-scale. Both charts highlight the difference in uncertainties between the core, bypass, and total flow streams. As expected, the core and bypass EICs (for random and bias) must sum to the total EIC. Overall, the specific heat ratio has the lowest impact, since it is largely seen in ratios such as $\gamma - 1/\gamma$ instead of just γ itself. Static temperature and static density have the largest impacts along with the specific gas constant and the freestream static pressure as these are used to calculate the expanded velocity in Eq. 1. The static temperature and static density influences have an inverse relationship with each other; The core exhaust has a relatively

high temperature and low-density flow, while the bypass has a relatively low temperature and high-density flow. The static density influence is relatively high for both the core and bypass because it is directly used in the force calculation (See Eq. 4). It should be noted that the EICs are also functions of the primary uncertainty (see Table 1). Therefore, Fig. 11 could change significantly if different primary uncertainties were chosen.

In conclusion, control volume uncertainty and bias uncertainty are the dominant contributors to the overall uncertainty. Random uncertainty will only play a major role in the overall uncertainty if the spatial resolution is poor. The linear assumption in using the propagation of errors equation leads to an easy-to-use analytic design tool. However, since the equations are slightly non-linear, a higher-order uncertainty bookkeeping method such as Monte Carlo simulations is needed if the accuracy in the uncertainty result needs to be below 1%.

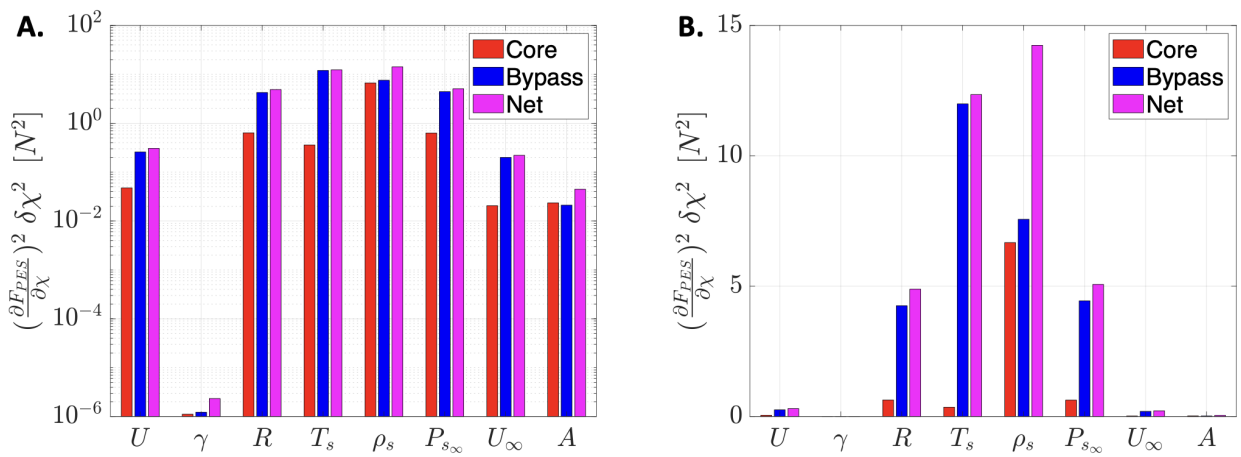

Fig. 11 Error influence coefficients (EIC) found in Eqs. 6 and 9 for all eight uncertain variables. $\mathcal{X}$ is a placeholder variable. A: Log scale. B: Linear scale.

V. Conclusions

The rich history of aerodynamic force decomposition, as it pertains to propulsive devices, culminated in Drela's parallel expanded streamtube method. This work has been extended here to the new method (EPES) with the use of the Townsend criterion and Prandtl's turbulent mixing length model to decompose the total exhaust force into core and bypass flow streams. Drag flow streams were not considered, however, the developed dividing streamsurface methodology can be easily expanded to include such flow streams. The EPES framework was then completed through uncertainty derivations and quantification including random, bias, and control volume uncertainty sources. A simulated experimental data set was constructed as a test case for the new method. Computational fluid dynamic (CFD) simulations and experimentation are needed for further validation of the method. This was left for future work.

This data set worked through to obtain force results for the total, core, and bypass forces using planar results in the exhaust of a turbofan engine. Uncertainty analysis was also performed, which showed that the static temperature and static density uncertainties were the main driving force for random and bias error while the axial velocity uncertainty

drove the control volume uncertainty.

Acknowledgments

The authors wish to acknowledge the Science, Mathematics, and Research for Transformation (SMART) scholarship, the Aerospace and Ocean Engineering department at Virginia Tech, and Pratt & Whitney for supporting the authors in the development of this extended control volume technique.

References

[1] Drela, M., "Power balance in aerodynamic flows," *AIAA Journal*, Vol. 47, No. 7, 2009, p. 1761–1771. https://doi.org/10.2514/1.42409.

[2] Drela, M., "Considerations in aerodynamic force decomposition," *AIAA AVIATION 2021 FORUM*, 2021. https://doi.org/10.2514/6.2021-2552.

[3] Méheut, M., and Bailly, D., "Drag-breakdown methods from wake measurements," *AIAA Journal*, Vol. 46, No. 4, 2008, p. 847–862. https://doi.org/10.2514/1.29051.

[4] Betz, A., "A Method for the Direct Determination of Wing-Section Drag," *NASA Technical Reports*, 1925. Document ID: 19930090720. Available at: https://ntrs.nasa.gov/citations/19930090720.

[5] Jones, B. M., "Measurement of Profile Drag by the Pitot-Traverse Method," *Cambridge University Aeronautics Laboratory*, 1936. Available at: https://www.google.com/books/edition/ The Measurement of Profile Drag by the P/2wwoMwEACAAJ?hl=en.

[6] Oswatitsch, K., "Gas Dynamics," *Academic Press*, 1956. Available at: https://www.cambridge.org/core/journals/ journal-of-fluid-mechanics/article/ gas-dynamics-by-klaus-oswatitsch-english-version-by-gustav-kuerti-new-york- academic-press-inc-1956-610-pp-1200/14EF591EB837FA1CD5709A62F489D920.

[7] Maskell, E. C., "Progress Towards a Method of Measurement of the Components of the Drag of a Wing of Finite Span," *Royal Aircraft Establishment TR 72232*, 1973.

[8] Kubrynski, K., "Wing-winglet design methodology for low speed applications," *41st Aerospace Sciences Meeting and Exhibit*, 2003. https://doi.org/10.2514/6.2003-215.

[9] Destarac, D., and Van der Vooren, J., "Drag/thrust analysis of jet-propelled transonic transport aircraft; definition of physical drag components," *Aerospace Science and Technology*, Vol. 8, No. 6, 2004, p. 545–556. https://doi.org/10.1016/j.ast.2004.03.004.

[10] Van der Vooren, J., and Slooff, J., "CFD-Based Drag Prediction; State-of-Art, Theory, Prospects," *National Aerospace Lab., NLR, TP 90247 U*, 1990.

[11] Kusunose, K., "A Wake Integration Method for Airplane Drag Prediction," *Tohoku Univ. Press*, 2005.

[12] Van Dam, C., "Recent experience with different methods of drag prediction," *Progress in Aerospace Sciences*, Vol. 35, No. 8, 1999, p. 751–798. https://doi.org/10.1016/s0376-0421(99)00009-3.

[13] Bailly, D., and Godard, J., "Méthodologie Expérimentale pour l'évaluation de la Traînée, Techniques de Post-Traitement, Préparation d'essais," *ONERA RT 116/1685 DAAP/Y*, 1999.

[14] Méheut, M., and Bailly, D., "Drag Prediction and Wake Survey Techniques," *CEAS/KATnet Conference on Key Aerodynamic Technologies [CD-ROM]*, 2005.

[15] Young., A., "Note on the Effect of Compressibility on Jones's Momentum Method of Measuring Profile Drag," *R M Report 1881, Aeronautical Research Council*, 1939.

[16] "SAE AIR1678B: Uncertainty of In-Flight Thrust Determination," , 2016. URL https://www.sae.org/standards/content/air1678b/?src=air1703a.

[17] "SAE AIR1703A: In-Flight Thrust Determination," , 2017. URL https://www.sae.org/standards/content/air1703a.

[18] "SAE AIR4065A: Propeller/Propfan In-Flight Thrust Determination," , 2012. URL https://www.sae.org/standards/content/air4065a/?src=air1703a.

[19] "SAE AIR5450: Advanced Ducted Propulsor In-Flight Thrust Determination," , 2014. URL https://www.sae.org/standards/content/air5450/?src=air1703a.

[20] "SAE AIR5771A: The Measurement of Engine Thrust in an Altitude Test Facility," , 2018. URL https://www.sae.org/standards/content/air5771a/?src=air5450.

[21] "SAE ARP755D: Aircraft Propulsion System Performance Station Designation and Nomenclature," , 2014. URL https://www.sae.org/standards/content/arp755d.

[22] Davidson, T. W., "Measurement of net thrust in flight," *Journal of Aircraft*, Vol. 1, No. 3, 1964, p. 107–113. DOI: 10.2514/3.43575.

[23] Townsend, A. A., *The structure of turbulent shear flow*, C.U.P., 1976.

[24] Grazzini, G., Mazzelli, F., and Milazzo, A., "Constructal design of the mixing zone inside a supersonic ejector," *International Journal of Heat and Technology*, Vol. 34, No. S1, 2016. https://doi.org/10.18280/ijht.34s114.

[25] Schetz, J., and Bowersox, R., *Boundary Layer Analysis*, American Institute of Aeronautics and Astronautics, 2012.

[26] Bendat, J. S., and Piersol, A. G., *Engineering applications of correlation and spectral analysis*, John Wiley amp; Sons, 1993.

[27] Box, M. J., "Bias in nonlinear estimation," *Journal of the Royal Statistical Society: Series B (Methodological)*, Vol. 33, No. 2, 1971, p. 171–190. https://doi.org/10.1111/j.2517-6161.1971.tb00871.x.

[28] Witkovsky, V., Wimmer, G., Durisova, Z., Duris, S., and Palencar, R., "Brief overview of methods for measurement uncertainty analysis: Gum Uncertainty Framework, Monte Carlo method, characteristic function approach," *2017 11th International Conference on Measurement*, 2017. https://doi.org/10.23919/measurement.2017.7983530.

[29] Phillips, S., Eberhardt, K., and Parry, B., "Guidelines for expressing the uncertainty of measurement results containing uncorrected bias," *Journal of Research of the National Institute of Standards and Technology*, Vol. 102, No. 5, 1997, p. 577. https://doi.org/10.6028/jres.102.039.

[30] "Piecewise and blended functions," , 2023. URL https://www.mathworks.com/matlabcentral/fileexchange/56530-piecewise-and-blended-functions.

Chapter 6 - Experimental Turbofan Ground Force Measurement and Accounting using Filtered Rayleigh Scattering and Control Volume Analysis

The contents of this chapter will be submitted to the *AIAA Journal* (Sean Powers, Gwibo Byun, K. Todd Lowe, and Joseph Schetz. "Experimental Turbofan Ground Force Measurement and Accounting using Filtered Rayleigh Scattering and Control Volume Analysis"). No significant portions have been discussed outside of this manuscript.

The objective of this chapter is to provide evidence that a derived control volume combined with filtered Rayleigh scattering shows promise for in-flight force measurements by using a ground test measurement in the exhaust of the Honeywell TFE731-2 at the Virginia Tech TurboLab. The techniques developed in this paper paved the path for an in-flight application of the combined FRS and control volume methodology and address the remaining knowledge gaps as discussed in subsection 2.3.

Experimental Turbofan Ground Force Measurement and Accounting using Filtered Rayleigh Scattering and Control Volume Analysis

Sean Powers *, Gwibo Byun†, K. Todd Lowe‡, and Joseph Schetz §
Virginia Polytechnic Institute and State University, Blacksburg, VA, 24060, United States

This study utilized a new control volume analysis and filtered Rayleigh scattering (FRS) to achieve high-accuracy force measurements in the exhaust of a Honeywell TFE731-2 turbofan engine at Virginia Tech's TurboLab. A companion paper describes the new control volume analysis. The particle swarm optimization technique was crucial to finding the global minimum of the fit between modeled and fitted FRS spectra across the data plane. The resulting FRS measured total force of 8995 N had an error of only 0.13% compared to the force balance measurement of 9007 N. The core and bypass flow streams were separated using the Townsend observation of a dividing streamline located at the maximum shear stress in a mixing layer. A turbulent shear stress mixing length model is employed such that the maximum shear stress can be approximated to occur at the maximum of the square of the velocity gradient. This grouping resulted in a core force of approximately 4085 N and a bypass force of approximately 4910 N. While no independent measurements of core and bypass force were available, the bypass ratio was experimentally determined to be 2.53 with a 2.3% error compared to the known value of 2.60. The final uncertainty quantification incorporated random, bias, and control volume sources, resulting in maximum uncertainties of approximately 0.25% for total force, 11% for core force, and 9% for bypass force. The decomposed exhaust forces have higher uncertainty due to the control volume uncertainty. Future experiments should prioritize increasing spatial resolution while maintaining an acceptable signal-to-noise ratio to decrease control volume uncertainty. Overall, this study highlights the success of combining FRS with control volume analysis to accurately decompose forces in non-ideal environments such as turbofan engines.

*SMART Fellow, Kevin T. Crofton Department of Aerospace and Ocean Engineering, 460 Old Turner St, Blacksburg, VA 24060, AIAA Student Member.

†Research Scientist, Kevin T. Crofton Department of Aerospace and Ocean Engineering, 460 Old Turner St, Blacksburg, VA 24060, AIAA Member.

‡Professor, Kevin T. Crofton Department of Aerospace and Ocean Engineering, 460 Old Turner St, Blacksburg, VA 24060, and AIAA Associate Fellow.

§Fred D. Durham Endowed Chair Emeritus, Kevin T. Crofton Department of Aerospace and Ocean Engineering, 460 Old Turner St, Blacksburg, VA 24060, and AIAA Life Fellow.

Nomenclature

A	=	bin area in m^2
CM	=	camera module
CV	=	control volume
D	=	diameter in m
EIC	=	error influence coefficient in N^2
$EPES$	=	extended parallel expanded streamtube method
f_D	=	Doppler shifted frequency
IR	=	intensity ratio
$\hat{i}$	=	laser propagation unit vector
N	=	number of bins
$\hat{o}$	=	camera observation unit vector
p	=	pressure in Pa
R	=	specific gas constant in kg/m^3
S	=	spectrum
SNR	=	signal-to-noise ratio in dB
T	=	temperature in K
U	=	x-velocity (+ right) or freestream velocity in m/s
V	=	y-velocity (+ up) in m/s
$\overline{V}$	=	expanded velocity in m/s
$\overrightarrow{V}$	=	total velocity in m/s
W	=	z-velocity or axial velocity (+ in) in m/s
x	=	axial distance downstream in m
γ	=	specific heat ratio
δ	=	uncertainty
∇	=	gradient
λ	=	wavelength in m
ν	=	wavenumber in cm^{-1}
τ_{I_2}	=	iodine transmission spectrum
$\mathcal{X}$	=	uncertainty variable placeholder

Subscripts

$Axial$	=	relating to the axial direction
$Bknd$	=	relating to background (geometric) scattering
$Core$	=	relating to the core flow stream
FRS	=	filtered Rayleigh scattering contribution
Mie	=	relating to Mie (particle) scattering
Ray	=	Rayleigh scattering contribution
$Sens$	=	relating to the sensed (measured) direction
s	=	static
TOT	=	total scattering
t	=	total
∞	=	freestream

I. Introduction

Experimentally measuring the necessary parameters to get an accurate assessment of forces in the exhaust of a turbofan engine without the use of a force balance is a non-trivial task. Even with the use of a force balance, force decomposition in the exhaust is very difficult [1]. The current industry standard methodology is a probe rake attached to a traverse that measures the gas properties at the nozzle exit which are then integrated over the entire area to obtain a final force value [2]. However, this method suffers from two major problems. The first is the ability of the probe rake to withstand such a harsh environment for long periods. Secondly, the physical size of the probes limits the spatial resolution of the measurement. The location and number of individual measurements required are highly reliant on the specific application. A simple turbojet with a mostly uniform exhaust would need fewer measurement locations than a large turbofan, for example. The rake size and pivot locations have to be designed in such a way that allows the rake to gather data over the entire exhaust plane. The complexity of such devices changes considerably when designing for ground tests or flight tests. Examples of ground and in-flight hardware can be seen in SAEAIR 1703A [2] and Davidson [3].

Many methods exist today to determine exhaust forces and exhaust force decomposition. However, none are easy to experimentally execute, and no industry-wide consensus has been made on which one to use. Almost all require some sort of ground testing before flight testing. This ranges from creating models based on ground data to simple testing of hardware on the ground. Many of these methods and their requirements can be found in SAEAIR 1703A [2] and SAEAIR 1678B[4]. These methods along with other theoretical methods are discussed by Drela [5, 6] and Powers et al. [7]. The current work follows Drela's [6] parallel expanded streamtube method (PES) as extended by Powers et al. [7] to create the extended parallel expanded streamtube method (EPES) combined with filtered Rayleigh scattering to experimentally measure the necessary parameters.

The filtered Rayleigh scattering (FRS) technique is capable of providing high-accuracy, high-resolution, non-intrusive measurements of 3-component velocity, static temperature, and static density. This has already been proven to work well in the inlet of a Honeywell TFE731-2 engine by Powers et al. [8] as well as in the exhaust of a small turbojet engine (JetCat P100-Rx [9]) by Powers et al. [10]. The use of the FRS technique along with the EPES control volume analysis by Powers et al. [7] enables the same kind of measurements done in the inlet to be made in the exhaust of the same Honeywell TFE731-2 turbofan at Virginia Tech's TurboLab [11]. The EPES control volume analysis shows how to decompose the forces within the exhaust into core and bypass forces.

II. Filtered Rayleigh Scattering Measurement Technique

This section provides an overview of the fundamentals of the filtered Rayleigh scattering (FRS) measurement technique. The effects of static temperature, static density, and velocity on the Rayleigh scattering spectrum will be visualized. Unwanted scattering signals such as Mie (particle) and background (geometric) scattering are discussed to describe the importance of filtering as a means to interrogate the spectral content of the Rayleigh scattering lineshape and rid the data of unwanted scattering signals. The authors refer the reader to Powers et al. [10] for in-depth descriptions of the fundamentals of filtered Rayleigh scattering.

A. Theory and Modeling

Rayleigh scattering (specifically Rayleigh-Brillouin scattering) is an optical phenomenon that occurs when light interacts with matter on a scale equal to or smaller than the wavelength of the incident light, in this case, continuous 532 *nm* wavelength light from a Coherent Verdi-V18, frequency-doubled $Nd:YVO_4$ diode-pumped solid-state laser. The scattering of light by gas molecules eliminates the need for tracer particles in the flow measurement, which sets it apart from other optical methods such as particle image velocimetry (PIV), Doppler global velocimetry (DGV), and laser Doppler velocimetry (LDV). Moreover, Rayleigh scattering can measure scalar quantities of static temperature and density as well as scalar and vector quantities of velocity simultaneously. To achieve this, it is important to understand the key attributes of the Rayleigh scattering signal. Firstly, the probability of photons scattering from a gas molecule increases with the amount of matter and the scattering cross-section of the gas, allowing for a measurement of static density. Secondly, light scattered off moving matter undergoes a Doppler shift in frequency proportional to its bulk velocity (see Eq. 1). The bulk velocity shift is referred to as the sensed velocity which is the velocity measured in the direction defined by the difference in the laser propagation direction ($\hat{i}$) and the observer direction ($\hat{o}$) as seen in Eq. 1. Thirdly, since individual molecules are always in motion, a Doppler shift proportional to the speed of the individual molecules allows for static temperature measurements. These principles enable direct measurements of static density and static temperature to compute static pressure from the state equation, while the mean Doppler shifted signal yields flow velocity. These effects are observed through a molecular absorption filter, which is an iodine vapor cell, in the case

of 532 *nm* incident laser light due to its sharp absorption lines.

$$f_D = \left(\hat{o} - \hat{i}\right) \lambda^{-1} \cdot \vec{V} \tag{1}$$

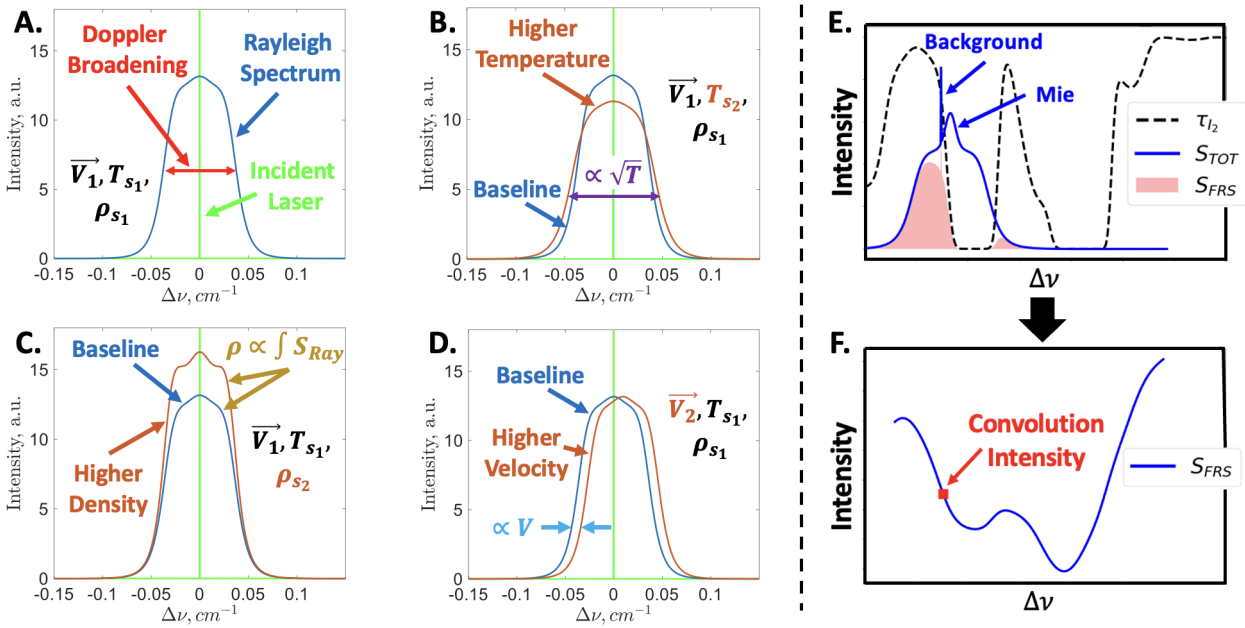

Fig. 1 A: Baseline Rayleigh scattering spectrum. B: Higher temperature Rayleigh scattering spectrum. C: Higher density Rayleigh scattering spectrum. D: Higher velocity Rayleigh scattering spectrum. E: Filtered Rayleigh scattering technique. F: Final convolution after frequency scanning. Modified and reprinted with permission from Powers et al. [8] and Warner et al. [12].

The left four charts (A-D) in Fig. 1 represent the influences of static temperature (Fig. 1.B), static density (Fig. 1.C), and velocity (Fig. 1.D) on the nominal Rayleigh scattering signal (Fig. 1.A). Figure 1.B depicts how an increase in static temperature leads to a wider full-width-half-maximum (FWHM) that is proportional to the square root of the increased static temperature. As an additional result, the peak intensity decreases. On the other hand, Fig. 1.C shows the impact of static density on the overall intensity of the Rayleigh scattering signal. An increase in static density corresponds to an increase in peak intensity. Finally, Fig. 1.C shows how a bulk velocity increase does not alter the shape or intensity of the Rayleigh scatter signal. Instead, the Doppler frequency shift causes the signal to shift left or right in frequency, which is proportional to the velocity magnitude and its directional dependence.

It is very difficult to obtain an ideal Rayleigh scattering signal outside of a meticulously controlled experiment. Unwanted scattering contributions manifest as Mie (particle) scattering and background (geometric) scattering. Mie scattering occurs when light scatters off particles that are on the same scale as or larger than the wavelength of the incident light. On the other hand, background scattering results from light scattering off stationary physical objects present within the camera's field of view.

These undesirable contributions are demonstrated in Fig. 1.E. The intensity of background scattering can be

substantial, and it always appears at the same frequency as the laser. Hence, it is located at a detuning wavenumber of zero ($\Delta\nu = 0$). Mie scattering can also exhibit high intensity, but it is Doppler shifted in frequency along with the Rayleigh scattering spectrum. As a result, it remains centered on the Rayleigh spectrum, as depicted. In this instance, the Mie and background contributions are not aligned, because a non-zero flow velocity has caused the spectrum to be Doppler-shifted. If the velocity were zero, the Mie and background contributions would combine to form a single, large central peak.

To minimize the impact of these unwanted scattering contributions, a molecular iodine vapor filter is employed. The term "filtered" in filtered Rayleigh scattering (FRS) is derived from this approach. FRS takes advantage of the sharp features that exist in the absorptivity spectrum of iodine vapor to analyze the spectral content of the Rayleigh scattering signal while reducing the effects of Mie and background scattering. Figure 1.E depicts a snapshot of this technique. The outcome of this convolution is depicted in Fig. 1.F, where the red dot corresponds to the convolution outcome from Fig. 1.E. This convolution is what a camera, looking through a molecular iodine cell, measures experimentally. However, filtering cannot always completely get rid of unwanted effects. To overcome this, Mie and background scattering are modeled and used as fitting parameters in the scattering model.

Powers et al. [10] offer a detailed description of the fundamental theory and equations for FRS. They also outline the processing methodology for turning unprocessed Rayleigh scattering signals into direct planar, line, or point measurements of static temperature, static density, and velocity.

B. Fitting Scheme

Powers et al. [10] used a non-linear least-squares fitting algorithm [13, 14] to match a modeled spectrum to an experimentally measured spectrum. This matching allows for static temperature, static density, velocity, and Mie and background scattering levels to be fit. This fitting is done for every pixel or pixel bin in an image to produce planar results. Similar techniques have been used by Doll et al. [15, 16] and Schroll et al. [17]. However, the ability of these techniques to produce the best fit can be dependent on initial conditions or fail when the objective function (a function that is minimized by the fitting algorithm) has multiple local minima that are similar in magnitude to the global minimum of the desired solution. In terms of turbofan exhaust conditions, the low-temperature, high-density bypass flow and high-temperature, low-density core flow pose this exact problem. A low-temperature and high-density spectra fit may be found when the correct solution is a high-temperature and low-density result if the initial conditions aren't perfect. The convolution spectra at these two different flow conditions are very similar when noise is present. To get around this, a solution less dependent on initial conditions and noise effects such as the particle swarm algorithm [18, 19] was introduced. Figure 2 is a simple visual explanation of why this change was needed.

Figure 2.A shows a 3D contour of the Styblinksi-Tang function [20]. This function was chosen as a simple example since it has three local minima with approximately the same magnitude as the global minimum. To better show the

dependence on initial conditions, sixteen evenly spaced starting points (shown in white) were placed around the planar function. Figure 2.B shows the more traditional minimum search algorithm [21] results. It can be seen that if the initial condition starts in the same quarter as the local minimum of that quarter, the algorithm cannot find the global minimum. In this simple 2D case, the minimum search algorithm approximates the performance of the non-linear least-squares function. This is in contrast to Fig. 2.C which shows the particle swarm optimization algorithm results. No matter where the solver was started, the global minimum was found. This leads to a more robust solver since it is effectively free of reliance on initial conditions. However, the time needed to solve the particle swarm result is generally longer than the minimum search algorithm. Therefore, both algorithms have merit, but they need to be applied correctly depending on the flow being measured and the accuracy required. Outside of this algorithm change, the rest of the FRS data processing here is the same as that described in Powers et al. [10].

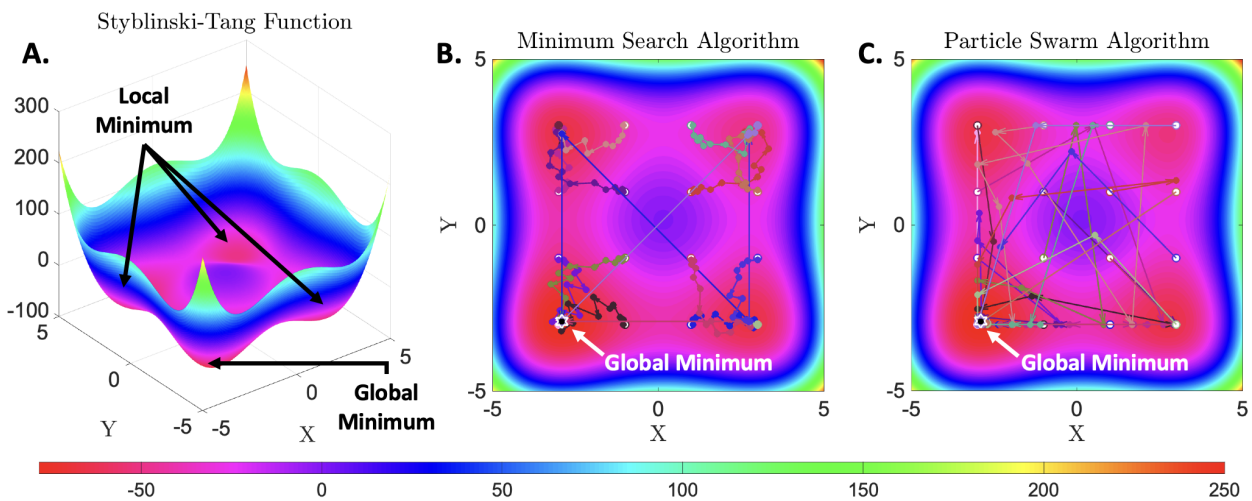

Fig. 2 Comparison of minimum search algorithms. A: Styblinski-Tang function. B: Derivative-free minimum search algorithm. C: Particle swarm optimization minimum search algorithm.

III. Experimental Setup at the Virginia Tech TurboLab

This section serves to outline the physical setup of the FRS measurement at an exhaust plane of the Honeywell TFE731-2 turbofan engine [22]. The engine and facility will be described first. Then, the FRS measurement setup will be presented. These will be done using Fig. 3.

Figure 3.A shows the hanging TFE731-2 engine inside the engine cell located at the Virginia Tech TurboLab [11]. The TFE731-2 is a 2:1 geared turbofan with an approximate inlet diameter of 700 mm and an overall pressure ratio of 13:1. The bypass ratio is approximately 2.6. This allows for a maximum thrust at sea level of approximately 15,500 N. All engine specification values come from references [22] and [23]. Referring to Fig. 3.A and Fig. 3.B, the engine is mounted on rails along with a hanging bellmouth such that the entire assembly may be pushed towards the front of the cell during operation. This allows the bellmouth to be outside of the test cell such that the engine only ingests

clean inlet air. The engine cell also necessitates the inclusion of an ejector downstream of the exhaust to safely channel the exhaust flow out of the test cell and to ensure that no recirculation has taken place. Finally, the TFE731-2 is hung from an assembly that is connected to a calibrated pneumatic force balance. The fuel mass flow is also measured via a calibrated flow meter. The engine was run at a corrected fan speed of approximately 80% at an altitude of approximately 640 m (altitude of Blacksburg, VA). The resulting force measurement at these conditions was approximately 9007 N.

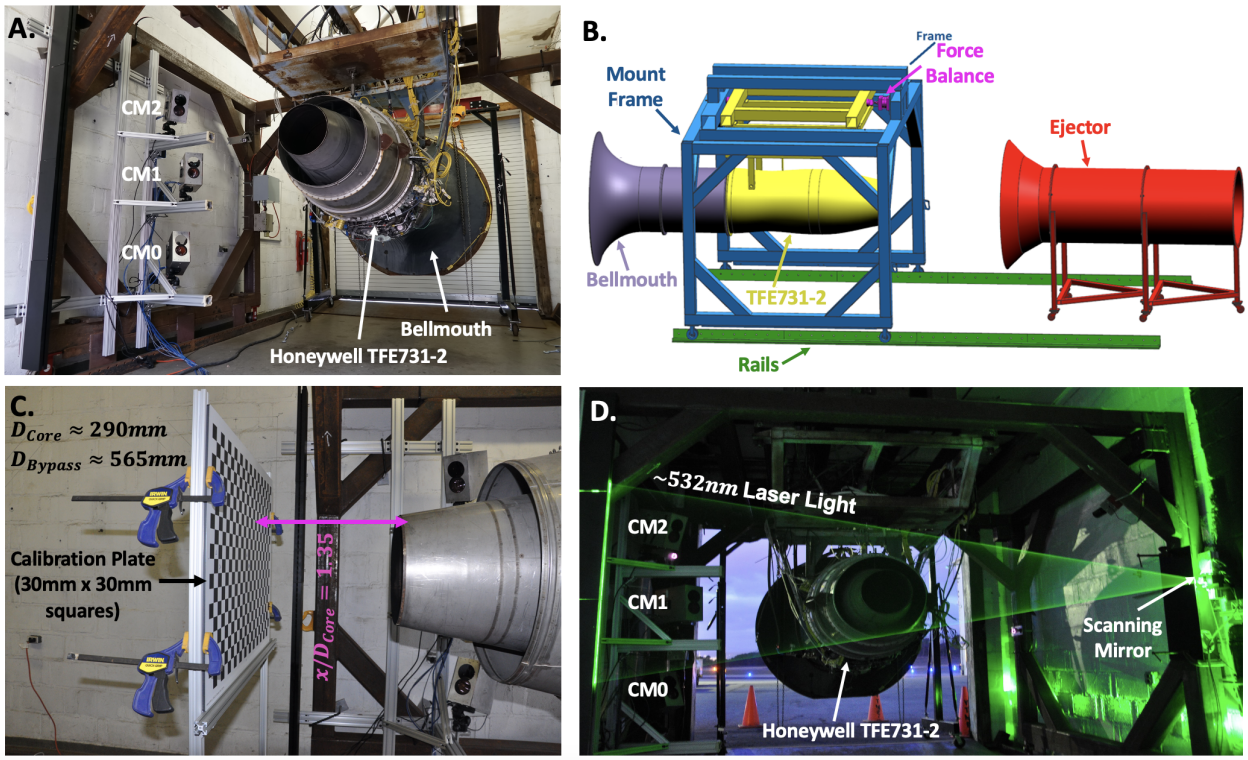

Fig. 3 A: View of engine cell with all three camera modules visible. B: Simple CAD model showing the location of the force balance. C: Calibration plate (FRS measurement plane) location in the exhaust of the Honeywell TFE731-2. D: Nominally 532 nm wavelength laser sheet made by a scanning mirror mounted on the wall.

Moving on to Fig. 3.C, the FRS measurement plane was placed at approximately 1.35 x/D_{Core} downstream of the core exhaust plane. The calibration plate used for camera calibration is seen with 30 mm x 30 mm squares to give a sense of scale. The laser sheet was located directly on the front face (face pictured) of the calibration plate. The laser sheet can be seen in Fig. 3.D and was made with a ThorLabs GVS211 scanning mirror [24]. The 532 nm wavelength light was produced by a Coherent Verdi-V18, frequency-doubled $Nd:YVO_4$ diode-pumped solid-state laser with an approximate beam power of 6 Watts at the measurement location. The laser sheet was made just wide enough to cover the entire exhaust plume but not so wide that laser power was a concern. The last things needed for the FRS measurement were the camera modules (CMs). The three camera modules can be seen on the left side of Fig. 3.A and Fig. 3.D. Each camera module contained two FLIR Blackfly BFLY-U3-23S6C-C cameras [25]. One camera was the "filtered" camera which looked through a 1 Torr molecular iodine vapor cell. The other was the "unfiltered" camera

which had an unobstructed view of the laser sheet. The "unfiltered" camera was used to normalize the measured data. The exposure time for the data set in this work was approximately two seconds with all six cameras synced together by the same trigger and data acquisition computer. Three camera modules were used such that three-component velocity measurements were possible and so that the scalar values could be averaged to reduce uncertainty.

IV. Filtered Rayleigh Scattering Results

This section serves to present the FRS results that were measured in the exhaust plume of the Honeywell TFE731-2. The directly measured planar results will be discussed first followed by a discussion of the derived planar results. Several spatial locations will be shown with corresponding measured and fitted spectra (process described by Powers et al. [10]). The section will end by separating the core and bypass flow streams using the EPES methodology developed by Powers et al. [7]. The two major equations from the extended parallel streamtube method (EPES) are copied below in Eq. 2 and 3. Equation 2 defines the expanded velocity equation which is the velocity that has been isentropically expanded to the Trefftz plane. Equation 3 defines the final force values with all quantities measured directly by FRS or derived from FRS only. The result of Eq. 2 and the variables needed to calculate the final force in Eq. 3 can be seen in Fig. 5. Note that the signal-to-noise ratio of the FRS data was too low (20 dB) for the modeling of exhaust gasses to have an impact on the final results which was explained in detail by Powers et al. [10]. Therefore, air is modeled for the Rayleigh scattering cross section as well as for the specific gas constant and specific heat ratio. The fuel contribution to the force was approximately 42 N, and this will be accounted for as an addition to the FRS core force in this work. This will not be distinctly shown in any of the results tables.

$$\overline{V}(p_t, h_t) = \sqrt{2h_t \left[1 - \left(\frac{p_\infty}{p_t}\right)^{\frac{\gamma-1}{\gamma}}\right]} \tag{2}$$

$$\mathcal{F}_{EPES} = \sum_{k=1}^{N_{Streams}} \sum_{l=1}^{N_{x_k}} \sum_{m=1}^{N_{y_k}} \left[\rho_{s_{(l,m,k)}} \left(\overline{V}_{(l,m,k)} - U_\infty\right) W_{(l,m,k)} A_{(l,m,k)}\right] + \dot{m}_{fuel} W_\infty \tag{3}$$

Figure 4 includes two raw FRS images from camera module 0. Figure 4.A is from the filtered camera which looks through the iodine vapor cell, and Fig. 4B is from the camera which directly views the region of interest unimpeded. These example images were taken at a frequency that corresponded to a low iodine transmission region which works to filter out most of the Mie and background scattering influences. However, the soot from the core flow was such that the Mie scattering influence remained high. This increase in Mie scattering was correctly captured and modeled with little impact on the final results for velocity, static temperature, and static density. Figure 5 shows the Mie scattering ratios in the core to be approximately four times higher than the Rayleigh scattering. If the Mie scattering was not modeled, all other values would have incurred large biases. The non-symmetry of the light intensity (soot pattern) remained

relatively constant across all laser frequencies and was captured well as seen in Fig 5.

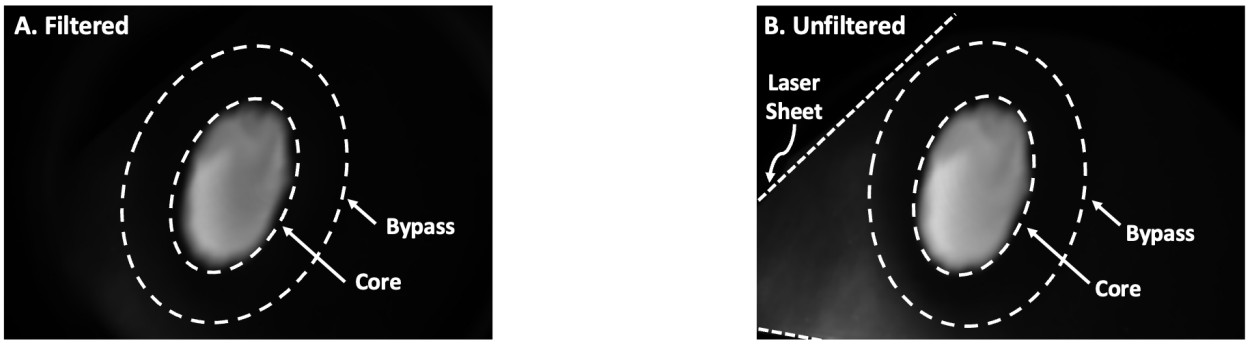

Fig. 4 Raw FRS images from the experiment. Images were taken at the same time in a low iodine transmission region. A: Image from the filtered camera showing large Mie scattering effects in the core. B: Image from the unfiltered camera in which the laser sheet is visible along with the core and bypass regions.

The green dashed lines that form a box in Fig. 5 indicate the directly measured variables from FRS. In this case, directly measured means independent primary measurements of three sensed velocities from the three camera modules, Mie scattering intensity ratio, background scattering intensity, static temperature, and static density. The Mie and background scattering values are specific to each camera module. The ones shown in Fig. 5 are from camera module 0, but they are representative of all three camera modules. The static temperature and static density results have been averaged over all three camera modules to reduce the final uncertainty values which will be discussed further in Section V. Sensed velocity is the velocity measured in the direction defined by the difference in the laser propagation direction ($\hat{i}$) and the observer direction ($\hat{o}$) as seen in Eq. 1. The sensed velocities need to be rotated back to orthogonal components as described by Cadel et al. [26] before conclusions about the flow field can be drawn.

The orange dashed lines that form a box in Fig. 5 indicate the derived measured variables from FRS. This means that the directly measured values in green have been used to produce those in orange. These values include the three orthogonal velocities, Mach number, static and total pressure, total temperature, total density, and the expanded velocity term as described by Drela [6] and Powers et al. [7] which will be needed for the final force calculation. Overall, the difference in the approximately static freestream, bypass stream, and core stream can be seen. The exhaust plume is non-symmetric with slightly higher velocity values on the right side of the plane. As discussed in Powers et al. [10], the Mie and background scattering values are not entirely independent from one another in the fitting scheme, so the background scattering values are not zero but are low and within the expected range given the experimental setup. Although no validation probe measurements were taken, the force calculated from these measurements will be shown later to match the measured force well. It should be noted that these results used a pixel bin of 5 x 5 pixels for an approximate spatial resolution of 2.5 mm x 2.5 mm which resulted in an approximate SNR of 20 dB. Overall, Fig. 5 clearly shows the expansive capability of a non-intrusive optical measurement technique such as FRS where many values can be measured simultaneously.

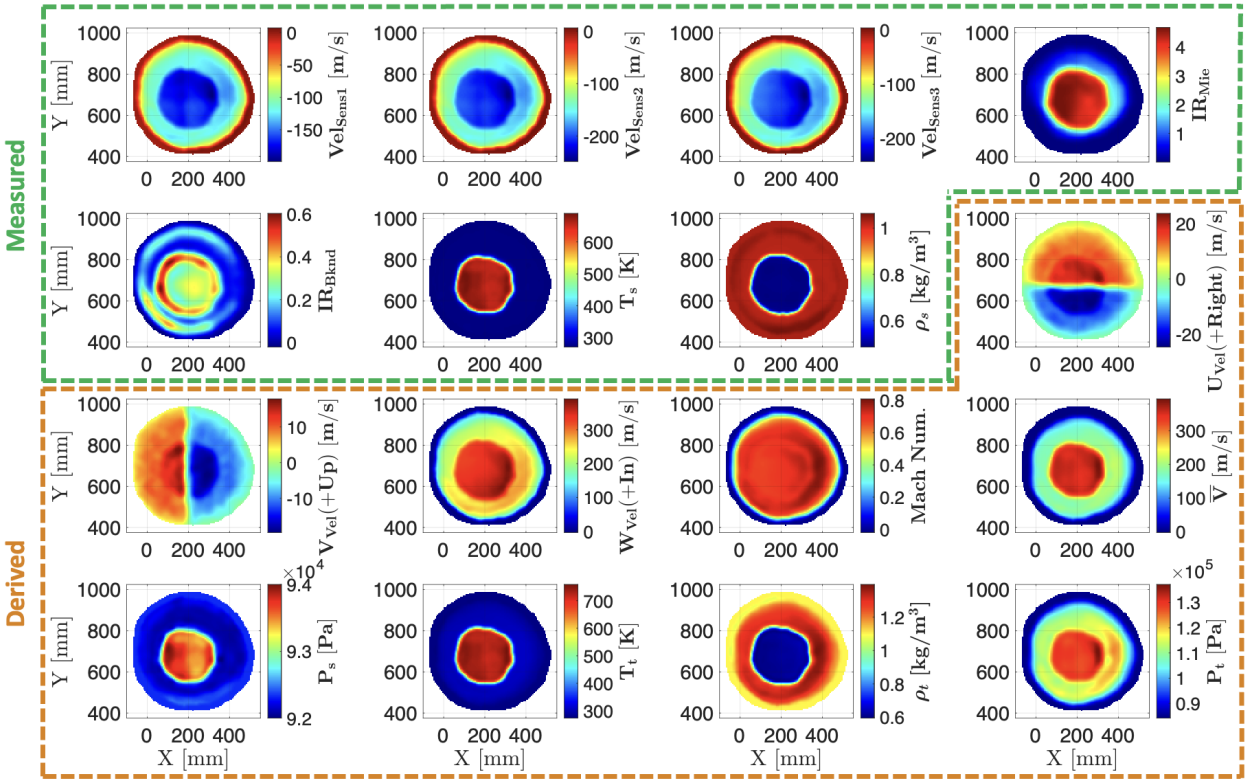

Fig. 5 Planar FRS results for the exhaust flow of a Honeywell TFE731-2. Green indicates directly measured quantities. Orange indicates derived quantities. Note: All figures have a 2x2 median filter applied.

To give credence to the fitting scheme discussed in Section II and the values found in Fig. 5, Fig. 6 has been included. The contour in the middle is of the axial velocity with the in-plane velocity component vectors plotted on top. In Fig. 6 the black and purple locations are in the core and the pink and orange locations are in the bypass flow stream. The red and purple locations were chosen to show that the modeled spectra can be fit to the measured spectra even though the core is non-symmetric as seen clearly in the static temperature and Mie intensity ratio planar results in Fig. 5. In both locations, the experimentally measured and fitted simulated spectra match well. Based on the intensity counts, the camera's dynamic range was almost fully maximized which allowed for easier fitting and the maximum amount of information to be extracted. The pink and orange locations were chosen such that the velocity values were slightly different as seen in the orthogonal velocities in Fig. 5. This slight velocity difference can be seen in the spectra where the orange spectra has more points to the left of its minimum point compared to the spectra outlined in pink. Since the wavenumber range was kept constant, the portion of the iodine absorption lines shown changes based solely on the Doppler shift from the bulk velocity. This velocity shift is clear when comparing the spectra from the red and purple locations (core flow) to the spectra from the orange and pink locations (bypass flow). Overall, the simulated spectra fit well with the measured spectra (average of 150 count difference across the entire plane and all cameras) giving high confidence in the results. Note that the noise in the bypass flow spectra seems higher than that of the core flow spectra. This is only because the bypass flow spectra have a much lower intensity count range than the core flow spectra.

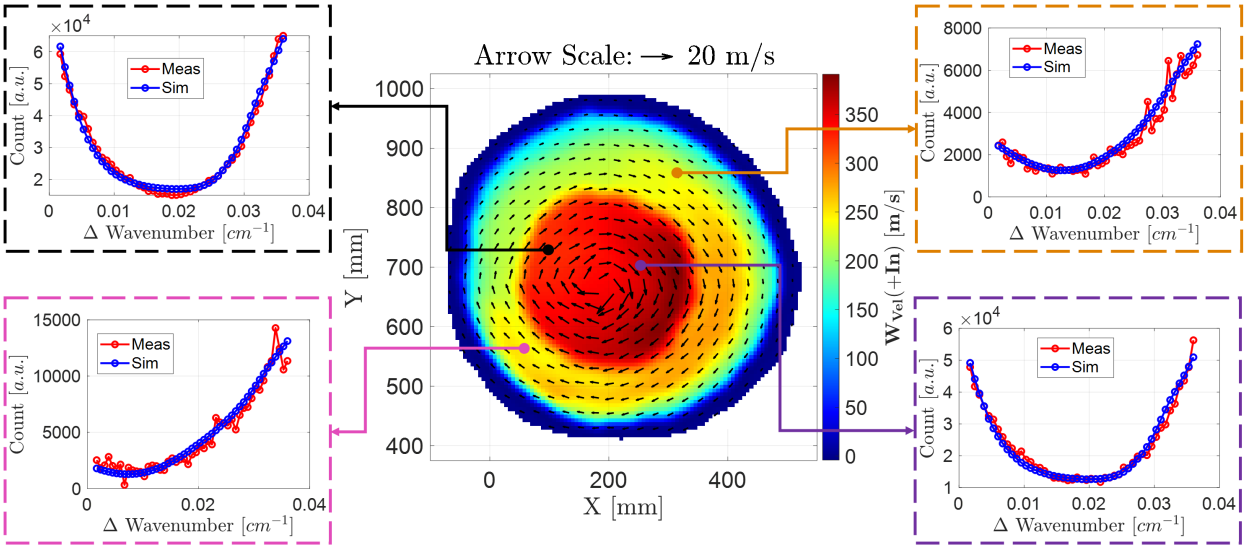

Fig. 6 Axial velocity contour with in-plane velocity vectors. Four representative spectra with plotted measured spectra in red and fitted modeled spectra in blue.

To decompose the exhaust flow stream into core and bypass streams, the methodology developed by Powers et al. [7] was employed. The radial gradient of the axial velocity is used along with Prandtl's mixing length model [27] to approximate the location of the maximum turbulent shear stress. Townsend [28] hypothesizes that a dividing streamline can be located at the maximum shear stress location where the mass flow below that line belongs to the first flow stream and the mass flow above that line belongs to a second flow stream. This will be used to decompose the exhaust flow into the core and bypass streams. It should also be noted that the momentum transfer across the dividing line is assumed negligible since only the total force is considered and the in-plane velocity components are not considered in the EPES method. However, if the force were to be decomposed into thrust and drag, the momentum transfer and in-plane components could not be assumed negligible. This kind of decomposition has been left for future work.

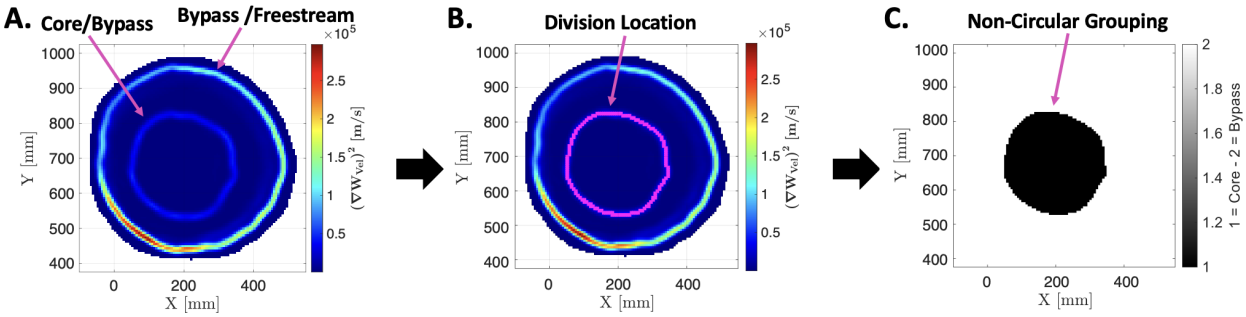

Fig. 7 Grouping of data into flow streams using the square of the axial velocity gradient. A: Clear indicators of the mixing layer between the three different regions. B: Maximum of the squared velocity gradient shown in magenta representing the dividing line between the flow streams. C: Final data grouping.

Figure 7 is a visual representation of the decomposition process. The square of the velocity gradient is used because it provides a clear distinction between the core and bypass streams as well as the bypass stream and the static freestream.

The rings seen in Fig. 7.A are essentially the mixing layers between the exhaust streams. However, only the core and bypass mixing layer is needed in this case. Any force contribution from the freestream must be due to entrained flow and therefore needs to be considered as part of the bypass force contribution. The location of the maximum squared velocity gradient in the core/bypass mixing layer is used as the dividing location between the two streams. This location has been highlighted by the pink ring in Fig. 7.B, and this can then be used to group the data into regions which can be seen in Fig. 7.C. It can be seen that the resulting core data is not perfectly circular which would be expected in a non-uniform exhaust case such as that in Fig. 5.

Now that the flow streams have been separated, the same grouping can be applied to the values seen in Fig. 5, which can then be used along with the extended parallel expanded streamtube method (EPES) as defined by Powers et al. [7] and Eq. 3 to determine the total force, core force, and bypass force. The term "force" is used instead of "thrust" since no effort is made to separate drag flow streams such as boundary layers in the flow streams. The final results can be seen in Table 1 where the first row is the total number of bins in each section and the second row contains the force values. The total FRS measured force (8995 N) compares well with the force balance measured force (9007 N) with an absolute percent difference of 0.13%. The bypass ratio was measured to be 2.53 which also compared well to the known bypass ratio of 2.60 with a difference of 2.7%. Section V will provide the full uncertainty breakdown for these force values as well as all values seen in Fig. 5. Again, the force from the fuel flow (42 N) has been incorporated into the core force value.

Table 1 Force results using FRS and control volume analysis.

	Total	*Core*	*Bypass*
Num. of Bins	7026	1808	5218
Force [N]	8995	4085	4910

V. Uncertainty Analysis

This section presents the uncertainty analysis for this FRS measurement by using the uncertainty framework in Powers et al. [7], with three different sources of uncertainty: random, bias, and control volume. The section will conclude with the force uncertainty breakdown as well as the error influence coefficients (EICs).

A. Random Uncertainty

To start, random uncertainty in the primary measured variables can be derived by using Monte Carlo simulations at representative flow conditions from the core and bypass flow streams. This has been done in Fig. 8 over a wide range of signal-to-noise ratios (defined by Eq. 4). Simulated spectra with Gaussian noise are used as "measured spectra" to use the same fitting code for the Monte Carlo simulations as was used in the actual experiment. The Monte Carlo simulations were not needed to deduce the primary uncertainties in Powers et al. [7] as those values were assumed for

demonstration purposes only.

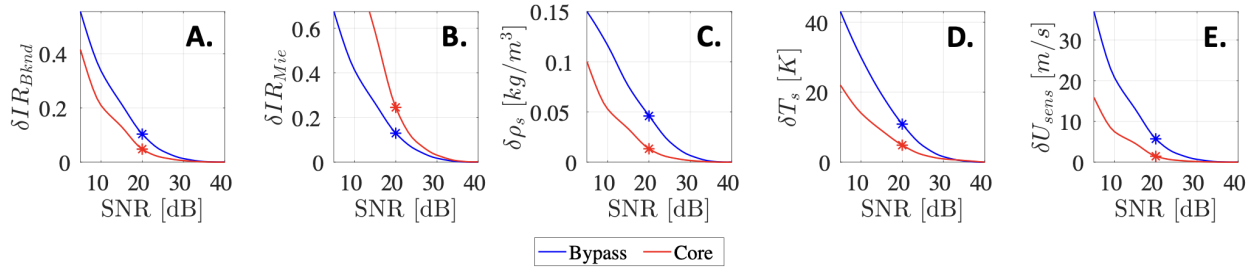

Fig. 8 Monte Carlo simulation results to get one-sigma (68%) primary uncertainties. A: Background scattering intensity ratio. B: Mie scattering intensity ratio. C: Static density. D: Static temperature. E: Sensed velocity.

$$SNR[dB] = 10log_{10}\left(\frac{\sigma_S^2}{\sigma_N^2}\right) \tag{4}$$

The SNR of the experimental data was approximately at an SNR level of 20 dB. Two stars have been plotted on top of the curves in Fig. 8 to reflect the core and bypass flow stream uncertainty values at this SNR level. The delta values on the y-axes represent one-sigma (68% confidence) uncertainty values. However, the values seen to the left of the triple vertical lines in Table 2 reflect two-sigma (95% confidence) uncertainty values. This has been done such that the final uncertainty values will all be two-sigma values. These five primary uncertainties reflect the same measured variables seen in Fig. 5.

Table 2 Two-sigma (95%) confidence intervals for all random uncertainty values. Values to the left of the triple vertical line are directly measured by FRS. Two decimal points are used to show relative magnitudes.

$\mathcal{X}$	$Core$	$Bypass$	$\mathcal{X}$	$Core$	$Bypass$	$\mathcal{X}$	$Core$	$Bypass$
δIR_{Bknd}	0.10	0.20	$\delta U[m/s]$	6.24	11.26	δM	0.02	0.06
δIR_{Mie}	0.50	0.26	$\delta V[m/s]$	6.52	11.96	$\delta P_s[Pa]$	2182.18	6633.06
$\delta\rho_s[kg/m^3]$	0.02	0.10	$\delta W[m/s]$	5.94	10.82	$\delta P_t[Pa]$	3435.56	8893.44
$\delta T_s[K]$	9.70	21.74	$\delta(\Delta U)^2[m^2/s^2]$	643.12	1265.64	$\delta T_t[K]$	9.82	21.78
$\delta U_{Sens}[m/s]$	2.90	11.46	$\delta\overline{V}[m/s]$	13.62	19.52	$\delta\rho_t[kg/m^3]$	0.02	0.12

The variables to the right of the three vertical lines are the two-sigma uncertainty values for the derived variables. Again, these values exist for the core and the bypass regions since the flow conditions are vastly different and the primary uncertainties are different in this region. Each uncertainty was found by using the propagation of uncertainty equation for random variables as seen in Powers et al. [7]. In some cases, the uncertainty becomes relatively high because of compounding primary uncertainties. This underlines the importance of achieving the highest SNR possible in any future experiments. The SNR could not be pushed higher in this work due to limited laser power, environmental factors such as sound levels and vibrations, and the cameras that were used to take the data. Future experimentation should seek to protect the measurement equipment from these environmental error sources. A higher dynamic range camera should also be used.

Table 3 Two-sigma (95%) confidence intervals for all random uncertainty values that are not dependent on FRS measurements or flow type.

$\delta A[m^2]$	$\delta R[J/kg*K]$	$\delta\gamma$	$\delta P_{s_\infty}[Pa]$	$U_\infty[m/s]$
$1.27e^{-7}$	0	0	0	0

On top of the primary and derived random uncertainties, Table 3 introduces the rest of the random uncertainties that could occur during an experiment like the one presented in this work and that are needed for force quantification. The individual bin area uncertainty is very small and comes from the camera location calibration. Since the SNR of the measurement is approximately 20 dB, any error in the specific gas constant and specific heat ratio is assumed zero since the effect on the Rayleigh scattering signal is below the noise floor (see Powers et al. [10] for a more detailed explanation). The freestream (in this case static freestream) random uncertainty is also assumed to be zero. Independent probe measurements were taken of each with negligible uncertainty. It is important to note that FRS could be used to measure the static freestream pressure and freestream velocity. However, since this work was done on the ground, it was effortless to take probe measurements of these variables. Now that the random uncertainty has been quantified, the second source of uncertainty, bias uncertainty, may be examined.

B. Bias Uncertainty

The bias uncertainty quantification again follows the equations derived by Powers et al. [7]. Specifically, the derivations follow the SUM*U* technique [29] where the bias uncertainty is added to the 95% confidence random uncertainty, but only with one-sigma values. This is the reason that Table 4 contains only one-sigma values. Unlike the primary random uncertainties, the primary bias uncertainties cannot be quantified using Monte Carlo simulations. Instead, the known freestream values were compared to the measured FRS values. The difference between those values was taken as the bias uncertainty. These values were also assumed constant over the entire plane. Future work will address measuring local bias values.

Table 4 Bias uncertainty values (one-sigma — 68%) to be used with the SUM*U* method. Values to the left of the triple vertical line are directly measured by FRS (values to the right are derived). Values to the right of the double vertical line are not dependent on FRS measurements. Two decimal points are used to show relative magnitudes.

$\mathcal{X}$	Bias	$\mathcal{X}$	Bias	$\mathcal{X}$	Bias	$\mathcal{X}$	Bias
$\delta U_{Sens}[m/s]$	+5.00	$\delta U[m/s]$	+2.86	δM	+0.03	$\delta A[m^2]$	0
$\delta T_s[K]$	+6.00	$\delta V[m/s]$	+3.12	$\delta P_S[Pa]$	+900.01, -1865.56	$\delta R[\frac{J}{kg*K}]$	0
$\delta\rho_s[kg/m^3]$	-0.01	$\delta W[m/s]$	+9.27	$\delta P_t[Pa]$	+1370.74, -2553.28	$\delta\gamma$	0
δIR_{Mie}	+0.01	$\delta(\Delta U)^2[\frac{m^2}{s^2}]$	+586.41	$\delta T_t[K]$	+6.25, -2553.28	$\delta P_{s_\infty}[Pa]$	0
δIR_{Bknd}	+0.04	$\delta\overline{V}[m/s]$	+7.03, -11.58	$\delta\rho_t[\frac{kg}{m^3}]$	+0.004, -0.013	$\delta U_\infty[m/s]$	0

The bias uncertainty values are also one-sided meaning they are either positive or negative. The propagation of uncertainty equation can still be used, however, it will have to be used for positive uncertainties only and then negative uncertainties only. Some of the derived values to the right of the triple vertical lines in Table 4 have both positive and

negative values depending on the associated primary variables. The non-FRS-related bias uncertainty variables are all assumed to have zero bias and can be seen to the right of the double vertical lines. Now that the random and bias uncertainties have been quantified, the control volume uncertainty can be investigated.

C. Control Volume Uncertainty

The control volume uncertainty is the easiest to quantify and is also expected to be the largest. Figure 9 is a good visual representation of the technique. Once the maximum squared axial velocity gradient points (Fig. 9.A) within the mixing layer between the core and bypass values are found, a two-sigma (95% confidence interval) can be drawn around those points and can be seen in Fig. 9.B. All of the data points within that bound are then considered for the uncertainty analysis. The force through each of these points is calculated using the EPES method. Each individual force is then summed to produce the force through this ring. This force is then considered to be the two-sigma control volume uncertainty. In this case, that value is 430 N. No control volume bound is needed between the bypass and freestream because only the plume boundary is used. Further, Eq. 3 shows that the force is based on a difference in velocity compared to the freestream. In other words, no net force is possible through the freestream so any freestream data points that are included in the analysis will not change the final force calculation.

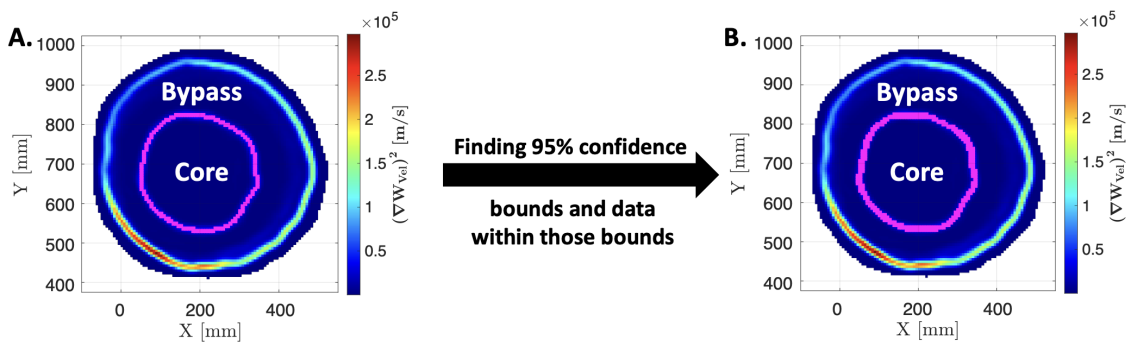

Fig. 9 Finding the control volume error by using confidence bounds and calculating the force through that area. A: Highlighted maximum locations. B: Grouped data points to be included in error calculation. Two decimal points are used to show relative magnitudes.

As seen in Powers et al. [7], spatial resolution has a large impact on the control volume uncertainty magnitude. Higher resolution drives down the standard deviation of the velocity gradient, therefore the 95% confidence bounds shrink and so too for the resulting force bounds. Future experiments should aim to increase the resolution while maintaining an acceptable SNR level. However, a high resolution is more impactful to the overall uncertainty.

D. Total Combined Uncertainty

Now that all three sources of uncertainty have been defined and the magnitudes found, they must be combined to give final uncertainty values. As seen in Table 5. The number of bins and force values has been repeated from Table 1 for clarity. The number of bins is important for random uncertainty since the random uncertainty scales with

$1/\sqrt{N}$. Even though some of the random uncertainty values were large, they become negligible because of this scaling. This scaling is not present in the bias or control volume uncertainty. By increasing the spatial resolution this scaling factor gets smaller and the control volume uncertainty also decreases. However, the SNR decreases and the random uncertainty goes up. A balance must be had between a low SNR and a high spatial resolution.

Table 5 Final force results with uncertainty values. Two-sigma (95%) confidence intervals as defined by the SUM*U* method. Magnitude and percent error is given.

	Total	Core	Bypass
Number of Bins	7026	1808	5218
Force [N]	8995	4085	4910
Random Uncertainty [N]	± 0.44 (± 0.005%)	± 1.87 (± 0.046%)	± 0.91 (± 0.019%)
Bias Uncertainty [N]	+23.25 (+0.26%) -18.93 (-0.21%)	+8.66 (+0.21%) -15.58 (-0.38%)	+21.56 (+0.44%) -10.75 (-0.22%)
Control Volume Uncertainty [N]	—	± 430 (± 10.53%)	± 430 (± 8.76%)
Total Uncertainty [N]	+23.25 (+0.26%) -18.93 (-0.21%)	+440.58 (+10.79%) -447.50 (-10.96%)	+452.53 (+9.22%) -441.72 (-9.00%)

The bias and control volume uncertainties are much larger than the random uncertainty. The bias uncertainty is relatively small at less than 0.5% in any region. However, the control volume uncertainty is large. The total force is unaffected by the control volume uncertainty since the exhaust forces are not decomposed. Therefore, the total force uncertainty is approximately 0.25%. Since the core force is the smallest and it is directly affected by the control volume uncertainty, the core force uncertainty is the largest, and approaches 11%. For the same reasons, the bypass force uncertainty is also high at approximately 9%. Again, these percentages could be much lower with an increased spatial resolution.

The results of an additional investigation into the error influence coefficients can be seen in Fig. 10. These coefficients are based solely on the primary random variables as seen in Table 2 and Table 3. However, a similar chart would follow for the bias values as well. Figure 10.A has a log y-axis, and Fig. 10.B has a linear y-axis. This was done to see all of the EICs on one chart but also the relative magnitudes. For example, the area uncertainty can only be seen with a log y-axis. Overall, static density has the largest impact on uncertainty, and that is followed by static temperature. This is the case with the EPES method since the static density directly impacts the force equation (Eq. 3) and the static density impacts the expanded velocity (Eq. 2) which feeds directly into the force equation. Notice that the static temperature and static density uncertainties have an inverse relationship between the core and bypass flow streams. The static temperature uncertainty in the core is low but the static density uncertainty is high and the opposite is true for the bypass flow stream. The magnitude of the sensed velocity and area uncertainties are much lower in general compared to the static temperature and static density. However, they are still non-negligible and efforts should be given to mitigate their impact.

Again, the other four primary uncertainties have been assumed zero. Their impact is below the noise floor of the FRS

experimental data. In actuality, these will never be zero. Powers et al. [7] showed that these can have a non-negligible impact on the overall uncertainty. Future work with higher SNR levels will have to quantify these values for a more accurate overall uncertainty framework. This may require additional flow measurement techniques or flow simulations that can measure or predict exhaust flow gas properties. Such investigations have been left for future work.

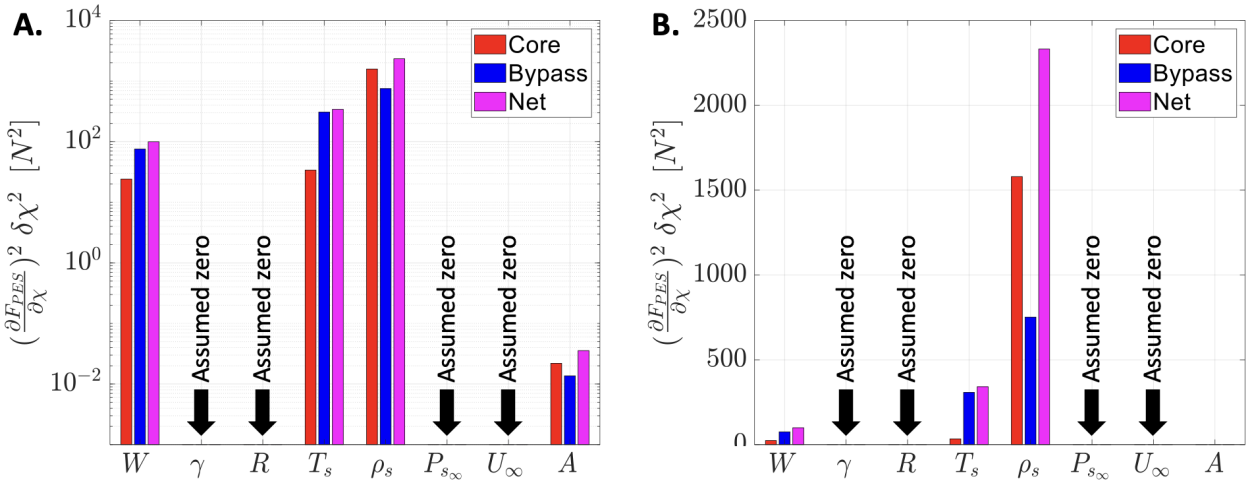

Fig. 10 Error influence coefficients (EICs) for all uncertain variables. $\mathcal{X}$ is a placeholder variable. A: Log scale. B: Linear scale.

VI. Conclusions

The introduction of the particle swarm optimization solver and control volume analysis enabled accurate filtered Rayleigh scattering measurements in the exhaust of a Honeywell TFE731-2 turbofan engine at the Virginia Tech TurboLab. The particle swarm optimization technique was needed to find the global minimum of the fit between the experimental spectra and modeled spectra over the entire plane of data. The final FRS measured force value of 8995 N has an error of 0.13% when compared to the 9007 N measured by the force balance. The core and bypass flow streams were separated using the method laid out in Powers et al. [7]. The measured core force was approximately 4085 N and the bypass force was approximately 4910 N. No independent measurements of the core and bypass force were available for comparison. However, the bypass ratio was also experimentally measured to be 2.53 which has a 2.3% error compared to the known value of 2.6. The final uncertainty values contained random, bias, and control volume sources which resulted in maximum uncertainty values of approximately 0.25% for the total force, 11% for the core force, and 9% for the bypass force. The total force uncertainty is much lower than the core and bypass flow uncertainty because no control volume uncertainty is introduced into the EPES total force calculation. Future experiments should seek to increase the spatial resolution while keeping the signal-to-noise ratio at acceptable levels to decrease the control volume uncertainty. Overall, it was shown that filtered Rayleigh scattering combined with teh EPES control volume analysis produces a powerful experimental tool that is capable of force decomposition in non-ideal environments.

Acknowledgments

The authors wish to acknowledge the Science, Mathematics, and Research for Transformation (SMART) scholarship, the Aerospace and Ocean Engineering department at Virginia Tech, and Pratt & Whitney for supporting the authors in the development of this extended control volume technique. The authors also wish to acknowledge Matt Boyda for his technical insight and assistance in data acquisition.

References

[1] Conners, T., and Sims, R., "Full flight envelope direct thrust measurement on a supersonic aircraft," *34th AIAA/ASME/SAE/ASEE Joint Propulsion Conference and Exhibit*, 1998. https://doi.org/10.2514/6.1998-3872.

[2] "SAE AIR1703A: In-Flight Thrust Determination," , 2017. URL https://www.sae.org/standards/content/air1703a.

[3] Davidson, T. W., "Measurement of net thrust in flight," *Journal of Aircraft*, Vol. 1, No. 3, 1964, p. 107–113. https://doi.org/10.2514/3.43575.

[4] "SAE AIR1678B: Uncertainty of In-Flight Thrust Determination," , 2016. URL https://www.sae.org/standards/content/air1678b/?src=air1703a.

[5] Drela, M., "Power balance in aerodynamic flows," *AIAA Journal*, Vol. 47, No. 7, 2009, p. 1761–1771. https://doi.org/10.2514/1.42409.

[6] Drela, M., "Considerations in aerodynamic force decomposition," *AIAA AVIATION 2021 FORUM*, 2021. https://doi.org/10.2514/6.2021-2552.

[7] Powers, S. W., Hanley, K., Lowe, K. T., and Schetz, J., "Control Volume Analysis for Experimental Force Bookkeeping on a Turbofan Engine," *AIAA Journal*, 2023. [Submitted].

[8] Powers, S. W., Byun, G., and Lowe, K. T., "Validation of Filtered Rayleigh Scattering Optical Rake Measurement Techniques in Turbomachinery Applications and Boundary Layers," *TurboExpo 2023 — GT2023-102014*, 2023. [Submitted].

[9] Quellwerke, "JetCat P100-RX," , 2023. URL https://www.jetcat.de/en/productdetails/produkte/jetcat/produkte/hobby/Engines/p100_rx.

[10] Powers, S. W., Byun, G., and Lowe, K. T., "Auto-Processing of Filtered Rayleigh Scattering Images Including Mie and Background Scattering Contributions," *Experiments in Fluids*, 2023. [Submitted].

[11] "TurboLab legacy," , Oct 2021. URL https://www.aoe.vt.edu/research/multidisciplinary-centers-labs/appl/turbolab.html.

[12] Warner, E. P., and Lowe, K. T., "Machine-Learned Background Quantification for Filtered Rayleigh Scattering Measurement Processing," *Submitted to AIAA SciTech 2023*, 2023.

[13] Marquardt, D. W., "An algorithm for least-squares estimation of nonlinear parameters," *Journal of the Society for Industrial and Applied Mathematics*, Vol. 11, No. 2, 1963, p. 431–441. https://doi.org/10.1137/0111030.

[14] "lsqnonlin," , 2023. URL https://www.mathworks.com/help/optim/ug/lsqnonlin.html.

[15] Doll, U., Dues, M., Bacci, T., Picchi, A., Stockhausen, G., and Willert, C., "Aero-thermal flow characterization downstream of an NGV cascade by five-hole probe and filtered Rayleigh scattering measurements," *Experiments in Fluids*, Vol. 59, No. 10, 2018. https://doi.org/10.1007/s00348-018-2607-z.

[16] Doll, U., Stockhausen, G., and Willert, C., "Endoscopic filtered Rayleigh scattering for the analysis of ducted gas flows," *Experiments in Fluids*, Vol. 55, No. 3, 2014. https://doi.org/10.1007/s00348-014-1690-z.

[17] Schroll, M., Doll, U., Stockhausen, G., Meier, U., Willert, C., Hassa, C., and Bagchi, I., "Flow Field Characterization at the outlet of a lean burn single sector combustor by laser-optical methods," *Volume 6: Ceramics; Controls, Diagnostics and Instrumentation; Education; Manufacturing Materials and Metallurgy*, 2016. https://doi.org/10.1115/gt2016-56365.

[18] Venter, G., and Sobieszczanski-Sobieski, J., "Particle swarm optimization," *AIAA Journal*, Vol. 41, No. 8, 2003, p. 1583–1589. https://doi.org/10.2514/2.2111.

[19] "particleswarm," , 2023. URL https://www.mathworks.com/help/gads/particleswarm.html.

[20] "Virtual library of simulation experiments:," , 2013. URL https://www.sfu.ca/~ssurjano/stybtang.html.

[21] "Fun," , 2023. URL https://www.mathworks.com/help/matlab/ref/fminsearch.html.

[22] "TFE731 turbofan engine," , 2023. URL https://aerospace.honeywell.com/us/en/products-and-services/product/hardware-and-systems/engines/tfe731.

[23] "TFE731-2 Specifications," , 2023. URL http://www.pilotfriend.com/aero_engines/engine_specs/Garrett/2.htm.

[24] "Thorlabs - GVS211 1D large beam (10 mm) diameter galvo system, Broadband Mirror (-E02), power supply not included," , 2023. URL https://www.thorlabs.com/thorproduct.cfm?partnumber=GVS211.

[25] "FLIR blackfly BFLY-U3-23S6C-C camera: Edmund optics," , 2023. URL https://www.edmundoptics.com/p/bfly-u3-23s6c-c-usb-30-blackfly-color-camera/3130?gclid=CjwKCAiAxvGfBhB-EiwAMPakqtnvcWM7x1aGRZ8duZYAXWuYul-Ul0n3jVMc7OCmwqVVPfOAGBVsjxoCiacQAvD_BwE.

[26] Cadel, D. R., and Lowe, K. T., "Cross-correlation Doppler Global Velocimetry (CC-DGV)," *Optics and Lasers in Engineering*, Vol. 71, 2015, p. 51–61. https://doi.org/10.1016/j.optlaseng.2015.03.012.

[27] Schetz, J., and Bowersox, R., *Boundary Layer Analysis*, American Institute of Aeronautics and Astronautics, 2012.

[28] Townsend, A. A., *The structure of turbulent shear flow*, C.U.P., 1976.

[29] Phillips, S., Eberhardt, K., and Parry, B., "Guidelines for expressing the uncertainty of measurement results containing uncorrected bias," *Journal of Research of the National Institute of Standards and Technology*, Vol. 102, No. 5, 1997, p. 577. https://doi.org/10.6028/jres.102.039.

Chapter 7 - Conclusions and Outlook

This present work focused on two main areas necessary for the advancement of an optical-based measurement of in-flight forces using filtered Rayleigh scattering (FRS). The first sought to fundamentally understand various scattering mechanisms and investigated how to properly model these effects. Along with this, an automatic post-processing scheme was divided and implemented to keep potential errors/bias from the user out of the final results. This effort led to an algorithm that efficiently and quickly processes raw FRS data for scattering angle, static temperature, 3-component velocity, Mie and background scattering intensity ratios, and static density whereby the isentropic gas and ideal gas assumption can be used to produce total flow and pressure values. The second involved the implementation of the new FRS technique for engine applications and understanding how to handle those types of conditions. Averaging techniques were explored and implemented to get the best possible final result and accuracy. Finally, the entire technique was validated by taking an accurate static ground force measurement.

7.1 Conclusions

This dissertation work describes the fundamental methodology behind the filtered Rayleigh scattering measurement technique and its combination with an extended control volume analysis to allow for force decomposition on the ground and in-flight for turbomachinery. Although seemingly narrow in focus, this research is relevant to both fundamental research as well as applied research. Fundamental research was completed on extending current FRS modeling techniques to add the ability to account for unwanted scattering effects such as Mie and background scattering. The derived processing techniques were needed for realizable application to non-ideal experiments and eventual flight tests. Previous control volume techniques were purely theoretical with no real-world validation. A fundamental control volume technique was extended and validated through extensive experimentation. The control volume work is applicable to any measurement technique (traditional probes, optical methods, etc.) that is capable of measuring the necessary variables. In working towards these advancements, the shortcomings in previous literature were described and assessed as part of the knowledge gap discussion. This work aimed to fill in those gaps. The findings of the works presented in this dissertation are summarized as follows:

- An FRS auto-processing iterative scheme using a non-linear least-squares fitting model can be used to quickly and accurately (1% at an SNR of 30 dB) determine flow variables in most applications. This includes unwanted scattering effects such as Mie and background scattering.
- Five different Raleigh-Brillouin scattering models were compared and Doll's analytic Tenti-S6-based model was ultimately selected for its efficiency and agreement with the numerical Tenti-S6 model.
- The FRS auto-processing scheme was validated using a mini turbojet (JetCat) with a comparison to traversing probe data. All flow variables (velocity, static and total values for temperature, pressure, and density) compared within 2% RMSE between the FRS and probe-measured data.
- Physical probe rakes off lower pointwise uncertainty (0.8% RMSE) compared to FRS optical rake measurements (2% RMSE).
- The spatial resolution of the FRS optical rake can be used with bin averaging to decrease the uncertainty to levels comparable to physical probe rakes.

- The information gained from precise measurements at a few locations (physical probe rake) cannot compete with approximately the same uncertainty measurement at many different locations (FRS optical rake).
- FRS optical rake data is approximately normally distributed. Spatial binning can lead to biasing away from a normal distribution.
- Mass-averaged inlet efficiency can be computed accurately with an FRS optical rake to within 0.1% of the physical probe rake.
- An FRS optical rake can be used with confidence on non-ideal (vibration and sound) rigs such as turbine engines.
- Drela's parallel expanded streamtube method (PES) can be extended to the extended parallel expanded streamtube method (EPES) which is capable of force decomposition in the exhaust flows of turbomachinery using Townsend's observation.
- FRS measured static temperature and static pressure uncertainties contribute the most to the random and bias uncertainty. The SUMU method is used to add bias and random uncertainties together.
- The squared gradient of axial velocity can be used to divide the flow streams. This division can be seen by the eye and is easy for an automatic algorithm to find.
- Particle swarm optimization solver is needed in place of the non-linear least-squares solver when high flow gradients are present.
- Total ground force measurements are possible with an FRS measurement to within approximately 0.1%. Bypass ratio measurement accuracy is approximately 2%.
- Control volume uncertainty is several orders of magnitude larger than random or bias uncertainty and leads to uncertainty values for the core and bypass force of approximately 10%.
- The spatial resolution of the FRS data should be maximized while also balancing the signal-to-noise ratio to decrease the control volume uncertainty.

Overall, this work has provided evidence that the combination of the filtered Rayleigh scattering technique along with the extended parallel expanded streamtube control volume

methodology is a powerful technique capable of force measurements and their decomposition. This work has laid the groundwork for future implementation into in-flight measurements.

7.2 Outlook

The work presented in this dissertation has greatly improved our understanding of combing a control volume methodology with the filtered Rayleigh scattering measurement technique as an application towards in-flight force measurements. Namely, this work was focused on two main tasks. The first was the production of a robust and quick post-processing methodology for raw FRS data. The second was the development of the extended parallel expanded streamtube method which allows for force components to be decomposed into individual contributions. this work laid the fundamental groundwork for in-flight testing. Nevertheless, several open questions still remain regarding these topics. These challenges are described as follows:

- Control volume analysis development including the freestream, pylon, boat tail, and wing. This can be considered the most important and remaining work. The introduction of these items into the analysis will raise the complexity of the techniques needed to separate the components to get individual thrust and drag components.
- The implementation of on-engine hardware and in-flight integration remains unknown. On-engine hardware such as fiber optics could be tested on the Honeywell TFE731-2 (or a shaker table if only looking at vibrations). In-flight integration will need to be done in conjunction with the airframer and engine manufacturer. This is especially true for the laser integration which will need a pressure and temperature-controlled containment unit to avoid frequency drifts.
- Analysis by Pitt et al. [121] shows that the addition of a UV laser in place of the 532nm green laser currently used shows promise in decreasing uncertainty and increasing SNR.
- The addition of machine learning techniques to speed up the post-processing of FRS data even further looks promising. It is worth looking into replacing the least-squares solver with a machine-learning algorithm. An initial foray into this by Warner et al. [133] seems to point to major time savings while retaining accuracy. This would be the first step towards a ”real-time” measurement.

- The implementation of a ”smart”, non-uniform, averaging technique could lead to large processing time savings. Changes in spectra could be compared to find areas of large and small change. The averaging grid could then be altered to average less in areas of high change and average more in areas of high change. This retains the flow shape and processing accuracy while saving time. The idea of multi-level processing was the first step toward this challenging optimization problem.

- Recent work by Doll et al. [134] provides evidence that time-resolved FRS measurements can be accomplished with the introduction of a multi-camera setup. This could be extremely useful for force measurements in situations that are not time-constant.

The results and conclusions of this work have provided significant knowledge to fill in current knowledge gaps relating to filtered Rayleigh scattering processing and modeling as well as control volume analysis for force decomposition. However, this work also highlights the need for continued investigation of faster FRS processing algorithms and more complete control volume definitions. This work also provided future avenues on which to improve and extend the overall technique. Some of which will be needed for in-flight implementation.

While this work showed significant evidence for a new force measurement capability, further validation and analysis are needed for the industry to accept it as the new standard. Specifically, the technology readiness level mus be elevated past its current state as a highly-specialized technique that few people have implemented. Recent growth in the interest of filtered Rayleigh scattering measurements is promising and should be capitalized on. Future work should focus on technique optimization and the exploration of new pathways such as physical rake replacement. As new technologies are developed and proven the industry standards are sure to adapt. This work and the proposed future work lay out the framework needed to continue pushing the technology forward.

References

[1] SAE AIR1703A: In-flight thrust determination. *SAE International*, Available at: https://www.sae.org/standards/content/air1703a, 2017.

[2] SAE AIR1678B: Uncertainty of in-flight thrust determination. *SAE International*, Available at: https://www.sae.org/standards/content/air1678b/?src=air1703a, 2016.

[3] SAE AIR4065A: Propeller/propfan in-flight thrust determination. *SAE International*, Available at: https://www.sae.org/standards/content/air4065a/?src=air1703a, 2012.

[4] SAE AIR5450: Advanced ducted propulsor in-flight thrust determination. Available at: https://www.sae.org/standards/content/air5450/?src=air1703a, 2014.

[5] SAE AIR5771A: The measurement of engine thrust in an altitude test facility. Available at: https://www.sae.org/standards/content/air5771a/?src=air5450, 2018.

[6] SAE ARP755D: Aircraft propulsion system performance station designation and nomenclature. Available at: https://www.sae.org/standards/content/arp755d, 2014.

[7] Theron W. Davidson. Measurement of net thrust in flight. *Journal of Aircraft*, 1(3):107–113, 1964. DOI: 10.2514/3.43575.

[8] Timothy Conners and Robert Sims. Full flight envelope direct thrust measurement on a supersonic aircraft. *34th AIAA/ASME/SAE/ASEE Joint Propulsion Conference and Exhibit*, 1998. DOI: 10.2514/6.1998-3872.

[9] SAE AIR5925: Measurement uncertainty applied to cost-effective testing. *SAE International*, Available at: https://www.sae.org/standards/content/air5925b/, 2016.

[10] M. Méheut and D. Bailly. Drag-breakdown methods from wake measurements. *AIAA Journal*, 46(4):847–862, 2008. DOI: 10.2514/1.29051.

[11] Mark Drela. Power balance in aerodynamic flows. *AIAA Journal*, 47(7):1761–1771, 2009. DOI: 10.2514/1.42409.

[12] A. Betz. A method for the direct determination of wing-section drag. *NASA Technical Reports*, Nov 1925. Document ID: 19930090720. Available at: https://ntrs.nasa.gov/citations/19930090720.

[13] B. Melvill Jones. Measurement of profile drag by the pitot-traverse method. *Cambridge University Aeronautics Laboratory*, 1936. Available at: https://www.google.com/books/edition/ The Measurement of Profile Drag by the P/2wwoMwEACAAJ?hl=en.

[14] K. Oswatitsch. Gas dynamics. *Academic Press*. Available at: https://www.cambridge.org/core/journals/ journal-of-fluid-mechanics/article/ gas-dynamics-by-klaus-oswatitsch-english-version-by-gustav-kuerti-new-york- academic-press-inc-1956-610-pp-1200/14EF591EB837FA1CD5709A62F489D920.

[15] E. C. Maskell. Progress towards a method of measurement of the components of the drag of a wing of finite span. *Royal Aircraft Establishment TR 72232*, 1973.

[16] D. Destarac and J. van der Vooren. Drag/thrust analysis of jet-propelled transonic transport aircraft; definition of physical drag components. *Aerospace Science and Technology*, 8(6):545–556, 2004. DOI: 10.1016/j.ast.2004.03.004.

[17] J. Van der Vooren and J. Slooff. Cfd-based drag prediction; state-of-art, theory, prospects. *National Aerospace Lab., NLR, TP 90247 U*, 1990.

[18] K. Kusunose. A wake integration method for airplane drag prediction. *Tohoku Univ. Press*, 2005.

[19] C.P. van Dam. Recent experience with different methods of drag prediction. *Progress in Aerospace Sciences*, 35(8):751–798, 1999. DOI: 10.1016/s0376-0421(99)00009-3.

[20] D. Bailly and J. Godard. Méthodologie expérimentale pour l'évaluation de la traînée, techniques de post-traitement, préparation d'essais. *ONERA RT 116/1685 DAAP/Y*, 1999.

[21] M. Méheut and D. Bailly. Drag prediction and wake survey techniques. *CEAS/KATnet Conference on Key Aerodynamic Technologies [CD-ROM]*, 2005.

[22] Mark Drela. Considerations in aerodynamic force decomposition. *AIAA AVIATION 2021 FORUM*, 2021. DOI: 10.2514/6.2021-2552.

[23] A.D. Young. Note on the effect of compressibility on jones's momentum method of measuring profile drag. *R M Report 1881, Aeronautical Research Council*, 1939.

[24] J. D. Denton and N. A. Cumpsty. Loss mechanisms in turbomachinery. *Inst. of Mechanical Engineers Paper C260/87*, 1987.

[25] J. D. Denton. The 1993 IGTI scholar lecture: Loss mechanisms in turbomachines. *Journal of Turbomachinery*, 115(4):621–656, 1993. DOI: 10.1115/1.2929299.

[26] Philippe R. Spalart. On the far wake and induced drag of aircraft. *Journal of Fluid Mechanics*, 603:413–430, 2008. DOI: 10.1017/s0022112008001146.

[27] Sho Sato. *The Power Balance Method for aerodynamic performance assessment*. PhD thesis, 2012.

[28] Drewan S. Sanders and Panagiotis Laskaridis. Full-aircraft energy-based force decomposition applied to boundary-layer ingestion. *AIAA Journal*, 58(10):4357–4373, 2020. DOI: 10.2514/1.j058695.

[29] Aurélien Arntz and David Hue. Exergy-based performance assessment of the nasa common research model. *AIAA Journal*, 54(1):88–100, 2016. DOI: 10.2514/1.j054127.

[30] Maurice J. Zucrow. *Aircraft and missile propulsion*. Wiley, 1958.

[31] Philip Graham Hill and Carl R. Peterson. *Mechanics and thermodynamics of propulsion*. 2014.

[32] Jack L. Kerrebrock. *Aircraft Engines and Gas Turbines*. MIT Press, 1996.

[33] A. Talezade Shirazi and M. Dehghan Manshadi. Streamlined bodies drag force estimation using wake integration technique. *Journal of the Brazilian Society of Mechanical Sciences and Engineering*, 42(6), 2020.

[34] Makoto Ueno, Kazuomi Yamamoto, Kentaro Tanaka, Mitsuhiro Murayama, and Renato Tognaccini. Far-field drag analysis of nasa common research model simulation. *Journal of Aircraft*, 50(2):388–397, 2013. DOI: 10.2514/1.c031766.

[35] M. Rivers. Nasa common research model | providing data worldwide. Available at: https://commonresearchmodel.larc.nasa.gov/>, 2012.

[36] N. Blaesser. Interference drag due to engine nacelle location for a single-aisle, transonic aircraft. *Ph.D. Dissertation Virginia Polytechnic Institute and State University*, 2019.

[37] D. Destarac and J. van der Vooren. Drag/thrust analysis of jet-propelled transonic transport aircraft; definition of physical drag components. *Aerospace Science and Technology*, 8(6):545–556, 2004. DOI: 10.1016/j.ast.2004.03.004.

[38] Ioannis Goulos, John Otter, Fernando Tejero, Josep Hueso Rebassa, David MacManus, and Christopher Sheaf. Civil turbofan propulsion aerodynamics: Thrust-drag accounting and impact of engine installation position. *Aerospace Science and Technology*, 111:106533, 2021. DOI: 10.1016/j.ast.2021.106533.

[39] M. Méheut and D. Bailly. Drag-breakdown methods from wake measurements. *AIAA Journal*, 46(4):847–862, 2008. DOI: 10.2514/1.29051.

[40] Arm aerial instrument workshop report. *U.S. Department of Energy*, 2020.

[41] Adam Steinberg and Sukesh Roy. *Laser Rayleigh Scattering, Filtered Rayleigh Scattering, and Interferometric Rayleigh Scattering.* AIAA, 2023.

[42] A. Cutler and T. Lowe. Optical diagnostics for reacting and non-reacting flow: Theory and practice. *AIAA Progress in Aeronautics [in press]*, 2022.

[43] L. Rayleigh. X. on the electromagnetic theory of light. *The London, Edinburgh, and Dublin Philosophical Magazine and Journal of Science*, 12:81–101, 1881.

[44] L. Rayleigh. Xxxiv. on the transmission of light through an atmosphere containing small particles in suspension, and on the origin of the blue of the sky. *The London, Edinburgh, and Dublin Philosophical Magazine and Journal of Science*, 47:375–384, 1899.

[45] J. W. Strutt. Lviii. on the scattering of light by small particles. *The London, Edinburgh, and Dublin Philosophical Magazine and Journal of Science*, 41:447–454, 1871.

[46] J. W. Strutt. Xv. on the light from the sky, its polarization and colour. *The London, Edinburgh, and Dublin Philosophical Magazine and Journal of Science*, 41:107–120, 1871.

[47] J. W. Strutt. Xxxvi. on the light from the sky, its polarization and colour. *The London, Edinburgh, and Dublin Philosophical Magazine and Journal of Science*, 41:274–279, 1871.

[48] Victor Twersky. Rayleigh scattering. *Applied Optics*, 3(10):1150, 1964. DOI: 10.1364/ao.3.001150.

[49] Andrew T. Young. Rayleigh scattering. *Applied Optics*, 20(4):533, 1981. DOI: 10.1364/ao.20.000533.

[50] Richard B Miles, Walter R Lempert, and Joseph N Forkey. Laser rayleigh scattering. *Measurement Science and Technology*, 12(5), 2001. DOI: 10.1088/0957-0233/12/5/201.

[51] Byun G. Boyda, M. and T. Lowe. Non-intrusive internal flow quantification using filtered rayleigh scattering. 2022.

[52] G. Tenti, C. D. Boley, and Rashmi C. Desai. On the kinetic model description of rayleigh–brillouin scattering from molecular gases. *Canadian Journal of Physics*, 52(4):285–290, 1974. DOI: 10.1139/p74-041.

[53] Xingguo Pan, Mikhail N. Shneider, and Richard B. Miles. Coherent rayleigh-brillouin scattering in molecular gases. *Physical Review A*, 69(3), 2004. DOI: 10.1103/physreva.69.033814.

[54] Ulrich Doll, Michael Dues, Tommaso Bacci, Alessio Picchi, Guido Stockhausen, and Christian Willert. Aero-thermal flow characterization downstream of an NGV cascade by five-hole probe and filtered rayleigh scattering measurements. *Experiments in Fluids*, 59(10), 2018. DOI: 10.1007/s00348-018-2607-z.

[55] Mie scattering. Available at: https://www.lavision.de/en/techniques/mie-rayleigh-raman/.

[56] Matthew T. Boyda, Gwibo Byun, Ashley J. Saltzman, and Todd Lowe. Influence of mie and geometric scattering contributions on temperature and density measurements in filtered rayleigh scattering. *AIAA Scitech 2020 Forum*, 2020. DOI: 10.2514/6.2020-1516.

[57] H. Shimizu, S. A. Lee, and C. Y. She. High spectral resolution lidar system with atomic blocking filters for measuring atmospheric parameters. *Applied Optics*, 22(9):1373, 1983. DOI: 10.1364/ao.22.001373.

[58] Joseph N. Forkey, Walter R. Lempert, and Richard B. Miles. Corrected and calibrated i_2 absorption model at frequency-doubled nd:yag laser wavelengths. *Applied Optics*, 36(27):6729, 1997. DOI: 10.1364/ao.36.006729.

[59] J. N. Forkey, N. D. Finkelstein, W. R. Lempert, and R. B. Miles. Demonstration and characterization of filtered rayleigh scattering for planar velocity measurements. *AIAA Journal*, 34(3):442–448, 1996. DOI: 10.2514/3.13087.

[60] Joseph Norman Forkey. Development and demonstration of filtered rayleigh scattering: A laser based flow diagnostic for planar measurement of velocity, temperature, and pressure. 1996.

[61] A. Yalin and R. Miles. Ultraviolet filtered rayleigh scattering temperature measurements using a mercury filter. *37th Aerospace Sciences Meeting and Exhibit*, 1999. DOI: 10.2514/6.1999-642.

[62] Andreas Fischer, Lars Büttner, Jürgen Czarske, Michael Eggert, and Harald Müller. Measurement uncertainty and temporal resolution of doppler global velocimetry using laser frequency modulation. *Applied Optics*, 47(21):3941, 2008. DOI: 10.1364/ao.47.003941.

[63] Hiroshi Shimizu, Kazuo Noguchi, and Chiao-Yao She. Atmospheric temperature measurement by a high spectral resolution lidar. *Applied Optics*, 25(9):1460, 1986. DOI: 10.1364/ao.25.001460.

[64] Madison E. Hetlage, Yue Wu, and Christopher Limbach. Feasibility analysis of optically pumped barium vapor for filtered rayleigh scattering at the nd:yag third harmonic. *AIAA Aviation 2019 Forum*, 2019. DOI: 10.2514/6.2019-3382.

[65] M. Boguszko and G.S. Elliott. Property measurement utilizing atomic/molecular filter-based diagnostics. *Progress in Aerospace Sciences*, 41(2):93–142, 2005. DOI: 10.1016/j.paerosci.2005.03.001.

[66] Daniel R. Cadel and K. Todd Lowe. Investigation of measurement sensitivities in cross-correlation doppler global velocimetry. *Optics and Lasers in Engineering*, 86:44–52, 2016. DOI: 10.1016/j.optlaseng.2016.05.003.

[67] Tom O. Charrett, David S. Nobes, and Ralph P. Tatam. Investigation into the selection of viewing configurations for three-component planar doppler velocimetry measurements. *Applied Optics*, 46(19):4102, 2007. DOI: 10.1364/ao.46.004102.

[68] Ulrich Doll, Eike Burow, Guido Stockhausen, and Christian Willert. Methods to improve pressure, temperature and velocity accuracies of filtered rayleigh scattering

measurements in gaseous flows. *Measurement Science and Technology*, 27(12):125204, 2016. DOI: 10.1088/0957-0233/27/12/125204.

[69] Thomas A. Mcmanus, Ignacio Trueba Monje, and Jeffrey A. Sutton. Experimental assessment of the tenti s6 model for combustion-relevant gases and filtered rayleigh scattering applications. *Applied Physics B*, 125(1), 2019. DOI: 10.1007/s00340-018-7121-8.

[70] F. B. Hanson. Kinetic models for a gas with internal structure. *Physics of Fluids*, 10(2):345, 1967. DOI: 10.1063/1.1762114.

[71] F. B. Hanson. Kinetic description of the propagation of plane sound waves in a diatomic gas. *Physics of Fluids*, 12(1):84, 1969. DOI: 10.1063/1.1692298.

[72] B. Witschas. Analytical model for rayleigh–brillouin line shapes in air. *Applied Optics*, 50(3):267, 2011. DOI: 10.1364/ao.50.000267.

[73] Gregory J Hunt, Cody R Ground, and Robin L Hunt. Fast approximations of spectral lineshapes to enable optimization of a filtered rayleigh scattering experiment. *Measurement Science and Technology*, 31(9):095203, 2020. DOI: 10.1088/1361-6501/ab8a7e.

[74] Ulrich Doll, Eike Burow, Guido Stockhausen, and Christian Willert. Methods to improve pressure, temperature and velocity accuracies of filtered rayleigh scattering measurements in gaseous flows. *Measurement Science and Technology*, 27(12):125204, 2016.

[75] Gustavo Olague and Roger Mohr. Optimal camera placement for accurate reconstruction. *Pattern Recognition*, 35(4):927–944, 2002. DOI: 10.1016/s0031-3203(01)00076-0.

[76] Camera calibration toolbox for matlab. Available at: http://robots.stanford.edu/cs223b04/ JeanYvesCalib/.

[77] R. Tsai. A versatile camera calibration technique for high-accuracy 3d machine vision metrology using off-the-shelf tv cameras and lenses. *IEEE Journal on Robotics and Automation*, 3(4):323–344, 1987. DOI: 10.1109/jra.1987.1087109.

[78] Antoni Buades, Bartomeu Coll, and Jean-Michel Morel. Non-local means denoising. *Image Processing On Line*, 1:208–212, 2011. DOI: 10.5201/ipol.2011.bcmnlm.

[79] Orcun Goksel and S E Salcudean. Image-based variational meshing. *IEEE Transactions on Medical Imaging*, 30(1):11–21, 2011. DOI: 10.1109/tmi.2010.2055884.

[80] Matthew T. Boyda and Kevin T. Lowe. Cross-correlation doppler global velocimetry using rayleigh and mie scattering. *2018 AIAA Aerospace Sciences Meeting*, 2018. DOI: 10.2514/6.2018-1766.

[81] M Boyda, G Byun, and K T Lowe. Investigation of velocity and temperature measurement sensitivities in cross-correlation filtered rayleigh scattering (ccfrs). *Measurement Science and Technology*, 30(4):044004, 2019. DOI: 10.1088/1361-6501/ab0350.

[82] Matthew Boyda, Gwibo Byun, Ashley Saltzman, and K Todd Lowe. Geometric scattering removal in cross-correlation doppler global velocimetry by structured illumination. *Measurement Science and Technology*, 31(6):064004, 2020. DOI: 10.1088/1361-6501/ab6b4f.

[83] Matthew Boyda, Gwibo Byun, and Todd Lowe. Filtered rayleigh scattering for aerodynamic measurements in confined flows. *Measurement Science and Technology*.

[84] Ulrich Doll, Guido Stockhausen, and Christian Willert. Endoscopic filtered rayleigh scattering for the analysis of ducted gas flows. *Experiments in Fluids*, 55(3), 2014. DOI: 10.1007/s00348-014-1690-z.

[85] Ulrich Doll, Guido Stockhausen, and Christian Willert. Pressure, temperature, and three-component velocity fields by filtered rayleigh scattering velocimetry. *Optics Letters*, 42(19):3773, 2017. DOI: 10.1364/ol.42.003773.

[86] U. Doll, M. Fischer, G. Stockhausen, and C. Willert. Frequency scanning filtered rayleigh scattering in combustion experiments. *16th Int Symp on Applications of Laser Techniques to Fluid Mechanics*, 2012.

[87] Ulrich Doll, Eike Burow, Manfred Beversdorff, Guido Stockhausen, Christian Willert, Christian Morsbach, Daniel Schluss, and Martin Franke. The flow field inside a ranque-hilsch vortex tube part i: Experimental analysis using planar filtered rayleigh scattering. *Proceeding of Ninth International Symposium on Turbulence and Shear Flow Phenomena*, 2015. DOI: 10.1615/tsfp9.800.

[88] J. Ireland. Applying the cramer-rao lower bound to spectroscopic measurements. *11th European Solar Physics Meeting*, 2005.

[89] J. Ireland. Precision limits to emission-line profile measuring experiments. *The Astrophysical Journal*, 620(2):1132–1139, 2005. DOI: 10.1086/427230.

[90] Daniel R. Cadel and K. Todd Lowe. Cross-correlation doppler global velocimetry (cc-dgv). *Optics and Lasers in Engineering*, 71:51–61, 2015. DOI: 10.1016/j.optlaseng.2015.03.012.

[91] Daniel Bivolaru, Andrew Cutler, and Paul Danehy. Spatially- and temporally-resolved multi-parameter interferometric rayleigh scattering. *49th AIAA Aerospace Sciences Meeting including the New Horizons Forum and Aerospace Exposition*, 2011. DOI: 10.2514/6.2011-1293.

[92] Isaac Yeaton, Pietro Maisto, and Kevin Lowe. Time resolved filtered rayleigh scattering for temperature and density measurements. *28th Aerodynamic Measurement Technology, Ground Testing, and Flight Testing Conference*, 2012. DOI: 10.2514/6.2012-3200.

[93] Jordi Estevadeordal, Naibo Jiang, Andrew D. Cutler, Josef J. Felver, Mikhail N. Slipchenko, Paul M. Danehy, James R. Gord, and Sukesh Roy. High-repetition-rate interferometric rayleigh scattering for flow-velocity measurements. *Applied Physics B*, 124(3), 2018. DOI: 10.1007/s00340-018-6908-y.

[94] Amy F. Mielke, Kristie A. Elam, and Chih-Jen Sung. Multi-property measurements at high sampling rates using rayleigh scattering. *AIAA Journal*, 47(4):850–862, 2009. DOI: 10.2514/1.37369.

[95] Andrew D. Cutler, Keith Rein, Sukesh Roy, Paul M. Danehy, and Naibo Jiang. 100-khz interferometric rayleigh scattering for multi-parameter flow measurements. *Optics Express*, 28(3):3025, 2020. DOI: 10.1364/oe.380934.

[96] Richard Miles, Joseph Forkey, and Walter Lempert. Filtered rayleigh scattering measurements in supersonic/hypersonic facilities. *28th Joint Propulsion Conference and Exhibit*, 1992. DOI: 10.2514/6.1992-3894.

[97] Fu-Quan Zhao and Hiroyuki Hiroyasu. The applications of laser rayleigh scattering to combustion diagnostics. *Progress in Energy and Combustion Science*, 19(6):447–485, 1993. DOI: 10.1016/0360-1285(93)90001-u.

[98] K. Todd Lowe. Laser velocimetry for turbofan inlet distortion applications. *Aircraft Engineering and Aerospace Technology*, 92(1):20–26, 2020. DOI: 10.1108/aeat-11-2018-0285.

[99] Ashley J. Saltzman, Matthew T. Boyda, Kevin T. Lowe, and Wing Ng. Filtered rayleigh scattering for velocity and temperature measurements of a heated supersonic jet with thermal non-uniformity. *25th AIAA/CEAS Aeroacoustics Conference*, 2019. DOI: 10.2514/6.2019-2677.

[100] Ashley J. Saltzman, Steven J. Beresh, Katya M. Casper, Brian P. Denk, Rajkumar Bhakta, Marie E. De Zetter, and Russell W. Spillers. Carbon dioxide seeding system for enhanced rayleigh scattering in sandia's hypersonic wind tunnel. *AIAA AVIATION 2022 Forum*, 2022.

[101] Tamara Guimarães, K. Todd Lowe, and Walter F. O'Brien. Streamvane turbofan inlet swirl distortion generator: Mean flow and turbulence structure. *Journal of Propulsion and Power*, 34(2):340–353, 2018. DOI: 10.2514/1.b36422.

[102] Rick Cressall, Robbie Schaap, Douglas R Neal, Alex Mychkovsky, John Charonko, and Barton L Smith. Accuracy of volumetric flow rate inflow/outflow measurement by integrating piv velocity fields. *Measurement Science and Technology*, 31(11):115303, 2020. DOI: 10.1088/1361-6501/ab9bb7.

[103] James E. Bridges and Mark P. Wernet. Piv measurements of a low-noise top-mounted propulsion installation for a supersonic airliner. *AIAA Scitech 2019 Forum*, 2019. DOI: 10.2514/6.2019-0252.

[104] Michael Miller, Mark Allen, and Tim Conners. Design and flight qualification of a diode laser-based optical mass flux sensor. *34th AIAA/ASME/SAE/ASEE Joint Propulsion Conference and Exhibit*, 1998. DOI: 10.2514/6.1998-3714.

[105] Kent H. Lyle, Jay B. Jeffries, and Ronald K. Hanson. Diode-laser sensor for air-mass flux 1: Design and wind tunnel validation. *AIAA Journal*, 45(9):2204–2212, 2007. DOI: 10.2514/1.26360.

[106] Kent H. Lyle, Jay B. Jeffries, Ronald K. Hanson, and Michael Winter. Diode-laser sensor for air-mass flux 2: Non-uniform flow modeling and aeroengine tests. *AIAA Journal*, 45(9):2213–2223, 2007. DOI: 10.2514/1.27683.

[107] K. Todd Lowe, Raul Otero, and Wing Ng. In-flight thrust monitoring: An acoustics-based approach. *Aircraft Engineering and Aerospace Technology*, 92(1):15–19, 2020. DOI: 10.1108/aeat-11-2018-0287.

[108] Quellwerke. P100-rx. *JetCat*, 2023. https://www.jetcat.de/en/productdetails/ produkte/jetcat/produkte/hobby/Engines/p100rx.

[109] Boyda, G Byun, and KT Lowe. Cross-correlation filtered rayleigh scattering (ccfrs). In *19th International Symposium on Application of Laser Techniques to Fluid Mechanics*, pages 16–19, 2018.

[110] J. Kennedy and R. Eberhart. Particle swarm optimization. *Proceedings of ICNN'95 - International Conference on Neural Networks*.

[111] Efrén Mezura-Montes and Carlos A. Coello. Constraint-handling in nature-inspired numerical optimization: Past, present and future. *Swarm and Evolutionary Computation*, 1(4):173–194, 2011.

[112] M.E.H. Pedersen and A.J. Chipperfield. Simplifying particle swarm optimization. *Applied Soft Computing*, 10(2):618–628, 2010.

[113] Thomas F. Coleman and Yuying Li. An interior trust region approach for nonlinear minimization subject to bounds. *SIAM Journal on Optimization*, 6(2):418–445, 1996.

[114] Thomas F. Coleman and Yuying Li. On the convergence of interior-reflective newton methods for nonlinear minimization subject to bounds. *Mathematical Programming*, 67(1-3):189–224, 1994.

[115] J.E. Dennis. Some computational techniques for the nonlinear least squares problem. *Numerical Solution of Systems of Nonlinear Algebraic Equations*, page 157–183, 1973.

[116] Kenneth Levenberg. A method for the solution of certain non-linear problems in least squares. *Quarterly of Applied Mathematics*, 2(2):164–168, 1944.

[117] Donald W. Marquardt. An algorithm for least-squares estimation of nonlinear parameters. *Journal of the Society for Industrial and Applied Mathematics*, 11(2):431–441, 1963.

[118] Jorge J. Moré. The levenberg-marquardt algorithm: Implementation and theory. *Lecture Notes in Mathematics*, page 105–116, 1978.

[119] J. More, B. Garbow, and K. Hillstrom. User guide for minpack-1. [in fortran]. 1980.

[120] H. K. McCue. Programs naes and ss: User-oriented programs for solving nonlinear algebraic equations and ordinary differential equations. [in fortran iv]. 1976.

[121] Garrett Pitt and K. Todd Lowe. Ultraviolet (uv) laser implementation and measurement sensitivities in filtered rayleigh scattering for aerodynamic flows [unpublished manuscript]. *Virginia Polytechnic Institute and State University*, 2022.

[122] Camera calibration toolbox for matlab. *Caltech DATA*, 2023. https://data.caltech.edu/records/jx9cx-fdh55.

[123] Pco edge 4.2 bi uv scientific cameras. *PCO*, Jul 2019. https://www.pco.de/scientific-cameras/pcoedge-42-bi-uv/.

[124] B.S. Reddy and B.N. Chatterji. An fft-based technique for translation, rotation, and scale-invariant image registration. *IEEE Transactions on Image Processing*, 5(8):1266–1271, 1996.

[125] Zhanying Chen, Xuekun Li, Zongyu Zhu, Zeming Zhao, Liping Wang, Sheng Jiang, and Yiming Rong. The optimization of accuracy and efficiency for multistage precision grinding process with an improved particle swarm optimization algorithm. *International Journal of Advanced Robotic Systems*, 17(1):172988141989350, 2020.

[126] Austin Davis, James Naleway, Alex Nguyen, Nick Scott, Emily Smith, and Luke Woodward. Design and test of turbine-powered uas propulsion system for methane fuel. 2018.

[127] Jeffrey A. Sutton and James F. Driscoll. Rayleigh scattering cross sections of combustion species at 266, 355, and 532 nm for thermometry applications. *Optics Letters*, 29(22):2620, 2004.

[128] Joseph Fielding, Jonathan H. Frank, Sebastian A. Kaiser, Mitchell D. Smooke, and Marshall B. Long. Polarized/depolarized rayleigh scattering for determining fuel concentrations in flames. *Proceedings of the Combustion Institute*, 29(2):2703–2709, 2002.

[129] W.C. Gardiner, Y. Hidaka, and T. Tanzawa. Refractivity of combustion gases. *Combustion and Flame*, 40:213–219, 1981.

[130] Mixing measurement by rayleigh scattering. *Engine Combustion Network*. https://ecn.sandia.gov/diesel-spray-combustion/experimental-diagnostics/mixing-measurement-by-rayleigh-scattering/.

[131] Rayleigh scattering. https://cefrc.princeton.edu/document/38.

[132] Thomas Coulon, Riley Johnson, Lauren Jones, Michael Mines, Grant Schumacher, and Colton Swart. Thrust to weight improvement of jetcat p100-rx turbojet engine.

[133] E. P. Warner and K. T. Lowe. Machine-learned background quantification for filtered rayleigh scattering measurement processing. *Submitted to AIAA SciTech 2023*, 2023.

[134] Ulrich Doll, Ingo Röhle, Michael Dues, and Ralf Kapulla. Time-resolved multi-parameter flow diagnostics by filtered rayleigh scattering: System design through multi-objective optimization. *Measurement Science and Technology*, 33(10):105204, 2022.